The Dissertation Committee for Kuo-Hsin Yang Certifies that this is the approved version of the following dissertation:

Stress Distribution within Geosynthetic-Reinforced Soil Structures

Committee:

Jorge G. Zornberg, Supervisor

Ellen M. Rathje

John L. Tassoulas

Stelios Kyriakides

Christianne D. L. Nogueira

Stress Distribution within Geosynthetic-Reinforced Soil Structures

by

Kuo-Hsin Yang, B.S., M.S.

Dissertation

Presented to the Faculty of the Graduate School of
The University of Texas at Austin
in Partial Fulfillment
of the Requirements
for the Degree of

Doctor of Philosophy

The University of Texas at Austin
August 2009

Dedication

To My Family

All the love and thanks in world

Acknowledgements

I would like to acknowledge my supervisor, Dr. Jorge Zornberg, for his encouragement, guidance and wisdom throughout my years as a PhD student. He provided me with a wonderful education on the geotechnical engineering specifically on the topic of geosynthetics application. He helped me to develop my research, teaching and presentation skills, which all are the foundations of my future career.

I would also like to thank Dr. Christianne Nogueira and her lovely family. They provide a great and warm help to me during my journey to Brazil as an exchange student. My knowledge was enhanced by the training of finite element programming and my perspective was enriched by the wonderful Brazilian culture.

I also want to thank Dr. Stephen Wright for sharing with me his wealth of knowledge, particularly with respect to soil mechanics, stability of earth structures and limit equilibrium analysis. I would also like to express my sincerest gratitude to Dr. Ellen Rathje, Dr. John Tassoulas and Dr. Stelios Kyriakides for serving on my doctoral committee. I appreciate all their advice and support along the way. Their advice was invaluable.

I also want to thank Dr. Jian-Ye Ching, Dr. Chia-Nan Liu, and Dr. Fu-Chun Wu, the professors in Taiwan. Their guidance helping me to develop my academic career in Taiwan is sincerely and deeply appreciated.

My study in the University of Texas was funded by Texas Department of

Transportation through a research project and by Cockrell School of Engineering through many scholarships and teaching assistantship. I give my sincerest appreciation to them for their financial support. I also greatly appreciated the opportunity to work on such an amazing project and the opportunity of teaching undergraduate geotechnical laboratory.

I would not have thoroughly enjoyed my time and my work here at UT without sharing my life with many friends and colleagues who I had the most delightful opportunity to get to know during my stint at UT. To my research group (John, Christine, Ranjiv, Jeff, Brian, Julio, Nate, Jongwan), you all are awesome. I have enjoyed our time together and I truly thank you from the very bottom of my heart. To my two year housemate, Ranjiv, I cannot express my thanks enough for being so supportive and generous. I truly enjoyed that we were working on the same path and seeking for the same goal. I also enjoyed the conversation with you related to the philosophy of life. To my American brothers, Michael and Nate, you are my best friends.

Most importantly, my eternal gratitude goes to my family, my Father, Mother, brother, sister in law and new coming niece, and my future wife, Chia-Chen. I am not sure there are words for how much I love you and how much your love and support have meant to me while I have been traveling down this hard, toilsome but incredibly rewarding road. But I have only been successful at achieving my goals because of you.

"Ph.D. is not only a degree for me but also a long process for me to redefine and challenge myself."

Dr. Zornberg and I at engineering graduation commencement,
May 22, 2009

Dissertation committee: (right to left) Dr. Tassoulas, Dr. Rathje, Dr. Zornberg, I, Dr. Nogueira, and Dr. Kyriakides after passing the defense examination, August 10, 2009

Stress Distribution within Geosynthetic-Reinforced Soil Structures

Publication No._____________

Kuo-Hsin Yang, Ph.D.
The University of Texas at Austin, 2009

Supervisor: Jorge G. Zornberg

This dissertation evaluates the behavior of Geosynthetic-Reinforced Soil (GRS) retaining structures under various soil stress states, with specific interest in the development and distribution of soil and reinforcement stresses within these structures. The stress distribution within the GRS structures is the basis of much of the industry's current design. Unfortunately, the stress information is often not directly accessible through most of current physical testing and full-scale monitoring methods. Numerical simulations like the finite element method have provided good predictions of conservatively designed GRS structures under working stress conditions. They have provided little insight, however, into the stress information under large soil strain conditions. This is because in most soil constitutive models the post-peak behavior of soils is not well represented. Also, appropriate numerical procedures are not generally available in finite element codes, the codes used in geotechnical applications. Such procedures are crucial to properly evaluating comparatively flexible structures like GRS structures.

Consequently, this study tries to integrate newly developed numerical procedures to improve the prediction of performance of GRS structures under large soil strain conditions. There are three specific objectives: 1) to develop a new softening soil model for modeling the soil's post-peak behavior; 2) to implement a stress integration algorithm, modified forward Euler method with error control, for obtaining better stress integration results; and 3) to implement a nonlinear reinforcement model for representing the nonlinear behavior of reinforcements under large strains. The numerical implementations were made into a finite element research code, named Nonlinear Analysis of Geotechnical Problems (ANLOG). The updated finite element model was validated against actual measurement data from centrifuge testing on GRS slopes (under both working stress and failure conditions).

Examined here is the soil and reinforcement stress information. This information was obtained from validated finite element simulations under various stress conditions. An understanding of the actual developed soil and reinforcement stresses offers important insights into the basis of design (e.g., examining in current design guidelines the design methods of internal stability). Such understanding also clarifies some controversial issues in current design. This dissertation specifically addresses the following issues: 1) the evolution of stresses and strains along failure surface; 2) soil strength properties (e.g., peak or residual shear strength) that govern the stability of GRS structures; 3) the mobilization of reinforcement tensions.

The numerical result describes the stress response by evaluating the development of soil stress level *S*. This level is defined as the ratio of the current mobilized soil shear strength to the peak soil shear strength. As loading increases, areas of high stress levels are developed and propagated along the potential failure surface. After the stress levels reach unity (i.e., soil reaches its peak strength), the beginning of softening of soil strength

is observed at both the top and toe of the slope. Afterward, the zones undergoing soil softening are linked, forming a band through the entire structure (i.e., a fully developed failure surface). Once the band has formed and there are a few loading increments, the system soon reaches, depending on the tensile strength of the reinforcements, instability. The numerical results also show that the failure surface corresponds to the locus of intense soil strains and the peak reinforcement strain at each reinforcement layer. What dominates the stability of GRS structures is the soil peak strength before the completed linkage of soil-softening regions. Afterward, the stability of GRS structures is mainly sustained by the soil shear strength in the post-peak region and the tensile strength of reinforcements. It was also observed that the mobilization of reinforcement tensions is disproportional to the mobilization of soil strength. Tension in the reinforcements is barely mobilized before soil along the failure surface first reaches its peak shear strength. When the average mobilization of soil shear strength along the potential failure surface exceeds approximately 95% of its peak strength, the reinforcement tensions start to be rapidly mobilized. Even so, when the average mobilization of soil strength reaches 100% of its peak shear strength, still over 30% of average reinforcement strength has not yet been mobilized. The results were used to explain important aspects of the current design methods (i.e., earth pressure method and limit equilibrium analysis) that result in conservatively designed GRS structures.

Key Words: GRS structures, Finite element simulation, Soil post-peak behavior, Soil strength softening, Stress development and distribution

Table of Contents

CHAPTER 1

CHAPTER 2

CHAPTER 3

CHAPTER 4

CHAPTER 5

CHAPTER 6

CHAPTER 7

CHAPTER 8

CHAPTER 9

List of Tables

List of Figures

List of Symbols and Nomenclature

English Letters-Upper Case

A	Variable in original softening law	
B	Variable in original softening law	
B [:,:]	Strain-displacement matrix	[1/L]
C	Material parameter in hardening law	
C_1	Material parameter in nonlinear reinforcement model	
C_2	Material parameter in nonlinear reinforcement model	
D	Variable in hardening law	
D [:,:]	Constitutive matrix	[F/L^2]
D_e [:,:]	Elastic constitutive matrix	[F/L^2]
D_{ep} [:,:]	Elasto-plastic constitutive matrix	[F/L^2]
D_p [:,:]	Plastic constitutive matrix	[F/L^2]
D_T	Total displacement	[L]
D_{tmax}	Load distribution factor	
D_r	Relative density of backfill	(%)
D_y	Vertical displacement	[L]
E	Young's modulus	[F/L^2]
E_i	Initial stiffness in hyperbolic reinforcement model	[F/L^2]
F_{ext} [:]	Global external force vector	[F]
F_{int} [:]	Global internal force vector	[F]
F_b^e [:]	Elemental external force vector from body force	[F]
F_{ext}^e [:]	Elemental external force vector	[F]
F_{int}^e [:]	Elemental internal force vector	[F]
F_s^e [:]	Elemental external force vector from surface load	[F]

F_δ^e [:]	Elemental external force vector from prescribed displacement	[F]
FS	Factor of Safety	
H	Height of GRS structures (Chap.2)	[L]
	Hardening and softening modulus (Chap.4)	[L^2/F]
I_1	The first invariant of the stress tensor	[F/L^2]
I_2	The second invariant of the stress tensor	[F^2/L^4]
I_3	The third invariant of the stress tensor	[F^3/L^6]
I_d	Number of iteration desired to reach convergence	
I_{i-1}	Number of iteration achieved at the previous step	
J [:,:]	Jacobian matrix	
J_2'	The second invariant of the deviatoric stress tensor	[F^2/L^4]
J_i	Tensile stiffness of an individual reinforcement layer	[F/L]
K_a	Theoretical Rankine active earth pressure coefficient	
K_{abh}	Horizontal component of active earth pressure coefficient	
K_{avh}	Horizontal component of active earth pressure coefficient for vertical walls	
K^e [:,:]	Elemental stiffness matrix	[F/L]
K_n	Normal stiffness of interface	[F/L^3]
K_o	Jaky at-rest earth pressure coefficient	
K_s	Shear stiffness of interface	[F/L^3]
M	Material parameter in elastic model	
N [:,:]	Shape function matrix	
N_f	Failure g-level	(g)
N_g	g-level	(g)
R	Relative error in stress integration algorithm	
R_d	Reinforcement strength reduction factor	
R_f	Failure ratio in hyperbolic reinforcement model	
S	Available soil strength (Chap.1)	[F/L^2]
	Soil stress level (Chap.4)	
S_{global}	Global reinforcement stiffness in K-stiffness method	[F/L]

S_{local}	Local reinforcement stiffness in K-stiffness method	[F/L]
S_m	Mobilized soil strength	[F/L^2]
S_q	Boundary domain of prescribed force	[L]
S_R	Reinforcement stress level	
S_u	Boundary domain of prescribed displacement	[L]
S_v	Vertical spacing between layers of reinforcement	[L]
$T_{confined}$	Confined reinforcement tension	[F/L]
T_m	Mobilized reinforcement strength	[F/L]
T_{max}	Maximum tension in each reinforcement layer	[F/L]
$T_{unconfined}$	Unconfined reinforcement tension	[F/L]
T_{ult}	Ultimate tensile strength of reinforcement	[F/L]
$T_{ult\_confined}$	Ultimate confined tensile strength of reinforcement	[F/L]
$T_{ult\_unconfined}$	Ultimate unconfined tensile strength of reinforcement	[F/L]
V	Volume of problem domain	[L^3]
W_p	Plastic work	[F/L^2]
$W_{p,0}$	Initial state of hardening parameter	[F/L^2]
$W_{p,temp}$	Temporary estimate of the updated hardening parameter	[F/L^2]
$(W_p)_{S=1}$	Plastic work at peak stress level	[F/L^2]
δW_p^I	The first estimate of the updated hardening parameter	[F/L^2]
δW_p^{II}	The second estimate of the updated hardening parameter	[F/L^2]
x,y,z	Local coordinate	[L]

English Letters-Lower Case

a	Material parameter in proposed softening model	
a'	Material parameter in failure criterion	
b	Material parameter in proposed softening model	
b [:]	Body force vector	[F/L^3]
b'	Material parameter in original softening law	

b^e [:]	Elemental body force vector	[F/L^3]
c	Cohesion of backfill materials (Chap.2)	[F/L^2]
	Material parameter in proposed softening model (Chap.4)	
d	Relative displacement between 5g and Ng	[L]
e_0	Void ratio	
e_{max}	Maximum void ratio	
e_{min}	Minimum void ratio	
f_n	Peak failure criterion	
$f_p(\cdot)$	Yield function	
f'_p	Shape of yield surface	
f''_p	Size of yield surface	
$(f''_p)_{S=1}$	Size of yield surface at peak stress level	
f''_{pr}	Size of residual yield surface	
$g_p(\cdot)$	Plastic potential function	
h	Material parameter in yield criterion	
k_r/K_a	Normalized horizontal earth pressure coefficient	
m	Material parameter in failure criterion (Chap.4)	
	Number of strain subincrements (Chap.5)	
n	Number of reinforcement layers	
n [:]	Normal vector of surface	
p	Material parameter in hardening law	
p_a	Atmospheric pressure	[F/L^2]
q	Variable in yield criterion (Chap.4)	
	Size of the next dimensionless step (Chap.5)	
	Deviatoric stress (Chap.8)	[F/L^2]
q [:]	Surface force vector	[F/L^2]
q^e [:]	Elemental surface force vector	[F/L^2]
tol	Specified tolerance	[L]

u [:]	Displacement vector	[L]
$\hat{u}$ [:]	Nodal displacement vector	[L]
Δu [:]	Displacement increment vector	[L]
$\Delta\hat{u}$ [:]	Incremental nodal displacement vector	[L]
$\Delta\hat{u}^0$ [:]	Prediction solution for displacement in iteration scheme	[L]
δu [:]	Virtual displacement vector	[L]
$\delta\Delta\hat{u}$ [:]	Correction solution for displacement in iteration scheme	[L]
z	Depth of the layer of reinforcement below the top of the backfill	[L]

Greek Letters-Upper Case

Φ_c	Influence factor of material cohesion in K-stiffness method	
Φ_{fb}	Influence factor of face batter in K-stiffness method	
Φ_{fs}	Influence factor of facing stiffness in K-stiffness method	
Φ_g	Influence factor of global reinforcement stiffness in K-stiffness method	
Φ_{local}	Influence factor of local reinforcement stiffness in K-stiffness method	
ξ,η,ζ	Natural coordinate	[L]
Ψ	Unbalanced force	[F]
Ψ_1	Parameter related to curvature parameter m	
Ψ_2	Material parameter in plastic potential model	

Greek Letters-Lower Case

α	Material parameter in yield criterion	
δ [:]	Prescribed displacement	[L]
δ_s	Horizontal relative displacement	[L]
ε [:]	Strain tensor	

ε_a	Axial strain	
ε_e [:]	Elastic strain tensor	
ε_p [:]	Plastic strain tensor	
ε_v	Volumetric strain	
$\Delta\varepsilon$ [:]	Strain increment	
$\delta\varepsilon$ [:]	Strain subincrement	
$\delta\varepsilon$ [:]	Virtual strain vector	
ϕ_{ps}	Peak fiction angle under plane strain conditions	(deg.)
ϕ_r	Residual strain fiction angle	(deg.)
ϕ_{tc}	Peak fiction angle under triaxial compression conditions	(deg.)
γ	Unit weight of backfill	[F/L^3]
η_1	Material parameter in failure criterion	
$\eta_{1,ps}$	Peak failure criterion under plane strain conditions	
$\eta_{1,tc}$	Peak failure criterion under triaxial compression conditions	
λ	Material parameter in elastic model	
$\Delta\lambda$	Incremental load factor	
$\Delta\lambda_0$	First incremental load factor	
$\Delta\lambda_{max}$	Maximum incremental load factor	
$\Delta\lambda_{min}$	Minimum incremental load factor	
$\delta\lambda_p$	Non negative scalar factor of proportionality	[F/L^2]
μ	Material parameter in plastic potential model	
ν	Poisson’s ratio	
ρ	Variable in hardening law	
σ [:]	Stress tensor	[F/L^2]
σ_0 [:]	Initial stress state	[F/L^2]
σ_1	Major principal stress	[F/L^2]
σ_2	Intermediate principal stress	[F/L^2]

σ_3	Minor principal stress and confining pressure	$[F/L^2]$
σ_h	Lateral earth pressure	$[F/L^2]$
σ_{temp} [:]	Temporary estimate of the updated stresses	$[F/L^2]$
σ_{v}	Overburden pressure	$[F/L^2]$
$\Delta\sigma$ [:]	Stress increment	$[F/L^2]$
$\delta\sigma^{I}$ [:]	The first estimate of the updated stresses	$[F/L^2]$
$\delta\sigma^{II}$ [:]	The second estimate of the updated stresses	$[F/L^2]$
$\delta\sigma^{I-II}$ [:]	Estimate of the local error in stress integration algorithm	$[F/L^2]$
τ	Shear stress	$[F/L^2]$
ψ	Dilatancy angle	(deg.)

Chapter 1: Introduction

1.1 MECHANICALLY STABILIZED EARTH RETAINING STRUCTURES

For millennia, civilizations have sought effective methods to construct stable soil retaining structures. In ancient China, for example, to reinforce soil to erect stable structures, builders incorporated into the soil layers of natural tensile elements. Today, reinforced soil retaining structures are often referred to as Mechanical Stabilized Earth (MSE) retaining structures. Over the last 40 years, MSE retaining structures have become a viable and cost-effective technique. They are now widely used in projects that include residences, highways, bridge abutments, and slope stabilization. Figure 1.1 shows several examples of MSE retaining structures.

MSE retaining structures have been constructed for such purposes as increasing Right of Way (ROW), resisting earth pressures, and providing load bearing on top of MSE structures, and allowing for changes of elevation in highway projects. A number of factors have propelled the acceptance of MSE retaining structures. These include qualities like aesthetics, reliability, and low cost. Moreover, good construction techniques, impressive seismic performances, and a striking ability to withstand large deformations without structural distress account for MSE structures desirability.

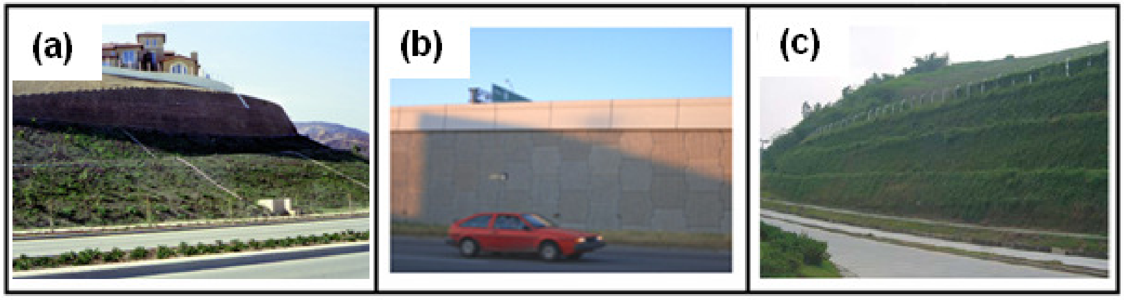

Figure 1.1: Application of MSE retaining structures: (a) residence; (b) highway bridge abutment; and (c) slope stability

MSE retaining structures have three main components: backfill, reinforcement, and facing element. For the backfill, to avoid the accumulation of water pressure, free drainage soils such as sand and gravel are often recommended. For the reinforcement, there are two main families divided according to their stiffness: inextensible reinforcement (e.g., metallic mat and strip) and extensible reinforcement (e.g., geogrid and geotextile). For the facing element, there are four families categorized, like the reinforcement, according to their stiffness characteristics. They range from flexible (like wrapped geosynthetic, gabion, or steel skin facings) to medium stiff (like articulated—incremental—concrete panels) to stiff (like full-height precast concrete panels) to rigid (like concrete gravity structures).

Unlike conventional gravity retaining structures, the stability of MSE retaining structures is sustained internally by the developed tensions along reinforcements. To be effective, the reinforcements must intersect potential failure surfaces in the soil mass. Strains within the soil mass generate strains in the reinforcements, which in turn, result in tensile loads in the reinforcements. These tensile loads act to restrict soil movement, thus imparting additional shear strength. This increase results in the composite soil/reinforcement system having significantly greater shear strength than the soil mass alone.

For forty decades researchers have studied the behavior and mechanism of MSE retaining structures. Many agencies have proposed design methods. However, due to the complex interaction between soil and reinforcement, the behavior and mechanics of MSE retaining structures are still not fully understood. To emphasize the importance of further study on the true understanding of the behavior and failure mechanisms of MSE retaining structures, Figure 1.2 provides examples of failures and collapses of MSE retaining structures.

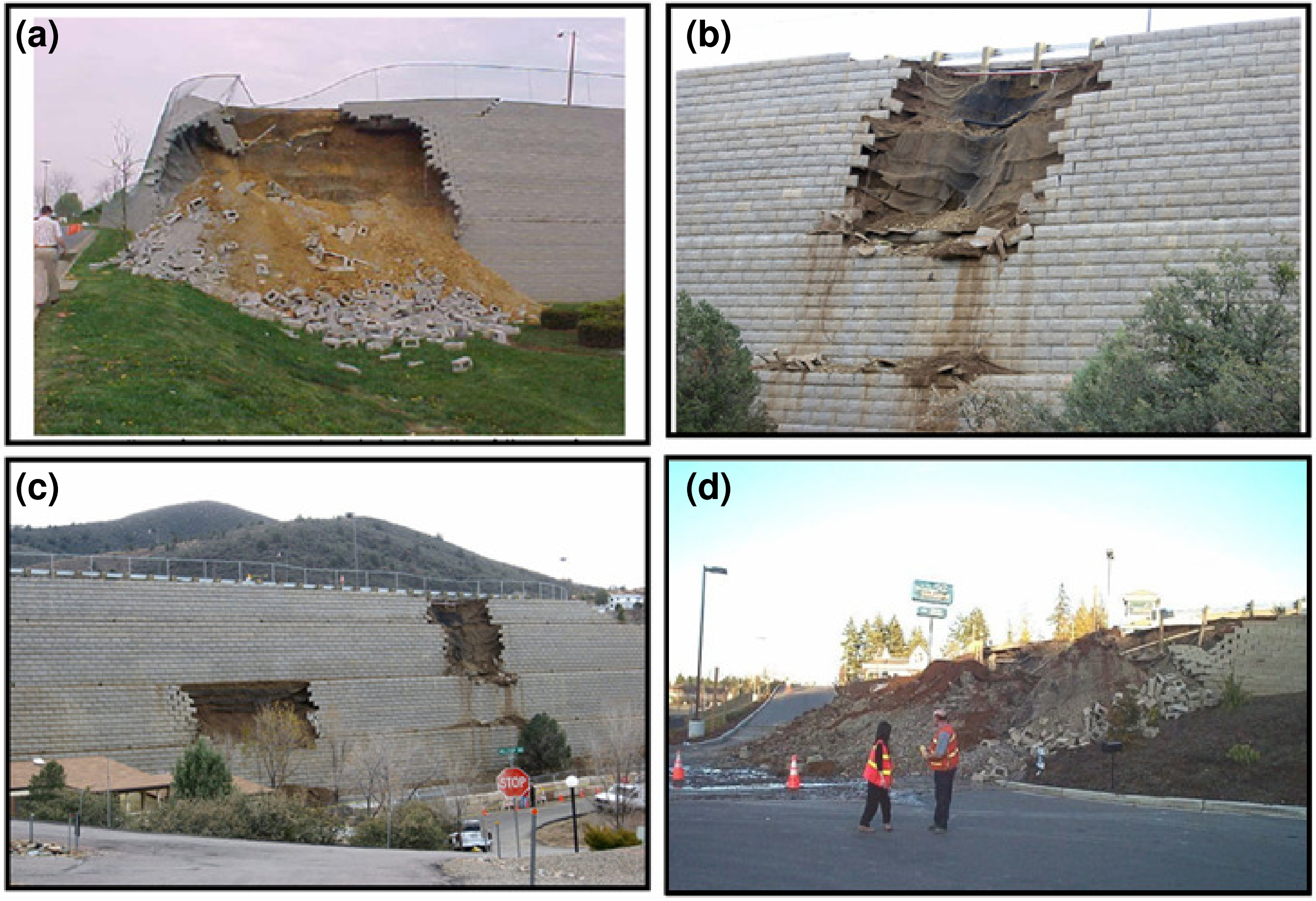

Figure 1.2: Examples of failures of MSE structures: (a) Valley and Ridge physiographic province of southwestern Virginia and eastern Tennessee; (b) and (c) Prescott, Arizona; (d) Turnwater, Washington

1.2 COMMON DESIGN METHODS FOR MSE RETAINING STRUCTURES

The design of MSE retaining structures in the United States is the result of a synergistic approach. The reinforced soil mass is analyzed for internal, external, and global stability as well as the stability under seismic loading and deformability. The design is conducted using different analyses to define the required reinforcement strength and length, as shown in Fig. 1.3. The three primary agencies identified in the most recent design specifications in North America are the American Association of State Highway and Transportation Officials (AASHTO 2002), Federal Highway Administration (FHWA) (Elias et al. 2001), and National Concrete Masonry Association (NCMA 1997 and 1998).

In analyzing the internal stability of GRS structures, the analyses produce the maximum reinforcement force, T_{max}, in each layer of reinforcement, the load at the connection to the facing, typically related to T_{max}, and the pullout resistive length enabling to develop T_{max}. As a result, the determination of T_{max} is the basis of design for internal stability. In addition, the selection of reinforcement strength based on T_{max} also has to account for several reduction factors, R_d, due to installation damage, creep and degradation in the field. For external stability, the analysis considers the reinforced soil mass as a rigid body. The rigid mass is treated as a gravity wall, which should have adequate bearing capacity and resistance to sliding and overturning (or limited eccentricity).

For areas with seismic hazards, stability under seismic forces is conventionally evaluated by considering two additional forces: the seismic thrust and horizontal inertia force. During an earthquake, in addition to the static thrust on the MSE wall, the retained fill exerts a dynamic horizontal thrust. Meanwhile, the reinforced soil mass is subjected to a horizontal inertia force from within itself. These two forces can be evaluated using pseudo-static Mononobe-Okabe analysis and the specific peak horizontal ground acceleration for the site of interest.

MSE structures must meet certain factors of safety, *FS*, against all failure models (internal, external, global…,etc.). The allowable factors of safety required by FHWA (Elias et al. 2001) are indicated in Fig. 1.3. For stability under seismic forces, the allowable minimum dynamic factors of safety are adopted as 75 percent of the static factors of safety.

Deformation criteria are also specified in FHWA design guidelines. MSE walls constructed with full-height panels should be limited to differential settlements of 1/500. Walls with dry-cast facing (MBW) should be limited to settlements of 1/200. For walls with welded wire facings, the maximum differential settlement should be 1/50. Experience also shows that if the safety factors of reinforced structures against all failure modes are satisfied, the deformation of reinforced structures will likely be within tolerable limits.

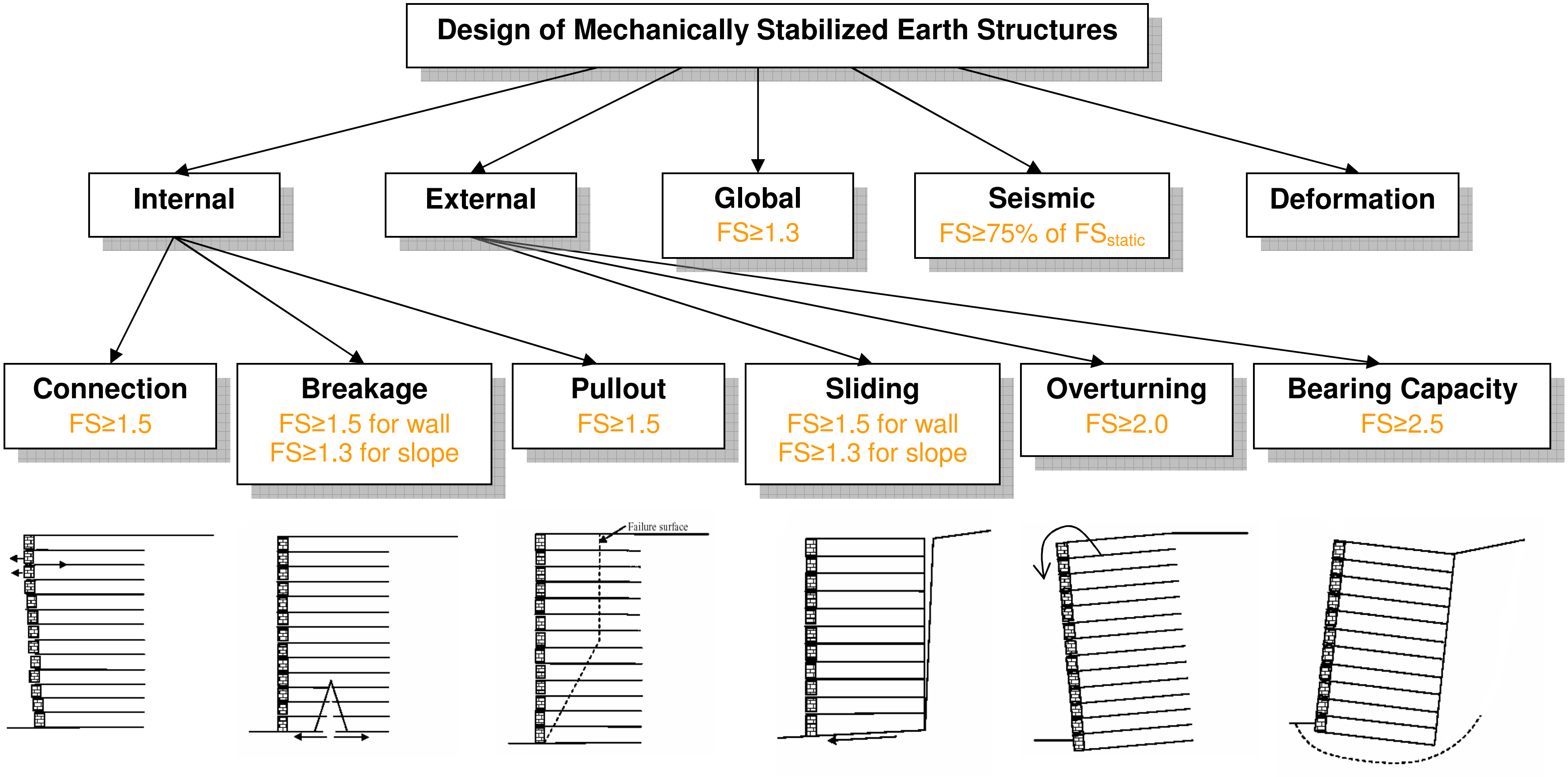

Figure 1.3: Failure modes and safety factors for the design of MSE structures as required by FHWA (2001)

1.3 RESEARCH MOTIVATION AND OBJECTIVES

1.3.1 Problem Definition: Simplified Design Rationale

For practical reasons, current design guidelines are established based on a simplified design rationale. Taking design of internal stability as an example, the design rationale is simply established on the concept of force balance or limit equilibrium. It assumes that the MSE retaining structures could be internally stabilized by the mobilization of reinforcement tensions. Because of the extensible properties of geosynthetics, the soil stresses may be expected to be mobilized rapidly, reaching its peak stress state or active conditions before the reinforcements achieve their ultimate tensile strength. Therefore, the mobilization of reinforcement tensions is assumed to be in equilibrium with active earth forces. These can be evaluated by Rankine's earth pressure theory (walls with horizontal backslope) or Coulomb's earth pressure theory (walls with an inclined front face or with a surcharge slope).

Historical performances of MSE retaining structures Specifically Geosynthetics-Reinforced Soil (GRS) retaining walls provide strong evidence of this, particularly in the prediction of reinforcement loads (Allen and Bathurst 2003, Bathurst et al. 2008). In addition, Allen et al. (2002a and 2002b) show that a number of well-documented geosynthetic walls that have demonstrated good long-term performance for up to 25 years were designed with significantly lower global resistance demand ratios than those that are required by current guidelines.

A possible explanation of this over conservatism is the inadequacy of simplified design rationale to represent the complex mechanism of soil and reinforcement interaction. As a result, this dissertation endeavors to *better understand the soil and reinforcement stresses developed within GRS retaining structures under various stress* *states* (i.e.*, working stress and large soil strain conditions*). GRS structures are constructed for their serviceability under working stress conditions. Nevertheless, an understanding of soil and reinforcement stresses that develop under large soil strain conditions is still important. This is because most design methods are based on the limit state of soil. For example, the design of GRS slopes using the limit equilibrium method is based on the limit equilibrium between required soil shear strength and developed shear stresses. The design of GRS walls using earth pressure theory is based on soil active conditions. For structures under soil active conditions, any further deformation due to additional loading will advance the conditions of structures into the soil's large strain conditions. Last, the stability of designed structures will be brought back to serviceability by considering the factor of safety as indicated in Fig. 1.3.

The basis for many current designs is the stress distribution within the GRS structures. Understanding the actual development of soil and reinforcement stresses offers an important insight into the basis of design. The stress information can be applied to examine the internal stability evaluation in current design guidelines. Also, the stress information should explain the conservatism of current design methods that are based on simplified design rationales like the earth pressure theory or the limit equilibrium method. Furthermore, as discussed below the stress information can be applied to clarify several current design arguments.

1.3.1.1 Evolution of Stresses and Strains along the Failure Surface

The failure surface within retaining soil structures is an important factor for design, specifically for internal stability analyses. Along the failure surface, the internal stability's failure mechanism is governed by the development of soil and reinforcement stresses. The location of the failure surface is commonly evaluated by Rankine's active earth pressure theory for retaining soil walls and by limit equilibrium analysis for retaining soil slopes. It has also been demonstrated that failure surface locations can be accurately predicted in retaining soil walls by Rankine's active earth pressure theory and in slopes by limit equilibrium analysis (Zornberg et al. 1998). Besides the factor of structure face inclination (the common distinction between walls and slopes in practice is 70^o), the location of failure surface is mainly governed by three factors: soil strength properties, reinforcement stiffness (geosynthetics or metallic reinforcement) (Elias et al. 2001), and wall geometry (wall aspect ratio) (Woodruff 2003, Yang et al. 2009). Further, Zornberg reported (1994) that by monitoring the development of the reinforcement strain at each layer within retaining soil structures, the location of potential failure surface corresponds to the locus of peak reinforcement strain at each layer (Zornberg 1994).

Until now, our knowledge of failure surfaces has limited us to predicting them and the corresponding information from the development of reinforcement strains along the failure surface. The information in regard to the development of soil stresses (or strains) along the failure surface has not yet been fully explored. As a result, the information of soils and reinforcements obtained in the study can be applied to understand the evolution of the failure surface.

1.3.1.2 Soil Strength Properties Governing the Stability of GRS Structures

There are a series of intense debates regarding selection of peak or residual strength for GRS retaining structure design (Leshchinsky 2001, Zornberg 2003, 2002, 2002a, 2002b and 2002c, Zornberg and Leshchinsky 2001). For the rationale of adopting the residual shear strength, this is because geosynthetics are classified as extensible reinforcements; consequently, the soil strength may be expected to mobilize rapidly, reaching and crossing its peak strength before the reinforcements achieve their ultimate strength. This is the case of commonly used design methods such as those proposed by Jewell (1991) and Leshchinsky and Boedeker (1989).

However, the experimental data gathered by Zornberg (2002) and Zornberg et al. (1998) from centrifuge modeling supports the use of peak shear strength parameters in the design of GRS structures. Moreover, the perceived conservatism of using residual strength in design is *not* supported by the generally observed good performance of monitored reinforced soil structures designed by using peak strength. In the US, the American Association of State Highway and Transportation Officials (AASHTO 2002), the Federal Highway Administration (Elias et al. 2001), and the National Concrete Masonry Association (NCMA 1997 and 1998) have commonly recommended using the peak friction angle.

Leshchinsky (2001) proposed a hybrid approach. He employs a design procedure in which peak soil shear strength properties would be used to locate the critical slip surface. The residual soil shear strength properties would subsequently be used along the located slip surface to compute the reinforcement requirements.

The key to answering the above controversy, in the author’s opinion, is to identify, specifically along the failure surface, the soil stress state within GRS retaining structures. Such information of stresses developed along failure surface could then be applied to investigate the soil strength properties that govern a structure’s stabilities.

1.3.1.3 Mobilization of Reinforcement Tensions

This section evaluates two concepts of how to consider the mobilization of reinforcement tensions in the limit equilibrium analyses of reinforced structures. In Method A, the effect of reinforcement tensions is contributed to increase the resistance of a slope system. The reinforcement forces used in the analysis are allowable forces and are not divided by the factor of safety *FS* calculated during the slope stability analysis. As shown in the following equation, the *FS* in the slope stability analysis is defined as the ratio of the mobilized soil stress to the peak soil shear strength:

$$FS = \frac{S}{S_m} \text{ and } T_m = \text{Constant} \tag{1.1}$$

where *S* is the available soil strength; S_m is the mobilized soil strength for equilibrium; T_m is the mobilized reinforcement tensile strength. In Method B, the effect of reinforcement tensions is contributed to decrease the driving force or moment of slope system. The reinforcement forces used in the analysis are ultimate forces and are divided by the *FS* calculated in the slope stability analysis. As shown in the equation below The *FS* in the slope stability analysis is defined as two ratios: the ratio of the peak soil shear strength to the mobilized soil stress and the ratio of the reinforcement ultimate tensile strength to the mobilized reinforcement tensions:

$$FS = \frac{S}{S_m} = \frac{T_{ult}}{T_m} \tag{1.2}$$

where T_{ult} is the ultimate tensile strength of reinforcements.

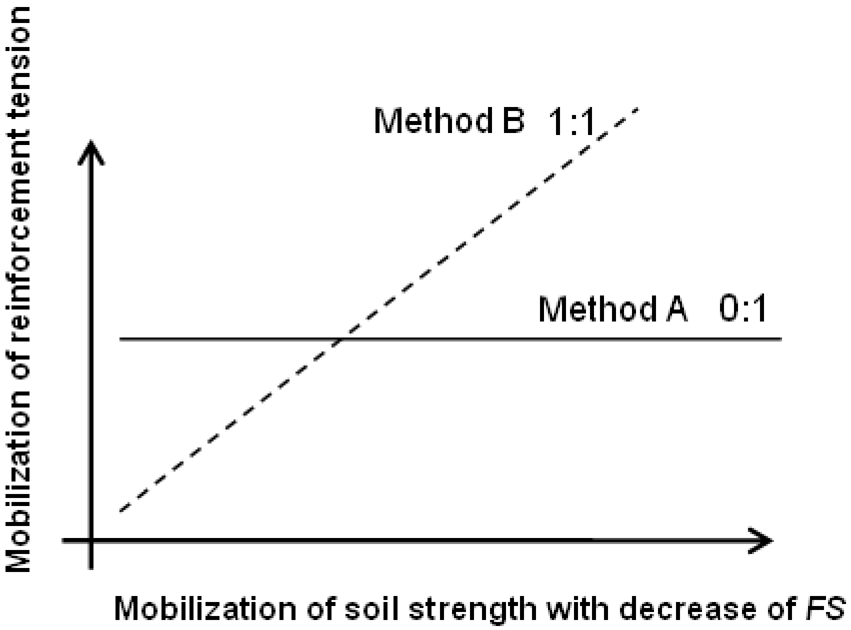

Figure 1.4: Mobilization of soil and reinforcement strength in two methods

Figure 1.4 illustrates the mobilization of soil and reinforcement strength in Method A and B. For the analysis using Method A, the available reinforcement strength is fully mobilized throughout the entire analysis. The mobilization of reinforcement strength and the mobilization of soil strength follow a 0:1 relationship. For the analysis using Method B, the soil strength and reinforcement tensions are divided by the same *FS*. Because of this the mobilization of reinforcement strength corresponding to the mobilization of soil strength follows a 1:1 relationship. This Method B is also called a balanced factor of safety.

Duncan and Wright (2005) claimed that Method A is preferable. The soil strength and the reinforcement forces, they note, have different sources of uncertainty. Therefore they involve different amounts of uncertainty. Factoring them separately makes it possible to reflect these differences. The constant reinforcement strength designated in Method A, however, fails to reflect the real case that reinforcement strength is mobilized with the mobilization of soil strength. Method B can reflect the mobilization of reinforcement strength during stability analysis. Nevertheless, there is a fundamental question regarding the 1:1 relationship between the mobilized reinforcement strength and the mobilized soil strength. In other words, should the same *FS* for soil be used for reinforcements? If different *FSs* are used for soil and reinforcements, is there any relationship and correlation between these two *FSs*, or are they just two independent values?

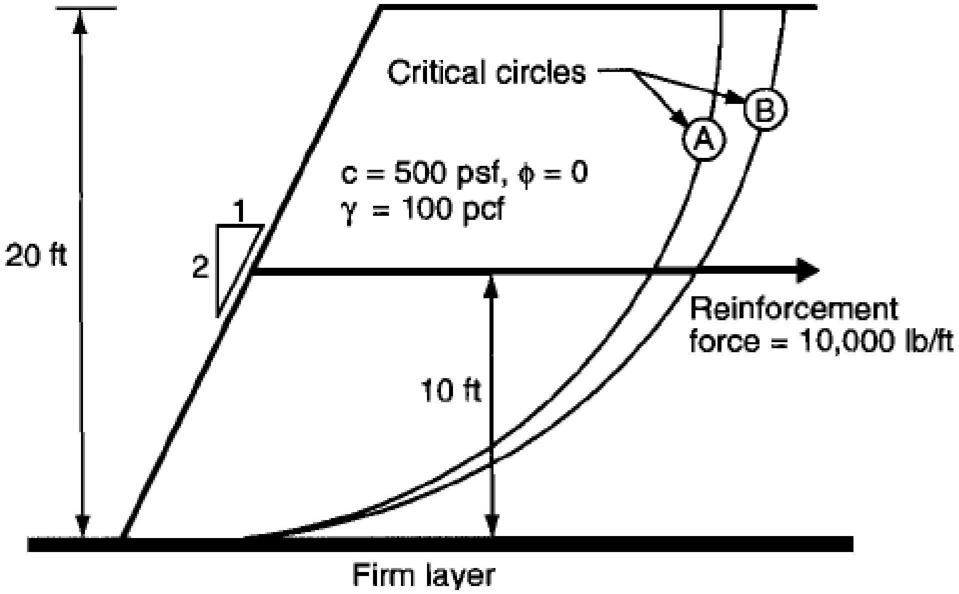

Figure 1.5: Evaluation of the stability of a reinforced slope by Method A and Method B (Duncan and Wright 2005)

Duncan and Wright (2005) evaluated the stability of a reinforced slope, illustrated in Fig. 1.5, by using the two approaches mentioned above. They found the calculated *FS* by Method A is 2.19 and by Method B is 1.72. The difference in *FS*s is significant if in current practice *FS*=1.3 is considered stable and *FS*=1.0 is considered failed. As a result, the key to obtaining a realistic *FS* of soil is to understand the actual interaction of strength mobilization between soil and reinforcement. By using the stress information of soils and reinforcements, one could examine the mobilization of the reinforcement tensions that correspond to the mobilization of soil strength. In this manner one could obtain a realistic *FS* of soil. This information could also potentially help explain the conservatism of current design methods.

1.3.2 Problem Definition: Conservative Design

As illustrated in Fig. 1.6, the source of conservatism in the current design methods comes from three factors. To begin with, design methods are based on simplified design rationales. This fact, aside from practical reasons, is due to a less than full understanding of the behavior mechanics of MSE structures. As discussed in Section 1.3.1, historical performances of GRS retaining structures provide strong evidence that current design methodologies are very conservative, particularly for predicting reinforcement loads. The second factor influencing design conservatism is compensation for the uncertainty about material properties and design methods. Hence designs impose large values of reduction factors R_d and factors of safety *FS* for design. Third, designs ignore the stability contributed by the facing elements.

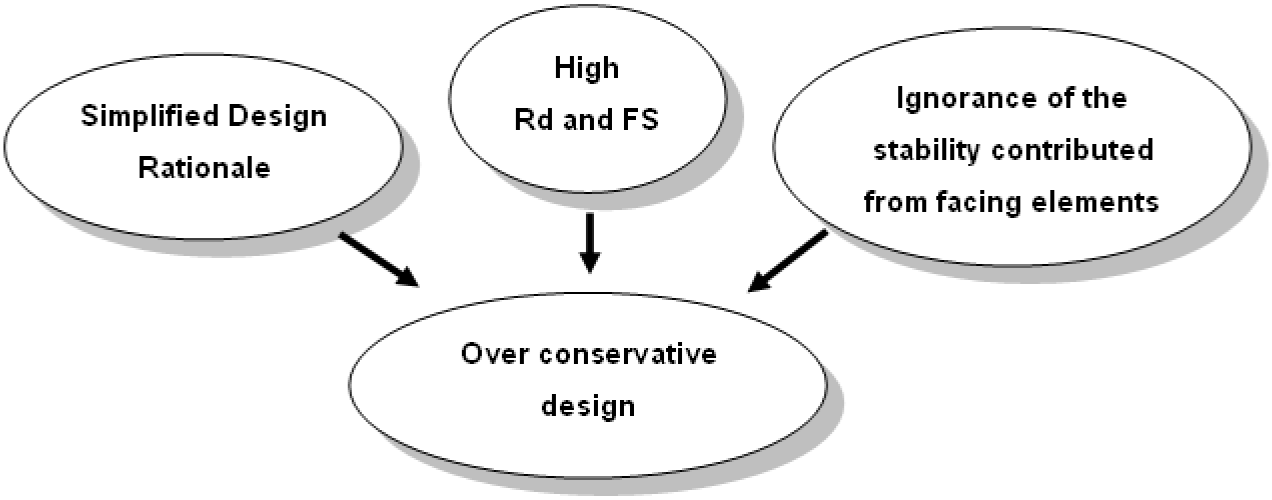

Figure 1.6: Source of conservatism in current design methods

What are the ramifications of these overly conservative designs? Two primary consequences are likely to be a waste of resources and inflated construction time. In the author's opinion, failure in civil engineering should be defined not merely as a collapse of a structure (as was seen in Fig 1.2) but also an overly conservative design that wastes taxpayer money. Consequently, the overarching motivation in this research is to *better understand the behavior of GRS structures and thereby provide design implications and considerations that optimize design methods.*

1.4 RESEARCH METHODOLOGIES

This section lays out the methodologies selected for the analysis. It also addresses the prioritization of the selected methodologies and the problems of other methods. The main objective here is to investigate the development and distribution of soil and reinforcement stresses within GRS structures under various stress states. As discussed previously, such information is rich and important to help understand the basis of design and to answer some current design arguments. Unfortunately, the stress information under large strain conditions (sometimes even under working stress conditions) is often, through most of current physical or numerical methods, inaccessible. The problems of accessing stress information by current research and design methods are discussed herein.

1.4.1. Problems with Physical Methods

Researchers have physically and experimentally investigated the behavior of GRS retaining structures. They have done so through in-situ monitoring of full-scale projects, reduced-scale models, and centrifuge tests. A common way to measure soil stresses in in-situ monitoring and full-scale tests is the utilization of pressure cells. However, it isn’t easy to adjust the direction of interest (e.g., along the direction of failure surface) before installation. In addition, there exists a concern of disturbing the development of soil stresses by using intrusive instruments. In measuring reinforcement stresses, information about them should always be deduced from information about reinforcement strains by assuming a known stress-strain relationship. Stress-strain relationships are commonly obtained from wide-width unconfined tensile test. However, the deduced stress information may differ from reality due to ignorance of the effect of reinforcement confinement and creep.

For centrifuge tests, the primary concern is obtaining soil stress information indirectly. Because the tests are small scale, the data from centrifuge tests has been obtained through non-intrusive techniques like digital image processing. The soil and reinforcement stress information needs to be interpreted from strain information which again has to be converted indirectly from displacement information based on some assumptions and fitting functions (Zornberg and Arriaga 2003).

1.4.2 Problems with Numerical Simulations

In addition to the physical tests discussed above, numerical simulations have provided little insight into stress information. Two numerical tools, limit equilibrium and finite element method, are discussed here.

In the limit equilibrium analysis, soil stress information (i.e., normal and shear stresses) at the base of each slope slice can be obtained along the failure surface. But the obtained stress information is true only when considering the mobilized reinforcement tensile strength. In addition, the obtained soil stress information beyond soil peak shear strength is limited. This is a crucial problem for the evaluation of comparatively flexible structures such as GRS structures.

The finite element method has provided good predictions of conservatively designed GRS structures under working stress conditions. The method, however, has not been successful at predicting failure or large deformation conditions. This is primarily because most soil constitutive models ignore the post-peak behavior of soil. Like one of the problems in limit equilibrium analysis, this is crucial to evaluating the structures' behavior under large soil strain conditions. This is especially true for comparatively flexible structures like GRS structures. In addition, special care is required for numerical accuracy and stability at the post-peak region of soil.

1.4.3 Selected Method

Based on the issues discussed above, this study, to investigate the behavior of MSE structures under large deformation conditions, utilizes the finite element method. The study makes use of the development and implementation of advanced soil and reinforcement constitutive models and computational techniques. The finite element development and implementation includes a soil strength softening model, a nonlinear reinforcement model, and a modified forward Euler stress integration algorithm with error control. A soil strength softening model is used to simulate the soil post-peak behavior. A nonlinear reinforcement model is used to model the nonlinearity of reinforcement under large deformations. The modified forward Euler stress integration algorithm with error control is to improve the accuracy of computation and reduce the calculation cost (i.e., effort and time). It is expected that implementing these three features will better capture the behavior of GRS structures under large soil strain conditions. The updated finite element model will first be validated by using the data from a series of centrifuge tests on GRS structures conducted by Arriaga (2003). After the validation of proposed finite element model, the soil and reinforcement stress information revealed from the simulation will be applied to study the issues discussed in Section 1.3.1.

1.5 DISSERTATION OUTLINE AND SIGNIFICANT CONTRIBUTION

This dissertation presents a study of how GRS structures behave under large soil strain conditions. It is guided by a specific interest in the development and distribution of soil and reinforcement stresses under various stress states. Including this introductory chapter, the dissertation is organized in such a manner.

Chapter 2 reviews the background information regarding the general behavior of GRS structures and various design methods according to different soil stress states. The design methods include earth pressure theory, limit equilibrium method, finite element method, and K-stiffness method. The chapter discusses the advantages and limitations of various design methods. Earth pressure theory and K-stiffness method, which are commonly recommended in current practice of GRS walls, will be examined using the proposed finite element model in Chapter 7.

Chapter 3 introduces a non-commercial finite element program ANLOG and the basic algorithm of finite element computation. ANLOG is a non-commercial finite element program written on the platform FORTRAN. The advantage of a non-commercial program like ANLOG is that it is an open source code, allowing users to modify existing routines and implement new features into the original source code. Furthermore, the program was developed using a structure of macro commands (Zienkiewicz 1989), making it particularly suitable for implementing new models and geotechnical construction procedures. Implemented into ANLOG will be the advanced soil and reinforcement models as well as new computational algorithms.

Chapter 4 describes the development of a soil strength softening model. The soil strength softening model is applied to simulate the soil post-peak behavior under large soil strain conditions. The chapter also illustrates the calibration and verification procedures of the proposed soil-softening model, which use two different frictional materials, Monterey No. 30 sand and Sacramento River sand. Also discussed is the effect of soil density and confining pressure on soil-softening. The original contribution of the proposed soil-softening model is to provide a numerical tool to better predict the stress-stress relationships, specifically at the region beyond soil peak strength.

Chapter 5 presents two stress integration algorithms to calculate stress information within materials in finite element analysis. The two stress integration algorithms are: 1) the forward Euler integration scheme with subincrements, and 2) the modified forward Euler integration scheme with error control. The implementation procedures are also discussed. The original contribution of the work is to evaluate the effect of two integration algorithms in regard to computational accuracy, error tolerances, and efficiency specifically for the proposed soil-softening model.

Chapter 6 introduces a finite element model to simulate the GRS structures under large soil strain conditions. The finite element model is presented in detail including mesh configurations, material models, issues related to the construction of GRS slope and issues related to finite element computations.

Chapter 7 presents the verification of the proposed finite element using data from centrifuge tests conducted by Arriaga (2003) to investigate the behavior and mechanism of GRS structures under working stress and failure conditions. The results of various deformation and strain information between prediction and measurement of a GRS slope model are compared. The original contribution of the work in Chapters 6 and 7 is to enhance the state of the art regarding finite element simulation of GRS structures. This is true particularly under large strains or failure conditions by implementing advanced constitutive models and computational techniques.

Chapter 8 examines the soil and reinforcement stress information obtained from the finite element simulation. The basis of many current designs is stress development and distribution within the GRS retaining structures. The issues raised in Section 1.3.1 regarding the basis of design and the arguments of current design will be discussed in Chapter 8. The design of GRS structures in current design guidelines will also be examined. The original contribution of this work is to provide the design consideration and implication based on the revealed stress information from finite element simulation.

Chapter 9 presents a summary of the conclusions drawn from the dissertation's work. Also included is a list of recommendations for future work in this area. The overall scope, objectives, methodologies and corresponding chapters of this dissertation are summarized in Fig 1.7.

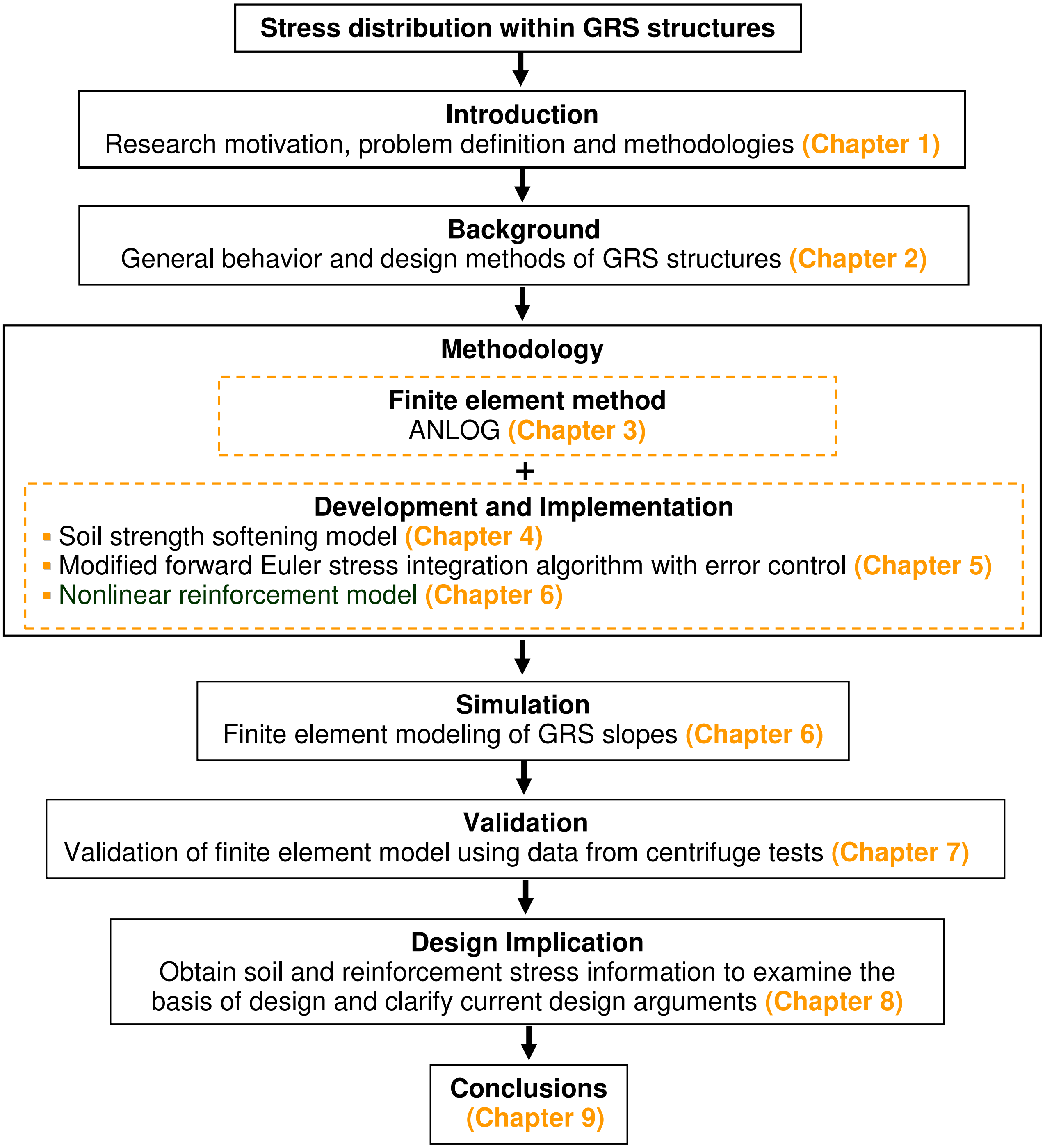

Figure 1.7: Overall scope and corresponding chapters in this dissertation

Chapter 2: Background of GRS Structures

2.1 GEOSYNTHETICS

Geosynthetics are defined as planar products manufactured from polymeric materials. As an integral part of a man-made project, structure, or system, they are used with soil, rock, or other geotechnical engineering-related material(ASTM 1995). Specific types of geosynthetics include geotextiles, geomembranes, geogrids, geonets, geosynthetic clay liners (GCLs), geocomposite sheet and strip (wick) drains, goecells, erosion control products and HDPE vertical barrier systems. These materials have been used to perform a variety of projects in transportation, water resources, environmental and geotechnical engineering. Functions that geosynthetics can perform include hydraulic barriers, filtration/separation, reinforcement, in-plane drainage or protection.

Geosynthetic inclusions within a soil mass, by developing tensile forces that help stabilize geosynthetic-soil composite like GRS retaining structures, can provide a reinforcement function.

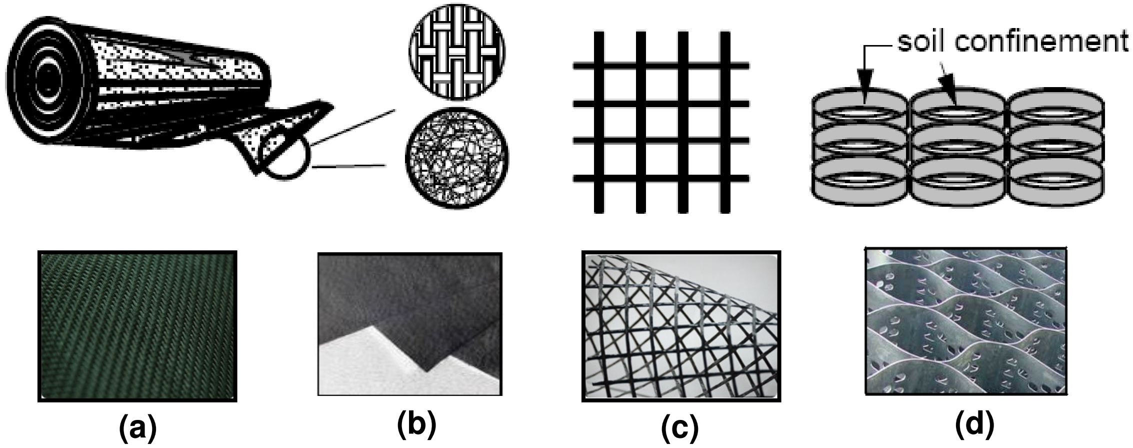

Figure 2.1: Geosynthetics family as reinforcement: (a) woven geotextile; (b) nonwoven geotextile; (c) geogrid; (d) geocell (Bathurst 2007)

Geosynthetic products typically used as reinforcement elements are woven geotextiles, nonwoven geotextiles geogrid, and geocells as shown in Figs. 2.1. In GRS retaining structures, geosynthetics are classified as extensible reinforcements (Elias et al. 2001) as opposed to inextensible reinforcements like metallic mats and strips. In fact, instead of comparing the relative stiffness among reinforcements, the criterion for characterizing reinforcements as extensible or inextensible has been established by comparing the horizontal strain in an element of reinforced backfill soil subjected to a given load, to the strain required to develop an active plastic state in an element of the same soil without reinforcements (Bonaparte and Schmertman 1987). We can summarize as follows:

- Reinforcement is classified as extensible when the tensile strain at failure in the reinforcement exceeds the horizontal extension required to develop an active plastic state in the soil.
- Reinforcement is classified as inextensible when the tensile strain at failure in the reinforcement is significant less than the horizontal extension required to develop an active plastic state in the soil.

Finally, the study presented in this dissertation will specifically focus on MSE retaining structures with extensible reinforcements, commonly called Geosynthetics-Reinforced Soil (GRS) retaining structures.

2.2 GENERAL BEHAVIOR OF GRS RETAINING STRUCTURES

This section discusses the general behavior of GRS retaining structures and corresponding design methodologies. The overall concept is illustrated in Figure 2.2. As discussed previously in regard to the definition of extensible reinforcements, before reinforcement reaches it peak shear strength, four soil stress states can be identified: 1) pre-peak state; 2) peak state; 3) post peak state and 4) residual state. The relative locations of various soil stress states and the corresponding reinforcement stress states are indicated in the stress-strain curves inserted in Fig. 2.2. According to various soil stress states, the conditions of GRS retaining structures can be separated into working stress and large soil strain conditions.

The GRS retaining structures under working stress conditions is defined as the average of soil stress states along a potential failure surface remains in the pre-peak region, not reaching the peak state. In general for frictional materials like sand and gravel, 3 to 5 percent of soil strain must be developed to mobilize soil peak strength. Under working stress conditions, system stability is sustained by the increase of soil strength and the development of reinforcement strength to accommodate the increase of loading.

The GRS retaining structures is under large soil strain conditions when the average of soil stress states along a potential failure surface crosses peak strength and reaches the post-peak region or even levels at the residual region. This condition does not necessarily result in a reinforcement rupture or a wall collapse. It does mean, however, that wall deformations likely become excessive. The increase of loading will cause a further loss of soil strength along failure surface. Therefore, the contribution of system stability from soils is decreased. The mobilization of reinforcement strength must increase significantly to maintain the system's stability. Collapse finally occurs when the mobilization of reinforcement tensions reaches its ultimate tensile strength. For extensile reinforcements like geogrids and geotextiles, it generally requires a development of 15 to 30 percent of reinforcement strain to reach ultimate reinforcement strength.

Indicated in the Fig 2.2 are the design methodologies, specifically for internal stability, corresponding to various soil stress states. The following sections discuss the detailed design procedures, highlighting the advantages and limitations of each approach.

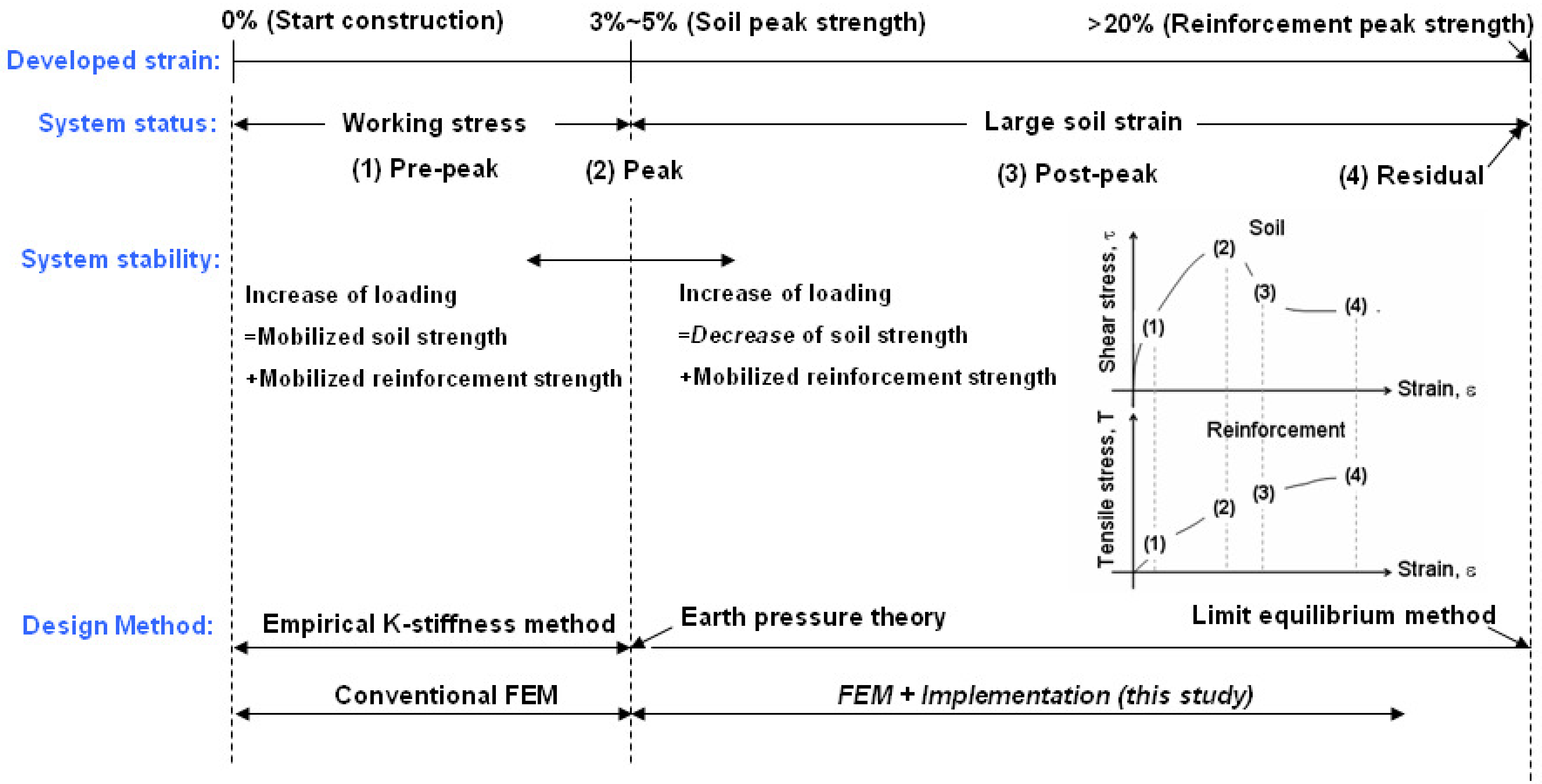

Figure 2.2: Behavior of GRS retaining structure and corresponding current design method

2.3 DESIGN METHODS

2.3.1 Earth Pressure Theory

Earth pressure theory has been used to predict reinforcement tensions. The design rationale assumes the tensile forces developed in reinforcements are in local equilibrium with the lateral earth pressure generated in MSE walls. This section discusses the design methods of reinforcements based on earth pressure theory in FHWA MSE wall design guidelines (Elias et al. 2001). FHWA design guidelines recommend using Eq. (2.1) to predict maximum tensile force developed at each layer of reinforcement.

$$T_{\max} = \left(\frac{k_r}{K_a}\right) K_a \gamma z S_v \tag{2.1}$$

where:

T_{max} is the maximum tensile force per unit width of reinforcement at each layer

k_r/K_a is the normalized horizontal earth pressure coefficient (see Fig. 2.3),

K_a is the theoretical Rankine active earth pressure coefficient,

γ is the unit weight of the reinforced backfill,

z is the depth of the layer of reinforcement below the top of the backfill,

S_v is the vertical spacing between layers of reinforcement,

The normalized horizontal earth pressure coefficient (k_r/K_a) varies with the type of reinforcements, as determined according to Fig. 2.3. The k_r/K_a for geosynthetic reinforced wall has a value of 1.0 and remains constant throughout the depth of wall. This implies that for flexible MSE walls or GRS walls, the horizontal movement occurring during construction is sufficient for the soil reaching active stress state and generating active earth pressure. The final computed tensile forces increases linearly from the topmost layer of reinforcement to the bottommost layer of reinforcement (proportional to the overburden pressure). In stiff MSE walls, the movement is limited, especially near the top of the wall. Consequently, the reinforced soil does not mobilize its full strength, resulting in higher lateral earth pressures resisted by the reinforcements near the top of the wall. Accordingly, the k_r/K_a for a steel reinforced wall has a high value (2.5 or 1.7 dependent on the type of steel reinforcements) at the top of the wall and decreases to 1.2 at a height of 6 m. Throughout the depth of the wall, the final computed tensile forces appear constant.

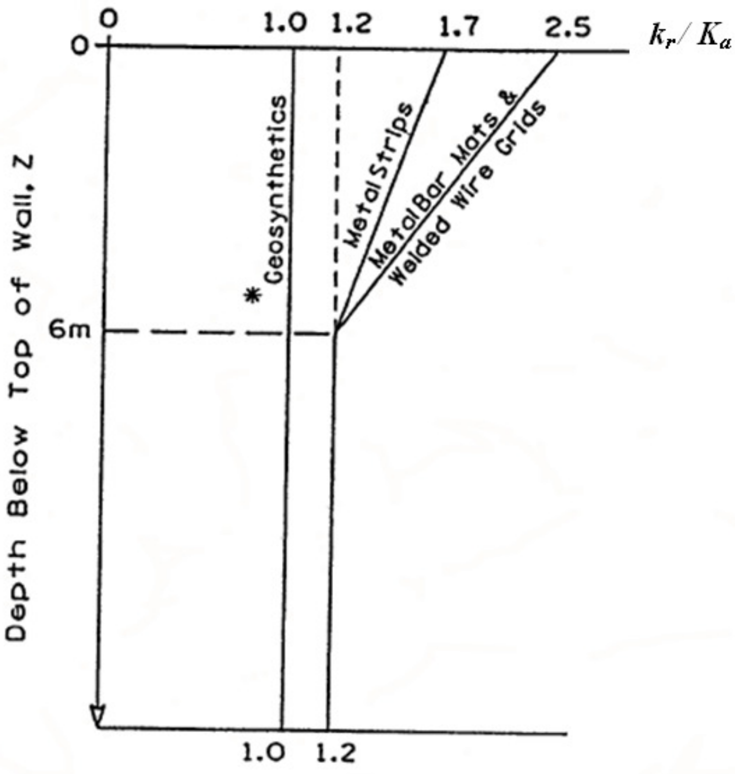

Figure 2.3: Variation of normalized horizontal earth pressure coefficient with depth in a MSE wall (Elias *et al* 2001)

Having knowledge of the forces in the reinforcements enables one to select reinforcements having adequate long-term strength. Moreover, one is able to calculate the length required to resist pullout within the stable soil zone, as well as the load where it joins the wall face. These three aspects of stability, assessed using the lateral earth pressure approach, are commonly termed: 1) internal stability, enabling one to determine the required long-term strength of the reinforcements; 2) the required connection strength to the facing; and 3) the required embedment length to ensure sufficient resistance to pullout.

The limitations of design based on earth pressure theory discussed by Christopher et al. (2005) are as follows:

- Experience from recent years shows that the lateral earth pressure approach could be overly conservative (i.e., the maximum reinforcement force can be over-predicted by as much as a factor of over two).
- Theoretically-based, it is thus limited to relatively simple geometric structures. It is difficult to extrapolate to complex geometries, such as narrow walls and multi-tiered walls.
- Limited to uniform granular soil; difficult to extrapolate to non-ideal reinforced fill soils.
- Do not consider pore water pressure in the reinforced fill.
- Does not determine global stability.
- Downdrag at connections is not evaluated.
- Unable to evaluate deformation of the wall structure or soil.
- Assume soil reaches its peak strength at active state. However, the GRS retaining structures are commonly designed for working stress conditions which soil stress states stay in pre-peak region.

In addition, the lateral earth pressure approach indicates that the required strength increases linearly with depth for uniform reinforcement spacing. The measured field data, however, shows nearly uniform mobilization of reinforcement strength with depth for walls under working stress conditions (Allen et al. 2003, Bathurst et al. 2008). Overall, the lateral earth pressure approach produces safe structures, but conservative, in terms of reinforcement strength for MSE structures on firm foundations and reinforced fills with no positive pore water pressures. This method does not include seepage forces and it assumes adequate drainage.

2.3.2 Limit Equilibrium Method

Limit equilibrium method has been used to analyze slope stability for many years by assuming the soil at failure obeys the perfectly plastic Mohr-Coulomb criterion. The analytical methods have been proposed by using various methods of vertical slices, e.g., Bishop (1955), Janbu (1954), Morgenstern and Price (1965) and Spencer (1967). An excellent review of popular limit equilibrium techniques for predicting slope stability can be found in Duncan and Wright (2005).

Limit equilibrium analyses of the design of reinforced soil structures have also been successfully reported. The stabilizing forces contributed by the reinforcement tensions are incorporated into the equilibrium equation (balance of force or moment) at “limit” state (right between stable and instable sates). The problem of GRS structures in limit equilibrium analysis is statically indeterminate. In particular, determination of the peak tension developed at each layer of reinforcement requires assumptions. Afterward, analysis searches for a critical failure surface that contains a minimum factor of safety. The general definition of *FS*, as defined in Eq. (1.1), is the available soil strength divided by mobilized soil strength for equilibrium. The uncertainties in limit equilibrium method include the assumption of force inclination between vertical interslices of soil mass in different analytical methods and the assumption of reinforcement tension distribution with depth (discussed later in this section).

Limit equilibrium can be applied to design complex problems (e.g., multi-tiered reinforced walls) and, in general, to non-homogeneous soils. It can include the effects of pore water pressure on the system stability. Limit equilibrium can also evaluate the global stability as well as local stability at any location or interface of interest. Compared with earth pressure theory in the case of geosynthetic reinforcements, the predicted forces in the reinforcement layers are reasonably conservative. In addition, compared with more rigorous continuum mechanics approaches like finite element method (Hammouri et al. 2008, Tan and Sarma 2008), limit equilibrium yields comparable results in terms of factor of safety and location of failure surface.

The limitations of design based on limit equilibrium method discussed by Christopher et al. (2005) are listed below.

- Current limited by FHWA recommendations to slop inclinations less than 70 degrees; however, this limitation is arbitrary and there is no theoretical reason why it could not be extended to vertical structures.
- Needs modification so that aspects such as connection load and effect of facing element can be assessed within the limit equilibrium analysis.
- Downdrag at connections is not evaluated.
- Does not consider deformation of the wall structure or soil.

In addition, it needs further verification that the distribution of reinforcement tensions with depth is a valid assumption. A triangular distribution of peak reinforcement tensions (proportional to the overburden pressure) has been assumed in the design of reinforced soil structures (Fig. 2.4a). This distribution has been assumed in design charts for GRS slopes that have been developed using limit equilibrium approaches (Schmertmann et al. 1987, Leschinsky and Boedeker 1989, Jewell 1991). FHWA design guidelines for reinforced soil slopes also recommend a reinforcement force distribution proportional to depth below the slope crest for the case of structures higher than 6m (Elias et al. 2001). In reality, however, measured field data shows nearly uniform mobilization of reinforcement strength with depth for GRS walls under working stress conditions (Allen et al. 2003, Bathurst et al. 2008) (Fig. 2.4b). For GRS slopes, the conventional triangular distribution of reinforcement peak forces with depth is not supported by a centrifuge investigation that evaluated the behavior of reinforced soil slopes under working stress conditions (Zornberg and Arriaga 2003) and failure conditions (Zornberg et al. 1998). In their studies, analysis of reinforcement strains results shows that the location of the reinforcement maximum peak strain does not occur near the toe of the structure. It was located, rather, at approximately midway up the reinforced slopes, at a point along the critical failure surface directly below the crest of the slope (Fig. 2.4c).

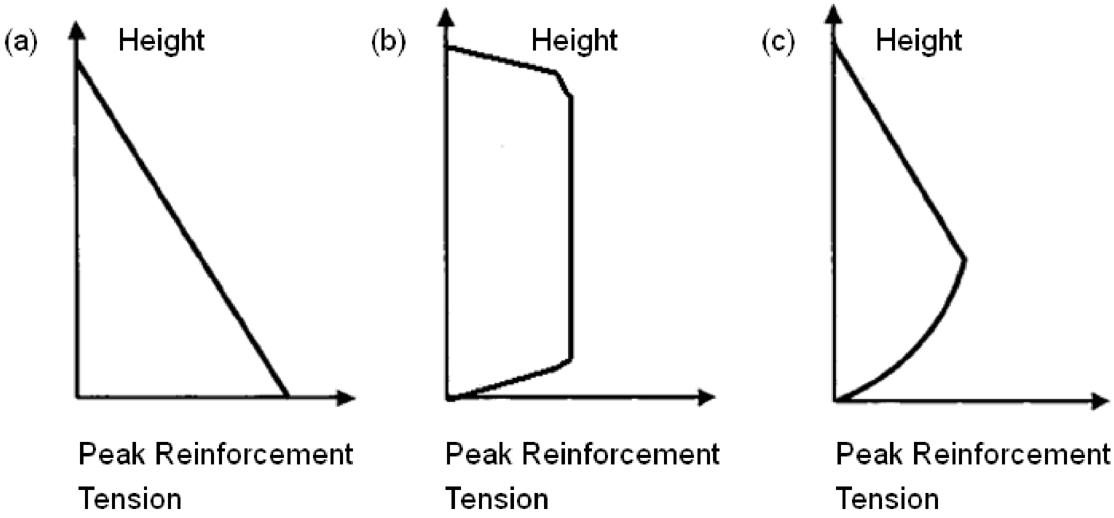

Figure 2.4: Distribution of peak reinforcement tensions with height: (a) use in design of GRS walls and slopes; (b) observed distribution for GRS walls; (b) observed distribution for GRS slopes

Last, as discussed in Section 1.3.1.3, the implicit relationship between the mobilization of soil and reinforcement strength in limit equilibrium analysis should be examined. For the analysis using Method A, the mobilized reinforcement strength is constant as the input value of allowable reinforcement tensile strength through the entire analysis. For the analysis using Method B, the mobilized reinforcement strength corresponding to the mobilized soil strength follows a 1:1 relationship. The relationships implied in Methods A and B should be examined and validated by further study on the development of soil and reinforcement stress information with various stress states.

2.3.3 Finite Element Method

Finite element method has been widely applied to model the behavior of full-scale instrumented GRS structures (e.g., Hatami and Richard 2005, Karpurapu and Bathurst 1995, Ling et al. 2000, Lopes et al. 1994) and to model reduced-scale GRS walls (e.g., Pinto et al. 1998, Simonini et al. 2000, Yogarajah and Andrawes 1994).

Analysis based on finite element method considers full continuum mechanics, e.g., the constitutive relationships of all materials involved (i.e., the stress-strain-time relationships). It satisfies boundary conditions, considers local conditions like the interface between soil and reinforcement, and can be applied to any loading condition and sequence (i.e., traffic loading, seismic loading, and step loading to simulate construction sequence). Unlike earth pressure theory and limit equilibrium method, its potential to produce displacements and compatibility between dissimilar materials is analytically assured. It can represent a problem in a most realistic fashion, and its prediction of performance can be quite accurate. It provides rich information (i.e., stress, strain, force, and displacement) and can be obtained at any location of interest (i.e., nodal and Gaussian Point).

The limitations of design based on finite element method discussed by Christopher et al. (2005) are listed below.

- Typically it requires a computational effort by a trained analyst.
- To produce relevant results, it requires comprehensive characterization of strength and compressibility for all soils, reinforcements and facings.
- Requires careful modeling to replicate the effects of soil-reinforcement-facing interactions.
- Predictions can be non-conservative, requiring careful evaluation of the reliability of input values and appropriate safety and/or resistance factors.

In addition, although it has provided good predictions of the behavior of GRS structures under working stress conditions, finite element has not been reported to successfully predict under failure or large deformation conditions. This is a crucial problem for the evaluation of the structure behavior, specifically for comparatively flexible structures such as GRS structures. Some specific development and implementation into finite element program are in need for modeling GRS structures under large soil strains conditions. For example, a soil constitutive model is required to model the soil post-peak behavior. Also, special care is needed for numerical accuracy and stability for simulation under large deformation conditions.

2.3.4 K-Stiffness Method

Allen et al. (2004, 2003) and Bathurst et al. (2005) investigated quantitatively the accuracy of reinforcement loads predicted by earth pressure theory using careful interpretation of a database of 11 well- monitored full-scale field walls. They concluded that the earth pressure theory was excessively conservative. Furthermore, the distribution of reinforcement loads in the instrumented walls was seen to be generally trapezoidal in shape rather than linear with depth as assumed in the earth pressure theory for walls with uniform reinforcement spacing. Figure 2.5 shows the comparison between the reinforcement loads (estimated from measured strains) in various instrumented GRS walls and the reinforcement loads predicted using earth pressure theory. It can be clearly observed in Fig. 2.5 that predicted loads for GRS walls are approximately five to eight times greater than estimated values for full-scaled instrumented walls. However, for steel reinforced walls, the conventional design method predictions are more accurate with maximum reinforcement loads approximately equal to the estimated values (not shown herein).

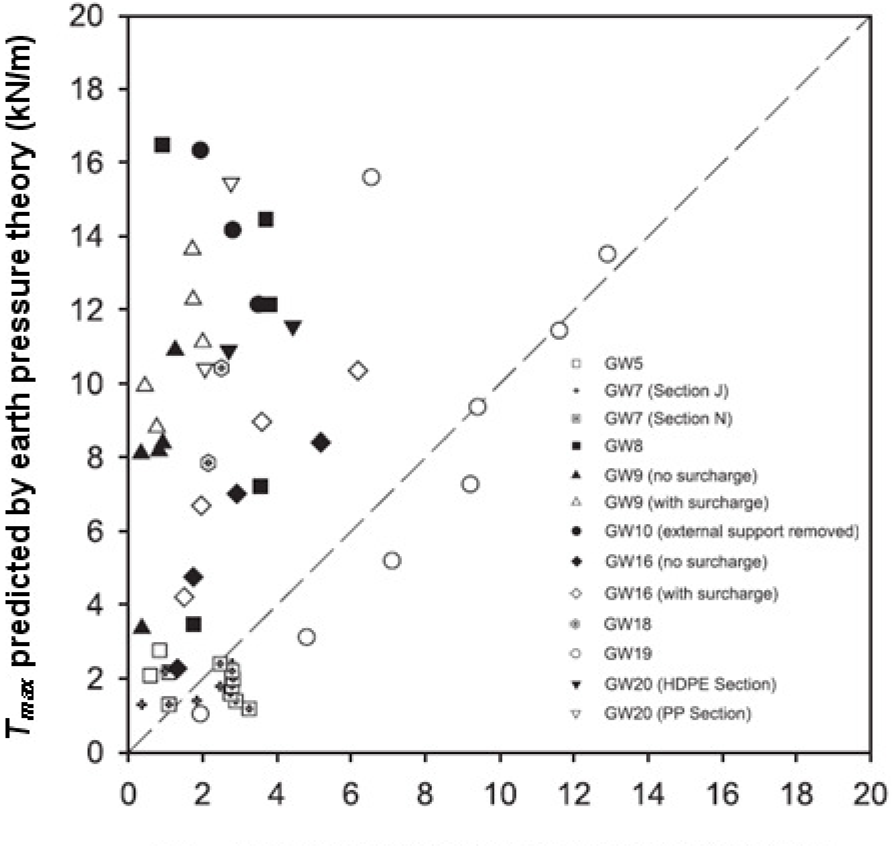

Figure 2.5: Comparison between the reinforcement loads in different GRS walls and those predicted using earth pressure theory (Allen et al. 2003)

To overcome these deficiencies, Allen et al. (2003) and Bathurst et al. (2005) proposed a new working stress method for estimation of reinforcement loads in GRS walls, known as K-stiffness Method. In the initial development of the K-stiffness method, a database of 11 wall case studies was used to calibrate an expression for the maximum load in a layer within the reinforced soil zone excluding the loads at or in close proximity to the wall facing (i.e., possible connection loads). The latest version of K-stiffness method (Bathurst et al. 2008) includes the effect of low quality backfill materials using nine additional new case studies from Japan and the US. The K-stiffness method has altered the typical equation for computing reinforcement loads by adding correction factors, as shown in Eq. (2.2).

$$T_{\max,i} = S_{v,i}\sigma_h D_{t\max}\Phi \tag{2.2a}$$

and

$$\Phi = \Phi_g \Phi_{local} \Phi_{fs} \Phi_{fb} \Phi_c \tag{2.2b}$$

where:

T_{max} is the maximum tensile force developed in reinforcement layer i;

S_v is the tributary area (equivalent to vertical spacing of the reinforcements in the vicinity of each layer);

σ_h is the at-rest lateral earth pressure acting over the tributary area;

D_{tmax} is the load distribution factor (Figs.2.6);

Φ is the influence factor that is the product of factors that account for the effects of global and local reinforcement stiffness, facing stiffness, face batter, and material cohesion.

The coefficient of lateral earth pressure to calculate σ_h is recommended by using the Jaky equation.

$$K = K_0 = 1 - \sin \phi_{ps} \tag{2.3}$$

where ϕ_{ps} is the peak plane strain fiction angle of the soil. Allen et al. (2003) explained that the use of K_0 in this method does not imply that at-rest conditions exist within the reinforced backfill. K_0 was used because it was simple to calculate and its value was independent of wall face batter.

Figures 2.6 show the load distribution factor D_{tmax} for geosynthetics (Fig. 2.6a) and steel reinforcements (Fig. 2.6b). In the x-axis, the maximum reinforcement load at each reinforcement layer T_{max} is normalized by maximum reinforcement load in the wall T_{mxmx} and by the influence factor for local reinforcement stiffness Φ_{local}. In the x-axis, the wall depth z is normalized by wall height H and includes the effect of equivalent height of uniform surcharge S (i.e., $S=q/\gamma$, where q is surcharge and γ is unit weight of backfill). As shown in Fig. 2.6a, the reinforcement loads are uniformly distributed within GRS walls under working stress conditions. The distributions of geosynthetic loads follow a trapezoidal shape. For the distribution of steel reinforcement loads shown in Fig. 2.6b, steel reinforcement is stiffer, and the reinforcement load distribution tends to more closely follow the increase in earth pressure with depth than is the case for geosynthetic walls. However, the distribution for steel walls is not fully triangular, possibly due to the effects of compaction stresses.

The influence factor Φ is the product of factors that account for the effects of global Φ_g and local Φ_{local} reinforcement stiffness, facing stiffness Φ_{fs}, face batter Φ_{fb}, and material cohesion Φ_c.

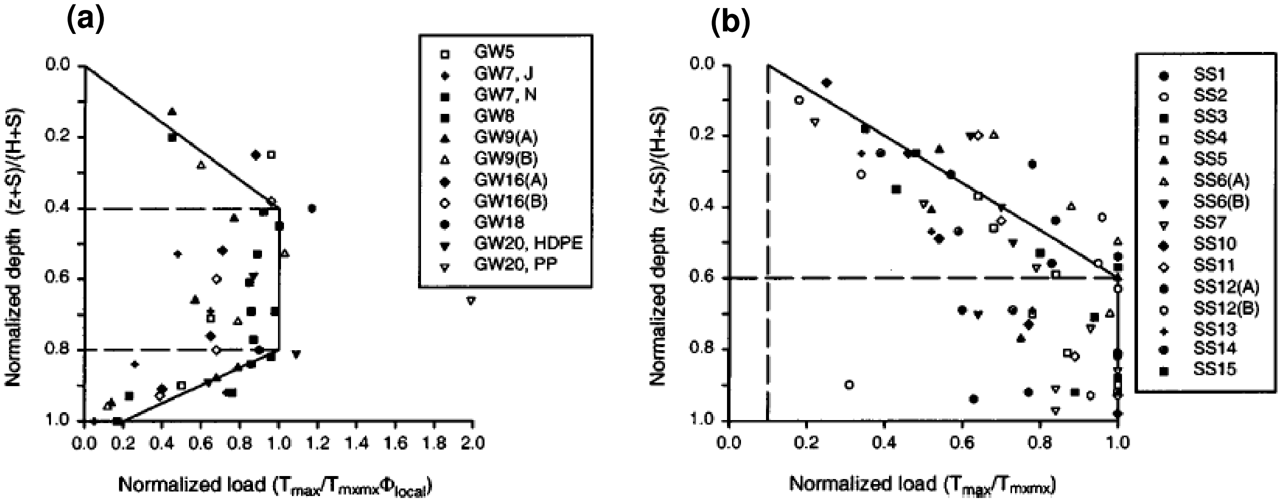

Figure 2.6: Load distribution for: (a) geosynthetic and (b) steel reinforcement (Allen et al. 2004)

Parameter Φ_g is a global stiffness factor that accounts for the influence of the stiffness and spacing of the reinforcement layers over the entire wall height and can be evaluated as:

$$\Phi_g = 0.25\left(\frac{S_{global}}{p_a}\right)^{0.25} \tag{2.4}$$

where S_{global} is the global reinforcement stiffness and normalized by the atmospheric pressure p_a=101 kPa. The global reinforcement stiffness value for a wall is calculated as:

$$S_{global} = \frac{\sum_{i=1}^{n} J_i / n}{H} \tag{2.5}$$

where J_i is the tensile stiffness of an individual reinforcement layer expressed in units of force per unit length of wall. n is the total number of reinforcement layers.

Parameter Φ_{local} is a local stiffness factor that accounts for the relative stiffness of the reinforcement layer with respect to the average stiffness of all reinforcement layers and can be evaluated as:

$$\Phi_{local} = \left(\frac{S_{local}}{S_{global}} \right)^{a} \tag{2.6}$$

The coefficient term is taken as a=1 for geosynthetic reinforced soil walls and as a=0 for steel systems. S_{local} is the local reinforcement stiffness for reinforcement layer i, calculated as:

$$S_{local} = \frac{J_i}{S_{v,i}} \tag{2.7}$$

Parameter Φ_{fs} (facing stiffness factor) is the factor that accounts for the influence of the facing stiffness. Φ_{fs}= 0.35 for modular block and propped concrete panel faced walls (stiff facings); Φ_{fs}= 0.5 for incremental precast concrete facings; and Φ_{fs}= 1.0 for all other types of wall facings like wrapped face, welded wire, or gabion faced (flexible facings).

The influence of wall facing batter on maximum reinforcement loads is adjusted in the proposed K-stiffness method using a facing batter factor Φ_{fb}, expressed as

$$\Phi_{fb} = \left(\frac{K_{abh}}{K_{avh}} \right)^{0.25} \tag{2.8}$$

where K_{abh} is the horizontal component of active earth pressure coefficient and K_{avh} is the horizontal component of active earth pressure coefficient if the wall face is vertical. The form of the equation shows that as the wall face batter angle $\omega \rightarrow 0$, the facing batter factor $\Phi_{fb} \rightarrow 1$.

The effect of soil cohesion is captured by the cohesion factor Φ_c as

$$\Phi_c = 1 - \lambda \frac{c}{\gamma H} \tag{2.9}$$

where the cohesion coefficient λ=6.5. c is cohesion of backfill material. It is possible that a combination of a short wall height and high cohesive soil strength could lead to $\Phi_c = 0$, which means, in practical terms, no reinforcement is required for internal stability.

The limitations of design based on K-stiffness method are listed below.

- The applicability of K-stiffness method is limited to walls with the range of parameters matching the database of case histories used to calibrate the method.
- Compared to earth pressure theory, K-stiffness method involves many design variables and long design procedure.
- Connection loads is not included into the K-stiffness method.
- This method is limited to relatively simple geometries structures.
- Do not consider pore water pressure in the reinforced fill. It is implicitly assumed that soils are well compacted and that good drainage practice is exercised to keep water from entering the reinforced soil zone.

In addition, the application of K-stiffness method is limited to GRS walls under working stress conditions. As shown in Fig. 2.7, a good prediction of reinforcement loads within GRS walls is demonstrated for GRS walls under working stress conditions (developed soil strain < 3%). For GRS structures, however, under large soil strain conditions, the K-stiffness method consistently under-predicts reinforcement loads.

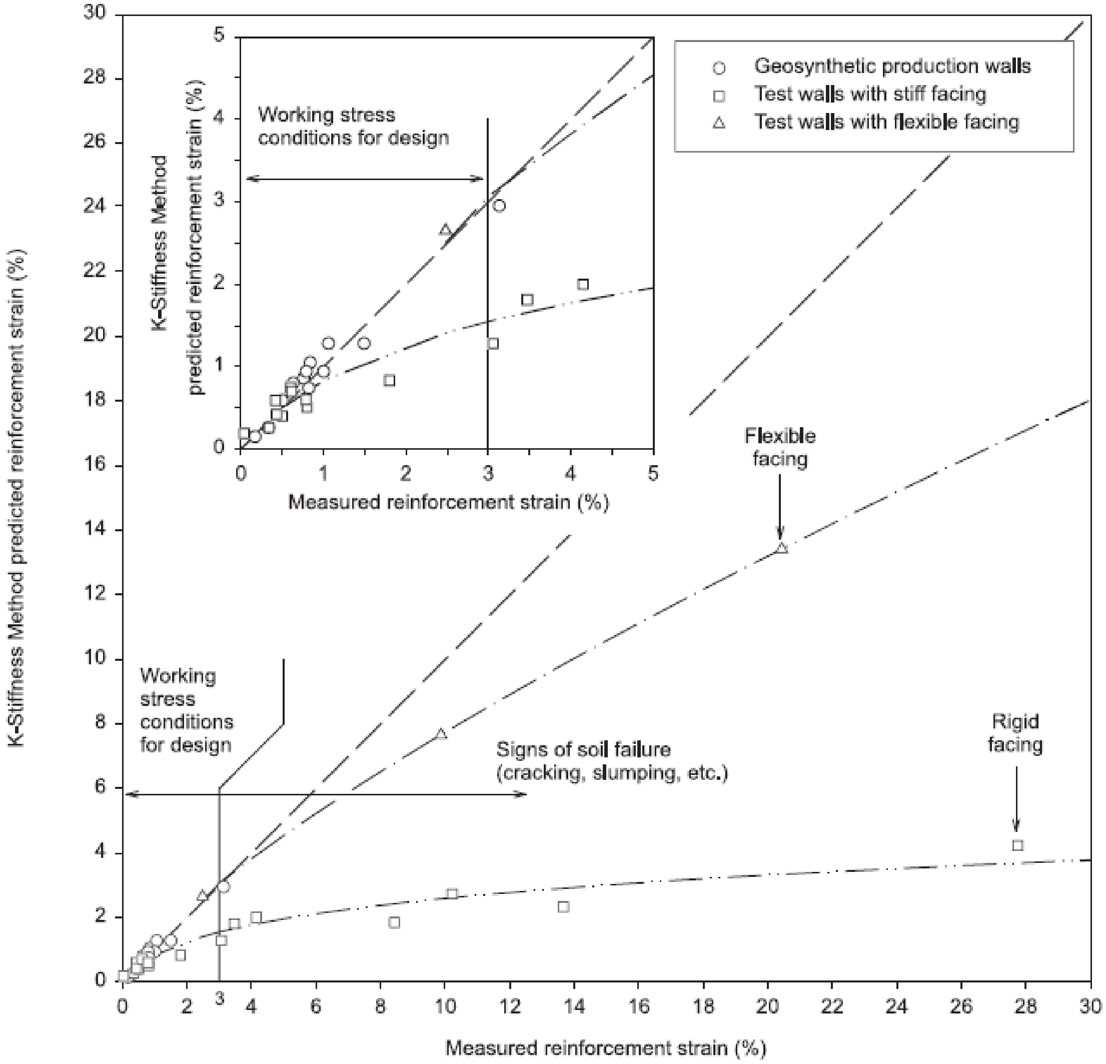

Figure 2.7: Predicted versus measured reinforcement strains (based on T_{mxmx}) using the K-stiffness method for full-scale production (field) and full-scale laboratory geosynthetic walls. The inset figure corresponds to a reinforcement strain range from 0% to 5%. (Allen et al. 2003)

Chapter 3: Finite Element Program ANLOG

This chapter presents a non-commercial finite element program ANLOG (Non Linear Analysis of Geotechnical Problems) and the basic computational algorithm in the finite element method. Unlike commercial finite element programs, ANLOG does not have advanced graphic interfaces; however, the advantage of using ANLOG is to fully access an open source code. This allows users to modify existing routines and implement new features into the original source code for specific project. For the purpose of the study in this dissertation, advanced soil and reinforcement models as well as new computational algorithms will be implemented into ANLOG. The updated finite element model will be applied to study the behavior of GRS structures under large soil strain conditions in the later chapters of this dissertation.

3.1 THE ANLOG PROGRAM

The ANLOG software is written by using FORTRAN language. Its first version was developed by Zornberg (1989) and was used to analyze mechanical elastoplastic problems considering plane and axisymmetric strain conditions. A new version was developed by Nogueira (1998) considering the flow and deformation coupling. Figure 3.1 shows the ANLOG can be executed in Windows platform. Figure 3.2 shows the pre and post processing tool, MTOOL software version 4 developed by TecGraf® (2002).

In both versions, the macro-command structure was used (Zienkiewicz 1989). This characteristic allows the simulation of the constructive process (for instance, excavation and fill). This software was applied to analyze different case histories (Zornberg 1989, Zornberg and Azevedo 1989, Nogueira 1998, Nogueira and Machado 1999) and good agreement has been found between numerical and field measured results.

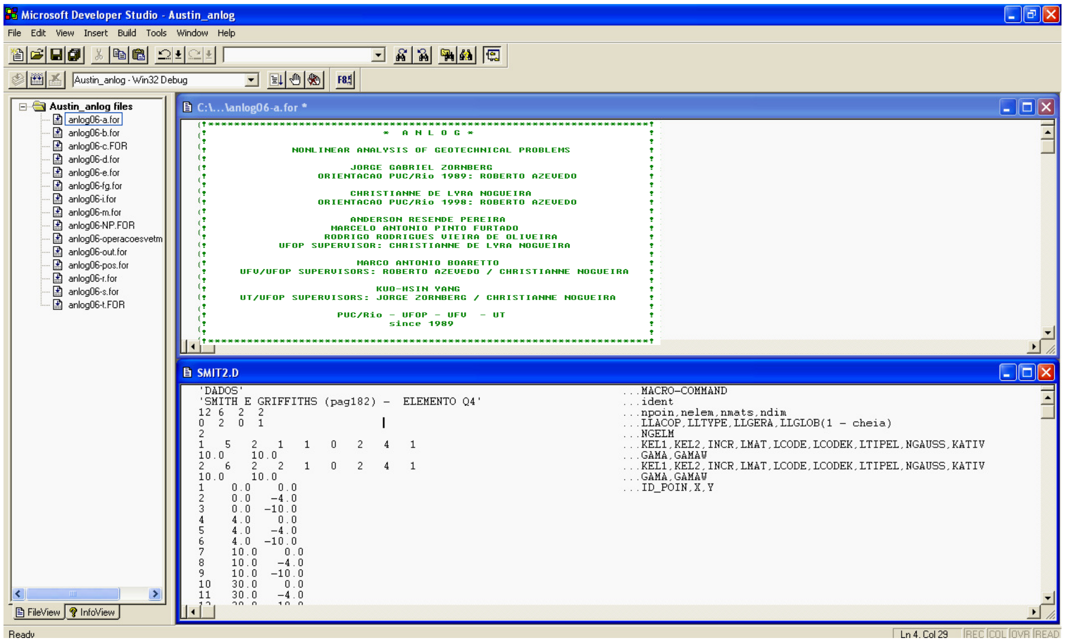

```
                       *  A N L O G *

        NONLINEAR ANALYSIS OF GEOTECHNICAL PROBLEMS

                  JORGE GABRIEL ZORNBERG
          ORIENTACAO PUC/Rio 1989: ROBERTO AZEVEDO

              CHRISTIANNE DE LYRA NOGUEIRA
          ORIENTACAO PUC/Rio 1998: ROBERTO AZEVEDO

               ANDERSON RESENDE PEREIRA
              MARCELO ANTONIO PINTO FURTADO
            RODRIGO RODRIGUES VIEIRA DE OLIVEIRA
        UFOP SUPERVISOR: CHRISTIANNE DE LYRA NOGUEIRA

                MARCO ANTONIO BOARETTO
   UFV/UFOP SUPERVISORS: ROBERTO AZEVEDO / CHRISTIANNE NOGUEIRA

                    KUO-HSIN YANG
   UT/UFOP SUPERVISORS: JORGE ZORNBERG / CHRISTIANNE NOGUEIRA

             PUC/Rio - UFOP - UFV  - UT
                     since 1989
```

```
'DADOS'                                                  ...MACRO-COMMAND
'SMITH E GRIFFITHS (pag182) -  ELEMENTO Q4'              ...ident
12 6  2  2                                               ...npoin,nelem,nmats,ndim
0  2  0  1                                               ...LLACOP,LLTYPE,LLGERA,LLGLOB(1 - cheia)
2                                                        ...NGELM
1   5   2   1   1   0   2   4   1                        ...KEL1,KEL2,INCR,LMAT,LCODE,LCODEK,LTIPEL,NGAUSS,KATIV
10.0    10.0                                             ...GAMA,GAMAW
2   6   2   2   1   0   2   4   1                        ...KEL1,KEL2,INCR,LMAT,LCODE,LCODEK,LTIPEL,NGAUSS,KATIV
10.0    10.0                                             ...GAMA,GAMAW
1    0.0     0.0                                         ...ID_POIN,X,Y
2    0.0    -4.0
3    0.0   -10.0
4    4.0     0.0
5    4.0    -4.0
6    4.0   -10.0
7    10.0    0.0
8    10.0   -4.0
9    10.0  -10.0
10   30.0    0.0
11   30.0   -4.0
```

Figure 3.1: ANLOG in FORTRAN workspace

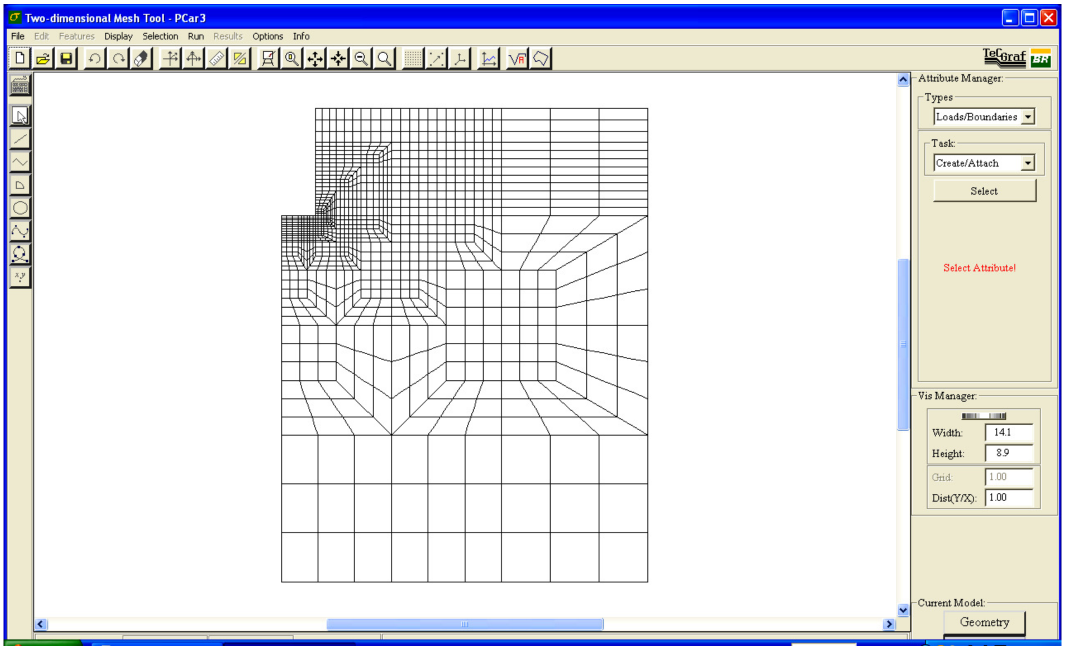

Figure 3.2: Pre and pos processing package, Mtool

3.1.1 Macro Commands

A macro-command is a key word which controls routines blocks to perform specific tasks. The user should provide the macro-command's sequence and all data set of input related to this macro-command. This macro-command's sequence defines the computational flow used during a specific problem's solution. Examples of the macro-command's sequences are depicted in Fig. 3.3.

Macro-command DADOS activates routine blocks which are responsible for reading the geometrics data (coordinates and connectivity), material data (constitutive models and properties) and boundary condition data.

Macro-commands CPOIN, CEDGE and CGRAV activate routine blocks that provide the nodal equivalent loading due to concentrated, linear and body forces, respectively.

Macro-commands ESCAV and FILL are used to simulate construction steps during excavation or filling. The weight of soil removed during excavation or filled during filling will be converted to additional nodal equivalent loadings.

Macro-commands TINK0 and TINIS are used to define an initial stress condition. Macro-command TINK0 is used to obtain a stress state for soil under at rest (K_0) conditions and macro-command TINIS is used to obtain an isotropic initial stress state.

Macro-command SOLVE is used to obtain the global characteristic matrix and solve the algebraic equation system. The primary variables (displacement, force,…,etc.) and secondary variables (strain, stress,...,etc.) can be obtained in this macro-command.

Macro-commands FEXEC is used at end of macro command sequence to close the program. Other available macro-commands in ANLOG are summarized in Table 3.1.

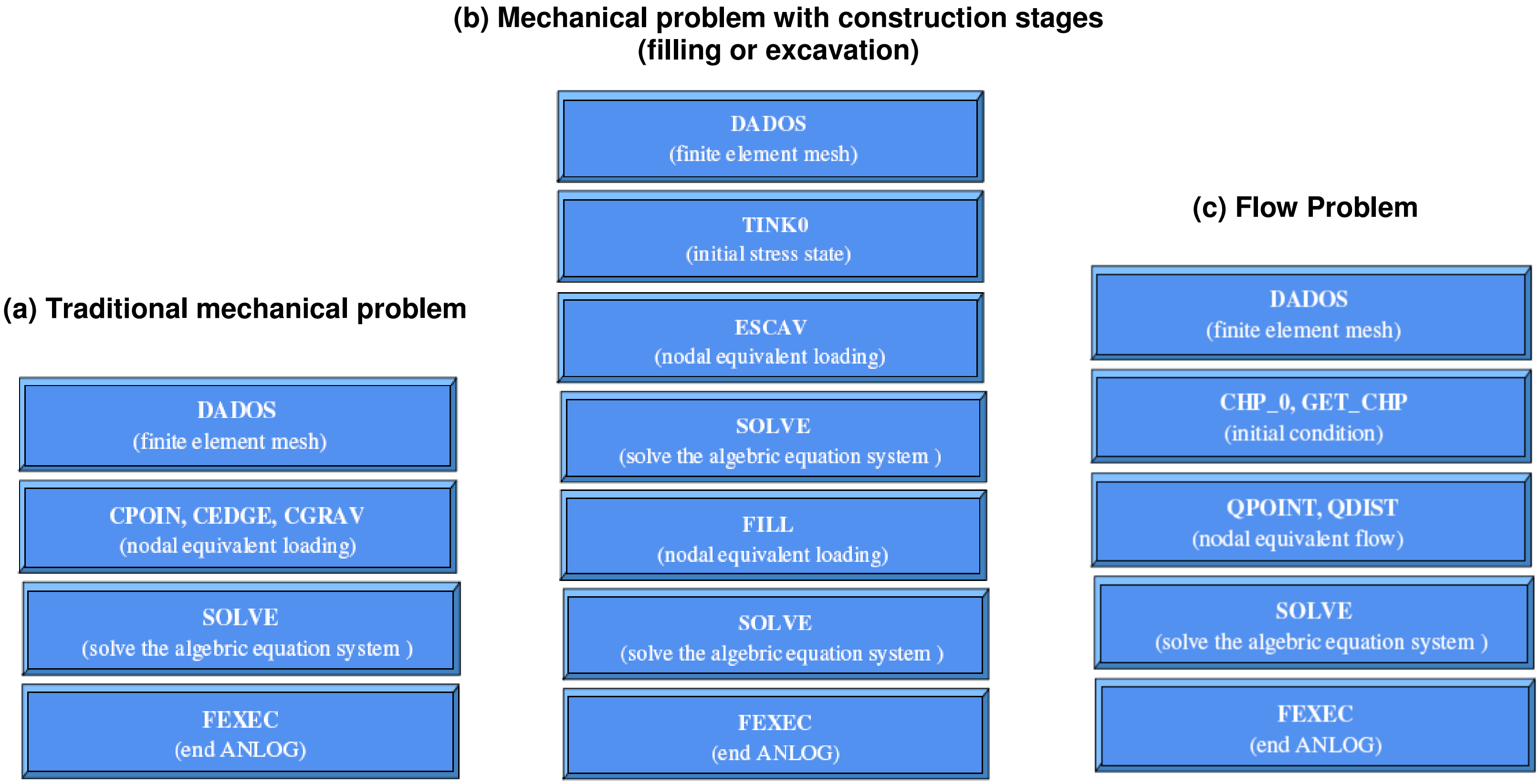

Figure 3.3: Examples of macro commands sequences

Table 3.1: Macro-Commands in ANLOG

COMMAND	**DESCRIPTION**	**SUBROUTINES**	**ANLOG FILES**
DADOS	Read input data including global, element and material variables	DADOS	Data_Reading.f90
		DATNPROP	
		DATMSH and DATMSH_NF	
		DATMAT	
		DATBOU and DATBOU_NF	
		RENID	
CCPRES	Prescribe boundary conditions	DATBOU_PR	Essential_Boundary_condition.f90
MUDCC	Change boundary conditions	MUDCC	
		RENID	
CPOIN	Input concentrated loads	CPOIN	Natural_Boundary_condition.f90
CEDGE	Input surface loads	CEDGE	
CGRAV	Input body loads	CGRAV	
CTEN	Input stress increments	CTEN	
CFHE	Input gravitational forces	CFHE	
QPOINT	Input concentrated flows	QPOINT	
ATERR	Execute fill process	ATERR	Fill_Process.f90
		RENID	
ESCAV	Execute excavation process	ESCAV	Excavation_Process.f90
		RENID	
BARAT	Activate bar/reinforcement elements	BARAT	Bar_Element_activ.f90
REINIC	Restart the analysis	REINID	Creating_Intermidiate_Files.f90
		REINIC	

		RENID	Creating_Intermidiate_Files.f90
CARIN	Create intermediate file data	CARIN	
WRITEN	Write a stress file	WRITEN	
READTEN	Read a stress file	READTEN	
ZDESL	Zero the displacement	ZDESL	Zera.f90
ZDEF	Zero the strain	ZDEF	
TINK0	Define geostatic initial stress state	TINK0	Initial_Stress_State.f90 Stress_Level.f90
TINIS	Define isotropic initial stress state	TINIS	
SUPIN	Define initial stress level	SUPIN	
SPPRE	Define stress level	SPPRE	
POSD	Produce final report file	POSD	Post_processing.f90
POSR	Produce final report file	POSR	
MVIEW	Produce file for post processing	MVIEW	
ATCOOR	Update coordinates		Manager.f90
SOLVE	Obtain the global characteristic matrix, solve the algebraic equations system, obtain secondary variables	SOLVE	General_Solve.f90 Correct_strategies.f90 Fload.f90 Stiffness_matrix.f90 Constitutive_matrix.f90 Properties_definition.f90 Equation_System_Solver.f90 Secundary_variables.f90 Stress_integration.f90 Printing_results.f90
FEXEC	Close the ANLOG program		

3.1.2 Variables

The variables in ANLOG are categorized into five main groups including: 1) analysis identifiers; 2) global variables; 3) element variables; 4) material variables; and 5) boundary condition variables. The functions of variables in each group are discussed in this section.

3.1.2.1 Analysis Identifiers

Analysis identifiers are variables used to control the program's flow. The variables include:

LLACOP: identify analysis types

LLACOP = 0 – stress strain analysis (displacement as a primary variable)
LLACOP = 1 – saturated coupled analysis (displacement and pore pressure as a as primary variables)
LLACOP = 2 – saturated coupled analysis (total head as a primary variable)
LLACOP = 3 – flow analysis (pore pressure as a primary variable)
LLACOP = 4 – unsaturated coupled analysis (displacement and pore pressure as primary variables)

LLTYPE: identify deformation state

LLTYPE = 1 – plane strain
LLTYPE = 2 – axisymmetric strain
LLTYPE = 3 – plane stress
LLTYPE = 4 – 3D problem

LLGERA: identify geometry, connectivity and boundary condition

LLGERA = 0 - use the read file (ARQE.D)
LLGERA = 1 - use the neutral file provided by MTOOL (ARQE.NF)
LLGERA = 2 - use the neutral file provided by MTOOL to geometry and connectivity (ARQE.NF) and the read file (ARQE.D) to boundary condition

LLGLOB: control stiffness matrix arrangement types

LLGLOB = 0 – Skyline matrix (nperfl – the skyline size)

LLGLOB = 1 – Full matrix (neq – equation's number)

LGAUS: control evaluation location of the secondary variable

LGAUS = 0 – at the center of elements
LGAUS = 1 – at the Gauss point

LLSIM: controls symmetry of the characteristic matrix

LLSIM = 1 – to Lade's model - symmetric matrix
LLSIM = 2 – to Lade's model - symmetric matrix (equivalent matrix - $D=1/2*(D + D^T)$)
LLSIM = 3 – to symmetric matrix (elastic matrix)
LLSIM = 4 – to non symmetric matrix

LLALGR: identify incremental strategy types

LLALGR=1 - NEWTON-RAPHSOM (INC/ITER)
LLALGR=5 - EULER (INC)

LLINT: identify stress integration scheme types

LLINT = 1 – Explicit scheme – forward Euler
LLINT = 21 – Explicit scheme with sub increment – (NSUB)
LLINT = 211 – Modified forward Euler integration scheme with error control
LLINT = 22 – Explicit scheme with sub increment – (DEFREF)
LLINT = 23 – Explicit scheme with sub increment – (P_0)
LLINT = 24 – Explicit scheme with sub increment – (SLR)

Note: The modified forward Euler integration scheme with error control is implemented in to ANLOG as LLINT=211. Detailed description of this integration scheme is presented in Chapter 5.

LLCONV: control convergence criteria of iteration scheme

LLCONV = 0 - convergence based on force balance ($\|\boldsymbol{\Psi}\| / \|\mathbf{F}_{ext}\|$)
LLCONV = 1 – convergence based on displacement balance ($\|\partial\Delta\hat{\mathbf{u}}\| / \|\hat{\mathbf{u}}\|$)

LLRESL: control actualization of stiffness matrix during the iteration scheme

LLRESL = 1 – Newton Raphson Standard
LLRESL = 2 - Newton Raphson Modified

LLOUTP: control result printing

LLOUTP = 0 – nothing
LLOUTP = 1 – displacement
LLOUTP = 2 – displacement, strain and stress
LLOUTP = 3 – displacement, strain, stress and stress level
LLOUTP = 4 – strain, stress and stress level
LLOUTP = 5 –principal strain, principal stress and stress level
LLOUTP = 6 –principal strain and principal stress
LLOUTP = 7 – strain and stress
LLOUTP = 8 – displacement, principal strain and principal stress

3.1.2.2 Global Variables

Global variables are used to define the dimensions of global matrix and vector. The variables include:

ndim: define the problem dimension

ndim =1 – 1D problem
ndim = 2 - 2D problem
ndim = 3 – to 3D problem

npoin: number of nodal point in FE mesh

nelem: number of element in FE mesh

nmats: number of different material types

ndof: number of degree of freedom per node

if LLACOP = 0 – ndof = 2 to 2D problem; ndof = 3 to 3D problem
if LLACOP = 1 or 2 or 4 – ndof = 3 to 2D problem; ndof = 4 to 3D problem
if LLACOP = 3 – ndof = 1 to 2D and 3D problem

3.1.2.3 Element Variables

Element variables are used to define the dimensions of elementary matrix and vector. The element variables in ANLOG are summarized in Table 3.2. The variables include:

ltipel: element identifier

ltipel=1 : quadratic quadrilateral element (Q8)
ltipel=2 : linear quadrilateral element (Q4)
ltipel=3 : quadratic triangular element (T6 or T6T3)
ltipel=4 : linear triangular element (T3)
ltipel=5 : quadratic truss element (B3)
ltipel=6 : linear truss element (B2)
ltipel=7 : quadratic joint element (J6)
ltipel=8 : linear joint element (J4)
ltipel=9 : quadratic axisymmetric reinforcement element (R3)
ltipel=10 : linear axisymmetric reinforcement element (R2)
ltipel=11 : quadratic interface element (I6)
ltipel=12 : linear interface element (I4)
ltipel=13 : quadratic solid element (C20)
ltipel=14 : linear solid element (C8)
ltipel=15 : linear joint element (GTB2)
ltipel=16 : linear joint element (LRH)

nnoel: number of element nodes

ndofel: number of degree of freedom per node (natural coordinate system)

ndimel: problem dimension (natural coordinate system)

ncomp: number of stress and strain components

ngauss – number of Gauss point

llintg – identify different types of numerical integration

Table 3.2: Element variables in ANLOG

<table>
<tr><th colspan="2">ELEMENT</th><th>LTIPEL</th><th>NNOEL</th><th>NDIMEL</th><th>NDOFEL</th><th>NCOMP</th><th>NGAUSS</th></tr>
<tr><td>Q8</td><td>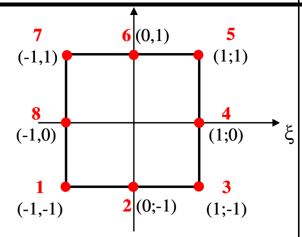
</td><td>1</td><td>8</td><td>2</td><td>2</td><td>4</td><td>4 or 9</td></tr>
<tr><td>Q4</td><td>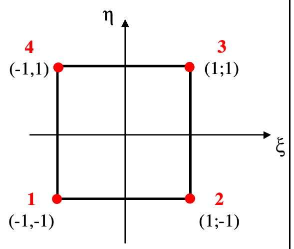
</td><td>2</td><td>4</td><td>2</td><td>2</td><td>4</td><td>4</td></tr>
<tr><td>T6</td><td>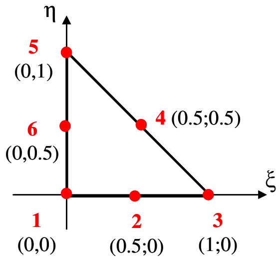
</td><td>3</td><td>6</td><td>2</td><td>2</td><td>4</td><td>3 or 7</td></tr>
<tr><td>T3</td><td>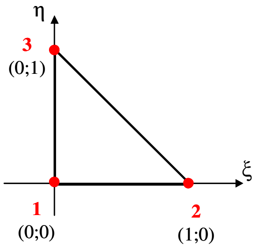
</td><td>4</td><td>3</td><td>2</td><td>2</td><td>4</td><td>3</td></tr>
<tr><td>B3</td><td>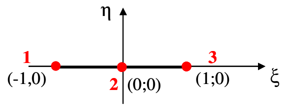
</td><td>5</td><td>3</td><td>1</td><td>1</td><td>1</td><td>2 or 3</td></tr>
<tr><td>B2</td><td>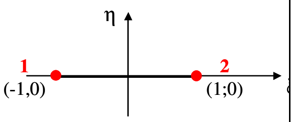
</td><td>6</td><td>2</td><td>1</td><td>1</td><td>1</td><td>2</td></tr>
<tr><td>J6</td><td>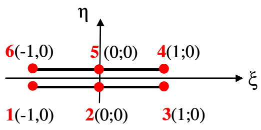
</td><td>7</td><td>6</td><td>1</td><td>2</td><td>2</td><td>3</td></tr>
</table>

ELEMENT		LTIPEL	NNOEL	NDIMEL	NDOFEL	NCOMP	NGAUSS
J4	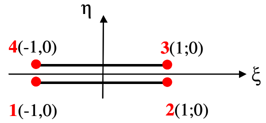	8	4	1	2	2	2
R3	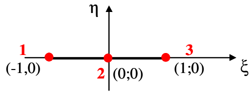	9	3	1	1	2	2 or 3
R2	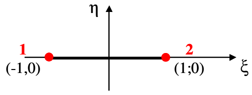	10	2	1	1	2	2
I6	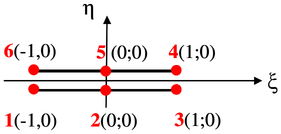	11	6	1	1	1	3
I4	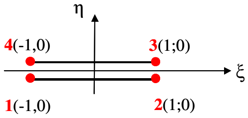	12	4	1	1	1	2
GTB2	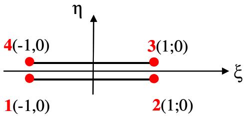	15	4	1	2	2	2
LRH	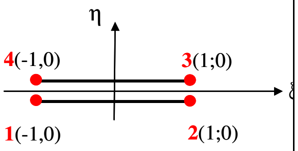	16	4	1	2	2	2
C20	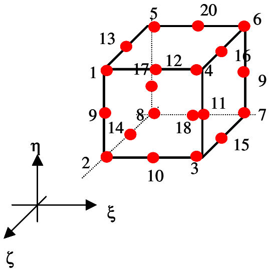	13	20	3	3	6	8 or 27
C8	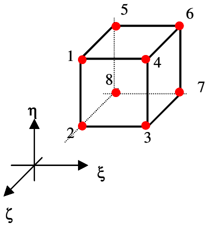	14	8	3	3	6	8 or 27

3.1.2.4 Material Variables

Material variables are used to characterize the behavior of materials into elements. Material variables in ANLOG are summarized from Table 3.3 to Table 3.6. The variables include:

lmat: material identifier

lcode: stress-strain constitutive model identifier (see Table 3.3 for 2-D solid elements, Table 3.4 for 1-D truss and reinforcement elements and Table 3.5 for joint and interface elements).

Note: The soil-softening model proposed in this study is developed and implemented into ANLOG as lcode=141. Detailed description of the soil-softening model is presented in Chapter 4.

The nonlinear reinforcement model is implemented into ANLOG as lcode=24. Detailed description of this reinforcement model is presented in Chapter 6.

nprop: number of parameters by stress-strain constitutive model

nsup: number of yield surface by stress-strain constitutive model

nenduc: number of hardening function by stress-strain constitutive model

lcodek: hydraulic constitutive model identifier (see Table 3.6)

npropk: number of parameters by hydraulic constitutive model

3.1.2.5 Boundary Condition Variable

A boundary condition variable is used to assign boundaries for element nodes in given directions. A variable value of 0 allows nodes to move freely in the designated direction (x, y, or z). Oppositely, a variable value of 1 is inputted to restrict the node movement in the designated direction. A variable value of 9 is assigned when the nodal displacements are prescribed by user.

Table 3.3: Material variables for 2-D solid elements in ANLOG

LCODE	MODEL	PARAMETERS	NPROP	NSUP	NENDUC
1	Linear elastic	$E, \nu,$	2	0	0
2	Hyperbolic (ν=cte)	$K_i, K_{ur}, n, \nu, p_a, c, \phi, R_f$	8	1	0
3	Bi-linear - Von Mises	$E, \nu, p_a, S_{u,}$	4	1	0
4	Bi-linear - Mohr-Coulomb	E, ν, p_a, c, ϕ	5	1	0
5	Bi-linear - Lade	$E, \nu, p_a, m, \eta_1, a$	6	1	0
6	Hyperbolic (B=cte)	$K_i, K_{ur}, n, p_a, c, \phi, R_f, K_b, m$	9	1	0
7	Lade 77- without CAP	$K_{ur}, n, \nu, p_a, m, \eta_1$, s1, s2, t1,t2, w1, w2, q1, q2, a	15	1	1
8	Lade 77 - CAP-sand	$K_{ur}, n, \nu, p_a, m, \eta_1$, s1, s2, t1,t2, w1, w2, q1, q2, C, p, a	17	2	2
9	Camclay	$\lambda, \kappa, \chi, \nu, p_a, M$	6	1	1
10	Lade & Kim 90	$K_{ur}, n, \nu, p_a, m, \eta_1, C, p, \psi_2, \mu, h, \alpha, a$	13	1	1
11	Lade 77 - CAP-clay	$K_{ur}, n, \nu, p_a, m, \eta_1$, s1, s2, t1,t2, w1, w2, q1, q2 C, p, a	17	2	2
12	Elastoplastico Drucker & Prager	E, ν, pa, c, ϕ, ψ	6	1	0
13	Elastoplastic Mohr-Coulomb	E, ν, pa, c, ϕ, ψ	6	1	0
14	Lade & Kim 90	$M, \lambda, \nu, p_a, m, \eta_1, C, p, \psi_2, \mu, h, \alpha, a$	13	1	1
15	Elastoplastic Drucker & Prager Modified	E, ν, pa, c, ϕ, ψ, a	7	1	0
16	Elastoplastic Mohr-Coulomb Modified	E, ν, pa, $c, \phi, \psi, \theta_T, a$	8	1	0
141	Lade-Kim + Soil-Softening Model	$M, \lambda, \nu, p_a, m, \eta_1, C, p, \psi_2, \mu, h, \alpha, a'$ a, b, f''_{pr}	16	1	2

Table 3.4: Material variables for 1-D truss and reinforcement elements in ANLOG

LCODE	MODEL	PARAMETERS	NPROP	NSUP	NENDUC
21	Linear elastic	Area, E	2	0	0
22/23	Bi-linear (compression /tension)	Area, E	2	0	0
24	Parabolic elastic	Area, a, b	3	0	0
25	Elsatoplastic	Area, E, T_{max}	3	1	0
26	Linear elastic (reinforcement)	Thicknes, E, ν	3	0	0
27	Parabolic elastic (reinforcement)	Thicknes, a, b, ν	4	1	0
28	Elastoplastic (reinforcement)	Thicknes, E, ν, T_{max}	4	1	0

Table 3.5: Material variables for joint and interface elements in ANLOG

LCODE	MODEL	PARAMETERS	NPROP	NSUP	NENDUC
31	Linear elastic	k_s, k_n	2	0	0
32	Elastoplastic Coulomb	k_s, k_n, c, ϕ, ψ	5	1	0

Table 3.6: Hydraulic material variables in ANLOG

LCODEK	MODEL	PARAMETERS	NPROPK
1	Saturated	$k_{1_{sat}};\text{factor};\beta$	3
2	Saturated (LLACOP=2)	$k_{1_{sat}};\text{factor};\beta;pp_{lim};pp_{sat};k_{1_{lim}};S_y$	7
21	linear interpolation	$k_{1_{sat}};\text{factor};\beta$	3
31	spline cubic interpolation	$k_{1_{sat}};\text{factor};\beta$	3
41	van Genuchten	$k_{1_{sat}};\text{factor};\beta;\alpha_{vg};\beta_{vg};n;\theta_{resid}$	7
51	Exponential Model	$k_{1_{sat}};\text{factor};\beta;\alpha_{sy};\theta_{sat};\theta_{resid}$	6

$*k_{3_{sat}} = \text{factor}\, k_{1_{sat}}$

3.2 MECHANICAL PROBLEM FORMULATED BY FEM

This section introduces the basic algorithm of finite element computation implemented into the ANLOG. A special focus will be placed on mechanical problem and formulations in finite element analysis.

3.2.1 System Equilibrium

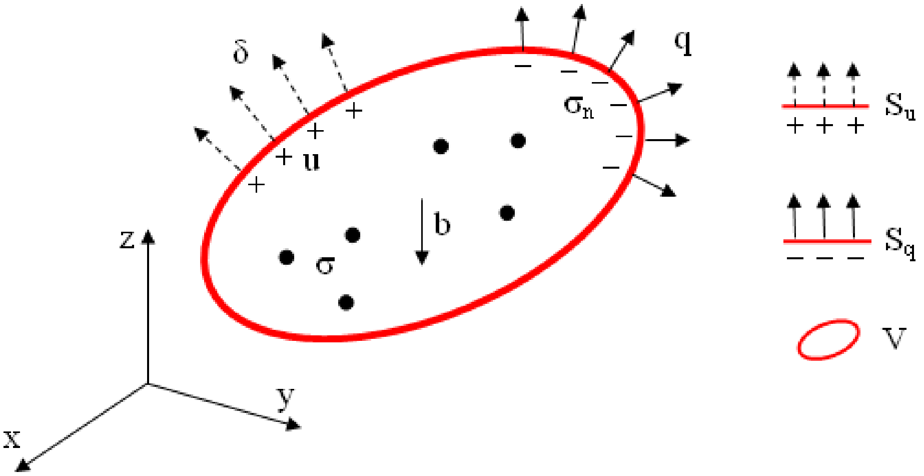

Figure 3.4: Illustration of problem and boundary domain

Static equilibrium of mechanical problem could be written in the following partial differential equation:

$$\nabla^{T}\sigma + b = 0 \quad \text{in } V \tag{3.1}$$

in which V is the problem domain of interest, ∇ is a first order differential operator and σ is the stress tensor that depend on the problem dimension and geometry (see Table 3.7). b is the body force vector. Eq. (3.1) should also satisfy the following boundary conditions:

$$\sigma \cdot n = q \quad \text{in } S_q \text{ (natural boundary condition)} \tag{3.2}$$

and

$$u = \delta \quad \text{in } S_u \text{ (essential boundary condition)} \tag{3.3}$$

in which S_q and S_u are the boundary domain of prescribed forces and displacements, respectively. n is the vector normal to the surface of S_q. q is the surface force vector. u is the displacement vector and δ is the prescribed value to the displacement along the surface of S_u..

Table 3.7: Delta differential operator and stress vector definition

Strain condition	**Delta differential operator ∇**	**Stress vector $\boldsymbol{\sigma}$**
One-dimensional	$\left[d/dx \right]$	$\left\{ \sigma_x \right\}$
plane	$\begin{bmatrix} \partial/\partial x & 0 \\ 0 & \partial/\partial y \\ 0 & 0 \\ \partial/\partial y & \partial/\partial x \end{bmatrix}$	$\begin{Bmatrix} \sigma_x \\ \sigma_y \\ \sigma_z \\ \tau_{xy} \end{Bmatrix}$
axisymmetric	$\begin{bmatrix} \partial/\partial x & 0 \\ 0 & \partial/\partial y \\ 1/x & 0 \\ \partial/\partial y & \partial/\partial x \end{bmatrix}$	$\begin{Bmatrix} \sigma_x \\ \sigma_y \\ \sigma_z \\ \tau_{xy} \end{Bmatrix}$
general	$\begin{bmatrix} \partial/\partial x & 0 & 0 \\ 0 & \partial/\partial y & 0 \\ 0 & 0 & \partial/\partial z \\ \partial/\partial y & \partial/\partial x & 0 \\ 0 & \partial/\partial z & \partial/\partial y \\ \partial/\partial z & 0 & \partial/\partial x \end{bmatrix}$	$\begin{Bmatrix} \sigma_x \\ \sigma_y \\ \sigma_z \\ \tau_{xy} \\ \tau_{yz} \\ \tau_{yz} \end{Bmatrix}$

Exact solution for the partial differential equation Eq. (3.1) is not trivial and sometimes this solution is only limited to very simple geometry, boundary and loading conditions. Therefore, instead of directly solving Eq. (3.1), a numerical procedure of has been applied to obtain an approximate solution of the general problem. The numerical procedure follows the principal of virtual work.

The principal of virtual work involves in multiplying Eq. (3.1) by a virtual displacement vector δu which can be any arbitrary vector and integrating the product of Eq. (3.1) and virtual displacement in respect to the volume of problem domain. The result is shown as:

$$\int_V \delta u^{\mathrm{T}} \left(\nabla^{\mathrm{T}} \sigma \right) \, \mathrm{d}V + \int_V \delta u^{\mathrm{T}} b \, \mathrm{d}V = 0 \tag{3.4}$$

Apply the integration by parts in the form of Green theorem to the first part of Eq. (3.4). The derivative of stress components can be replaced by the derivative of the virtual displacement. Afterward, Eq. (3.4) can be transformed into

$$\int_{S_q} \delta u^{\mathrm{T}} \left(\sigma \ n \right) - \int_V \left(\nabla^{\mathrm{T}} \delta u \right) \sigma \, \mathrm{d}V + \int_V \delta u^{\mathrm{T}} \ b \, \mathrm{d}V = 0 \tag{3.5}$$

Introduce the nature boundary condition Eq. (3.2) into the first item of Eq. (3.5). Define the derivative of the virtual displacement equal to the virtual strain $\delta \varepsilon$ for the second item of Eq. (3.5). And rearrange the equation into

$$\int_V \delta \varepsilon^{\mathrm{T}} \sigma \, \mathrm{d}V = \int_V \delta u^{\mathrm{T}} \ b \, \mathrm{d}V + \int_{S_q} \delta u^{\mathrm{T}} q \, \mathrm{d}S_q \tag{3.6}$$

Eq. (3.6) implies the equilibrium between internal work on the right hand side of Eq. (3.6) and external work on the left hand side of Eq.(3.6). Later, it will be shown the introduced δu is cancelled out at both sides of equation. As a result, the work equilibrium is transformed into force equilibrium. Equation (3.6) can be rewritten as

$$F_{int} = F_{ext} \tag{3.7}$$

The equilibrium equation can be solved by introducing an assumed displacement field. The accuracy of solution depends on the order of equation for assumed displacement field. In general, the higher order of equation for displacement field, the closer to the exact solution. In fact, only the first or second order of polynomial equation is commonly used in finite element computation rather than the very high order of equation. However, the problem dominate is divided into many small elements or called *finite* elements. Finite elements would achieve solution accuracy as similar as that obtained by using very high order of equation for displacement field. In such case, F_{int} becomes the global internal force vector assembled from the elemental internal force vector F_{int}^{e} for each individual element. The source of F_{int}^{e} comes from the stresses σ inside the element. F_{ext} becomes the global external force vector assembled from the elemental external force vector F_{ext}^{e} for each individual element. The source of F_{ext}^{e} comes from prescribed forces and displacements. The evaluation of F_{int}^{e} and F_{ext}^{e} is discussed in following sections.

3.2.2 Strain-Displacement relationships: Compatibility

The evaluation of F_{int}^{e} and F_{ext}^{e} starts at the compatibility between strains and displacements in the element.

$$\varepsilon = -\nabla^{\mathrm{T}} u \tag{3.8}$$

where u is the displacement vector and ε is the strain vector at any location in an element. The minus signal in Eq. (3.8) represents the convention of signal (compression is positive). The displacement vector u in any place of an element domain can be obtained by interpolating from a known nodal displacement vector $\hat{u}$.

$$u = N\hat{u} \tag{3.9}$$

where N is the shape function matrix used to interpolate the calculated displacement sat nodes in an element to any location of interest in the same element. N contains the interpolation functions N_i that depends on element types.

$$N = \begin{bmatrix} N_1 & 0 & 0 & & N_{nnoel} & 0 & 0 \\ 0 & N_1 & 0 & \ldots & 0 & N_{nnoel} & 0 \\ 0 & & N_1 & & 0 & 0 & N_{nnoel} \end{bmatrix} \tag{3.10}$$

where subscript *nnoel* is the number of nodes in the element. The shape functions for various element types are summarized in Table 3.8. Combine Eqs. (3.8) and (3.9), the strains at any location in an element can be evaluated from the nodal displacements.

$$\varepsilon = -B\hat{u} \tag{3.11}$$

where

$$B = [B_1 \quad \ldots \quad B_{nnoel}] \tag{3.12}$$

and

$$B_i = \nabla N_i \tag{3.13}$$

where B is the strain-displacement matrix which contains the derivative of the interpolation functions N_i. The formulations of strain-displacement relationships for various element types are listed in Table 3.9.

Table 3.8: Shape Functions

ELEMENT		**SHAPE FUNCTION**
Q8	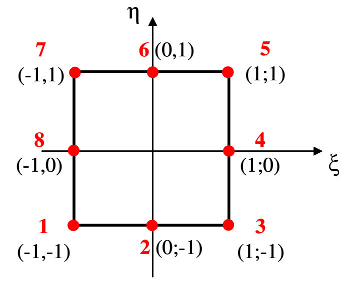	$N_1(\xi,\eta) = 0.25(1-\xi)(1-\eta)(-\xi-\eta-1)$ $N_2(\xi,\eta) = 0.5(1-\eta)(1-\xi^2)$ $N_3(\xi,\eta) = 0.25(1+\xi)(1-\eta)(\xi-\eta-1)$ $N_4(\xi,\eta) = 0.5(1+\xi)(1-\eta^2)$ $N_5(\xi,\eta) = 0.25(1+\xi)(1+\eta)(\xi+\eta-1)$ $N_6(\xi,\eta) = 0.5(1+\eta)(1-\xi^2)$ $N_7(\xi,\eta) = 0.25(1-\xi)(1+\eta)(-\xi+\eta-1)$ $N_8(\xi,\eta) = 0.5(1-\xi)(1-\eta^2)$
Q4	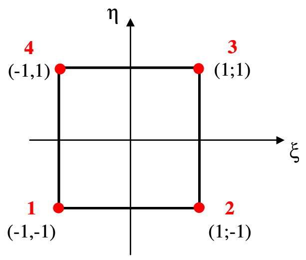	$N_1(\xi,\eta) = 0.25(1-\xi)(1-\eta)$ $N_2(\xi,\eta) = 0.25(1-\eta)(1+\xi)$ $N_3(\xi,\eta) = 0.25(1+\xi)(1+\eta)$ $N_4(\xi,\eta) = 0.25(1-\xi)(1+\eta)$
T6	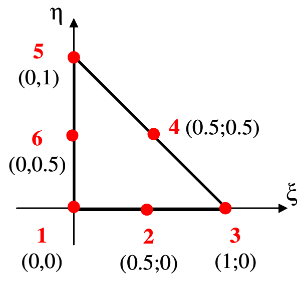	$N_1(\xi,\eta) = 1.0 - 3.0\cdot(\xi+\eta) + 2.0\cdot(\xi+\eta)^2$ $N_2(\xi,\eta) = 4.0\cdot\xi\cdot(1.0-\xi-\eta)$ $N_3(\xi,\eta) = \xi\cdot(2.0\cdot\xi-1.0)$ $N_4(\xi,\eta) = 4.0\cdot\xi\cdot\eta$ $N_5(\xi,\eta) = \eta\cdot(2.0\cdot\eta-1.0)$ $N_6(\xi,\eta) = 4.0\cdot\eta\cdot(1.0-\xi-\eta)$
T3	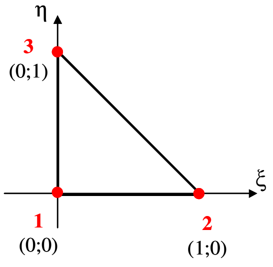	$N_1(\xi,\eta) = 1.0 - \xi - \eta$ $N_2(\xi,\eta) = \xi$ $N_3(\xi,\eta) = \eta$

B3/R3	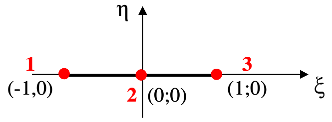	$N_1(\xi,\eta)=0.5(\xi^2-\xi)$ $N_2(\xi,\eta)=(1-\xi^2)$ $N_3(\xi,\eta)=0.5(\xi^2+\xi)$
B2/R2	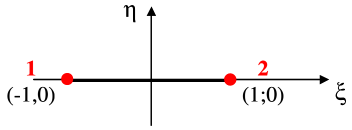	$N_1(\xi,\eta)=0.5(1-\xi)$ $N_2(\xi,\eta)=0.5(1+\xi)$
J6/I6	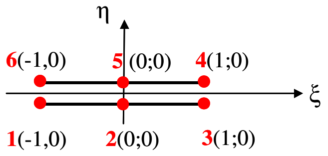	$N_1=N_6=0.5(\xi^2-\xi)$ $N_2=N_5=(1-\xi^2)$ $N_3=N_4=0.5(\xi^2+\xi)$
J4/I4	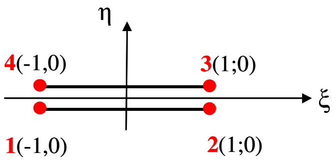	$N_1=N_4=0.5(1-\xi)$ $N_2=N_3=0.5(1+\xi)$
C8	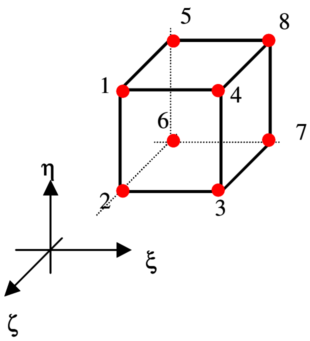 1(-1,+1,+1) 2(-1,-1,+1) 3(+1,-1,+1) 4(+1,+1,+1) 5(-1,+1,-1) 6(-1,-1,-1) 7(+1,-1,-1) 8(+1,+1,-1)	$N_1(\xi,\eta)=0.125(1-\xi)(1+\eta)(1+\zeta)$ $N_2(\xi,\eta)=0.125(1-\xi)(1-\eta)(1+\zeta)$ $N_3(\xi,\eta)=0.125(1+\xi)(1-\eta)(1+\zeta)$ $N_4(\xi,\eta)=0.125(1+\xi)(1+\eta)(1+\zeta)$ $N_5(\xi,\eta)=0.125(1-\xi)(1+\eta)(1-\zeta)$ $N_6(\xi,\eta)=0.125(1-\xi)(1-\eta)(1-\zeta)$ $N_7(\xi,\eta)=0.125(1+\xi)(1-\eta)(1-\zeta)$ $N_8(\xi,\eta)=0.125(1+\xi)(1+\eta)(1-\zeta)$

C20	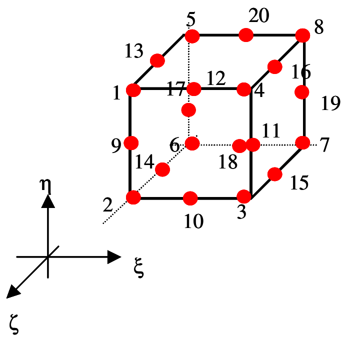 1(-1,+1,+1) 2(-1,-1,+1) 3(+1,-1,+1) 4(+1,+1,+1) 5(-1,+1,-1) 6(-1,-1,-1) 7(+1,-1,-1) 8(+1,+1,-1) 9 (-1,0,+1) 10(0,-1,+1) 11(+1,0,+1) 12(0,+1,+1) 13(-1,0,0) 14(0,-1,0) 15(+1,0,0) 16(0,+1,0) 17(-1,0,-1) 18(0,-1,-1) 19(+1,0,-1) 20(0,+1,-1)	$N_1(\xi,\eta) = 0.125(1-\xi)(1+\eta)(1+\zeta)(-\xi+\eta+\zeta-2)$ $N_2(\xi,\eta) = 0.125(1-\xi)(1-\eta)(1+\zeta)(-\xi-\eta+\zeta-2)$ $N_3(\xi,\eta) = 0.125(1+\xi)(1-\eta)(1+\zeta)(+\xi-\eta+\zeta-2)$ $N_4(\xi,\eta) = 0.125(1+\xi)(1+\eta)(1+\zeta)(+\xi+\eta+\zeta-2)$ $N_5(\xi,\eta) = 0.125(1-\xi)(1+\eta)(1-\zeta)(-\xi+\eta-\zeta-2)$ $N_6(\xi,\eta) = 0.125(1-\xi)(1-\eta)(1-\zeta)(-\xi-\eta-\zeta-2)$ $N_7(\xi,\eta) = 0.125(1+\xi)(1-\eta)(1-\zeta)(+\xi-\eta-\zeta-2)$ $N_8(\xi,\eta) = 0.125(1+\xi)(1+\eta)(1-\zeta)(+\xi+\eta-\zeta-2)$ $N_9(\xi,\eta) = 0.25(1-\xi)(1-\eta^2)(1+\zeta)$ $N_{10}(\xi,\eta) = 0.25(1-\xi^2)(1-\eta)(1+\zeta)$ $N_{11}(\xi,\eta) = 0.25(1+\xi)(1-\eta^2)(1+\zeta)$ $N_{12}(\xi,\eta) = 0.25(1-\xi^2)(1+\eta)(1+\zeta)$ $N_{13}(\xi,\eta) = 0.25(1-\xi)(1+\eta)(1-\zeta^2)$ $N_{14}(\xi,\eta) = 0.25(1-\xi)(1-\eta)(1-\zeta^2)$ $N_{15}(\xi,\eta) = 0.25(1+\xi)(1-\eta)(1-\zeta^2)$ $N_{16}(\xi,\eta) = 0.25(1+\xi)(1+\eta)(1-\zeta^2)$ $N_{17}(\xi,\eta) = 0.25(1-\xi)(1-\eta^2)(1-\zeta)$ $N_{18}(\xi,\eta) = 0.25(1-\xi^2)(1-\eta)(1-\zeta)$ $N_{19}(\xi,\eta) = 0.25(1+\xi)(1-\eta^2)(1-\zeta)$ $N_{20}(\xi,\eta) = 0.25(1-\xi^2)(1+\eta)(1-\zeta)$

Table 3.9: Strain-displacement relationships

Strain condition	**Strain vector ($\boldsymbol{\varepsilon}$)**	$\mathbf{B}_i = \nabla N_i$	**Displacement vector ($\mathbf{u}$)**	**Nodal Displacement vector ($\hat{\mathbf{u}}$)**
One-dimensional	$\{\varepsilon_x\}$	$[\partial N_i/\partial x]$	$\begin{Bmatrix} u \\ v \end{Bmatrix}$	$\begin{Bmatrix} u_1 \\ v_1 \\ \vdots \\ u_{nnoel} \\ v_{nnoel} \end{Bmatrix}$
plane	$\begin{Bmatrix} \varepsilon_x \\ \varepsilon_y \\ 0 \\ \gamma_{xy} \end{Bmatrix}$	$\begin{bmatrix} \partial N_i/\partial x & 0 \\ 0 & \partial N_i/\partial y \\ 0 & 0 \\ \partial N_i/\partial y & \partial N_i/\partial x \end{bmatrix}$	$\begin{Bmatrix} u \\ v \end{Bmatrix}$	$\begin{Bmatrix} u_1 \\ v_1 \\ \vdots \\ u_{nnoel} \\ v_{nnoel} \end{Bmatrix}$
axisymmetric	$\begin{Bmatrix} \varepsilon_x \\ \varepsilon_y \\ \varepsilon_y \\ \gamma_{xy} \end{Bmatrix}$	$\begin{bmatrix} \partial N_i/\partial x & 0 \\ 0 & \partial N_i/\partial y \\ N_i/x & 0 \\ \partial N_i/\partial y & \partial N_i/\partial x \end{bmatrix}$	$\begin{Bmatrix} u \\ v \\ w \end{Bmatrix}$	$\begin{Bmatrix} u_1 \\ v_1 \\ w_1 \\ \vdots \\ u_{nnoel} \\ v_{nnoel} \\ w_{nnoel} \end{Bmatrix}$
general	$\begin{Bmatrix} \varepsilon_x \\ \varepsilon_y \\ \varepsilon_z \\ \gamma_{xy} \\ \gamma_{yz} \\ \lambda_{yz} \end{Bmatrix}$	$\begin{bmatrix} \partial N_i/\partial x & 0 & 0 \\ 0 & \partial N_i/\partial y & 0 \\ 0 & 0 & \partial N_i/\partial z \\ \partial N_i/\partial y & \partial N_i/\partial x & 0 \\ 0 & \partial N_i/\partial z & \partial N_i/\partial y \\ \partial N_i/\partial z & 0 & \partial N_i/\partial x \end{bmatrix}$		

3.2.3 Stress-Strain relationships: Material Constitutive Model

For the evaluation of F_{int}^{e}, it also requires a constitutive relationship between stresses and strains. The stress-strain relationships can be expressed as an constitutive equation which is commonly written in an incremental form as

$$\Delta\sigma = D\Delta\varepsilon \tag{3.14}$$

where D is the material constitutive matrix or called tangent stiffness matrix. The value of D depends on the constitutive model adapted to represent the stress-strain behavior of the material. For the stress-strain behavior of the material used in this study, a development of soil-softening model to better predict soil post-peak behavior will be discussed in Chapter 4. A nonlinear reinforcement model to represent the nonlinearity of reinforcement behavior under large deformation will be discussed in Chapter 6.

In addition, for elastoplastic model and nonlinearly elastic model, stress increment $\Delta\sigma$ can not be directly obtained by Eq. (3.14). This is because the value of D varies nonlinearly with the change of stress and strain state. As a result, for the problem of nonlinearity, $\Delta\sigma$ is commonly evaluated by various stress integration algorithms. Forward Euler integration scheme with subincrement is commonly used in finite element analysis. In this integration scheme, $\Delta\varepsilon$ is subdivided into many small pieces which also called subincrements. The size of strain subincrements has to small enough so that the stress-strain relationships in this subincrement can be approximately linear. The forward Euler integration scheme with subincrements can be expressed as:

$$\Delta\sigma = \sum_{i=1}^{m} D^{i} \frac{\Delta\varepsilon}{m} \tag{3.15}$$

However, because the forward Euler integration scheme requires extra computational cost (i.e., effort and time) to spend on each subincrement, this approach turns out to be computationally expensive and inefficient. Modified forward Euler integration scheme with error control is selected in this study to reduce the computational cost as well as improve accuracy. A detailed discussion of forward Euler integration schemes and modified forward Euler integration will be presented in Chapter 5.

3.2.4 Evaluate Elemental Internal Force Vector

By introducing the strain-displacement relationships in Eq.(3.11) into to the internal forces expression in Eq. (3.6). The elemental internal force vector F_{int}^{e} becomes:

$$F_{int}^{e} = \int_{V_e} \delta\varepsilon^{\mathrm{T}}\sigma \;\mathrm{d}V_e = \int_{V_e} \delta\hat{u}^{\mathrm{T}} B^{\mathrm{T}}\sigma \;\mathrm{d}V_e = \delta\hat{u}^{\mathrm{T}} \int_{V_e} B^{\mathrm{T}}\sigma \;\mathrm{d}V_e \tag{3.16}$$

where $\delta\hat{u}$ is the virtual nodal displacement vector. Since $\delta\hat{u}$ can be a vector with any arbitrary value, $\delta\hat{u}$ can be removed from the inside of integration by selecting a constant value for $\delta\hat{u}$. Further, it will be demonstrated later that $\delta\hat{u}$ appears at both sides of Eq. (3.6). Therefore, effect of $\delta\hat{u}$ can be canceled out. Last, by introducing the constitutive equation Eq. (3.14) into Eq. (3.16), Eq. (3.16) can be rewritten as

$$F_{int}^{e} = \int_{V_e} B^{\mathrm{T}}\sigma \mathrm{d}V_e = \int_{V_e} B^{\mathrm{T}} D_t \varepsilon \mathrm{d}V_e = \underbrace{\int_{V_e} B^{\mathrm{T}} D_t B \mathrm{d}V_e}_{K^e} \hat{u} = K^{e}\hat{u} \tag{3.17}$$

where K^e is the elemental stiffness matrix. The integration of Eq. (3.17) is conducted by the Gauss-Legender integration scheme or Gauss-Lobato integration scheme for interface element. The integration scheme to obtain K^e and F_{int}^e are showed in Tables 3.10 and 3.11 respectively. A sample of the Gauss's point and weight for linear and quadratic quadrilateral elements (Q4 and Q8) are listed in Table 3.12.

Table 3.10: Element stiffness matrix

Dimension	$\mathbf{K}_e$
1D	$\int_{-1}^{+1} \underbrace{B^T D_t B\ t\ c\ \det J}_{T^K(\xi)} d\xi = \sum_{i=1}^{ngauss} \left[w_{\xi_i} T^K(\xi_i) \right]$
2D	$\int_{-1}^{+1}\int_{-1}^{+1} \underbrace{B^T D_t B\ t\ c\ \det J}_{T^K(\xi,\eta)} d\xi d\eta = \sum_{i=1}^{ngauss} \left[w_{\xi_i} w_{\eta_i} T^K(\xi_i,\eta_i) \right]$
3D	$\int_{-1}^{+1}\int_{-1}^{+1}\int_{-1}^{+1} \underbrace{B^T D_t B\ \det J}_{T^K(\xi,\eta)} d\xi d\eta d\zeta = \sum_{i=1}^{ngauss} \left[w_{\xi_i} w_{\eta_i} w_{\zeta_i} T^K(\xi_i,\eta_i,\zeta_i) \right]$

Table 3.11: Elemental internal force vector

Dimension	$\mathbf{F}_{int}^{\ e}$
1D	$\int_{-1}^{+1} \underbrace{B^T \sigma\ t\ c \det J}_{T^\sigma(\xi)} d\xi = \sum_{i=1}^{ngauss} \left[w_{\xi_i} T^\sigma(\xi_i) \right]$
2D	$\int_{-1}^{+1}\int_{-1}^{+1} \underbrace{B^T \sigma\ t\ c \det J}_{T^\sigma(\xi,\eta)} d\xi d\eta = \sum_{i=1}^{ngauss} \left[w_{\xi_i} w_{\eta_i} T^\sigma(\xi_i,\eta_i) \right]$
3D	$\int_{-1}^{+1}\int_{-1}^{+1}\int_{-1}^{+1} \underbrace{B^T \sigma \det J}_{T^\sigma(\xi,\eta,\zeta)} d\xi d\eta d\zeta = \sum_{i=1}^{ngauss} \left[w_{\xi_i} w_{\eta_i} w_{\zeta_i} T^\sigma(\xi_i,\eta_i,\zeta_i) \right]$

Table 3.12: Gauss-Legneder integration scheme

Element	**Natural coordinate (ξ_i ,η_i)**		**Weight ($W_{\xi i}$,$W_{\eta i}$)**	
Q8	ngauss=4	ngauss=9	ngauss=4	ngauss=9
	$\begin{bmatrix} -\sqrt{3}/3 & -\sqrt{3}/3 \\ \sqrt{3}/3 & -\sqrt{3}/3 \\ \sqrt{3}/3 & \sqrt{3}/3 \\ -\sqrt{3}/3 & \sqrt{3}/3 \end{bmatrix}_{\xi;\eta_i}$	$\begin{bmatrix} -\sqrt{3/5} & -\sqrt{3/5} \\ 0 & -\sqrt{3/5} \\ \sqrt{3/5} & -\sqrt{3/5} \\ -\sqrt{3/5} & 0 \\ 0 & 0 \\ \sqrt{3/5} & 0 \\ -\sqrt{3/5} & \sqrt{3/5} \\ 0 & \sqrt{3/5} \\ \sqrt{3/5} & \sqrt{3/5} \end{bmatrix}_{\xi;\eta_i}$	$\begin{bmatrix} 1 & 1 \\ 1 & 1 \\ 1 & 1 \\ 1 & 1 \end{bmatrix}_{w_{\xi_i};w_{\eta_i}}$	$\begin{bmatrix} 5/9 & 5/9 \\ 8/9 & 5/9 \\ 5/9 & 5/9 \\ 5/9 & 8/9 \\ 8/9 & 8/9 \\ 5/9 & 8/9 \\ 5/9 & 5/9 \\ 8/9 & 5/9 \\ 5/9 & 5/9 \end{bmatrix}_{w_{\xi_i};w_{\eta_i}}$
Q4	ngauss=4		ngauss=4	
	$\begin{bmatrix} -\sqrt{3}/3 & -\sqrt{3}/3 \\ \sqrt{3}/3 & -\sqrt{3}/3 \\ \sqrt{3}/3 & \sqrt{3}/3 \\ -\sqrt{3}/3 & \sqrt{3}/3 \end{bmatrix}_{\xi;\eta_i}$		$\begin{bmatrix} 1 & 1 \\ 1 & 1 \\ 1 & 1 \\ 1 & 1 \end{bmatrix}_{w_{\xi_i};w_{\eta_i}}$	
	$\begin{bmatrix} -\sqrt{3}/3 \\ \sqrt{3}/3 \end{bmatrix}_{\xi;\eta_i}$		$\begin{bmatrix} 1 \\ 1 \end{bmatrix}_{w_{\xi_i};w_{\eta_i}}$	

Table 3.13: Jacobian matrix

<table>
<tr><th>Dimension</th><th>Transformation between local and natural coordinates</th></tr>
<tr><td>Plane condition</td><td>$\begin{Bmatrix} \frac{\partial}{\partial\xi} \\ \frac{\partial}{\partial\eta} \end{Bmatrix} = \underbrace{\begin{bmatrix} \frac{\partial x}{\partial\xi} & \frac{\partial y}{\partial\xi} \\ \frac{\partial x}{\partial\eta} & \frac{\partial y}{\partial\eta} \end{bmatrix}}_{J} \begin{Bmatrix} \frac{\partial}{\partial x} \\ \frac{\partial}{\partial y} \end{Bmatrix}$</td></tr>
<tr><td>General condition</td><td>$\begin{Bmatrix} \frac{\partial}{\partial\xi} \\ \frac{\partial}{\partial\eta} \\ \frac{\partial}{\partial\zeta} \end{Bmatrix} = \underbrace{\begin{bmatrix} \frac{\partial x}{\partial\xi} & \frac{\partial y}{\partial\xi} & \frac{\partial z}{\partial\xi} \\ \frac{\partial x}{\partial\eta} & \frac{\partial y}{\partial\eta} & \frac{\partial z}{\partial\eta} \\ \frac{\partial x}{\partial\zeta} & \frac{\partial y}{\partial\zeta} & \frac{\partial z}{\partial\zeta} \end{bmatrix}}_{J} \begin{Bmatrix} \frac{\partial}{\partial x} \\ \frac{\partial}{\partial y} \\ \frac{\partial}{\partial z} \end{Bmatrix}$</td></tr>
<tr><td colspan="2">$\frac{dx}{d\xi} = \sum_{i=1}^{nnoel} \frac{dN_i}{d\xi} x_i \;;\; \frac{dy}{d\xi} = \sum_{i=1}^{nnoel} \frac{dN_i}{d\xi} y_i \;;\; \frac{dz}{d\xi} = \sum_{i=1}^{nnoel} \frac{dN_i}{d\xi} z_i$
$\frac{dx}{d\eta} = \sum_{i=1}^{nnoel} \frac{dN_i}{d\eta} x_i \;;\; \frac{dy}{d\eta} = \sum_{i=1}^{nnoel} \frac{dN_i}{d\eta} y_i \;;\; \frac{dz}{d\eta} = \sum_{i=1}^{nnoel} \frac{dN_i}{d\eta} z_i$
$\frac{dx}{d\zeta} = \sum_{i=1}^{nnoel} \frac{dN_i}{d\zeta} x_i \;;\; \frac{dy}{d\zeta} = \sum_{i=1}^{nnoel} \frac{dN_i}{d\zeta} y_i \;;\; \frac{dz}{d\zeta} = \sum_{i=1}^{nnoel} \frac{dN_i}{d\zeta} z_i$</td></tr>
</table>

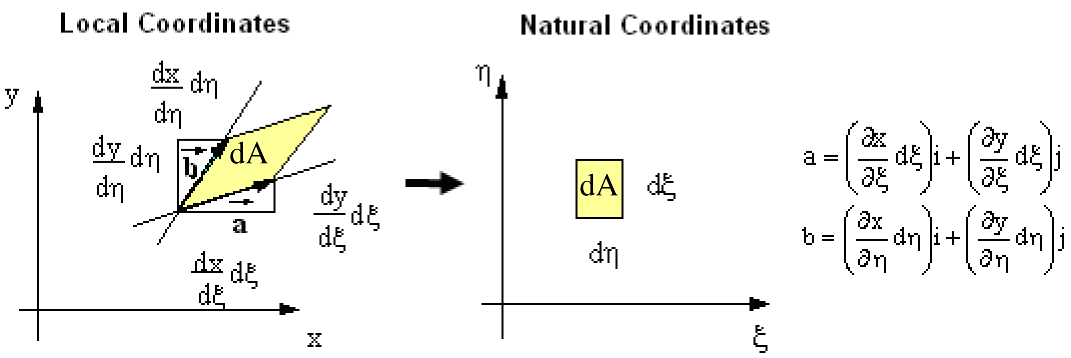

Figure 3.5: Element transformation between local and natural coordinates

An issue of Gauss integration scheme is to map the original local coordinate system (x,y,z) into natural coordinate system (ξ,η,ζ). These two systems relate to each other through Jacobian matrix J as shown in Table 3.13. Jacobin matrix also indicates how an element in the local coordinate system differs from a standard element in the natural coordinate system. The element transformation is illustrated in Figure 3.5. In Fig. 3.5, a infinitesimal area (d*A*) in the local coordinate system which can be defined as the internal product of the vectors a and b along two sides of d*A*.

The element transformation from local coordinates into natural coordinates can be expressed as:

$$\mathrm{d}A = \mathrm{a} \cdot \mathrm{b} = \det \mathrm{J}\, \mathrm{d}\xi\, \mathrm{d}\eta \tag{3.18}$$

where det J is the determinant of Jacobian matrix J which can be calculated as:

$$\det \mathrm{J} = \left(\frac{\partial x}{\partial \xi} \frac{\partial y}{\partial \eta} \right) - \left(\frac{\partial x}{\partial \eta} \frac{\partial y}{\partial \xi} \right) \tag{3.19}$$

For the problems of plane strain, plane stress and axisymmetry, the infinitesimal volume dV can be written in natural coordinates as:

$$\mathrm{d}V = t\ c\ \mathrm{d}A = t\ c\ \det \mathrm{J}\, \mathrm{d}\xi\, \mathrm{d}\eta \tag{3.20}$$

where:

$t = 1 \Rightarrow$ for plane strain problems.

$t = 2\pi r \Rightarrow$ for axisymmetric deformation problems.

t = thickness $\Rightarrow$ for plane stress problems

c = 1 for quadrangular elements and 0.5 for triangular elements

For general 3D problems, the infinitesimal volume dV can be written in natural coordinates as:

$$\mathrm{d}V = \det \mathrm{J}\, \mathrm{d}\xi\, \mathrm{d}\eta\, \mathrm{d}\zeta \tag{3.21}$$

3.2.5 Evaluate External Force Vector

Three potential sources of external forces acting along the surface of element are from: 1) surface force F_s^e (e.g., normal load or traction); 2) body force F_b^e (e.g., gravitational force); and 3) prescribed displacement F_δ^e . F_{ext}^e can be defined as the combination of these three forces:

$$F_{ext}^e = F_s^e + F_b^e + F_\delta^e \tag{3.22}$$

Surface load F_s^e is the first part on the right hand side of Eq. (3.6). By introducing the displacement-nodal displacement relationships in Eq.(3.9) , the surface load F_s^e can be obtained as:

$$F_s^e = \int_{S_{qe}} \delta\hat{u}^{\mathrm{T}} q^e \,\mathrm{d}S_{qe} = \int_{S_{qe}} \delta\hat{u}^{\mathrm{T}} N^{\mathrm{T}} q^e \,\mathrm{d}S_{qe} = \delta\hat{u}^{\mathrm{T}} \int_{S_{qe}} N^{\mathrm{T}} q^e \,\mathrm{d}S_{qe} \tag{3.23}$$

It can be proved that $\delta\hat{u}$ appears at both sides of Eq. (3.6). Therefore, effect of $\delta\hat{u}$ can be canceled out. Eq. (3.23) can be rewritten as

$$F_s^e = \int_{S_{qe}} N^{\mathrm{T}} q^e \,\mathrm{d}S_{qe} \tag{3.24}$$

Body load F_b^e is the second part on the right hand side of Eq. (3.6). The body load F_b^e can be expressed as:

$$F_b^e = \int_{V_e} \delta u^{\mathrm{T}} b^e \,\mathrm{d}V_e = \int_{V_e} \delta\hat{u}^{\mathrm{T}} N^{\mathrm{T}} b^e \,\mathrm{d}V_e = \delta\hat{u}^{\mathrm{T}} \int_{V_e} N^{\mathrm{T}} b^e \,\mathrm{d}V_e \tag{3.25}$$

and then

$$F_b^e = \int_{V_e} N^{\mathrm{T}} b^e \,\mathrm{d}V_e \tag{3.26}$$

Prescribed displacement δ can be viewed as the load F_δ^e which causes the displacement of δ. F_δ^e can be evaluated using the same concept of Eq. (3.17).

$$F_\delta^e = K^e \hat{\delta} \tag{3.27}$$

where, $\hat{\delta}$ is a nodal prescribed displacement vector.

3.2.6 Solution of Nonlinear Equation System

The equilibrium equation in Eq. (3.7) assembled from elemental internal and external force vectors is a nonlinear equation system. Because the nonlinear equation system can not be solved straightforwardly, an iteration scheme like Newton-Raphson method should be applied to satisfy the convergence of calculation in each external force increment ΔF_{ext} .The convergence criterion is defined by norm as:

$$\frac{\|\Psi\|}{\|F_{ext}\|} \leq toler \tag{3.28}$$

where

$$\Psi = F_{ext} - F_{int} \tag{3.29}$$

Ψ is the unbalanced force and *toler* is a tolerance that is inputted by user depended on the desired accuracy of results. If this criterion is not satisfied, the following correction procedure must be conducted.

$$\Delta\hat{u} = \Delta\hat{u}^0 + \sum_{k=1}^{iter} \delta\Delta\hat{u}^k \tag{3.30}$$

in which $\Delta\hat{u}$ is the incremental nodal displacement vector. $\delta\Delta\hat{u}^k$ is correction solution and can be computed by

$$\delta\Delta\hat{u}^k = \left[K^k\right]^{-1} \Psi^k \tag{3.31}$$

where K^k is the global stiffness matrix evaluated at beginning of iteration or every time of iteration depended on the iterative scheme. k is the number of iteration from 1 to an allowable iteration number *iter* inputted by user.

$$\Delta\hat{u}^0 = \left[K^{k=1}\right]^{-1} \Delta F_{ext} \tag{3.32}$$

$\Delta\hat{u}^0$ is the prediction solution that depends on the global stiffness matrix evaluated at the beginning of the increment, and

$$\Delta F_{ext} = \Delta\lambda_i \cdot F_{ext} \tag{3.33}$$

where ΔF_{ext} is the incremental external force vector. $\Delta\lambda_i$ is the incremental load factor which depends on the types of automatic load increment strategy (Nogueira 1998). A good strategy for load increment is to provide big increments when the structural response is linear and small when the structural response is strongly nonlinear. In the ANLOG, the following procedure is adopted (Criesfield 1991)

$$\Delta\lambda_i = \Delta\lambda_{i-1}\left(\frac{I_d}{I_{i-1}}\right)^{\alpha} \tag{3.34}$$

where $\Delta\lambda_{i-1}$ is the incremental load factor at the previous step; I_d is the number of iteration desired to reach convergence; I_{i-1} is the number of iteration achieved at the previous step; and α is an exponent usually with a value of 0.5 suggested by Crisfield (1991). The first incremental load factor is defined as

$$\Delta\lambda_0 = \frac{1}{ninc} \tag{3.35}$$

where, *ninc* is a variable defined by user, which indicates the desired number of load increment. The incremental load factor $\Delta\lambda$ controls the incremental procedure. The value of $\Delta\lambda$ varies from 0 to 1 through the loading path. At end of last ΔF_{ext}, the summation of total incremental load factors should equal to 1. Last, the automatic evaluation of incremental load factor must be limited between maximal and minima values, $\Delta\lambda_{max}$ and $\Delta\lambda_{min}$. This can prevent an infinite iterative loop occurring if the convergence criterion cannot be met.

The flow chart of finite element computation is illustrated in Figure 3.6. Numbers indicate the computational sequence. Steps (4)~(10) should be repeated until convergence criterion is satisfied. After convergence criterion is satisfied, load factor λ, displacement u, material strain ε, material stress σ, and material hardening parameters h are updated and next load increment starts until completion of external loading at λ reach 1.

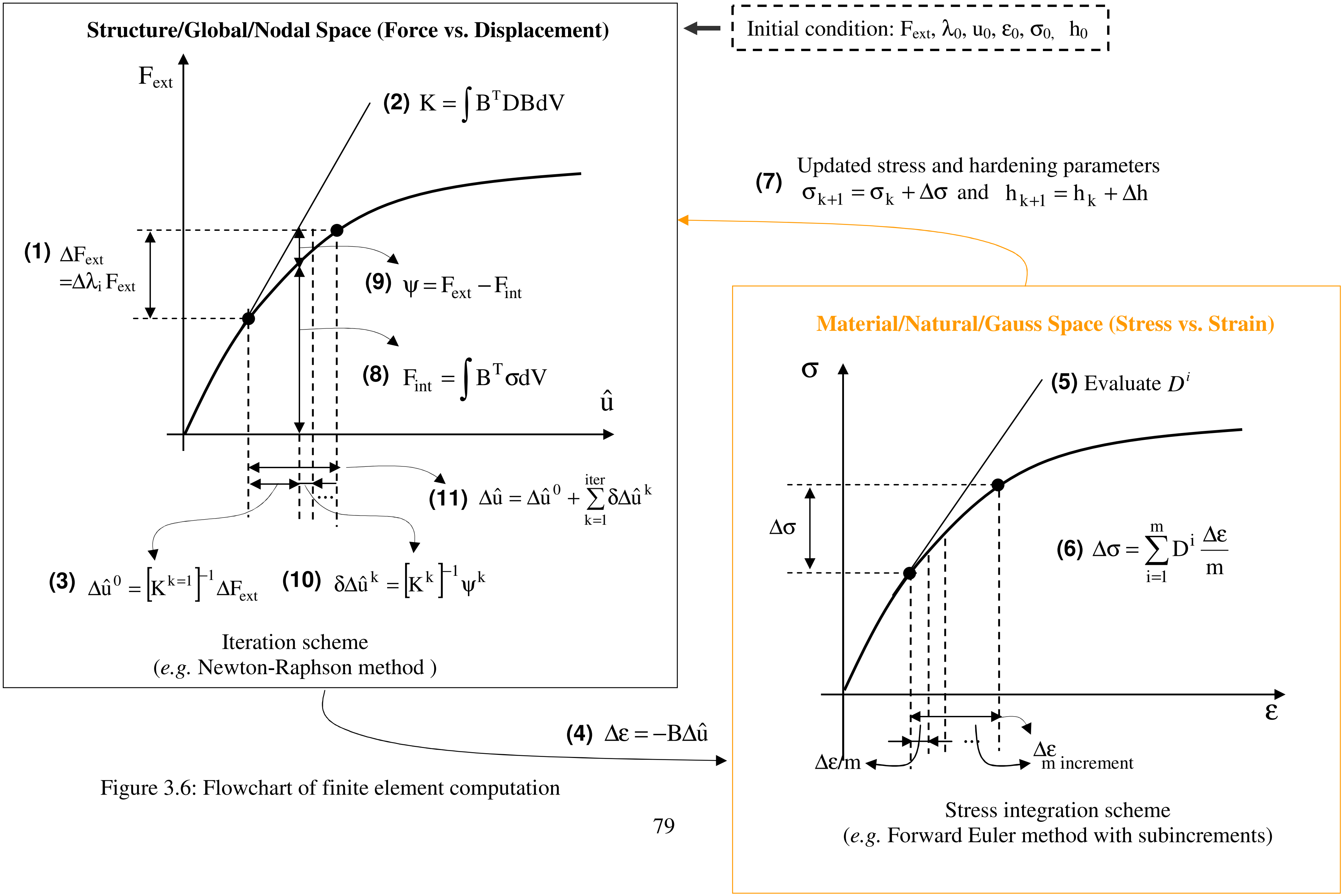

Figure 3.6: Flowchart of finite element computation

Chapter 4: Soil-Softening Model

In this chapter, an isotropic work soil-softening model is developed to better predict the post-peak behavior of frictional geomaterials. The calibration procedure and verification of the proposed soil-softening model are demonstrated. This model is used within the framework of the elastoplastic model of Lade and Kim (Kim and Lade 1988, Lade and Kim 1988a, 1988b and 1995, Lade and Jakobsen 2002). However, it will be shown in this chapter that the proposed soil-softening model gives better predictions of soil post-peak behavior than the soil-softening model proposed by Lade and Kim.

4.1 BACKGROUND

The terminology of soil "softening" is referred to, after soil reaches peak strength, the soil strength enters into the post-peak region in which soil strength would decrease with increasing deformation. This softening behavior can be often observed from conventional laboratory tests, specifically from triaxial tests (Lade and Prabucki 1995, Chu et al. 1996, Yoshida and Tatsuoka 1997, Suzuki and Yamada 2006, etc.). Figure 4.1a illustrates a typical stress-strain behavior of frictional soil under triaxial compression. Strength hardening is developed initially and then softening after the deviatoric stress reaches peak value. The softening will cease at a residual value. The stress state approaching residual strength is also called critical state by some researchers (Wroth 1958, Wood 1974, Atkinson 1981). The soil specimen will eventually "collapse" at large soil strains. In Fig. 4.1b, the rate of changing deviatoric stress with axial strain is close to zero at peak strength then gradually and smoothly decreases to a minimum negative value during softening and slowly increases back to zero again. Figure 4.1c shows the corresponding volumetric strain behavior.

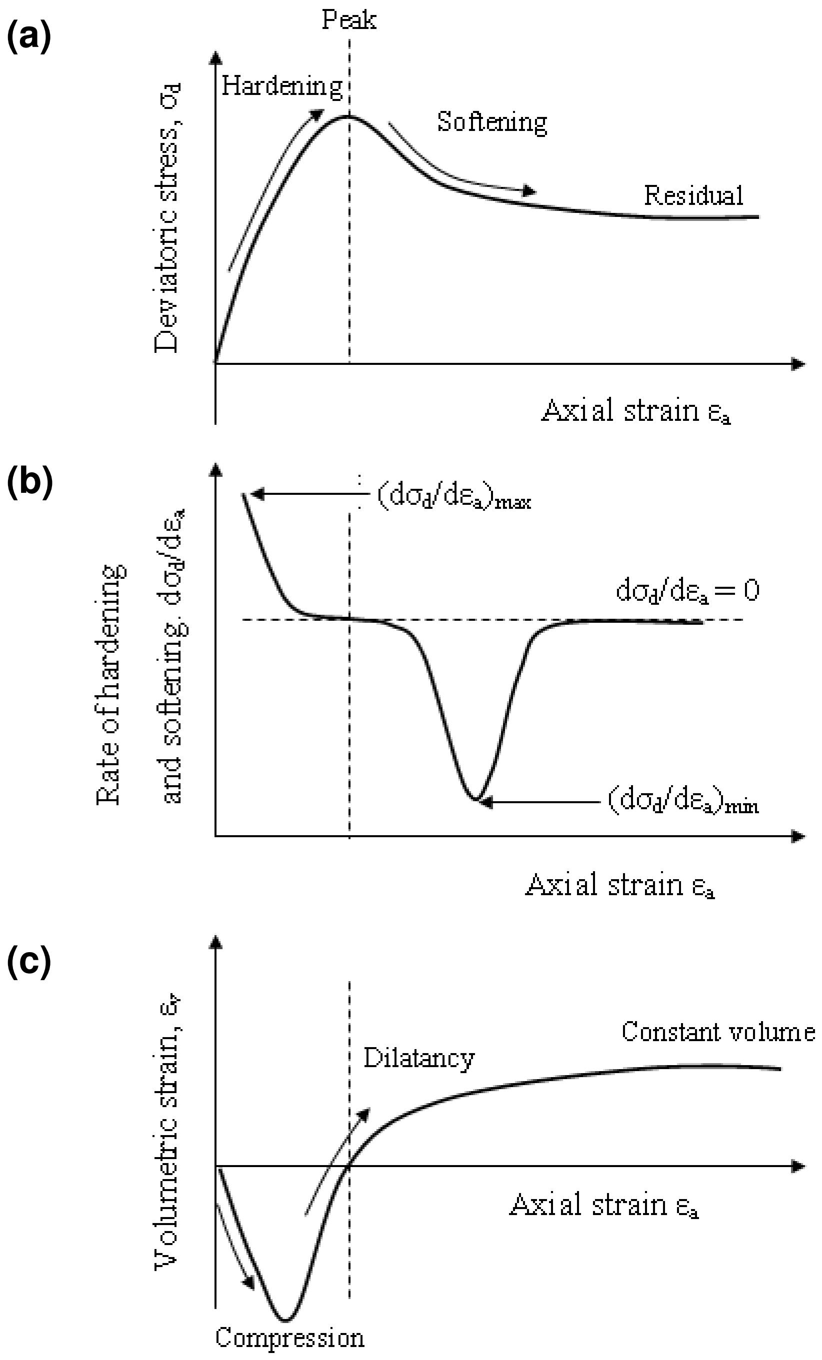

Figure 4.1: Typical stress-strain behavior of frictional soils: (a) deviatoric stress vs. axial strain; (b) rate of hardening and softening vs. axial strain; (c) volumetric strain vs. axial strain

The volumetric compression and dilatancy occurs during shearing and then the dilatancy will level out to a constant volumetric strain.

In addition, the literature listed above also reported the magnitude of strength softening is mainly governed by soil types, soil properties (i.e., relative density D_r or initial void ratio e_o) and stress state (i.e., confining pressure σ_3).

Beside the laboratory observations, the softening behavior is also often noticed in the field for earth structures under large loading and deformation conditions or in structures having an intensive soil-structures interaction; for example, landslide, foundation and platform, soil anchors, soil piles and geosynthetic-reinforced soil (GRS) structures (e.g., Murff 1980, Huang et al. 1994, Leschinsky 2001, Liu et al. 2004, Hsu 2005, Troncone 2005, etc.).

Because of various practical reasons, numerical methods have been frequently adopted to study the behavior of the structures in soil under various loading conditions. The merit of numerical analyses mainly include the relatively low-cost, less labor and capability of reduplication compared to physical tests; however, the interactive behavior between an earth structure and soil is difficult to analyze accurately by a simple numerical model. The soil constitutive model used to analyze the nonlinear behavior of frictional soils within earth structures is often considered as a nonlinearly elastic model: e.g., Duncan hyperbolic model (Duncan and Chang 1970), elastic-perfectly plastic model: e.g., Mohr-Coulomb model, and an elastoplastic model: e.g., Hardening Soil model (Schanz 1999, PLAXIS 2005) and Lade-Kim soil model (Kim and Lade 1988, Lade and Kim 1988a, 1988b and 1995, Lade and Jakobsen 2002, Jakobsen and Lade 2002, etc.) Although those models have their own specialties for analyzing specific problems; the natures of strength softening and volumetric dilatancy of frictional soil are usually not taken into account. This is a crucial problem for the evaluation of comparatively flexible structures such as geosynthetics-reinforced soil structures.

Among the aforementioned models, the Lade-Kim soil constitutive model (Kim and Lade 1988, Lade and Kim 1988a,1988b and 1995, Lade and Jakobsen 2002) equips both work hardening and softening model and allow volumetric dilatancy of frictional soil. It has been applied to model the behavior of soils or rocks in numerous studies (e.g., Lee et al. 2002, Borja 2004, Baxvanisetal et al. 2006). A brief review of Lade-Kim model is provided in Section 4.2. In Lade-Kim model, the soil hardening and softening behavior is modeled by an isotropic inflation and deflation of yield surface which is governed by hardening and softening laws. The hardening and softening laws are functions of plastic work W_p. The advantages of using plastic work characterizing yield behavior because it does not involve tests with complicated stress-paths and it also avoids difficulties in determination of yield points on stress-strain curves. In addition, computation of plastic work is straight forward and plastic work appears to capture yielding in terms of shear strains as well as volumetric strains. The evaluation of the yield criterion was performed in the hardening regime where the soil behavior has been studied experimentally and was reasonably well known. However, Lade and Kim just simply assumed the decrease of yield surface continuously as an exponential decay because the softening regime was much less known in the past.

This chapter presents a study to develop and demonstrate an isotropic work softening model. The motivation for the research is twofold. First, the new softening model should represent better the soil post-peak behavior observed in the literature (summarized in Fig. 4.1). Second, the model parameters in the new softening model should be able to reflect the soil properties and stress state. The development of the softening model is based on the Lade-Kim constitutive soil model but improves previous work by characterizing the size of a decaying yield surface more realistically by assuming an inverse sigmoid function. Compared to the original softening model, which used an exponential decay function, the benefits of using the inverse sigmoid function are highlighted as: 1) smooth the abruptly transition from hardening to softening occurring at the peak strength point; and 2) limit the decrease of yield surface until a residual yield surface is reached.

This chapter first reviews the Lade-Kim soil mode with a special focus on softening law in Section 4.2. The new softening model and governing equations are introduced in Section 4.3. The incremental forms of constitutive model and issues related to implementation are discussed in Section 4.4. The data from triaxial compression testing on two frictional geomaterials, Monterey No. 30 sand and Sacramento River sand, is used to demonstrate the proposed model in Sections 4.5 and 4.6, respectively. Section 4.5 focuses on the detail of calibration procedure and the comparison of calibration and prediction results between original and proposed softening models. Section 4.6 is designed to examine the applicability of proposed model for different soil types.

4.2 REVIEW OF LADE-KIM SOIL CONSTITUTIVE MODEL

Lade-Kim (or single hardening) soil constitutive model (Kim and Lade 1988, Lade and Kim 1988a, 1988b and 1995, Lade and Jakobsen 2002) is an elastoplastic model composed by following components: elastic model, failure criterion, plastic potential function for non-associated flow rule, yield criterion, isotropic hardening and softening laws. The formulation is developed based on experimental data sets of testing frictional materials under various loading conditions. The model incorporates thirteen parameters and all parameters can be determined using data from isotropic compression and triaxial compression tests.

The framework and the components of the latest version of Lade-Kim soil model (Lade and Jakobsen 2002) are reviewed below. A special focus will be placed on introducing the softening model in Lade-Kim soil model. Readers are also encouraged to refer to Lade and Jakobsen (2002) for other details. In order that the presentation follows a logic developmental sequence, the components are presented in the following sequence: elastic model, failure criterion plastic potential and flow rule, yield criterion and work hardening and softening laws.

4.2.1 Elastic Model

The elastic strain increments are calculated following Hook's law. The Young's modulus E nonlinearly varies with stress state. The expression of Young's modulus was derived from the principle of energy conservation. According to this derivation, Young's modulus can be expressed in following equation in term of a power law:

$$E = Mp_a\left[\left(\frac{I_1}{p_a}\right)^2 + 6\left(\frac{1+\nu}{1-2\nu}\right)\frac{J_2'}{p_a^2}\right]^\lambda \tag{4.1}$$

where I_1 is the first invariant of the stress tensor; J_2' is the second invariant of the deviatoric stress tensor, given as follows:

$$I_1 = \sigma_{11} + \sigma_{22} + \sigma_{33} \tag{4.2}$$

and

$$J_2' = \frac{1}{6}\left[(\sigma_{11}-\sigma_{22})^2 + (\sigma_{22}-\sigma_{33})^2 + (\sigma_{33}-\sigma_{11})^2\right] + \sigma_{12}^2 + \sigma_{23}^2 + \sigma_{31}^2 \tag{4.3}$$

where σ_{11}, σ_{22}, σ_{33} are normal stresses and σ_{12}, σ_{23}, σ_{31} are shear stresses on three mutually perpendicular planes. The parameter p_a is the atmospheric pressure in the same units as E and I_1; M, λ and Poisson's ratio ν are constant dimensionless material parameters, which can be obtained from simple tests like triaxial compression tests.

4.2.2 Failure Criterion

A three-dimensional failure criterion is expressed in terms of the first I_1 and third I_3 invariants of the stress tensor, as follow:

$$f_n = \left(\frac{I_1^3}{I_3} - 27 \right) \left(\frac{I_1}{p_a} \right)^m \tag{4.4}$$

$$f_n = \eta_1 \quad \text{at failure} \tag{4.5}$$

and

$$I_3 = \sigma_{11}\sigma_{22}\sigma_{33} + \sigma_{12}\sigma_{23}\sigma_{31} + \sigma_{21}\sigma_{32}\sigma_{13} - (\sigma_{11}\sigma_{23}^2 + \sigma_{22}\sigma_{31}^2 + \sigma_{33}\sigma_{12}^2) \tag{4.6}$$

$f_n = \eta_1$ means current stress state reaches material peak failure surface. Another parameter a' is required in order to include the effective cohesion and the tension which can be sustained by concrete and rock. A translation of the principal stress space along the hydrostatic axis is performed; thus, a constant stress $a'p_a$ is added to the normal stresses before substitution into Eq. (4.4). The value of $a'p_a$ reflects the effect of the tensile strength of the material. The parameters m, η_1 and a' are constant dimensionless numbers, which may be determined from results of triaxial compression tests.

4.2.3 Plastic Potential and Flow Rule

The plastic potential surface has a conical shape with a tip toward the stress origin and is written in terms of the three invariants of the stress tensor and presented in Eq. (4.7). Note that this function is different from the yield function and non-associated flow is consequently obtained.

$$g_p = \left(\Psi_1 \frac{I_1^3}{I_3} - \frac{I_1^2}{I_2} - \Psi_2 \right) \left(\frac{I_1}{p_a} \right)^{\mu} \tag{4.7}$$

where I_2 is the second invariant of the stress tensor, defined as:

$$I_2 = \sigma_{12}^2 + \sigma_{23}^2 + \sigma_{31}^2 - (\sigma_{11}\sigma_{22} + \sigma_{22}\sigma_{33} + \sigma_{33}\sigma_{11}) \tag{4.8}$$

The material parameters Ψ_2 and μ are dimensionless constants that may be determined from triaxial compression tests. The parameter Ψ_1 is related to the curvature parameter m of the failure criterion as follows:

$$\Psi_1 = 0.00155 m^{-1.27} \tag{4.9}$$

4.2.4 Yield Criterion

The yield surface areis associated with and derived from surfaces of constant plastic work, as explained by Lade and Kim (1988a). The isotropic yield function is expressed as follows:

$$f_p = f_p'(\sigma) - f_p''(W_p) = 0 \tag{4.10}$$

in which $f'_p(\sigma)$ defines the shape of the yield surface and is a function of the stress state. $f'_p(\sigma)$ is expressed in Eq. (11); $f''_p(W_p)$ is hardening or softening law which defines the increasing or decreasing size of yield surface. $f''_p(W_p)$ is a function of plastic work. The formula for hardening and softening laws are discussed later.

$$f'_p = \left(\Psi_1 \frac{I_1^3}{I_3} - \frac{I_1^2}{I_2} \right) \left(\frac{I_1}{p_a} \right)^h e^q \tag{4.11}$$

where h is constant and q varies from zero at the hydrostatic axis to unity at the peak failure surface $f_n = \eta_1$. The constant parameter h is determined on the basis that the plastic work is constant along a yield surface. The value of q varies with stress level S defined as the ratio of f_n to η_1.

$$S = \frac{f_n}{\eta_1} = \frac{1}{\eta_1} \left(\frac{I_1^3}{I_3} - 27 \right) \left(\frac{I_1}{p_a} \right)^m \tag{4.12}$$

The stress level S varies from zero at the hydrostatic axis to unity at the peak failure surface. S can also be viewed as an index of mobilized soil strength which is defined as the ratio of current mobilized soil strength to the peak soil strength. The variation of q with S is expressed as:

$$q = \frac{\alpha S}{1 - (1 - \alpha) S} \tag{4.13}$$

in which α is a constant. The material parameters α and h are dimensionless constants that may be determined from triaxial compression tests.

4.2.5 Work Hardening Model

For soil during hardening, the yield surface inflates isotropically with plastic work according to the following equation:

$$f_p'' = \left(\frac{W_p}{p_a D}\right)^{\frac{1}{\rho}} \tag{4.14}$$

where the values of ρ and *D* are constant for a given material. f_p'' varies with plastic work only. The values of ρ and *D* are given by:

$$D = \frac{C}{(27\Psi_1 + 3)^{\rho}} \tag{4.15}$$

and

$$\rho = \frac{p}{h} \tag{4.16}$$

The parameters *C* and *p* are used to model the plastic work during isotropic compression:

$$W_p = C p_a \left(\frac{I_1}{p_a}\right)^{p} \tag{4.17}$$

The material parameters *C* and *p* are dimensionless constants that may be determined from isotropic compression tests. As the plastic work increases, the isotropic yield surface inflates until the current stress point reaches the peak failure surface at *S*=1. The relationship between the increasing yield surface f_p'' and plastic work W_p (normalized by atmospheric pressure p_a) is described by a monotonically increasing function whose slope decreases with increasing plastic work, as shown in Fig. 4.2.

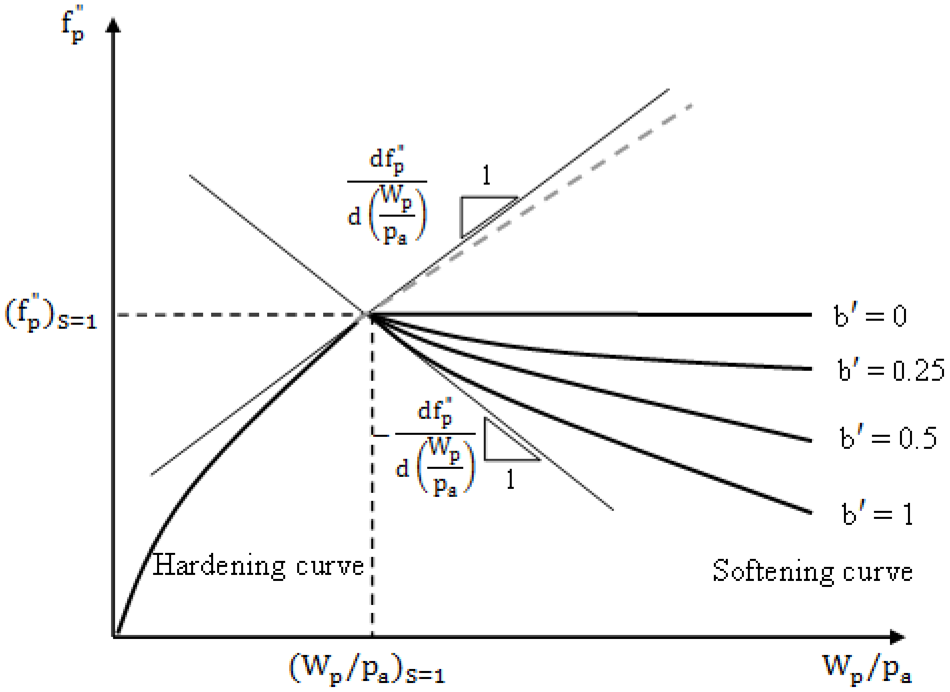

Figure 4.2**:** Modeling of work hardening and softening (Lade and Jakobsen, 2002)

4.2.6 Work Softening Model

The softening model is one of two components of isotropic yield function in Eq. (4.10). As discussed previously, the yield function describes the shape and size of the yield surface; the shape of the yield surface is governed by the yield criterion $f'_p(\sigma)$ in Eq. (4.11) and the increasing and decreasing size of yield surface is controlled by the hardening and softening law $f''_p(W_p)$. The hardening law has been introduced in the previous section and the softening law will be discussed herein.

After a stress state reaches the peak failure surface at *S*=1, the soil strength leaves pre-peak behavior (hardening region) to post-peak behavior (softening region). During soil-softening, the increase of plastic work will cause the deflation of the yield surface.

The yield surface is assumed deflating isotropically according to an exponential decay function in Lade-Kim soil model:

$$f_p'' = Ae^{\frac{-BW_p}{p_a}} \tag{4.18}$$

in which A and B are positive constants to be determined on the basis of the location and slope of the hardening curve at S=1.

$$A = \left[f_p'' e^{\frac{BW_p}{p_a}} \right]_{S=1} \tag{4.19}$$

and

$$B = \left[b' \frac{\mathrm{d} f_p''}{\mathrm{d}(W_p / p_a)} \frac{1}{f_p''} \right]_{S=1} \tag{4.20}$$

in which both the size of the yield surface f_p'' and the derivative $\mathrm{d} f_p'' / \mathrm{d}(W_p / p_a)$ are obtained from the hardening curve at S=1. The value of $\mathrm{d} f_p''$ is negative during softening. The only parameter in the softening model is b', which is suggested as a positive dimensionless constant ($b' \geq 0$). The parameter b' value equal to zero corresponds to a perfect plastic material. The magnitude of softening increases as b' value increases. The effect of b' on softening curve is illustrated in Fig. 4.2. Table 4.1 summarized all model components, parameters and governing equations in the Lade-Kim soil constitutive model.

Table 4.1: Summary of Lade-Kim soil model components

Model component	Parameters	Equations
Elastic model	M, λ, ν	Eq. (1)
Failure criterion	m, η_1, a'	Eqs. (4),(5)
Plastic potential	ψ_2, μ	Eqs. (7),(9)
Yield criterion	h, α	Eqs. (10)~(13)
Hardening law	C, p	Eqs. (14)~(17)
Softening law	b'	Eqs. (18)~(20)

4.3 PROPOSED SOIL-SOFTENING MODEL

4.3.1 Problem Definition

Based on the general observation of soil post-peak behavior stated in Section 4.1 and the experience of using and calibrating the original softening model in the Lade-Kim soil model, it was found two main problems in the softening model proposed by Lade and Kim.

First, the softening parameter b' in the Lade-Kim soil model is suggested as a constant value which can not reflect the actually soil-softening behavior on soil stress state (i.e., confining pressure σ_3). Since softening happens right after hardening at S=1, softening model has already included the effect of relative density by using both the size of the yield surface f_p'' and the derivative $\mathrm{d} f_p'' / \mathrm{d}(W_p / p_a)$ from the hardening curve at S=1, as shown in Eqs. (4.18), (4.19) and (4.20). However, the effect of confining pressures on softening is not involved in the original softening model.

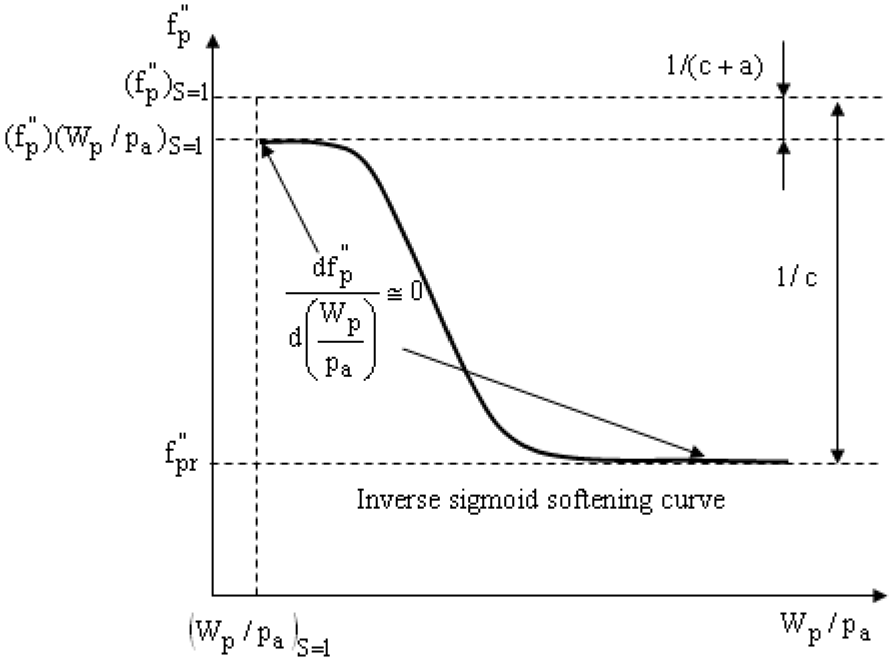

Figure 4.3: New softening model based on inverse sigmoid function

Second, the shape of the decaying yield surface should be more like an inverse sigmoid curve rather than an exponential decay curve. This observation will be demonstrated using the data from triaxial compression tests in later sections.

Figure 4.3 illustrates the inverse sigmoid function for the proposed softening model. The improvement of predicting softening behavior by using inverse sigmoid function is highlighted by the following two factors:

1. Provide a smoother transition from hardening to softening at the peak strength point. The abrupt transition observed in Fig. 4.2 indicates a suddenly rate changing from hardening to softening at the peak strength point; however, this doesn’t agree with the observation in Fig. 4.1b which shows the rate changing from hardening to softening is gradual and smooth.

2. Limit the deflation of the yield surface until a residual yield surface f''_{pr} is reached. In Eq. (4.18), the softening model in the Lade-Kim soil model allow the size of the yield surface to shrink to zero if plastic work is large enough. This implies the deviatoric stress will go back to zero or the stress state is going to the original stress state before loading starts. However, as shown in Fig. 4.1b, the stress state should stay at a residual strength when soil experiences large strains. This can be simulated by introducing a model parameter f''_{pr} in the proposed softening model.

Indeed, the numerical misdescription of soil physical behavior in softening would affect the accuracy in not only calibration results but also in predictions. Further, a numerical instability may occur when the decreasing yield surface without limits during softening. In addition, the calibration procedure of how to obtain parameter b' in the original softening model is not able to be found in any relevant literature. This is improved by providing the user a clear and simple calibration procedure for the proposed model.

4.3.2 Model Description

To solve all the problems discussed in Section 4.3.1, a new softening model based on inverse sigmoid function is proposed as follows and illustrated in Fig. 4.3. The proposed softening model is function of W_p. The governing equation is expressed as:

$$f''_p = (f''_p)_{S=1} - \frac{1}{c + a\exp\left\{-b\left[\frac{W_p}{p_a} - \left(\frac{W_p}{p_a}\right)_{S=1}\right]\right\}} \tag{4.21}$$

where $(f_p'')_{S=1}$ is the size of yield surface at peak condition and $(W_p / p_a)_{S=1}$ is the value of normalized plastic work at peak condition which can be evaluated from the hardening curve at S=1. c can be calculated as:

$$c = \frac{1}{(f_p'')_{S=1} - f_{pr}''} \tag{4.22}$$

where f_{pr}'' is the yield function at residual condition which can be obtained by substituting the stress components at the residual state into Eq. (4.11). However, a 95% of f_{pr}'' is recommended when calculating c. This attempt allows calculated f_{pr}'' slightly lower than observed f_{pr}'' so the data in the residual part can still be applicable for parameter calibration.

One can observe that the yield surface approaches to two horizontal asymptotes at two ends of x axis: when W_p / p_a equals to $(W_p / p_a)_{S=1}$, f_p'' equals or is close to $(f_p'')_{S=1}$; when W_p / p_a is large enough compare to $(W_p / p_a)_{S=1}$, f_p'' approaches residual yield surface f_{pr}''.

Parameters *a, b* and f_{pr}'' are three parameters for the proposed softening model. All parameters are positive and dimensionless real numbers: *a* controls the magnitude/size of yield surface at initiation of softening and the curvature of upper part of softening curve; *b* controls the curvature of lower part of softening curve; and f_{pr}'' controls the size of yield surface at residual strength. A sensitivity study (each parameter is varied $\pm 20\%$ from baseline case) is presented in Fig. 4.4 to indicate the effect of parameters *a, b* and f_{pr}'' values on softening curve. Parameters *a, b* and f_{pr}'' can be simply calibrated to a set of triaxial compression tests. All softening parameters can be regressed as a linear or power law function of confining pressure f(σ_3).

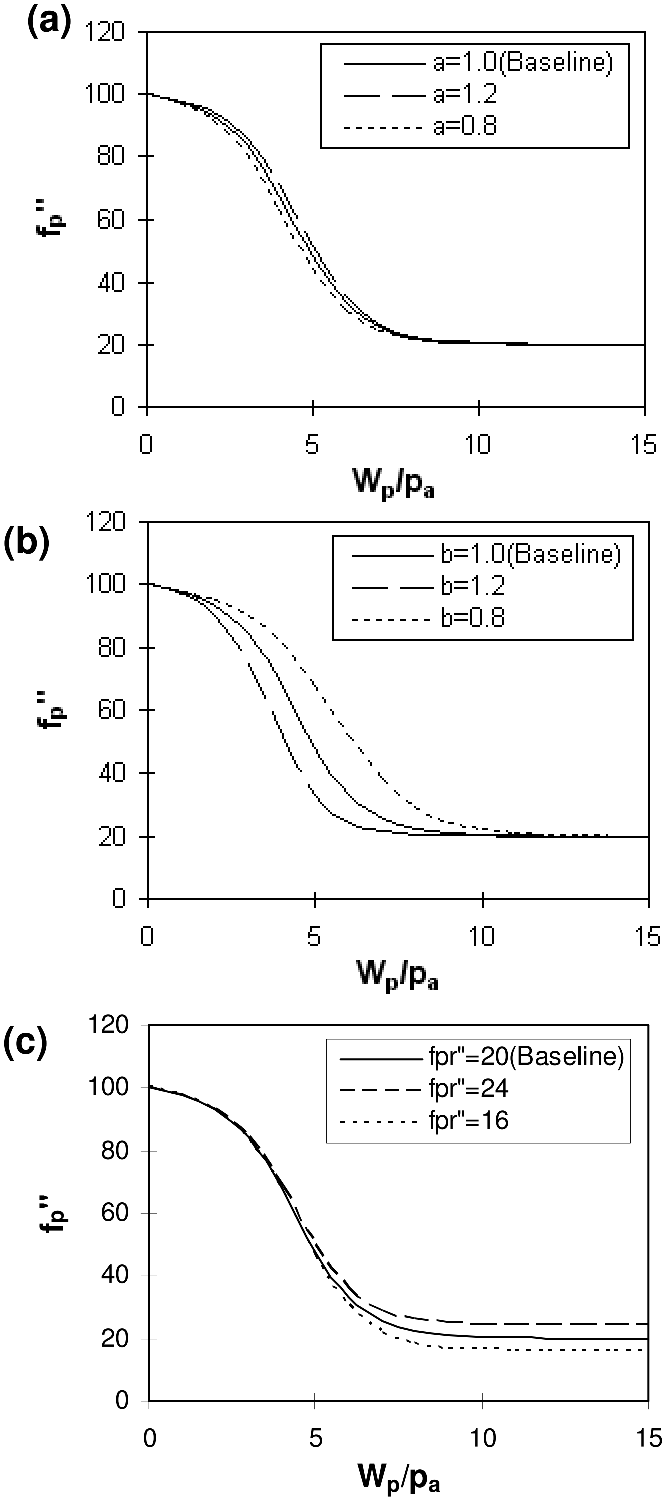

Figure 4.4: Sensitivity of model parameters: (a) a; (b) b; (c) f''_{pr}

4.4 IMPLEMENTATION

4.4.1 Constitutive Matrix

The implementation of soil constitutive model into ANLOG or other finite element programs, such as ABAQUS (ABAQUS 1995) and PLAXIS (2005), through a user-defined material module requires an incremental form in which the stress increments are expressed in terms of the total strain increments, as follows:

$$\mathrm{d}\underline{\sigma} = \underline{\underline{D_{ep}}}\,\mathrm{d}\underline{\varepsilon} \tag{4.23}$$

where D_{ep} is the material constitutive matrix also called elasto-plastic constitutive matrix. D_{ep} is commonly obtained through an incrementalization procedure expressed as follows:

$$\mathrm{d}\underline{\sigma} = (\underline{\underline{D_e}} - \underline{\underline{D_p}})\,\mathrm{d}\underline{\varepsilon} = \underbrace{\left[\underline{\underline{D_e}} - \frac{\underline{\underline{D_e^T}}\left(\frac{\partial g_p}{\partial \underline{\sigma}}\right)\left(\frac{\partial f_p}{\partial \underline{\sigma}}\right)^{\mathrm{T}}\underline{\underline{D_e}}}{\left(\frac{\partial f_p}{\partial \underline{\sigma}}\right)^{\mathrm{T}}\underline{\underline{D_e}}\left(\frac{\partial g_p}{\partial \underline{\sigma}}\right) + H}\right]}_{\underline{\underline{D_{ep}}}}\mathrm{d}\underline{\varepsilon} \tag{4.24}$$

where D_e is the elastic constitutive matrix, D_p is the plastic constitutive matrix, g_p is the plastic potential function in Eq. (4.7), f_p is the yield function in Eq. (4.11), H is the hardening and softening modulus. Each item in Eq. (4.24) is introduced as follows.

The plastic work increment $\mathrm{d}W_p$ can be obtained by:

$$\mathrm{d}W_p = \underline{\sigma}\,\mathrm{d}\underline{\varepsilon_p} \tag{4.25}$$

where:

$$\mathrm{d}\underline{\varepsilon}_p = \mathrm{d}\lambda_p \frac{\partial g_p}{\partial \underline{\sigma}} \tag{4.26}$$

and

$$\mathrm{d}\lambda_p = \frac{(\frac{\partial f_p}{\partial \underline{\sigma}})^{\mathrm{T}} \underline{\underline{D_e}}}{(\frac{\partial f_p}{\partial \underline{\sigma}})^{\mathrm{T}} \underline{\underline{D_e}} (\frac{\partial g_p}{\partial \underline{\sigma}}) + H} \mathrm{d}\underline{\varepsilon} \tag{4.27}$$

4.4.2 Elastic Constitutive Matrix

The elastic constitutive matrix D_e defined for a general state of stresses as

$$\underline{\underline{D_e}} = \frac{E}{(1+\nu)(1-2\nu)} \begin{bmatrix} 1-\nu & \nu & \nu & 0 & 0 & 0 \\ \nu & 1-\nu & \nu & 0 & 0 & 0 \\ \nu & \nu & 1-\nu & 0 & 0 & 0 \\ 0 & 0 & 0 & \frac{1-2\nu}{2} & 0 & 0 \\ 0 & 0 & 0 & 0 & \frac{1-2\nu}{2} & 0 \\ 0 & 0 & 0 & 0 & 0 & \frac{1-2\nu}{2} \end{bmatrix} \tag{4.28}$$

where E is the Young's modulus can be evaluated using Eq. (4.1) and ν is Poisson's ratio.

4.4.3 Derivatives of the Plastic Potential

The plastic potential function is expressed in terms of stress invariants. The derivatives of plastic potential function with regards to stresses may be obtained through the chain rule:

$$\frac{\partial g_p}{\partial \underline{\sigma}} = \frac{\partial g_p}{\partial I_1}\frac{\partial I_1}{\partial \underline{\sigma}} + \frac{\partial g_p}{\partial I_2}\frac{\partial I_2}{\partial \underline{\sigma}} + \frac{\partial g_p}{\partial I_3}\frac{\partial I_3}{\partial \underline{\sigma}} \tag{4.29}$$

where

$$\frac{\partial g_p}{\partial I_1} = \left(\psi_1(\mu+3)\frac{I_1^2}{I_3} - (\mu+2)\frac{I_1}{I_2} + \frac{\mu\psi_2}{I_1} \right)\left(\frac{I_1}{p_a}\right)^{\mu} \tag{4.30}$$

$$\frac{\partial g_p}{\partial I_2} = \frac{I_1^2}{I_2^2}\left(\frac{I_1}{p_a}\right)^{\mu} \tag{4.31}$$

$$\frac{\partial g_p}{\partial I_3} = -\psi_1\frac{I_1^3}{I_3^2}\left(\frac{I_1}{p_a}\right)^{\mu} \tag{4.32}$$

and the derivatives of the stress invariants with respect to general state of stresses are

$$\frac{\partial I_1}{\partial \underline{\sigma}} = \begin{bmatrix} 1 \\ 1 \\ 1 \\ 0 \\ 0 \\ 0 \end{bmatrix} \tag{4.33}$$

$$\frac{\partial I_2}{\partial \underline{\sigma}} = \begin{bmatrix} -(\sigma_{22}+\sigma_{33}) \\ -(\sigma_{33}+\sigma_{11}) \\ -(\sigma_{11}+\sigma_{22}) \\ 2\sigma_{23} \\ 2\sigma_{31} \\ 2\sigma_{12} \end{bmatrix} \tag{4.34}$$

$$\frac{\partial I_3}{\partial \underline{\sigma}} = \begin{bmatrix} \sigma_{22}\sigma_{33} - \sigma_{23}^2 \\ \sigma_{33}\sigma_{11} - \sigma_{31}^2 \\ \sigma_{11}\sigma_{22} - \sigma_{12}^2 \\ 2(\sigma_{12}\sigma_{13} - \sigma_{11}\sigma_{23}) \\ 2(\sigma_{23}\sigma_{12} - \sigma_{22}\sigma_{31}) \\ 2(\sigma_{12}\sigma_{13} - \sigma_{33}\sigma_{12}) \end{bmatrix} \tag{4.35}$$

4.4.4 Derivatives of the Yield Function

Using the chain rule, the derivatives of the yield function Eq. (4.10) can be written as:

$$\frac{\partial f_p}{\partial \underline{\sigma}} = \frac{\partial f_p^{'}}{\partial \underline{\sigma}} \tag{4.36}$$

then

$$\frac{\partial f_p^{'}}{\partial \underline{\sigma}} = \frac{\partial f_p^{'}}{\partial I_1}\frac{\partial I_1}{\partial \underline{\sigma}} + \frac{\partial f_p^{'}}{\partial I_2}\frac{\partial I_2}{\partial \underline{\sigma}} + \frac{\partial f_p^{'}}{\partial I_3}\frac{\partial I_3}{\partial \underline{\sigma}} \tag{4.37}$$

where

$$\frac{\partial f_p^{'}}{\partial I_1} = \left(\frac{3+h}{I_1} + \frac{\partial q}{\partial I_1}\right) f_p^{'} + \frac{I_1}{I_2}\left(\frac{I_1}{p_a}\right)^h e^q \tag{4.38}$$

$$\frac{\partial f_p^{'}}{\partial I_2} = \frac{I_1^2}{I_2^2}\left(\frac{I_1}{p_a}\right)^h e^q \tag{4.39}$$

$$\frac{\partial f_p^{'}}{\partial I_3} = f_p^{'}\frac{\partial q}{\partial I_3} - \psi_1 \frac{I_1^3}{I_3^2}\left(\frac{I_1}{p_a}\right)^h e^q \tag{4.40}$$

The exponent *q* varies with stress level *S* as defined by Eq. (4.13). Using the chain rule, the derivatives of *q* with respect to the stress invariants are

$$\frac{\partial q}{\partial I_1} = \frac{\partial q}{\partial S}\frac{\partial S}{\partial I_1} \tag{4.41}$$

then

$$\frac{\partial q}{\partial I_1} = \frac{\alpha}{\eta_1(1-(1-\alpha)S)^2}\left(\frac{mS\eta_1}{I_1} + \frac{3I_1^2}{I_3}\left(\frac{I_1}{p_a}\right)^m\right) \tag{4.42}$$

and

$$\frac{\partial q}{\partial I_3} = \frac{\partial q}{\partial S}\frac{\partial S}{\partial I_3} \tag{4.43}$$

then

$$\frac{\partial q}{\partial I_3} = \frac{\alpha}{\eta_1(1-(1-\alpha)S)^2} \frac{I_1^3}{I_3^2} \left(\frac{I_1}{p_a} \right)^m \tag{4.44}$$

4.4.5 Hardening and Softening Modulus

The hardening and softening modulus can be evaluated by

$$H = -\frac{\partial f_p}{\partial W_p} \underline{\sigma} \frac{\partial g_p}{\partial \underline{\sigma}} \tag{4.45}$$

where by using the yield criteria Eq. (4.10)

$$\frac{\partial f_p}{\partial W_p} = -\frac{\partial f_p^{"}}{\partial W_p} \tag{4.46}$$

when soil state is under hardening, and the hardening function, Eq. (4.14), is used

$$\frac{\partial f_p^{"}}{\partial W_p} = \frac{1}{\rho (D p_a)^{1/\rho}} W_p^{1/\rho - 1} \tag{4.47}$$

when soil state is under softening, and the original softening function, Eq. (4.18), is used

$$\frac{\partial f_p^{"}}{\partial W_p} = -\frac{AB}{p_a} e^{-B \frac{W_p}{p_a}} \tag{4.48}$$

when soil state is under softening and the proposed softening model, Eq. (4.21), is used

$$\frac{\partial f_p''}{\partial W_p}=\frac{-ab\exp\left\{-b\left[\frac{W_p}{p_a}-\left(\frac{W_p}{p_a}\right)_{S=1}\right]\right\}}{p_a\left[c+a\exp\left\{-b\left[\frac{W_p}{p_a}-\left(\frac{W_p}{p_a}\right)_{S=1}\right]\right\}\right]^2} \tag{4.49}$$

4.4.6 Other Implementation Issues

In order to distinguish the stress level during hardening or softening, it is necessary to define the stress level *S* during softening. The method of evaluating *S* during softening is recommended as:

$$S=1+(1-\frac{f_n}{\eta_1}) \tag{4.50}$$

S ranges from zero to unity (including unity) during hardening and ranges from unity (excluding unity) to two during softening.

Last, a discontinuity could happen between hardening and softening yield surface at *S*=1. At beginning of softening, the size of yield surface $(f_p'')_{(W_p/p_a)S=1}$ calculated using Eq.(4.21) would differ from peak yield surface $(f_p'')_{S=1}$ calculated from hardening curve. The difference equals 1/(*c*+*a*) is indicated in Fig.4.3. Preliminary study shows that the effect of *c* is usually negligible compared to parameter *a* and the discontinuity between $(f_p'')_{S=1}$ and $(f_p'')_{(W_p/p_a)S=1}$ becomes 1/*a*. Therefore, the discontinuity could be eliminated by just selecting a smaller value of 1/*a* or larger value of *a*, i.e., 1/*a* is recommend less than 1% of $(f_p'')_{S=1}$. In addition, to avoid any computational problem of applying hardening or softening law at *S*=1, the user should clearly define that hardening law governs the yield surface at *S*≤1 and softening law governs the yield surface since *S*>1.

4.5 MODEL DEMONSTRATION: MONTEREY NO. 30 SAND

4.5.1 Properties of Monterey No. 30 Sand

Data of triaxial compression testing on Monterey No. 30 sand (Li 2005) was selected to demonstrate the detail of calibration procedure and show the comparison of calibration and prediction results between original and proposed softening models. The reason of selecting Monterey No. 30 sand is because this sand is used as the backfill in the centrifuge test on GRS slope conducted by Arriaga (2003). The centrifuge tests are used to validate the proposed finite element model discussed later in this dissertation.

Monterey No. 30 sand is clean uniformly graded sand classified as SP in the unified system. The properties of Monterey No. 30 sand are listed in Table 4.2.

Table 4.2: Soil properties of Monterey No. 30 sand

Soil Type	**Monterey No. 30 sand**
D_{50} (mm)	0.4
Uniformity coefficient, C_u	3
Coefficinet of gradation, C_z	1.1
Specific gravity, G_s	2.65
Soil classification	SP
Max. dry unit weight, $\gamma_{d,\,max}$ (kN/m^3)	16.7
Min. dry unit weight, $\gamma_{d,\,min}$ (kN/m^3)	14.76
Maximum void ratio, e_{max}	0.76
Minimum void ratio, e_{min}	0.56

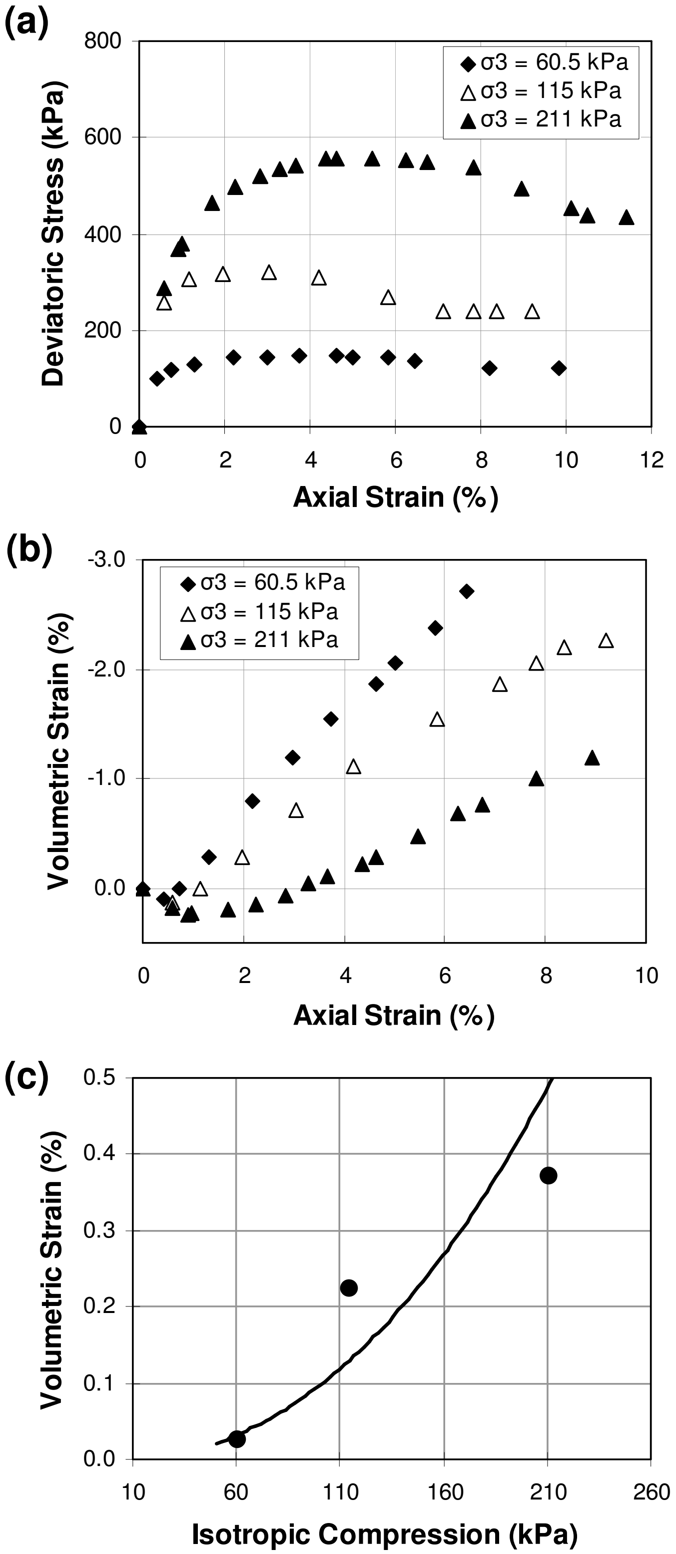

Figure 4.5: Results of triaxial compression test on Monterey No.30 sand: (a) deviatoric stress and axial strain; (b) volumetric and axial strain; and (c) compression and volumetric strain

The specimen with relative density of 65% was tested under three confining pressures. Figure 4.5a shows the relationship between deviatoric stress and strain. A clear strength softening behavior in stress-train curve can be observed at larger confining pressure. Figure 4.5b shows the relationship between volumetric and axial strain. Figure 4.5c shows the relationship between isotropic compression and volumetric strain. Note the data in Fig. 4.5c is only for calibrating the hardening parameters, *C* and *p* in Eq. (4.17), and not necessary for obtaining the proposed softening parameters.

4.5.2 Calibration Procedure

The step of calibration procedure is listed as follows:

1. Calibrate all model parameters except for the softening parameters. Select the data points until the peak strength point and follow the calibration procedure addressed by Lade and Kim (Kim and Lade 1988, Lade and Kim 1988a,1988b) Obtain representative values for model parameters and also calculate $(f_p'')_{S=1}$ and $(W_p)_{S=1}$ at S=1 from hardening curve.
2. Calibrate softening parameters. Select the data points from the peak strength point to the last data point for each triaxial test. Calculate f_p'' using equation Eq. (4.11) and obtain softening parameter f_p'' from the calculated f_p'' at the last data point or the point of minimum deviatoric stress.
3. Calculate W_p using following equation:

$$W_p = (W_p)_{S=1} + dW_p \tag{4.51}$$

where

$$\mathrm{d}W_p \approx \sum_{i=1}^{i=j} \frac{\underline{\sigma}_i + \underline{\sigma}_{i+1}}{2} \cdot \mathrm{d}\underline{\varepsilon}^{p}_{i} \tag{4.52}$$

and σ and $d\varepsilon_p$ are the stress and incremental plastic strain tensors in three principle directions, *i* is the number of data points. $d\varepsilon_p$ can be calculated by subtracting elastic strain increment $d\varepsilon_e$ from total strain increment $d\varepsilon$, as follows:

$$d\underline{\varepsilon_p} = d\underline{\varepsilon} - d\underline{\varepsilon_e} \tag{4.53}$$

where

$$d\underline{\varepsilon_e} = \frac{1}{E}\begin{bmatrix} 1 & -\nu & -\nu \\ -\nu & 1 & -\nu \\ -\nu & -\nu & 1 \end{bmatrix} d\underline{\sigma} \tag{4.54}$$

where Young's modulus *E* can be obtained from Eq. (4.1)

4. Calculate *c* using Eq. (4.22). A 95% of f''_{pr} is recommended when calculating *c*.
5. Plot the data points in X' and Y' coordinates

$$X' = W_p / p_a - (W_p / p_a)_{S=1} \tag{4.55}$$

and

$$Y' = \frac{1}{(f''_p)_{S=1} - f''_p} - c \tag{4.56}$$

The softening function in Eq. (4.21) now is translated into new coordinates as follows:

$$Y' = ae^{-bX'} \tag{4.57}$$

The softening parameters *a* and *b* can be obtained by best fitting the plotted data points X' and Y' using an exponential function. Figures 4.6 shows the best fitting curve and the obtained model parameters *a* and *b* values from three confining pressures. Table 4.3 summarizes the calibrated parameter values.

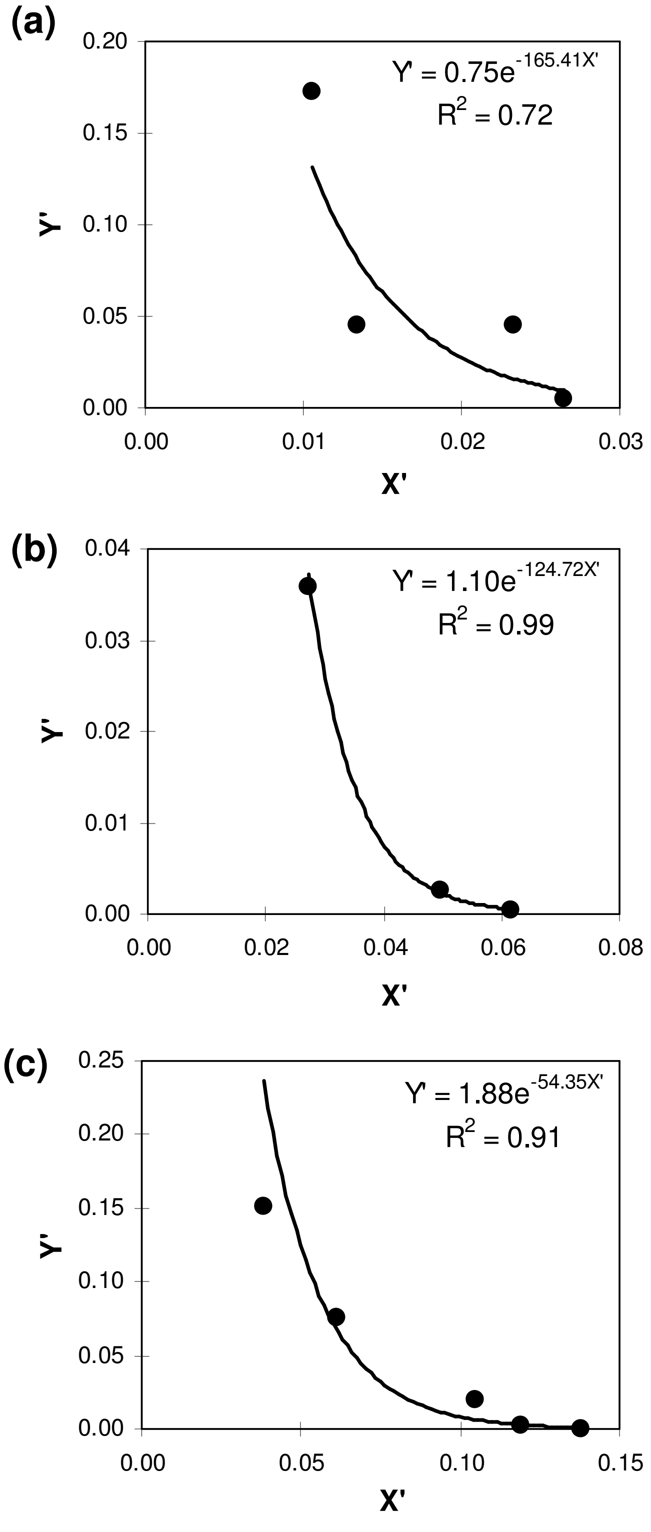

Figure 4.6: Best fitting curve for obtaining model parameters *a* and *b*: (a) σ_3= 60.5 kPa; (b) σ_3= 115 kPa; and (c) σ_3= 211 kPa for Monterey No.30 sand

Table 4.3: Material parameters for Monterey No. 30 sand

Model component	**Parameter**	**Monterey No. 30 sand**
Elastic model	M, λ, ν	705, 0.257, 0.35
Failure criterion	m, η_1, a'	0.0214, 24, 0
Plastic potential	ψ_2, μ	-8.51, 2.2
Yield criterion	h, α	0.67, 0.2
Hardening law	C, p	5.07E-05, 1.9
Softening law	Confining Pressures (kPa)	60.5, 115, 211
	a	0.75, 1.10, 1.88
	b	165.4, 124.7, 54.3
	f''_{pr}	41.19, 52.48, 85.68

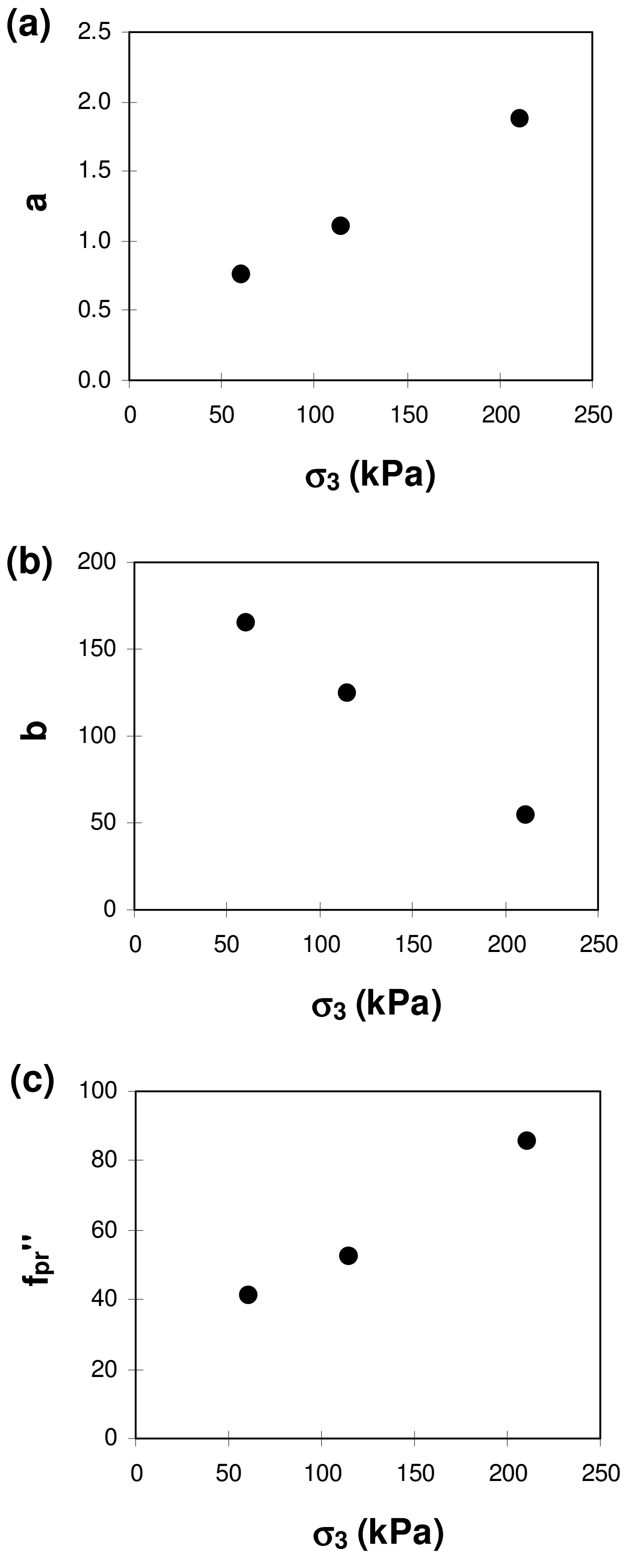

Figure 4.7: Correlation of softening model parameters with confining pressures: softening parameter (a) a; (b) b; (c) f''_{pr}

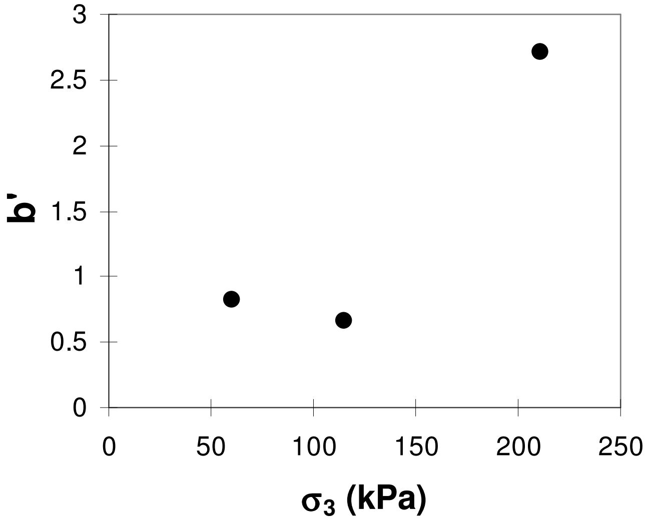

Figure 4.8: Correlation of original softening model parameter b' with confining pressures

Figures 4.7 show the correlations of calibrated softening parameters with confining pressures. Figures 4.7 demonstrate the softening model parameters are highly correlated to confining pressure. When confining pressure increases, the values of parameters a and f''_{pr} increase and the value of parameter b decreases. The values of original softening parameter $b^{'}$ are presented in Fig. 4.8. The value of b' is determined by varying b' until maximum correlation (i.e., maximum R^2) between the experimental data and calculated calibration curves was found. It can be observed in Fig. 4.8 that the original softening parameter $b^{'}$ seems not correlated well with confining pressure.

Figures 4.9 show the final calibration results in the f''_p and W_p / p_a coordinates. The calibration curves using original softening model are also included for comparison. It should be noted that different b's were used in three calibration curves although a constant value for softening parameter b' was suggested by Lade and Kim. As shown in Figs. 4.9, original approach using exponential decaying function could not capture the trend of experiment data well. A suddenly rate changing from hardening to softening at peak strength point can be observed from the curves of original softening model. In addition, due to without a control of residual strength, the original approach either overestimated the size of residual yield surface (the last data point) in Fig. 4.9a or underestimated that in Fig. 4.9b. It is fair to conclude that the new softening model based on inverse sigmoid function can depict the trend of experimental data better than original approach by exponential decaying function. Further, Figures 4.9 also indicate the discontinuity between $(f_p'')_{S=1}$ and $(f_p'')_{(W_p/p_a)S=1}$ discussed in Section 4.4.6 is insignificant and barely distinguished.

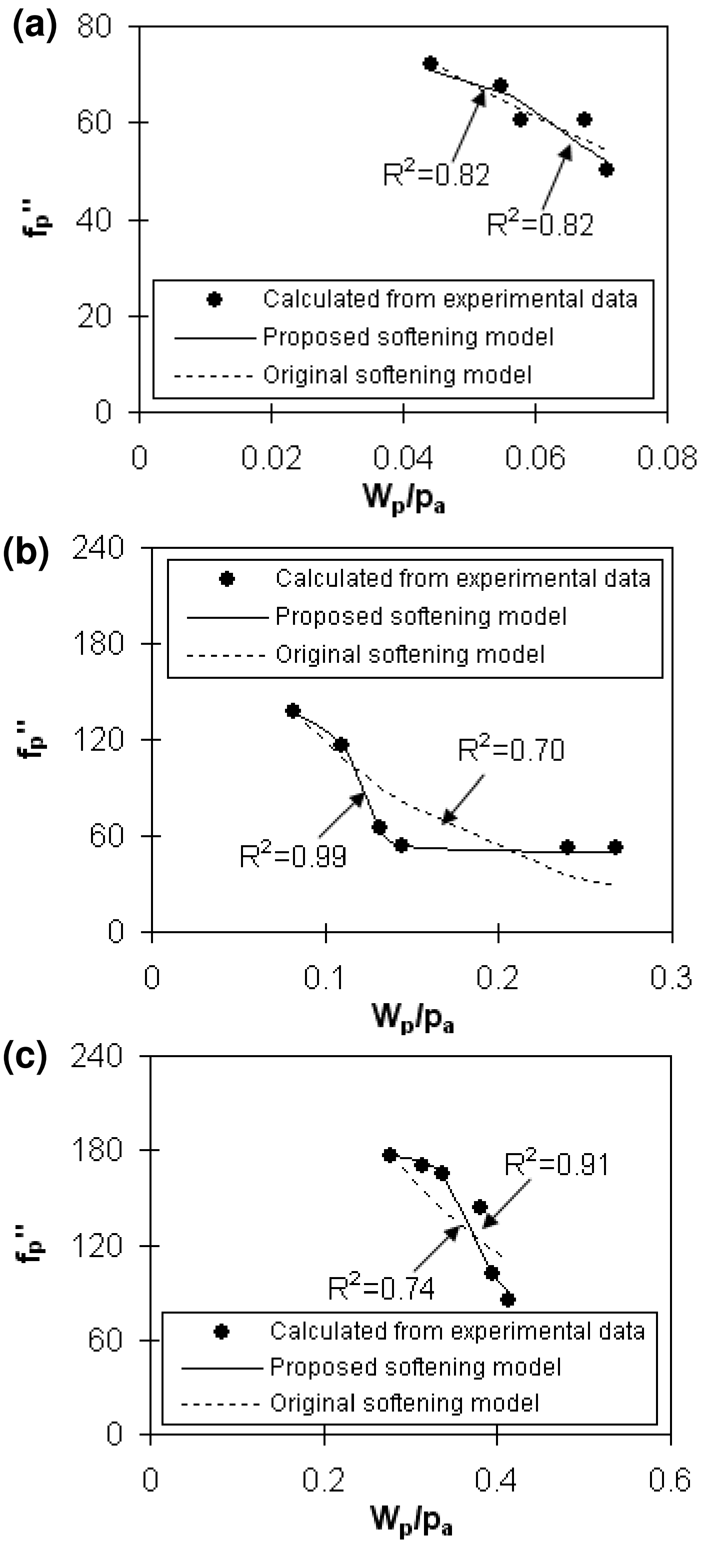

Figure 4.9: Comparison of calibration results with different confining pressures: (a) σ_3= 60.5 kPa; (b) σ_3= 115 kPa; and (c) σ_3= 211 kPa

4.5.3 Prediction Results

After calibrating softening parameters, the prediction of stress-strain relationships of Monterey No. 30 sand was conducted. The proposed softening model was implemented into ANLOG. For modeling triaxial tests, the soil specimen was simulated using an 8-node quadratic quadrilateral element under axisymmetric conditions. Boundary conditions of preventing lateral and vertical displacements were imposed to the right and bottom of element respectively. A total of four gauss points were assigned for the quadrilateral element. An initial stress corresponding to the confining pressure in each triaxial test was applied. Afterward, a series of prescribed displacements was added on the top of element. The prescribed displacements were set large enough for soil to reach residual strength at large soil strains.

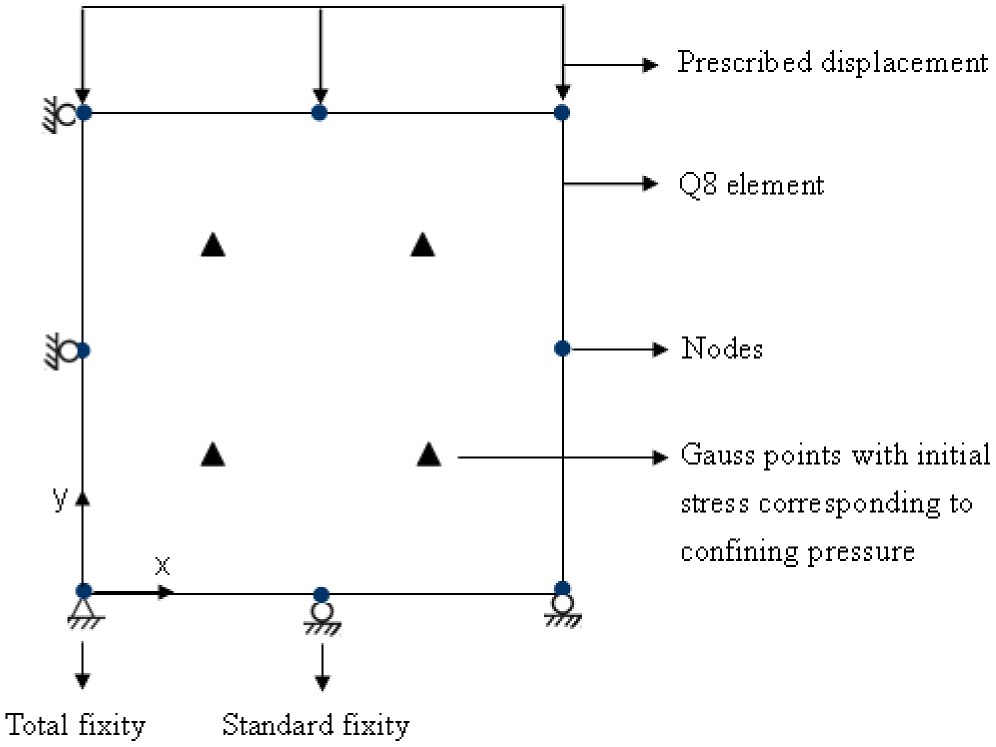

Figure 4.10: Finite element model of triaxial test

The modified forward Euler scheme with error control (Jakobsen and Lade 2002) was adopted to integrate stresses at each strain subincrement. In modified forward Euler scheme, the size of each strain subincrement is determined so that the new stress state fulfils the specified tolerance and only the absolutely necessary number of strain subdivision are applied. A detailed description of modified forward Euler scheme will be presented in Chapter 5. For the simulations in this study, the tolerance of modified forward Euler scheme and global convergence criteria were set very strictly ($=10^{-5}$) to minimize errors from numerical computation rather than soil model itself.

The prediction results are shown in Figs. 4.11. Due to the over and under estimation of yield surface sizes during calibration, the original softening model also shows an over and under estimation of prediction in Fig. 4.11a. In other words, the new softening model produces more accurate prediction for stress-strain curve specifically at residual region. Further, the observation from Figure 4.11a confirms the proposed softening model predict the stress-strain relationships better and capture well different magnitudes of strength softening under different confining pressures.

The prediction results of volumetric and axial strain relationships are shown in Fig. 4.11b. Because volumetric strain is mainly computed using plastic potential function in Eq. (4.7), the difference between using proposed and original softening model to predict volumetric strain is slight. The discrepancy between measured and predicted results is observed in Fig. 4.11b. This is likely because Lade-Kim model using the calibrated material variables from hardening region mis-predicts the compressive volumetric strain at initial stage of loading. In addition, instead of the constant Poisson’s ratio as used in this study, the prediction of volumetric strain may be improved by using a tangent Poisson’s ratio which would vary with confining pressure and deviatoric stress.

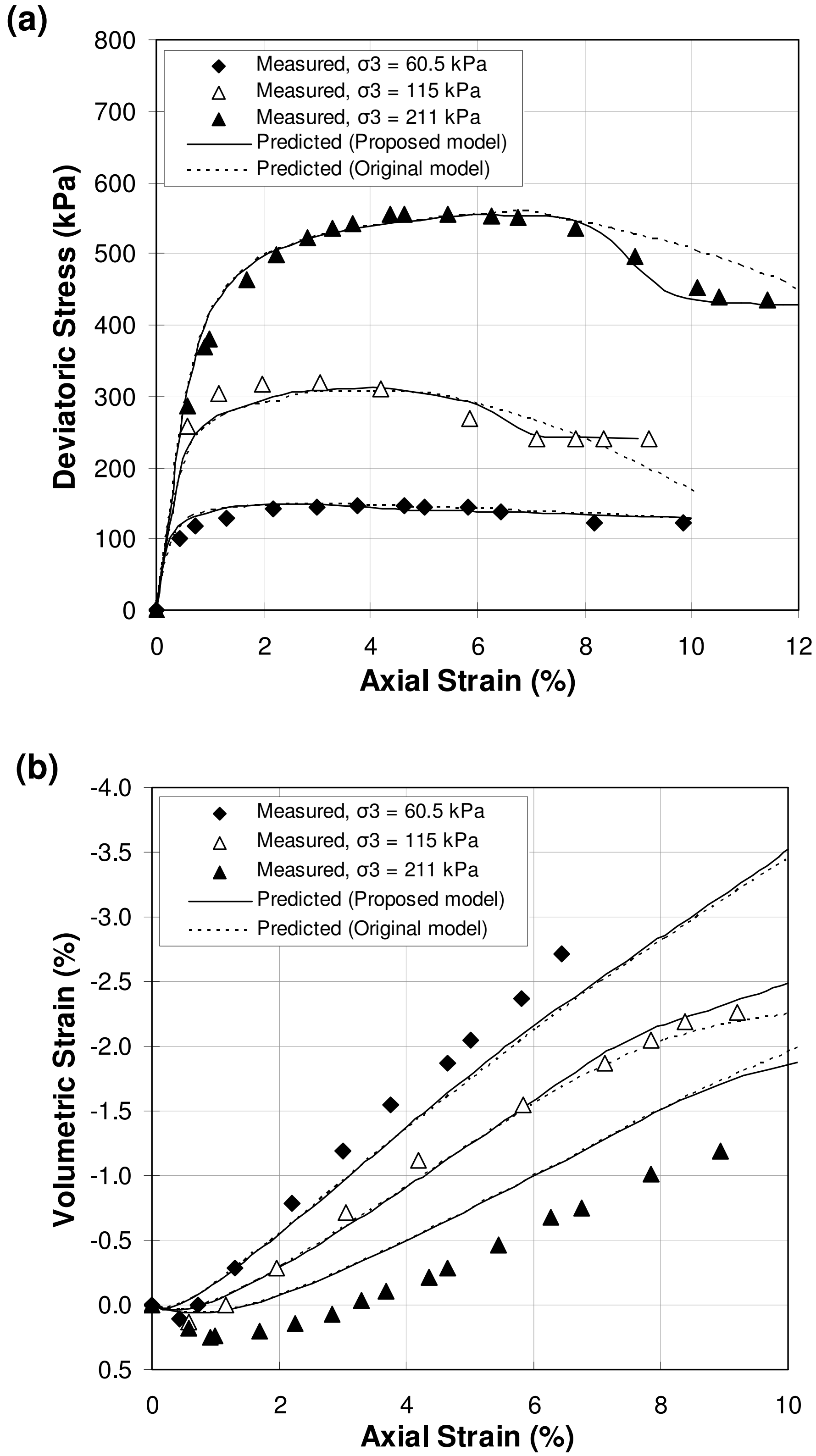

Figure 4.11: Comparison of prediction results by original and proposed softening model: (a) deviatoric stress and axial strain; (b) volumetric and axial strain

4.6 MODEL DEMONSTRATION: SACRAMENTO RIVER SAND

4.6.1 Properties of Sacramento River Sand

Another set of data from triaxial compression testing on Sacrament River sand (Lee and Bolton 1967, Lade and Duncan 1975, Lade 1977) was adapted. The main purpose of this exercise is to examine the applicability of proposed model for different soil types. Sacrament River sand is clean uniformly graded sand classified as SP in the unified system. The properties of Sacrament River sand is summarized in Table 4.4. The specimen with relative density of 100% was tested under various confining pressures. The relationship between stress and strain is shown in Figs. 4.12. A clear softening behavior in stress-train curve can be observed in this case. The values of model parameters (except for softening parameters) for dense Sacrament River sand were reported by Lade and Kim (1995); therefore, the relationship between isotropic compression and volumetric strain is not necessary.

Table 4.4: Soil properties of Sacramento River sand

Soil Type	**Sacramento River sand**
D_{50} (mm)	0.2
Uniformity coefficient, C_u	1.67
Coefficinet of gradation, C_z	0.86
Specific gravity, G_s	2.68
Soil classification	SP
Max. dry unit weight, $\gamma_{d,\,max}$ (kN/m^3)	16.33
Min. dry unit weight, $\gamma_{d,\,min}$ (kN/m^3)	12.95
Maximum void ratio, e_{max}	1.03
Minimum void ratio, e_{min}	0.61

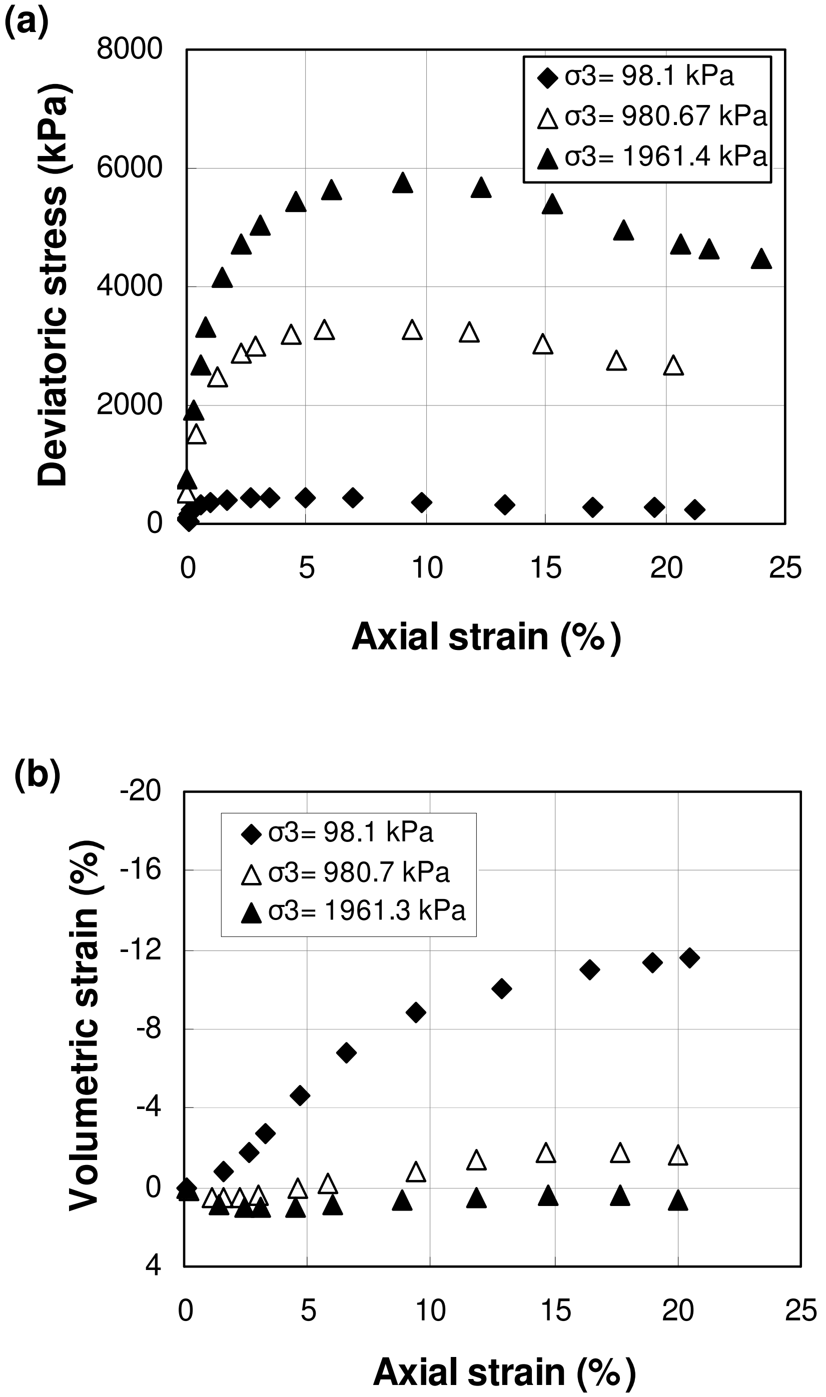

Figure 4.12: Triaxial compression test results: (a) deviatoric stress and axial strain; (b) volumetric and axial strain

4.6.2 Calibration and Prediction

The softening parameters were calibrated following the calibration procedure as discussed in Section 4.5.2. Figures 4.13 shows the best fitting curve and the obtained model parameters *a* and *b* from three confining pressures. The calibrated parameter values are summarized in Table 4.5.

Figures 4.14 illustrate the correlation of calibrated softening parameters with confining pressures. It is demonstrated in Fig. 4.14 that the softening model parameters are correlated to confining pressure well. When confining pressure increases, the values of parameter f''_{pr} increase and the values of parameters *a* and *b* decreases.

Note that the increasing or decreasing trend of parameter *a* and *b* values with confining pressure are primarily depended on softening nature which would vary soil by soil; for example, the trend of parameter *a* value changing with confining pressure in Sacramento River sand (Fig. 4.14a) is opposite to the trend in Monterey No. 30 sand (Fig. 4.7a). However, the value of parameter f''_{pr} should always increase with the increasing confining pressure regardless soil type (Figs. 4.7c and 4.14c).

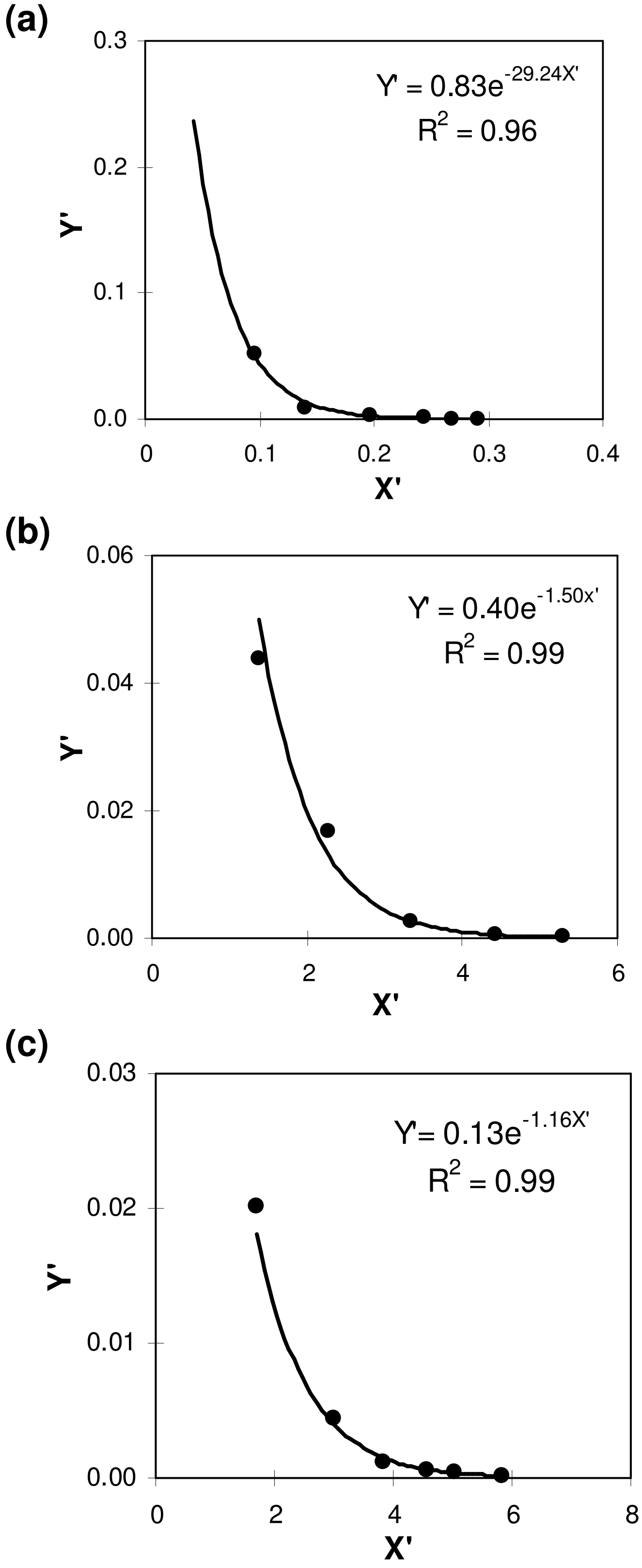

Figure 4.13: Best fitting curve for obtaining model parameters *a* and *b*: (a) 98.1 kPa; (b) 980.67 kPa; and (c) 1961.4 kPa

Table 4.5: Material parameters for Sacramento River sand

Model component	**Parameter**	**Sacramento River sand**
Elastic model	M, λ, ν	900, 0.28, 0.2
Failure criterion	m, η_1, a'	0.23, 80, 0
Plastic potential	ψ_2, μ	-3.09, 2.0
Yield criterion	h, α	0.765, 0.229
Hardening law	C, p	3.96E-05, 1.82
Softening law	Confining Pressures (kPa)	98.1, 980.67, 1961.4
	a	0.83, 0.39, 0.13
	b	29.24, 1.49, 1.16
	f''_{pr}	17.96, 138.21, 191.86

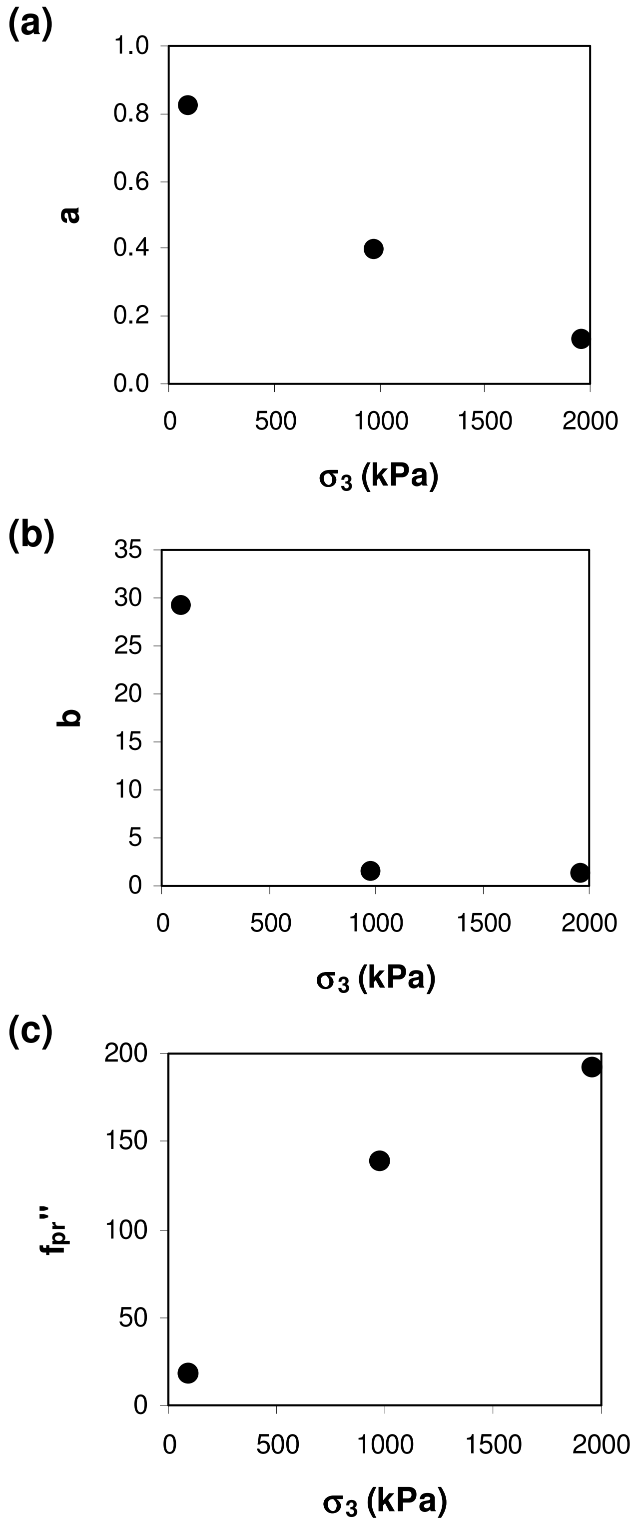

Figure 4.14: Correlation of softening model parameters with confining pressures: softening parameter (a) a; (b) b; (c) f''_{pr}

Figures 4.15 show the final calibration results. The trend of experiment data in the f''_p and W_p / p_a coordinates is more like a inverse sigmoid curve rather than decaying exponential curve; as a result, the new softening model based on inverse sigmoid function depicts the trend of experimental data favorably well. Also in Figures 4.15, the discontinuity between $(f''_p)_{S=1}$ and $(f''_p)_{(W_p / p_a)S=1}$ discussed in Section 4.4.6 is insignificant in this case.

Figures 4.16 indicate the results of stress-strain and volumetric strain-axial strain relationships from measurement and prediction. The finite element model for simulating triaxial compression test and the integration algorithm has been discussed previously. The proposed softening model shows a well capability to predict the stress-strain relationships and captures different magnitudes of strength softening under various confining pressures. Although the discrepancy exists between measured and predicted results of volumetric and axial strain relationships, this may be because the calibrated material variables in hardening region could not provide a close prediction on the volumetric strain. In summary, this section demonstrates the proposed softening model can be successfully applied for different types of soil.

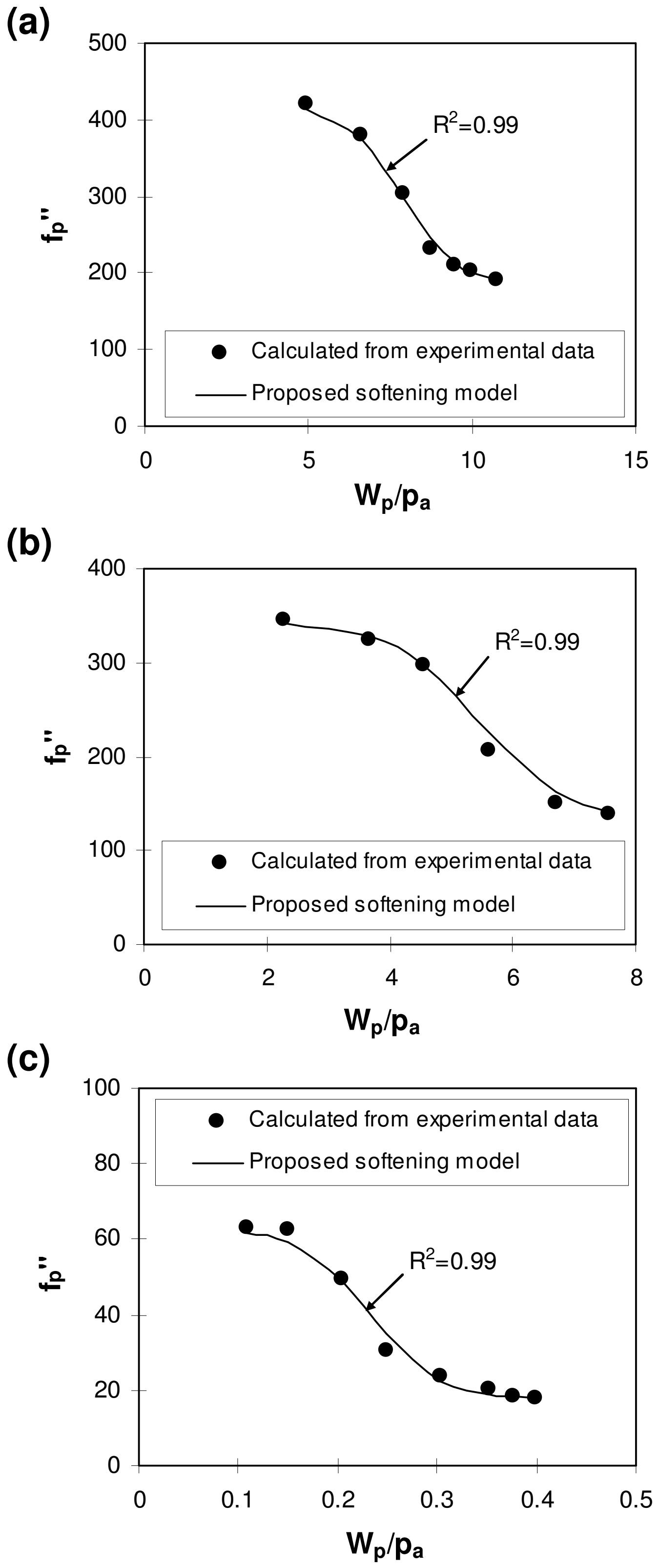

Figure 4.15: Comparison of calibration results with different confining pressures: (a) 98.1 kPa; (b) 980.67 kPa; and (c) 1961.4 kPa

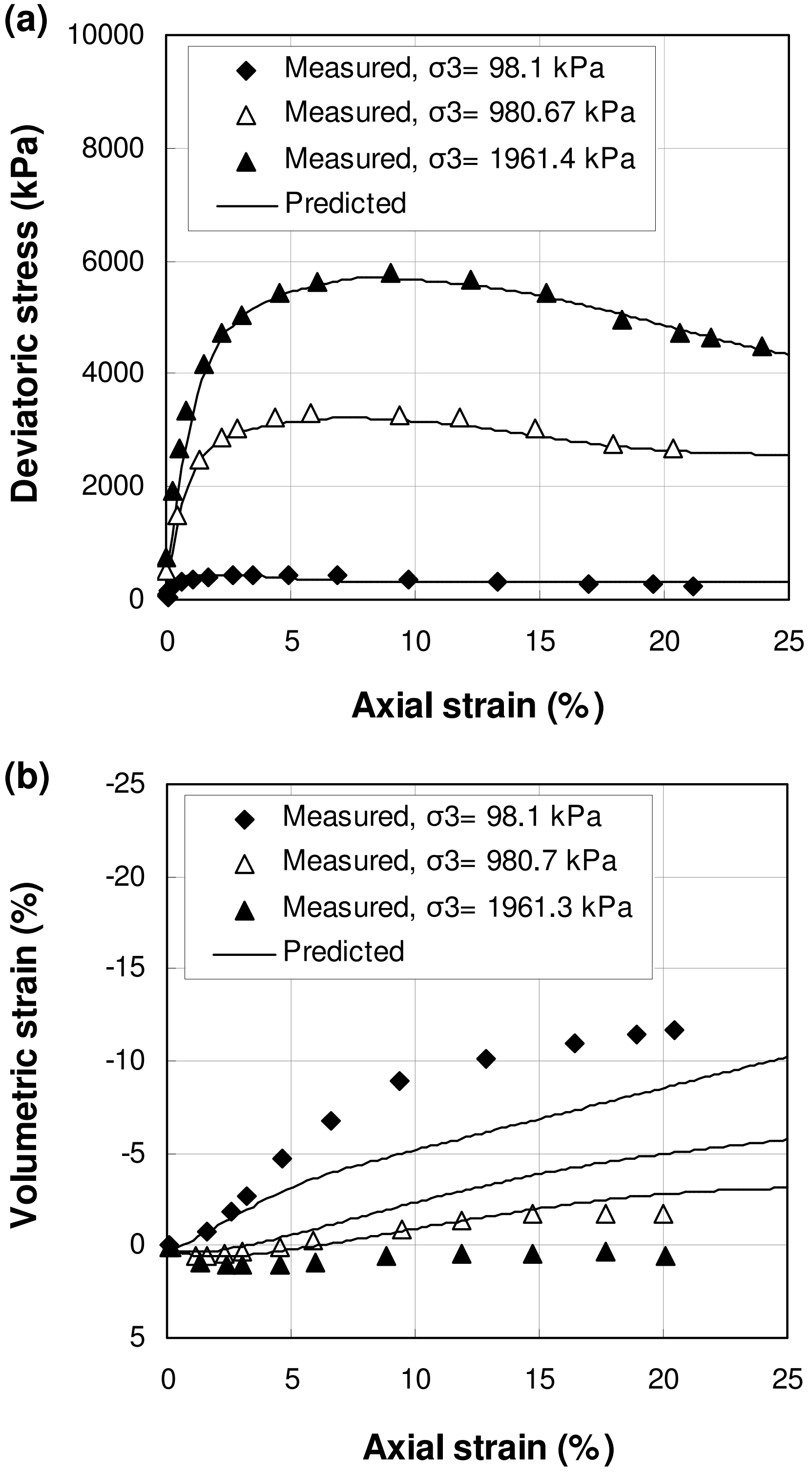

Figure 4.16: Comparison of predicted and measured results: (a) deviatoric stress and axial strain; (b) volumetric and axial strain for Sacramento River sand

Chapter 5: Stress Integration Algorithm

In the finite element analysis, stress information within materials is obtained by using stress integration algorithms. In this chapter, two stress integration algorithms are introduced in detail including: 1) the forward Euler integration scheme with subincrements; 2) the modified forward Euler integration scheme with error control. The implementation procedures are also presented. The effect of two stress integration algorithms in regard to computational accuracy, error tolerances and efficiency are evaluated specifically for the proposed soil-softening model.

5.1 BACKGROUND

The employment of more advanced and accurate elastoplastic constitutive models to represent the true material behavior is often avoided due to a substantial increase in the computational costs. However, the problem of excessive computational costs could be possibly limited by a critical assessment of the selected integration schemes. The selection of suitable integration schemes is twofold: 1) for the computation of updated stresses and hardening parameters by integration of the constitutive relation; 2) for establishment of the overall equilibrium of equation system.

In the latter case, as discussed previously in Chapter 3, the solution of nonlinear finite element problems involving the mechanical behavior of materials usually consists of a series of load steps, each involving iterations to establish equilibrium between internal and external forces at each new load level. This global iteration process is conventional handled by the iteration scheme such as Newton-Raphson method in finite element analysis. However, the evaluation of the internal forces and displacements in the global iterations depends on the updated stresses and hardening parameters which are provided by stress integration schemes. As a result, the integration schemes have a direct impact on both accuracy and efficiency of computation.

As already explained in Chapter 3, the forward Euler integration scheme is commonly used in the finite element analysis. Due to the nonlinearity of constitutive matrix, this scheme is only accurate for small strain increments. If the strain increment is relatively large, the accuracy of calculation can be improved by subdividing the strain increment into a fixed number of subincrements. However, this strategy turns out to be computationally expensive and inefficient. This is because of the disadvantage of using the equal size subincrements. In order to achieve certain computational accuracy in estimating stresses, only few subincrements is required when the stress-strain relationships are linear but many subincrements is in need for the stress-strain relationships under nonlinear religion. Accordingly, the number of subincrements must be determined by trial-and-error so that the maximum error is within some close tolerance; otherwise, the error will be accumulated during subsequent load steps and likely leads to unacceptable results. Moreover, this scheme has the disadvantage that the stress state predicted at the end of the elastoplastic load increment may not lay on the current yield surface exactly. In other words, the consistency condition of yield function may be violated, i.e., $f_p = f'_p(\sigma) - f''_p(W_p) \neq 0$. This error will essentially depend on the size of the strain increment and number of subdivisions. If the yield criterion is not fulfilled, the stress increments tend to drift away from the updated yield surface and a scheme for the correction of yield surface drift should be applied. As all the problems stated above, a refined subincremental version of the forward Euler scheme with active error control have been investigated and implemented in this study.

Jakobsen and Lade (2002) demonstrated the effectiveness of the aforementioned integration schemes using an example of numerical simulation of triaxial compression testing on Eastern Scheldt sand under undrained conditions (constant volume strains). The simulation was conducted by imposing a number of strain increments with equal size $\Delta\varepsilon^{T} = 10^{-4} \mathrm{x}[5 \quad -2.5 \quad -2.5 \quad 0 \quad 0 \quad 0]$ and using the two integration schemes for determination of the corresponding change in stresses. For the integration of the given strain increment, the error in calculated stress can be suppressed under 10^{-4} approximately with a maximum number of subincrements of 700 by using the forward Euler scheme with subincrement. However, the same error criterion can be achieved with a maximum number of subincrements of 29 when the modified forward Euler scheme with error control was used. Because of less subincrements required, the computational time by using the modified forward Euler schemes was approximately 65 times less compared to the required time by using the forward Euler scheme. Last, it was shown by Jakobsen and Lade (2002) that the computational accuracy by using the modified forward Euler schemes was largely unaffected by the correction of yield surface drift. However, the correction of yield surface drift became important when using the forward Euler scheme because it reduced the errors in stresses by at least 70%.

5.2 FORWARD EULER INTEGRATION SCHEME WITH SUBINCREMENTS

The forward Euler integration scheme with subincrements is a commonly used integration scheme for integrating elastoplastic stress-strain relationships. This section discusses the detail procedure of the forward Euler integration scheme. In the following, it is assumed that the initial state of stresses is located on the yield surface and that the next stress increment causes the elastoplastic strains. The stresses are updated by an incremental relation:

$$\Delta\sigma = D_{ep}(\sigma_0, W_{p,0})\Delta\varepsilon \tag{5.1}$$

where the elastoplastic constitutive matrix D_{ep} is evaluated at the initial state of stresses σ_0 and hardening parameter $W_{p,0}$. The hardening parameter depends on the selected soil constitutive models. For the soil model used in this study, the hardening parameter is the plastic work W_p which is used to descript the soil hardening and softening behavior. As the elastoplastic constitutive matrix depends on the stress and strain history, the linear approximation is only accurate for very small strain increments. The method may be refined by a piece wise linear integration where the strain increment is subdivided into smaller subincrements (Crisfield 1991, Sloan 1987, Chen and Mizuno 1990, Smith 1988, Zienkiewicz and Taylor 1991).

$$\delta\varepsilon = \Delta S \Delta\varepsilon = \frac{\Delta\varepsilon}{m} \tag{5.2}$$

where $\delta\varepsilon$ is the strain subincrement. ΔS is a dimensionless step of fixed size. m is the number of subincrements. The stress increment $\Delta\sigma$ is evaluated as the sum of the m subincrements $\delta\sigma_i$ which can be expressed as:

$$\delta\sigma_i = D(\sigma_0 + \Delta\sigma_{i-1}, W_{p,0} + \Delta W_{p,i-1})\delta\varepsilon \tag{5.3}$$

and

$$\delta W_{p,i} = \delta\lambda_p(\sigma_0 + \Delta\sigma_{i-1}, W_{p,0} + \Delta W_{p,i-1}, \delta\varepsilon)(\sigma_0 + \Delta\sigma_{i-1}) \left.\frac{\partial g_p}{\partial\sigma}\right|_{\sigma_0 + \Delta\sigma_{i-1}} \tag{5.4}$$

where $\delta\lambda_p$ is the scalar factor of proportionality defined in Eq. (4.27). g_p is the plastic potential function.

$$\Delta\sigma_{i-1} = \sum_{j=1}^{i-1} \delta\sigma_j \tag{5.5}$$

and

$$\Delta W_{p,i-1} = \sum_{j=1}^{i-1} \delta W_{p,i-1} \tag{5.6}$$

Figure 5.1 schematically illustrates the 1-Dimension stress-strain increment and subincrement in the forward Euler integration scheme. The algorithm for implementation is listed in the box of Fig. 5.2.

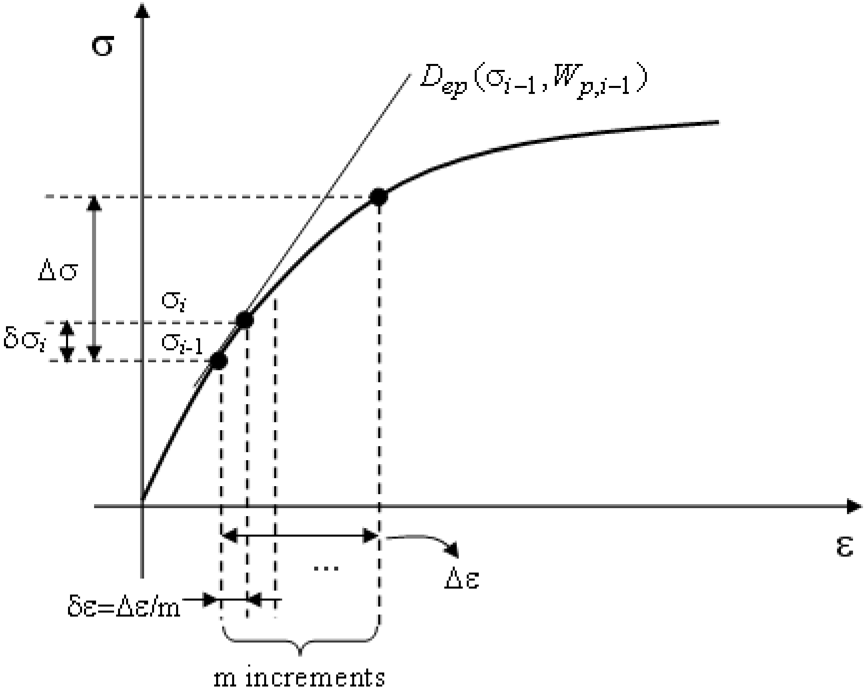

Figure 5.1: Stress-strain increment and subincrement in the forward Euler integration scheme

```
Initial state $\sigma_0$, $W_{p,0}$, $\Delta\varepsilon$, $\delta\varepsilon = \frac{\Delta\varepsilon}{m}$

DO strain subincrement i=1,2,…,m,
    (1) Evaluate stress and hardening parameters for next strain subincrement
        $\delta\sigma_i = D(\sigma_{i-1}, W_{p,i-1})\delta\varepsilon$
        $\delta W_{p,i} = \delta\lambda_p(\sigma_{i-1}, W_{p,i-1}, \delta\varepsilon)(\sigma_{i-1})\frac{\partial g_p}{\partial(\sigma_{i-1})}$
    (2) Updated stress and hardening parameters
        $\sigma_i = \sigma_{i-1} + \delta\sigma_i$
        $W_{p,i} = W_{p,i-1} + \delta W_{p,i}$
END DO, strain subincrement when i=m

Finial state $\sigma_i, W_{p,i}, D(\sigma_i, W_{p,i})$
```

Figure 5.2: Algorithm of the forward Euler scheme with subincrements for evaluation of new stress state, plastic work and constitutive matrix.

5.3 MODIFIED FORWARD EULER SCHEME WITH ERROR CONTROL

In order to avoid the necessarily of conducting the yield surface drift and reduce computational costs of the forward Euler scheme, the modified Euler scheme with active error control is selected (Sloan 1987, Sloan and Booker 1992). Instead of using a fixed number of subincrements with equal size, the size of the subincrements can be varied flexibly through the integration process. Accordingly, the size of each subincrement is determined so that the new stress state fulfils the yield criterion within some small tolerance and only the absolutely necessary number of subdivision are applied.

The modified scheme uses a pair of first- and second-order Euler formulas to estimate the error produced by the standard forward Euler scheme at the end of each strain subincrement $\delta\varepsilon$. The integration is started by choosing a value of the dimensionless step ΔS. Then, by knowing the initial stress state, the modified scheme computes the first and second estimate of updated stresses and the work hardening parameters. The first estimate of the updated stresses and the hardening parameter at the end of the strain increment is given by:

$$\sigma = \sigma_0 + \delta\sigma^I \tag{5.7}$$

$$W_p = W_{p,0} + \delta W_p^I \tag{5.8}$$

where

$$\delta\sigma^I = D_{ep}(\sigma_0, W_{p,0})\delta\varepsilon \tag{5.9}$$

$$\delta W_p^I = \delta\lambda_p(\sigma_0, W_{p,0}, \delta\varepsilon)\sigma_0 \left.\frac{\partial g_p}{\partial\sigma}\right|_{\sigma_0} \tag{5.10}$$

The second and temporary estimate of the updated stress state can be evaluated as:

$$\sigma_{temp} = \sigma_0 + \frac{1}{2}(\delta\sigma^I + \delta\sigma^{II}) \tag{5.11}$$

$$W_{p,temp} = W_{p,0} + \frac{1}{2}(\delta W_p^I + \delta W_p^{II}) \tag{5.12}$$

where

$$\delta\sigma^{II} = D_{ep}(\sigma_0 + \delta\sigma^I, W_{p,0} + \delta W_p^I)\delta\varepsilon \tag{5.13}$$

$$\delta W_p^{II} = \delta\lambda_p(\sigma_0 + \delta\sigma^I, W_{p,0} + \delta W_p^I, \delta\varepsilon)(\sigma_0 + \delta\sigma^I)\left.\frac{\partial g_p}{\partial\sigma}\right|_{\sigma_0 + \delta\sigma^I} \tag{5.14}$$

The modified scheme is to evaluate two sequent elastoplastic constitutive matrixes D_{ep} from two iterations in each subincrement. The difference of the stress states between the first and second estimate can be applied to evaluate the local error in σ:

$$\delta\sigma^{I-II} \approx \sigma_{temp} - \sigma = \frac{1}{2}(\delta\sigma^{II} - \delta\sigma^{I}) \tag{5.15}$$

This estimated error serves as a guide for selecting the size of the next step ΔS when integrating over the total strain increment $\Delta\varepsilon$.The relative error R for a subincrement is defined by the norm:

$$R_i = \frac{\left\|\delta\sigma^{I-II}\right\|}{\left\|\sigma_{temp}\right\|} \tag{5.16}$$

The size of each step is continually adjusted until R is less than some specified tolerance *tol*. If $R \le tol$, the new stresses and hardening parameter are updated as σ_{temp} and $W_{p,temp}$. Otherwise, if $R > tol$, it requires to reduce ΔS and repeat the calculation procedure. The size of the next dimensionless step is generally given as:

$$\Delta S = q\Delta S \tag{5.17}$$

where

$$q = 0.9\left(\frac{tol}{R}\right)^{1/2} \tag{5.18}$$

The exponent 1/2 relates to the local truncation error O(ΔS^2) of the first-order formulae, whereas the factor of 0.9 is introduced to reduce the number of subincrement that are likely to be rejected during the integration process. Equation (5.18) indicates when $R \le tol$, the size of next subincrement will be automatically increased. Otherwise, when $R > tol$, the computational results of current subincrement are rejected and the process of integration is repeated by decreasing the size of current subincrement. Last, the size of the new increment is constrained between an upper and lower bound of q.

$$0.01 \le q \le 2 \tag{5.19}$$

Figure 5.3 schematically illustrates the 1-Dimension stress-strain increment and subincrement in the modified forward Euler integration scheme. The algorithm for implementation is listed in the box of Fig. 5.4.

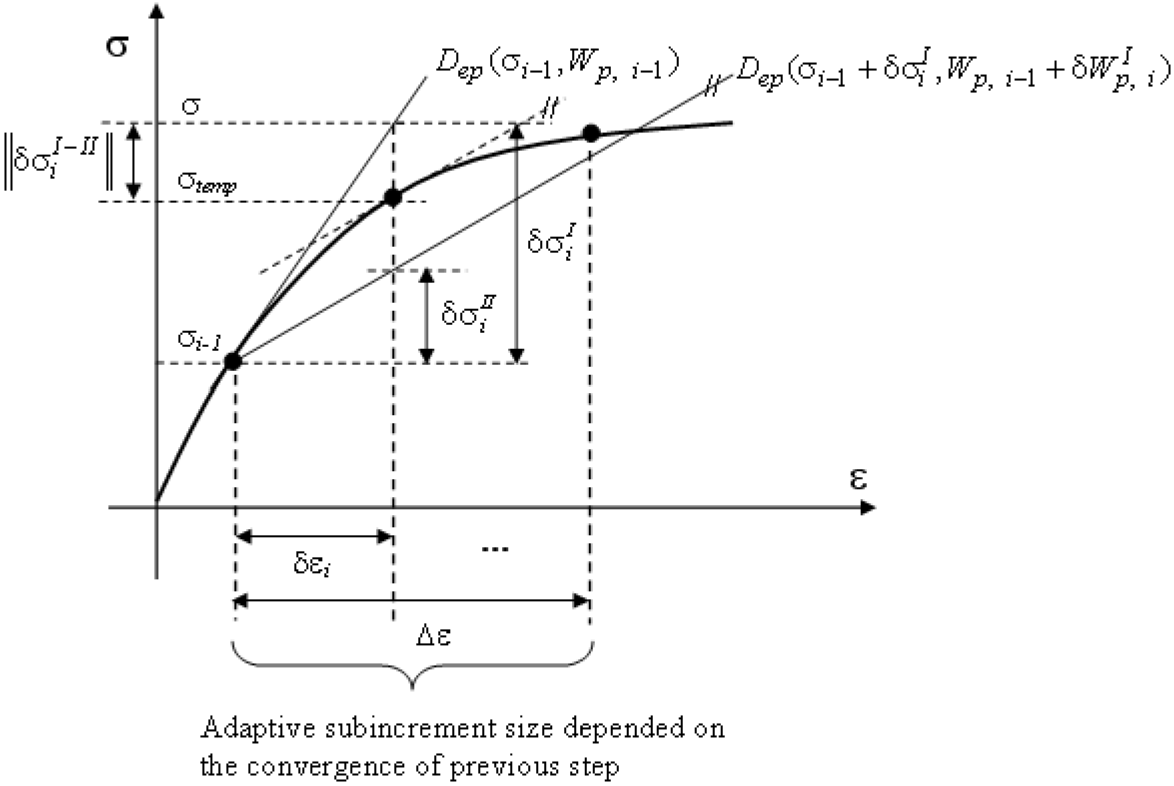

Figure 5.3: Stress-strain increment and subincrement in the modified forward Euler integration scheme

```
Initial state $\sigma_0$, $W_{p,0}$, $\Delta\varepsilon$, $\delta\varepsilon_0 = \Delta\varepsilon$, $q$=1
DO strain subincrement i=1,2,…,n, While $\sum_{i=1}^{n-1} \delta\varepsilon_i < \Delta\varepsilon$ ,
    (1) Evaluate stress and hardening parameters for two sequent iterations
        $\delta\varepsilon_i = q\delta\varepsilon_{i-1}$
        $\delta\sigma_i^I = D(\sigma_{i-1}, W_{p,i-1})\delta\varepsilon_i$
        $\delta W_{p,i}^I = \delta\lambda_p(\sigma_{i-1}, W_{p,i-1}, \delta\varepsilon_i)\sigma_{i-1}\frac{\partial g_p}{\partial\sigma}$
        $\delta\sigma_i^{II} = D(\sigma_{i-1} + \delta\sigma_i^I, W_{p,i-1} + \delta W_{p,i}^I)\delta\varepsilon_i$
        $\delta W_{p,i}^I = \delta\lambda_p(\sigma_{i-1} + \delta\sigma_i^I, W_{p,i-1} + \delta W_{p,i}^I, \delta\varepsilon_i)(\sigma_{i-1} + \delta\sigma_i^I)\frac{\partial g_p}{\partial\sigma}$
    (2) Evaluate a temporary stress and hardening parameters
        $\sigma_{temp,i} = \sigma_{i-1} + \frac{1}{2}(\delta\sigma_i^I + \delta\sigma_i^{II})$
        $W_{p,temp,i} = W_{p,i-1} + \frac{1}{2}(\delta W_{p,i}^I + \delta W_{p,i}^{II})$
    (3) Evaluate relative error: $R$
        $\delta\sigma_i^{I-II} \approx \frac{1}{2}(\delta\sigma_i^{II} - \delta\sigma_i^I)$
        $R_i = \frac{\left\|\delta\sigma_i^{I-II}\right\|}{\left\|\sigma_{temp,i}\right\|}$
        IF $R>tol$, than redo evaluation using smaller strain increment
            $q = \max\left[0.9\left(\frac{tol}{R_i}\right)^{\frac{1}{2}}, 0.01\right]$, goto (1)
        ElSE R<$tol$, than update stress and hardening parameters
```

Figure 5.4: Algorithm of the modified forward Euler scheme with error control for evaluation of new stress state, plastic work and constitutive matrix.

```
        $\sigma_i = \sigma_{temp,i}$ and $W_{p,i} = W_{p,temp,i}$
        $q = \max\left[0.9\left(\frac{tol}{R_i}\right)^{\frac{1}{2}}, 2\right]$
END DO, strain subincrement when $\sum_{i=1}^{n} \delta\varepsilon_i = \Delta\varepsilon$
Finial state $\sigma_i, W_{p,i}, D(\sigma_i, W_{p,i})$
```

Figure 5.4: (Continued)

5.4 COMPARISON OF INTEGRATION SCHEMES

The effect of the integration schemes specifically for the proposed soil-softening model is examined in this section. The computational accuracy, error tolerances and efficiency of two integration schemes are compared. For the purpose of examination, a single stress/strain point numerical program composed of the selected soil constitutive model and stress integration scheme was used to simulate the triaxial compression testing on Monterey #30 sand. The properties and parameters of Monterey # 30 have been discussed earlier in Section 4.5. A total vertical strain of 12% is imposed, which is large enough for soil to occur softening and reach final residual strength. During simulation, the imposed vertical strain is divided into 12 increments with equal size, 1% for each strain increment. The simulation begins at an isotropic confining pressure of 211 kPa and then the prescribed vertical strains are applied. Then, two integration schemes are applied to determine the corresponding change in stresses. Figure 5.5 shows a comparison of the calculated stress-strain relationships using two integration schemes.

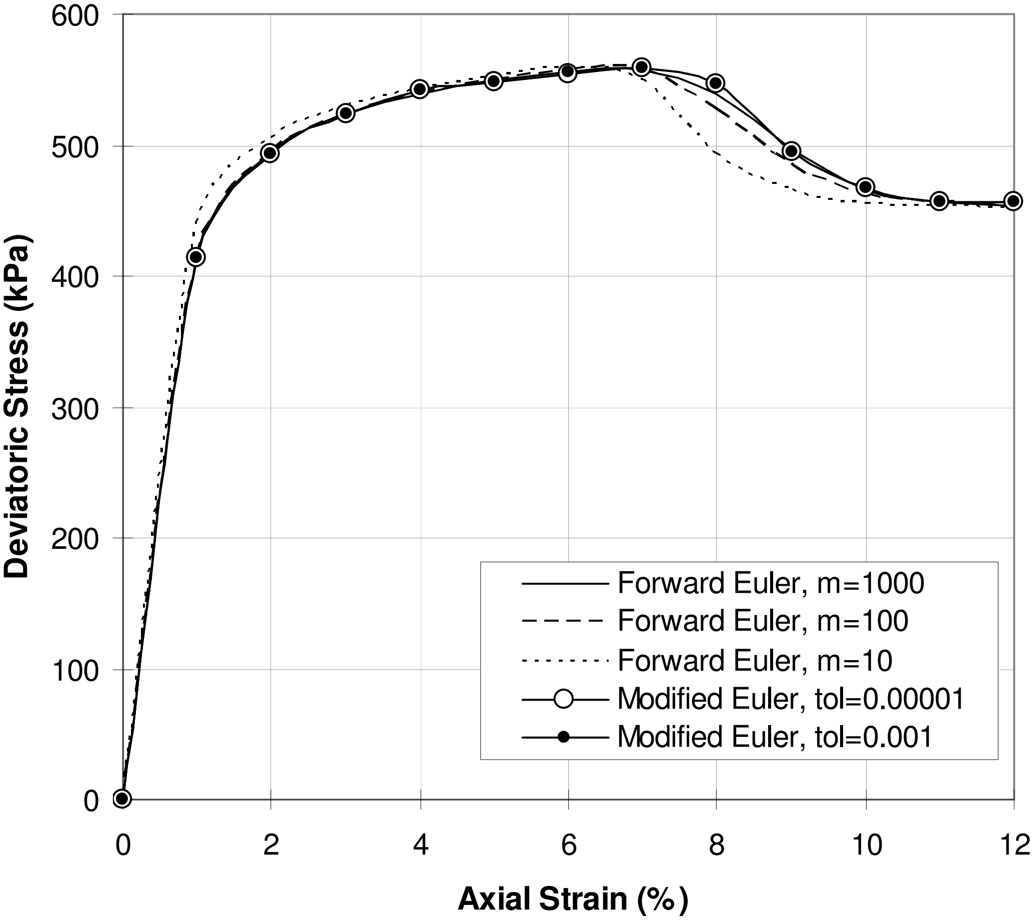

Figure 5.5: Comparison of calculated stress-strain relationships using two integration schemes with various subincrement and tolerance

In Fig. 5.5, for the forward Euler scheme with fewer subincrements (*m*=10), it tends to over predict the stresses in soil pre-peak region and under predict the stresses in soil post-peak region. Figure 5.6 shows an enlargement of this trend around peak area. The reason of over predication in pre-peak region can be explained by the change of soil module with developed strains. Typically, soil module has the highest value at initial strain and, afterward, decreases with the increase of developed strains.

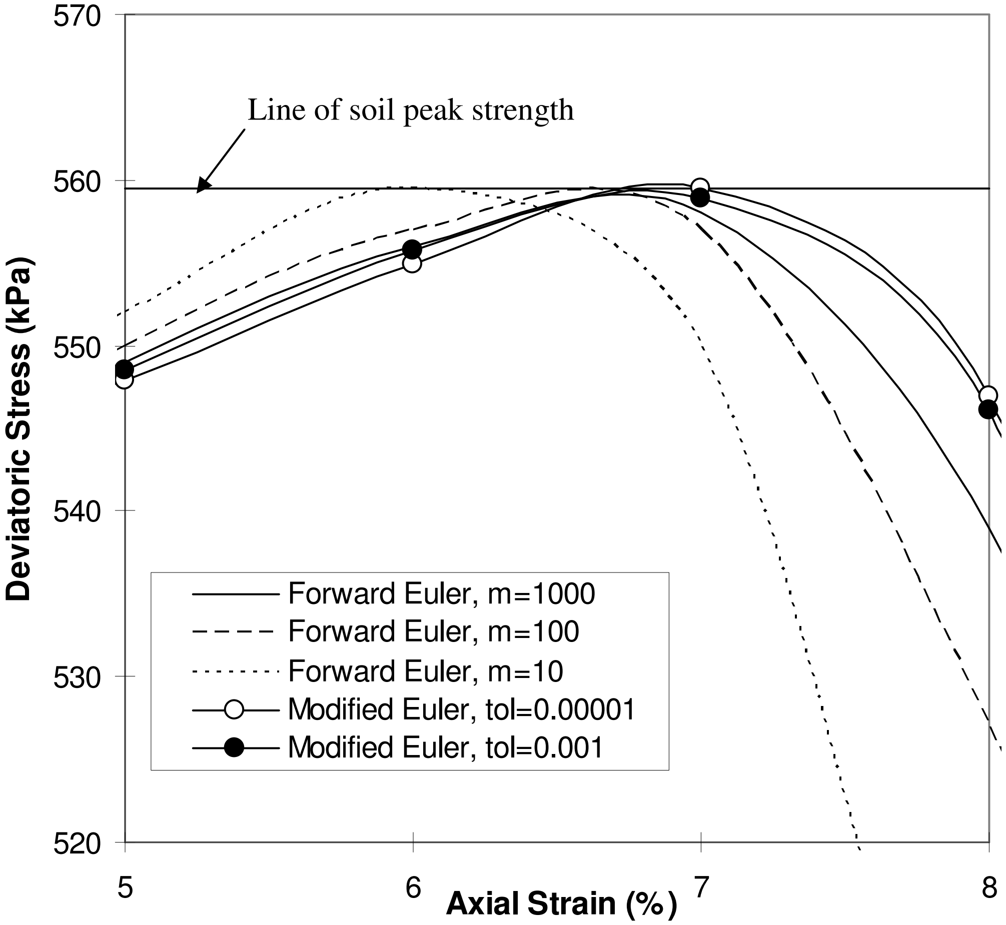

Figure 5.6: Segment of stress-strain relationships around the soil peak area

The high module at low strain level causes the over prediction of stresses when fewer subincrements in each strain increment are used. Further, the over prediction of stresses will reach soil peak strength and initiate softening earlier. It can be observed in Fig. 5.6 that the calculated stresses reach the soil peak strength at different strains. As a result, the stresses which reach soil peak strength and initiate softening earlier are considerably under predicted in the post-peak region. Finally, all the calculated stresses will converge at same residual strength, which is governed by the residual parameter f''_{pr} in soil-softening model. If a soil model without the limit in residual strength such as the original soil-softening model in Lade-Kim model is used, the under prediction of stresses in the soil post-peak region becomes significant. However, the applicability of the forward Euler scheme improves as the number of subincrements in the integration process is increased. It is shown that the result using the forward Euler scheme with 1000 subincrements is close to the results computed by the modified forward Euler schemes. Similar observations hold for the development in the volumetric strain and the hardening parameters W_p, as indicated in Figs. 5.7 and 5.8.

The computational accuracy and cost between different integration schemes are quantitvely measures and compared in Table 5.1. In Table 5.1, m is the number of strain subincrements $\delta\varepsilon$. User can define the desired number of subincrements in the forward Euler scheme (e.g., m=10, 100, and 1000). m in the modified forward Euler scheme do not have to be defined by user; it is an automatic procedure based on calculated error in each iteration loop. m is a minimum number of subincrements automatically determined to satisfy the allowable tolerance given by user. The m presented in Table 5.1 for the modified forward Euler scheme is an average number of subincrements among 12 strain increments. Because the modified forward Euler scheme requires two iterations to evaluate the size of next subincrement, the actual number of evaluations should be m x 2 if computational cost is compared. Table 5.2 summarizes the number of subincrements in each strain increment during simulation. Table 5.2 indicates the first few increments are decisive for the maximum number of subincrements needed for fulfillment of a given error tolerance in the modified forward Euler scheme. This is because the stress increments are large due to high soil modulus at the first few strain increments.

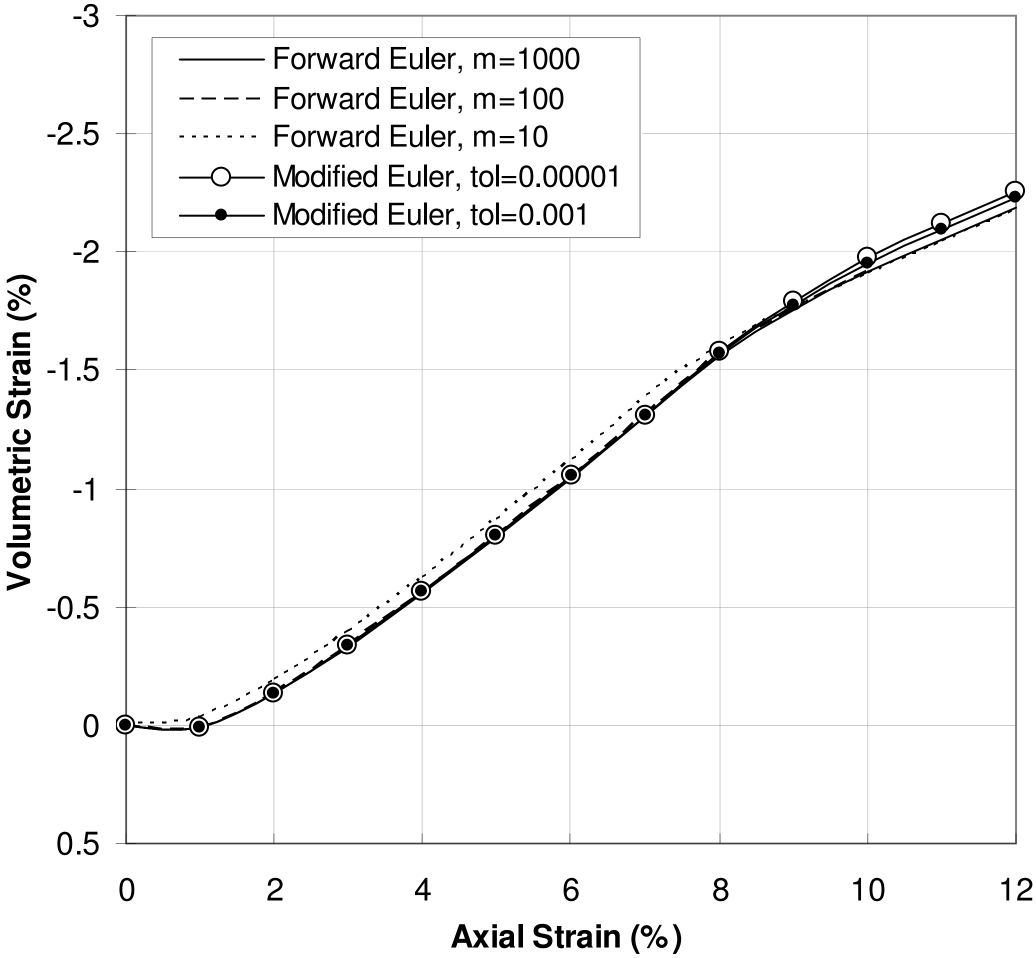

Figure 5.7: Comparison of volumetric-axial strain relationships using two integration schemes with various subincrements and tolerances

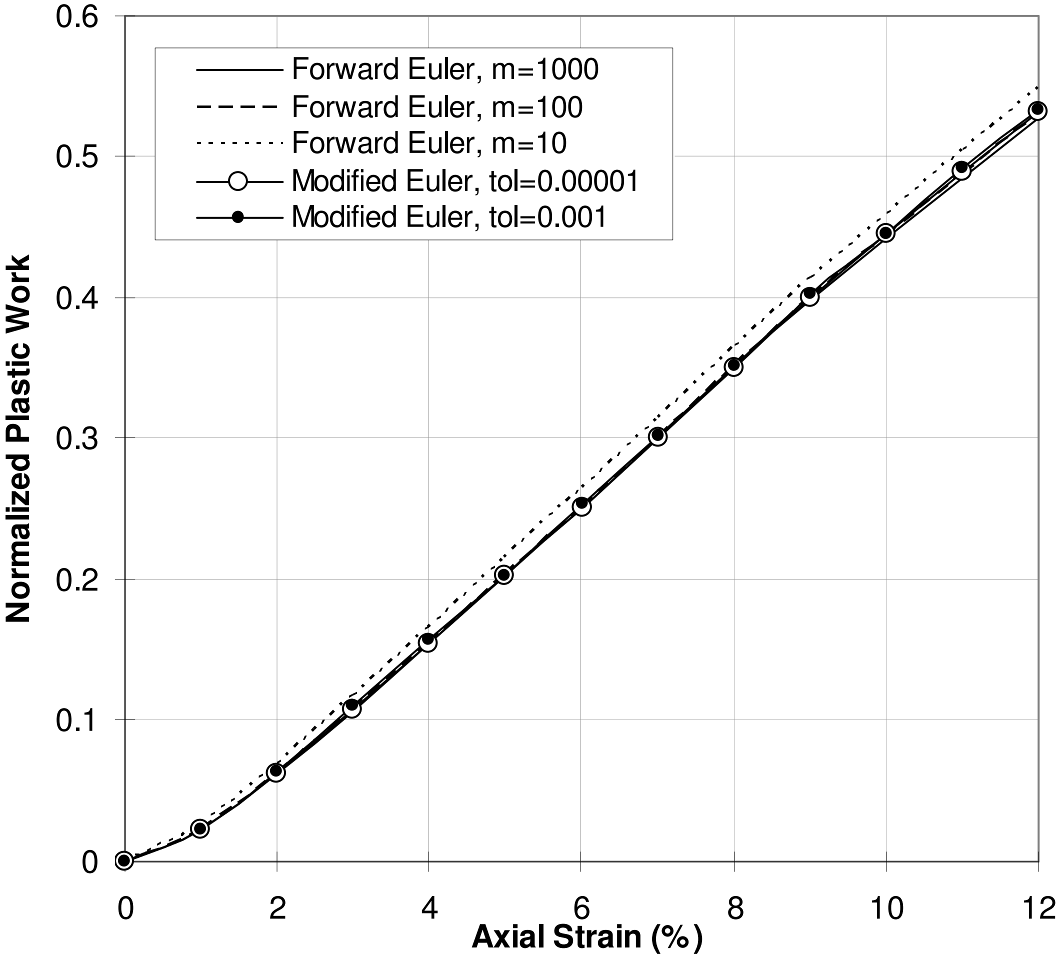

Figure 5.8: Comparison of normalized plastic work-axial strain relationships using two integration schemes with various subincrements and tolerances

Table 5.1: Comparison of computational accuracy and cost

Algorithm	**m**	**tol**	$\mathbf{E_{max}}$	$\mathbf{E_{avg}}$	**Computation Time (sec)**
FE	1000		1.03E-02	2.81E-03	0.67
	100		2.44E-02	5.59E-03	0.06
	10		6.61E-02	1.82E-02	0.01
MFE	140(X2)	10^{-5}	0	0	0.05
	20(X2)	10^{-3}	1.00E-03	4.76E-04	0.02

Table 5.2: Comparison of required subincrements using different schemes

	FE			**MFE**	
Number of increments	m=1000	m=100	m=10	tol=10^{-5}	tol=10^{-3}
1	1000	100	10	426	48
2	1000	100	10	198	25
3	1000	100	10	124	19
4	1000	100	10	91	15
5	1000	100	10	76	13
6	1000	100	10	63	13
7	1000	100	10	55	12
8	1000	100	10	87	16
9	1000	100	10	160	22
10	1000	100	10	115	17
11	1000	100	10	71	15
12	1000	100	10	55	11
Average of subincrements	1000	10	10	139.5	20.0

The error in each strain increment, Δε=1%, for different schemes can be expressed as:

$$E_i = \frac{\left\| \sigma_i - \sigma_{i,ref} \right\|}{\left\| \sigma_{i,ref} \right\|} \tag{5.20}$$

In this simulation, since no analytical solution is available for integrating the relations of the soil-softening model exactly, the calculated stresses by the modified Forward Euler scheme with *tol*=10-5 are taken as a reference. The average and maximum errors along the stress path are given by:

$$E_{avg} = \frac{1}{12} \sum_{i=1}^{12} E_i \tag{5.21}$$

and

$$E_{\max} = \max \left\{ E_i \mid i = 1, 2, 3 \ldots 12 \right\} \tag{5.22}$$

Table 5.1 indicates FE (m=10) has worst accuracy. The accuracy increases with the increase of the number of subincrements in the forward Euler scheme. However, the efficiency in term of computational time is sacrificed to the increase of computational accuracy. The computational cost can be measured by the time to complete the simulation. Table 5.1 indicates the forward Euler scheme shows a largely proportional growth in the number of subincrements and computational time. However, for the modified Euler scheme, the computational time grows slightly with the reduction of the error tolerance.

It can be learned from above analysis that a reduction of strain subincrement size in the forward Euler scheme may:

1. Change the appearance of the stress path and lead to results closer to the "correct solution".
2. Reduce the discrepancy between the integration schemes.
3. However, it requires high computational cost.

The choice of the strain subincrement will therefore essentially depend on the required accuracy of both global and local solutions. The integration schemes merely can be viewed as a tool to provide an accurate stress update for a given strain increment. In other words, it is possible to obtain similar results using different schemes but another consideration involves their computation efficiencies. Further, the choice of integration scheme is specifically related to the selected constitutive model. For the soil-softening model used in this study, it can be concluded the modified forward Euler integration scheme is in general found to be superior to the forward Euler schemes in terms of both accuracy and computational costs.

Chapter 6: Finite Element Simulation of GRS Slopes

This chapter presents a finite element study conducted to simulate the GRS structures under various loading conditions. First, a series of centrifuge testing on GRS slopes conducted by Arriaga (2003) is reviewed. The data from centrifuge studies will be used to verify the finite element model in the next chapter. Then, a finite element model to simulate the centrifuge slope model is introduced. Each component of finite element model and the reasons of selection of input parameter values are clearly documented.

6.1 CENTRIFUGE MODELING OF GRS SLOPES

A series of centrifuge studies was conducted by Arriaga (2003) under the supervision of Dr. Zornberg at the University of Colorado at Boulder. The centrifuge studies were to investigate the behavior and mechanism of GRS slopes under various stress states (i.e., working stress and failure conditions). The main objective of the centrifuge study was to obtain the information of strain distribution along the reinforcement layers of GRS slopes. The review of the centrifuge study presented herein will focus on the aspects of finite element applications discussed later in this chapter. Readers are referred to Arriaga (2003) for other aspects relevant to the behavior of GRS slopes under various stress states.

There are two reasons for selecting Arriaga's centrifuge test results for evaluation in this study. First, the full-scaled test or in-situ instrumentation and monitoring of GRS structures are often designated for working stress conditions. Testing rarely reaches large soil strain conditions. As a result, data for GRS structures under large soil strain conditions is rarely reported. Second, because the data from centrifuge tests is fully accessible, the data from centrifuge tests can be reassessed and reprocessed if other important aspects are of interest.

6.1.1 Centrifuge Model Layout

The centrifuge tests include 18 different slopes with various slope angles (1H:1.5V, 1H:2V, 1H:2.5V and 90^o), reinforcement types/strengths (Pellon Sew-In and Pellon Tru-Grid nonwoven geotextiles), reinforcement spacings (uniform spacing of 9 and 12 layers and non-uniform spacing), and the soil relative densities (50% and 70%). The backfill, Monterey No. 30 sand, was air pluviated under constant flow rate and drop height to achieve target backfill relative density values of 50% and 70%. The unit weight of the Monterey No. 30 sand at the relative densities of 50% and 70% were 15.7 kN/m^3 and 16.08 kN/m^3, respectively. The foundation layer was pluviated to a denser condition. Scope of the testing program is summarized in Table 6.1.

All models were built with the same total height of 254 mm. They consisted of 228 mm high geotextile-reinforced structures built on a 25 mm thick foundation layer. The geotextile was placed as the targeted layout (length of 203 mm and vertical spacing) and folded the geotextile back to form wrap-around facing and a secondary layer (overlap) of 50 mm long. Figure 6.1 shows a typical layout of centrifuge slope model M1.

Table 6.1: Summary of centrifuge testing program (Arriaga 2003)

Model	Slope Angle	Geotextile Layers	Vertical Spacing (mm)	Geotextile Type	Backfill Relative Density	G-Level at Failure, N_f	Failure Type
M1	1H:2V	9	25.4	Pellon Sew-In	70%	50	Progressive
M2	1H:2V	12	19.05	Pellon Sew-In	70%	69	Progressive
M3	1H:2V	9	25.4	Pellon Sew-In	50%	36	Progressive
M4	1H:2V	12	19.05	Pellon Sew-In	50%	48	Progressive
M5	1H:2V	9	25.4	Pellon Tru-Grid	50%	80	Sudden
M6	1H:2.5V	9	25.4	Pellon Sew-In	70%	39	Progressive
M7	1H:2.5V	12	19.05	Pellon Sew-In	70%	53	Progressive
M8	1H:2.5V	9	25.4	Pellon Sew-In	50%	29	Progressive
M9	1H:2.5V	12	19.05	Pellon Sew-In	50%	39	Progressive
M10	1H:2.5V	9	25.4	Pellon Tru-Grid	70%	86	Sudden
M11	1H:2.5V	9	25.4	Pellon Tru-Grid	50%	67	Sudden
M12	90^o	9	25.4	Pellon Tru-Grid	70%	33	Sudden
M13	1H:1.5V	9	25.4	Pellon Sew-In	50%	69	Progressive
M14	90^o	12	19.05	Pellon Sew-In	70%	19	Progressive
M15	1H:2V	12	25.4; 12.7	Pellon Sew-In	50%	43	Progressive
M16	1H:2V	12	25.4; 12.7	Pellon Sew-In	50%	53	Progressive
M17	1H:2.5V	12	25.4; 12.7	Pellon Sew-In	70%	50	Progressive
M18	1H:2.5V	12	25.4; 12.7	Pellon Sew-In	70%	45	Progressive

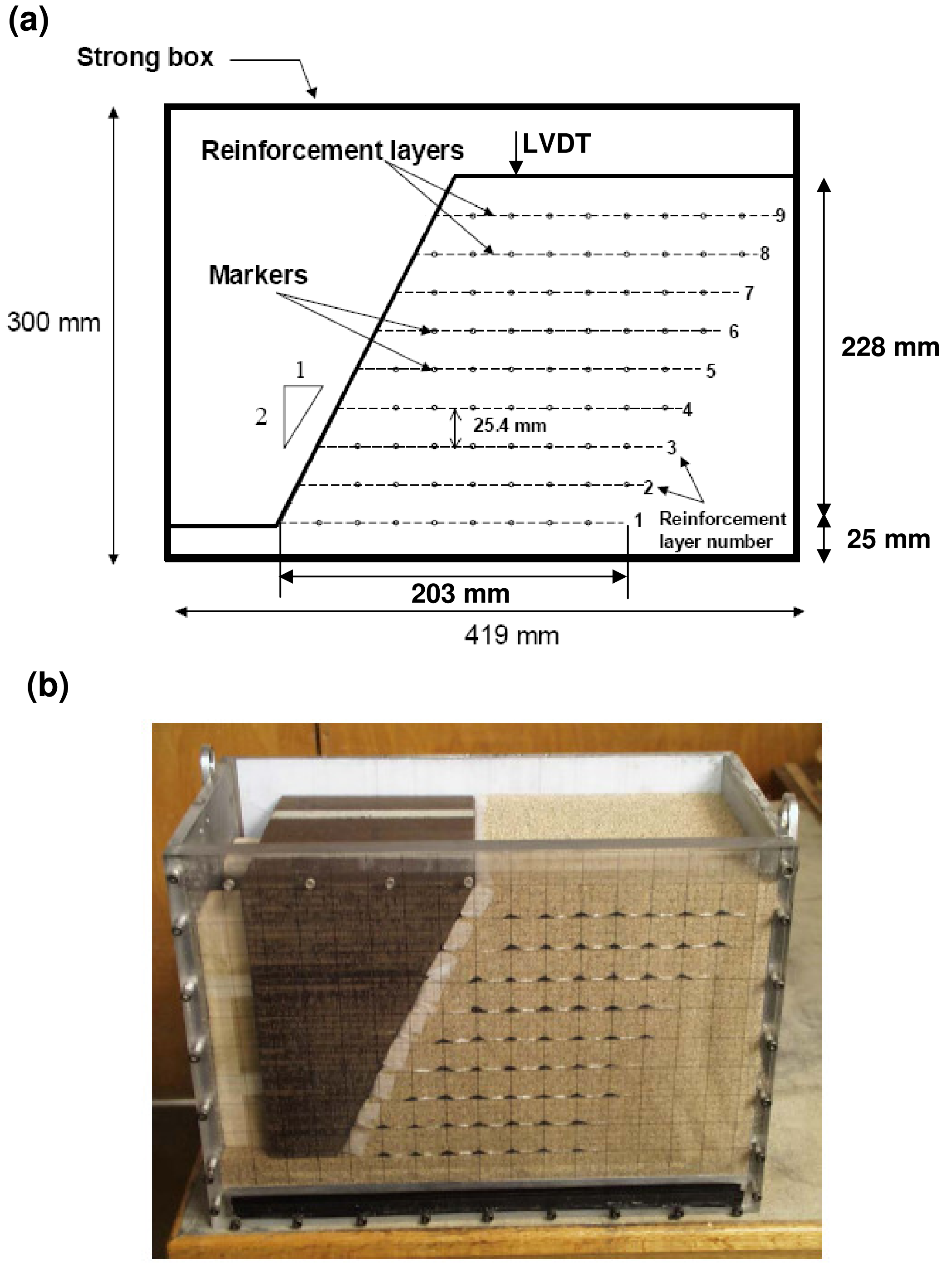

Figure 6.1: Centrifuge slope model M1: (a) geometry; (b) view of the physical model ready for test (Arriaga 2003)

6.1.2 Backfill Properties

6.1.2.1 Sand Characterization

All slope models were built using Monterey No. 30 sand, which is clean uniformly graded sand classified as SP in the Unified System. The particles are rounded to subrounded, as seen in the Figs. 6.2. The properties of Monterey No. 30 sand were listed in Table 4.2 in Chapter 4. A minimum dry density of 14.76 kN/m^3 was obtained by carefully pouring the sand into a container of known volume using a rigid pouring device provided with a spout according to ASTM D4254. A maximum dry density of 16.70 kN/m^3 was obtained using a vibratory table according to ASTM D4253. A reported value of 2.65 was adopted for the specific gravity of the sand (Bolton et al. 1994). The maximum void ratio, $e_{max} = 0.76$, was calculated using the minimum dry density and the specific gravity. Similarly, the minimum void ratio, $e_{min} = 0.56$, was calculated using the maximum dry density and specific gravity.

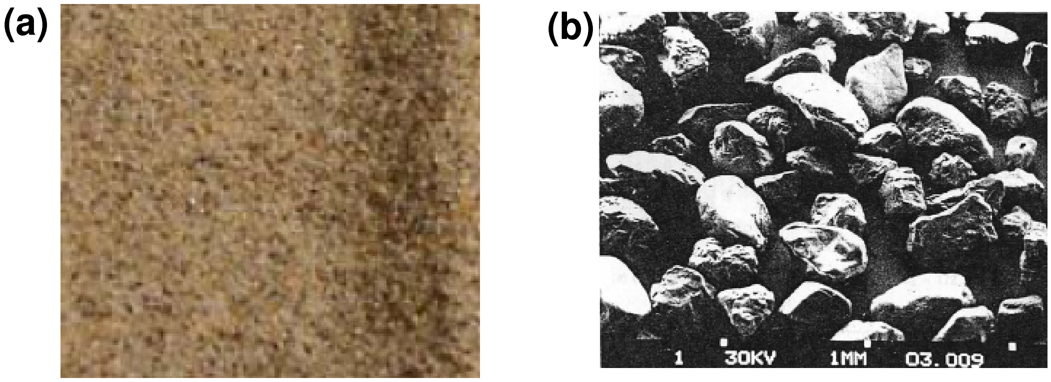

Figure 6.2: Monterey No. 30 sand: (a) normal view; (b) photomicrograph (after Veyera and Charlie 1990)

6.1.2.2 Shear Strength Properties under Triaxial Compression

Two series of triaxial tests were performed by Li (2005) to evaluate the soil stress-strain behavior for the Monterey No. 30 sand as a function of relative density and confining pressure. Figure 6.3a presents the stress-strain relationships for Monterey No. 30 sand with relative density 48 % and 65% (close to the targeted densities 50% and 70% in centrifuge tests). The results in Fig. 6.3a indicate that the peak shear strength of Monterey No. 30 sand increases with increasing relative density and confining pressure. The soil peak friction angles ϕ_{tc} under triaxial compression are 34.7^o for relative densities of 48% and 36.4^o for relative densities of 65%.

Under large soil strains, the soil strength under two different relative densities converges to similar residual strength values. This is because the residual strength is mainly a function of mineralogy and has no influence by soil density (Bolton 1986). In addition, it appears in Fig. 6.3a that the soil residual strength increases with the increasing confining pressure. Further, it is observed the soil-softening behavior in the post-peak region is more significant at the higher relative density. Overall, the residual friction angles ϕ_r appear to converge to a value of 32.5^o. This value agrees with the critical state friction angle for Monterey No. 0 sand obtained by Riemer (1992). (Note: The Monterey No. 0 and No. 30 are the same sand.)

Figure 6.3b shows the axial-volumetric strain relationships. Typical dilatant behavior of frictional materials is also observed in Monterey No. 30 sand. Figure 6.3b indicates that the magnitude of dilatancy increases with the increasing density and the decreasing confining pressure. Johonston and Romstad (1989) reported the soil dilation is an important mechanism that controls the strength of soils and the efficiency of load transfer from the soil to the reinforcement during shear deformations in reinforced soil structures. Karpurapu and Bathurst (1995) also reported that, by the comparison of predicted structure response using soil constitutive model with and without the function of dilatancy, the accuracy of numerical predictions can be improved by including the effect of soil dilatancy into the soil model in the FE simulations.

6.1.2.3 Shear Strength Properties under Plane Strain Conditions

To better represent the soil stress state within reinforced soil structures, the plane strain is suggested (e.g., Jewell 1990) to be considered in the analysis of the behavior of reinforced soil structures. Kulhaway and Mayne (1990) suggested the ratio of the plane strain friction angle ϕ_{ps} to the triaxial friction angle ϕ_{tc} varies with relative density and is, in general, on the order of 1.12 to 1.18 (D_r=30% to 90%).

The specific correlations for the Monterey sand used in the centrifuge study were obtained from results of plane strain tests (Zornberg et al. 1998). Lade and Duncan (1973) reported plane strain friction angles for Monterey No. 0 sand, obtained from true triaxial tests on cubical specimens. Additionally, Marachi et al. (1981) reported the results of a series of tests on Monterey No. 20 sand obtained using triaxial and plane strain devices. The friction angle ratios ϕ_{ps}/ϕ_{tc} for Monterey No. 0 and Monterey No. 20 sands are indicated in Fig. 6.4. The friction angle ratios for the two Monterey sands increase with increasing relative density of the sand. Based on this correlation, the ratios ϕ_{ps}/ϕ_{tc} used in this study for Monterey No.30 sand at 50% and 70% relative densities are 1.13 and 1.15, respectively. Consequently, the values of the plane strain friction angles for relative densities of 50% and 70% are $\phi_{ps}=39.1^{o}$ and $\phi_{ps}=42.0^{o}$, respectively.

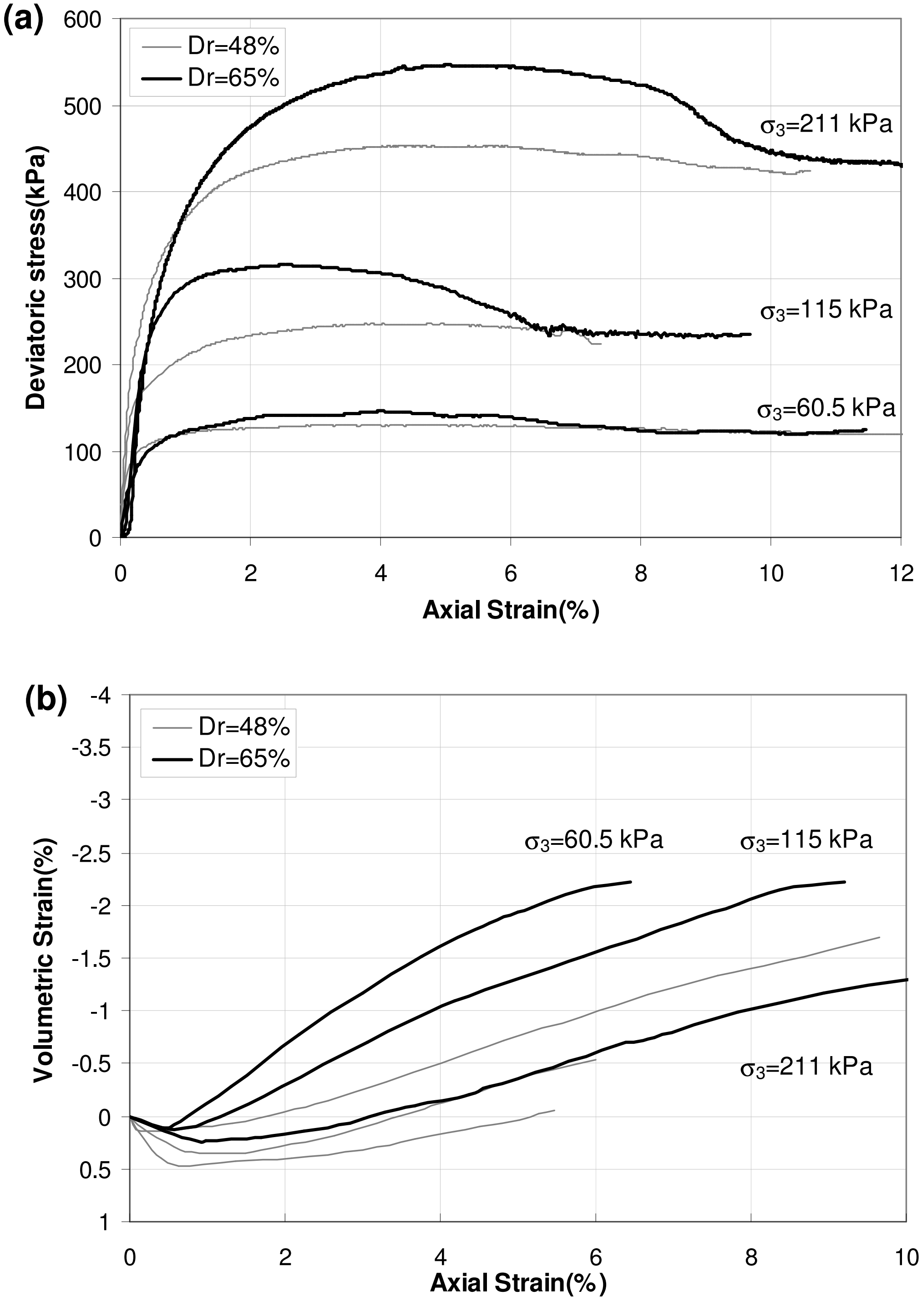

Figure 6.3: Monterey No 30 sand with different relative densities: (a) stress-strain; (b) volumetric-axial strain relationships

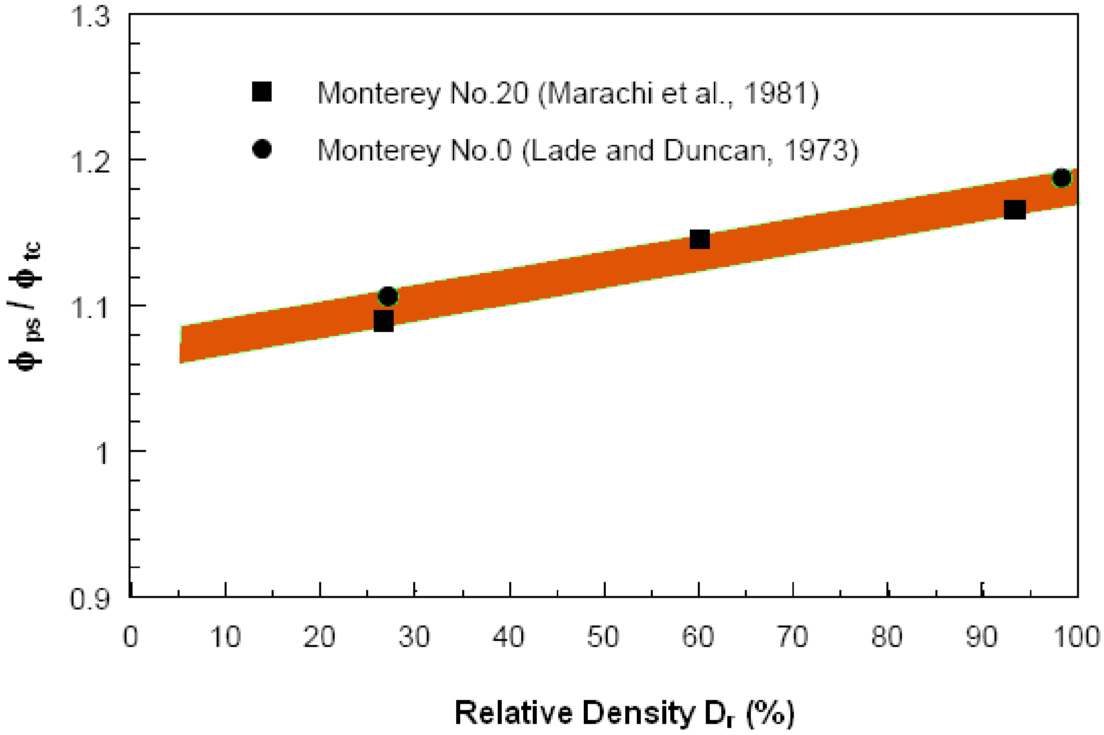

Figure 6.4: Ratio of friction angles under plane strain and triaxial compression conditions for Monterey sand (Zornberg et al. 1998)

6.1.3 Geotextile Reinforcement Properties

6.1.3.1 Unconfined Tensile Strength

The reinforcements used in centrifuge study were commercially available nonwoven geotextile and had two types: Pellon True-grid and Pellon Sew-in. The tensile strength of both fabrics is highly anisotropic, with the lower strength along the cross machine direction. All centrifuge models were built using the fabrics oriented in the cross machine direction. Consequently, the tensile strength of both geotextiles was evaluated along this direction.

Pellon True-grid was a white 60% polyester and 40% rayon fabric with mass per unit area of 28 g/m^2. The fabric, tested by wide-width strip tensile tests (ASTM D4595), had tensile strength T_{ult} of 0.09 kN/m in cross machine direction. Pellon Sew-in was a white 100% polyester fabric with a unit weight of 24.5 g/m^2. The fabric had tensile strength of 0.03 kN/m in the cross-machine direction. Figure 6.5 shows a wide-width test to measure the load-extension response of nonwoven geotextile. Figure 6.6 shows average wide-width test results for Pellon Sew-In and Pellon Tru-Grid.

6.1.3.2 Confined Tensile Strength

Although the wide-with tensile test is widely adopted for determining the tensile strength properties of geotextiles, the results provided by unconfined testing are not representative for field conditions. This is because when a geotextile is placed under the confinement of the soil, the geotextile, specifically for unwoven geotextile, may behave differently. This is likely due not only to soil confinement, but also to the interaction between soil particles in contact with geotextile fibers (Montalvo and Sickler 1993).

For the case of nonwoven geotextiles, it has been reported that, for a given strain, higher tensile loads are exhibited for the confined conditions (e.g., Ling et al. 1992). It has also been reported that the ultimate confined tensile strength increases with confining pressure (Leschinsky and Field 1987).

Figure 6.5: Wide-width test of Pellon Sew-In (Arriaga 2003)

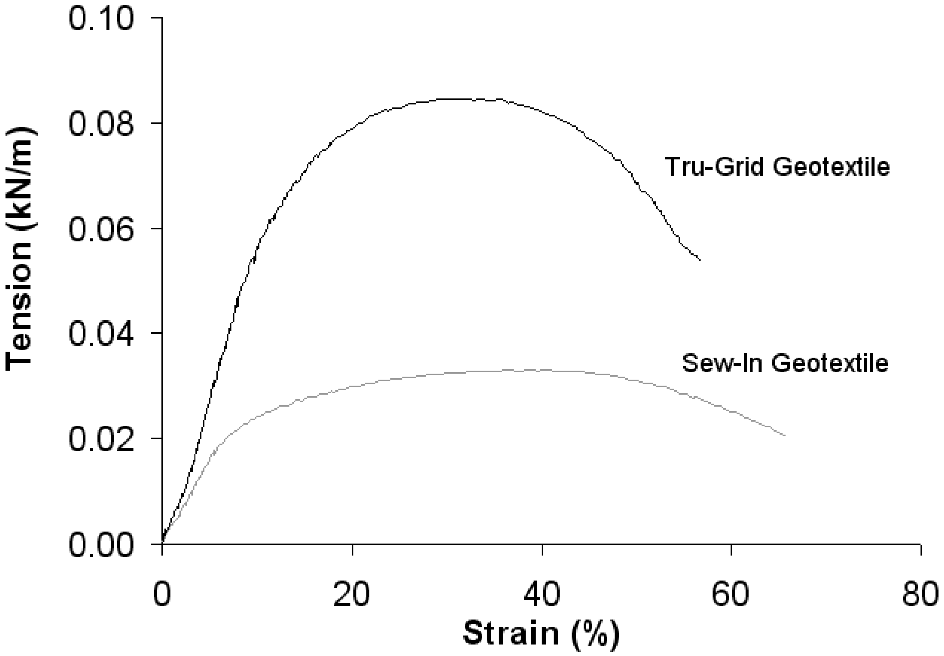

Figure 6.6: Average wide-width results for the geotextile reinforcements (Arriaga 2003)

Accordingly, in order to evaluate the confined tensile strength of the geotextiles used as the reinforcement in the centrifuge tests, Arriaga (2003) and Zornberg et al. (1998) performed a series of limit equilibrium analysis to backcalculate the confined tensile strength value for each mode at failure. A uniform distribution of reinforcement forces with depth was assumed in the limit equilibrium analysis. Different from the limit equilibrium analysis used in conventional design, no reduction factors due to installation damage, creep and degradation were considered (all reduction factors were 1.0). This is because the construction of centrifuge model was carefully handled with a sure warrant of no installation damage and the test duration was relatively short without any long-term behavior like creep and degradation observed. The ultimate confined tensile strength was determined when the g-level corresponding to calculated $FS=1$ in limit equilibrium analysis equals the failure g-level observed in each centrifuge test. Consequently, the backcalculated tensile strength should correspond to the average reinforcement tension at the moment of failure.

Figure 6.7 contains the results of confined reinforcement tensile strength from uniformly reinforced slopes only. The results indicate that the confined tensile strength of Pellon Sew-In and Pellon Tru-Grid can be characterized by a constant average value. Based on these results, the average constant confined tensile strength of Pellon Sew-In and Pellon Tru-Grid adopted for this study are 0.124 kN/m and 0.281 kN/m, respectively. The improvement of the strength properties of nonwoven geotextiles under soil confinement is approximately 4 times higher for Pellon Sew-In and approximately 3 times higher for Pellon Tru-Grid.

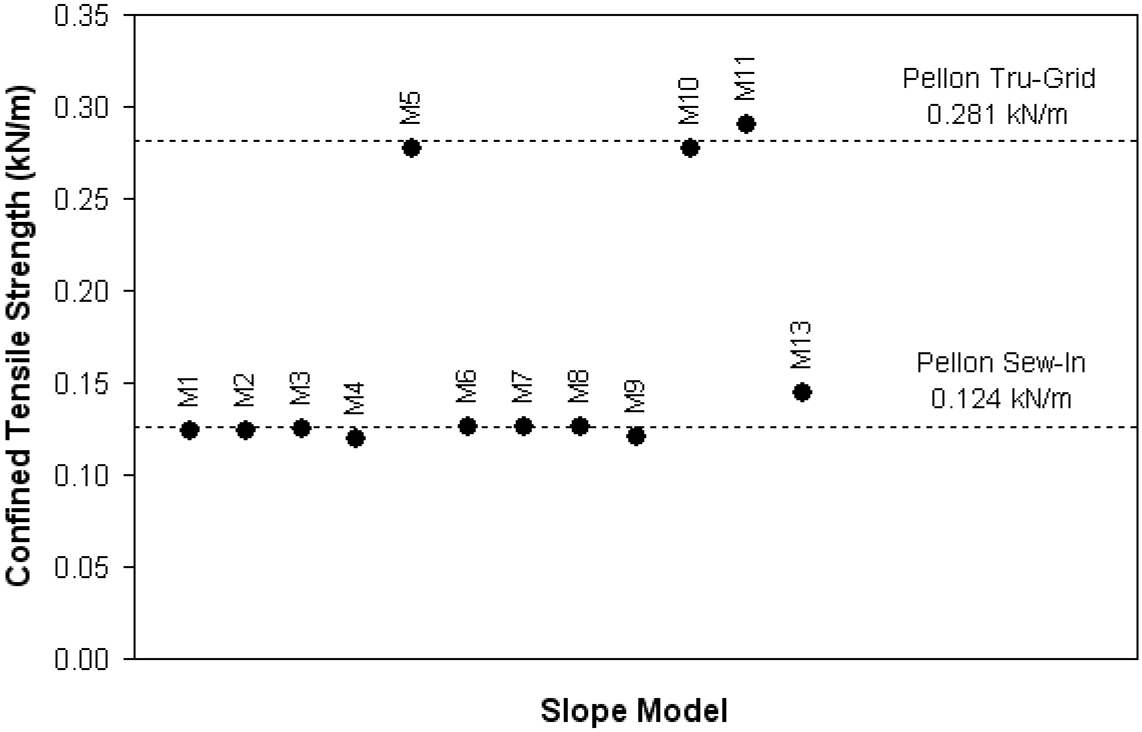

Figure 6.7: Constant backcalculated values of the reinforcement confined tensile strength for uniformly reinforced slopes (Arriaga 2003)

6.1.4 Centrifuge Test and Instrumentation

In the centrifuge tests, all models were subjected to a gradually increasing centrifugal acceleration until failure occurred and the failure g-level N_g was recorded. The failure was determined by a sudden increase in settlement, as measured by an LVDT located at the top of the slope (at a distance of 38mm away from the crest). Acceleration levels were increased by 5 g increments during the initial stages of the test and by lower g increments towards the final stages of the test. In each g increment, acceleration was increased over a period of 100 seconds and held constant for another 200 seconds to allow equalization of the load. The total duration is approximately 300 seconds(=5 minutes) for each g-level increment.

Because of the small scale tests, the force-related data in centrifuge tests can not be obtained due to the difficulty and possible disturbances from internal instrumentation. Instead, the centrifuge model cross section visible through the Plexiglas wall was marked with colored sand and a digital image acquisition system was used to obtain the displacement-related data (see Fig. 6.1b). As the model deformed, the black colored sand markers moved with the adjacent soil. Images acquired by high-speed digital cameras were used to record the deformations within the slope at the end of each acceleration interval. Accordingly, displacements within the reinforcement layers can be obtained by processing the image recorded from high-speed digital cameras.

After completion of the tests, the backfill material was vacuumed and the geotextile reinforcements were recovered. The retrieved geotextile layers were used to evaluate the breakage pattern and to locate the critical failure surface which can be determined by the location of the observed reinforcement tears relative to the slope face.

The data monitored from centrifuge tests suitable for the comparison against the results from finite element modeling are summarized in Table 6.2. Figure 6.8 shows a series of in-fly snapshots of slope model M1. The measured g-level, calculated *FS* (from limit equilibrium analysis discussed in next section), and corresponded soil stress state are indicated in Fig. 6.8.

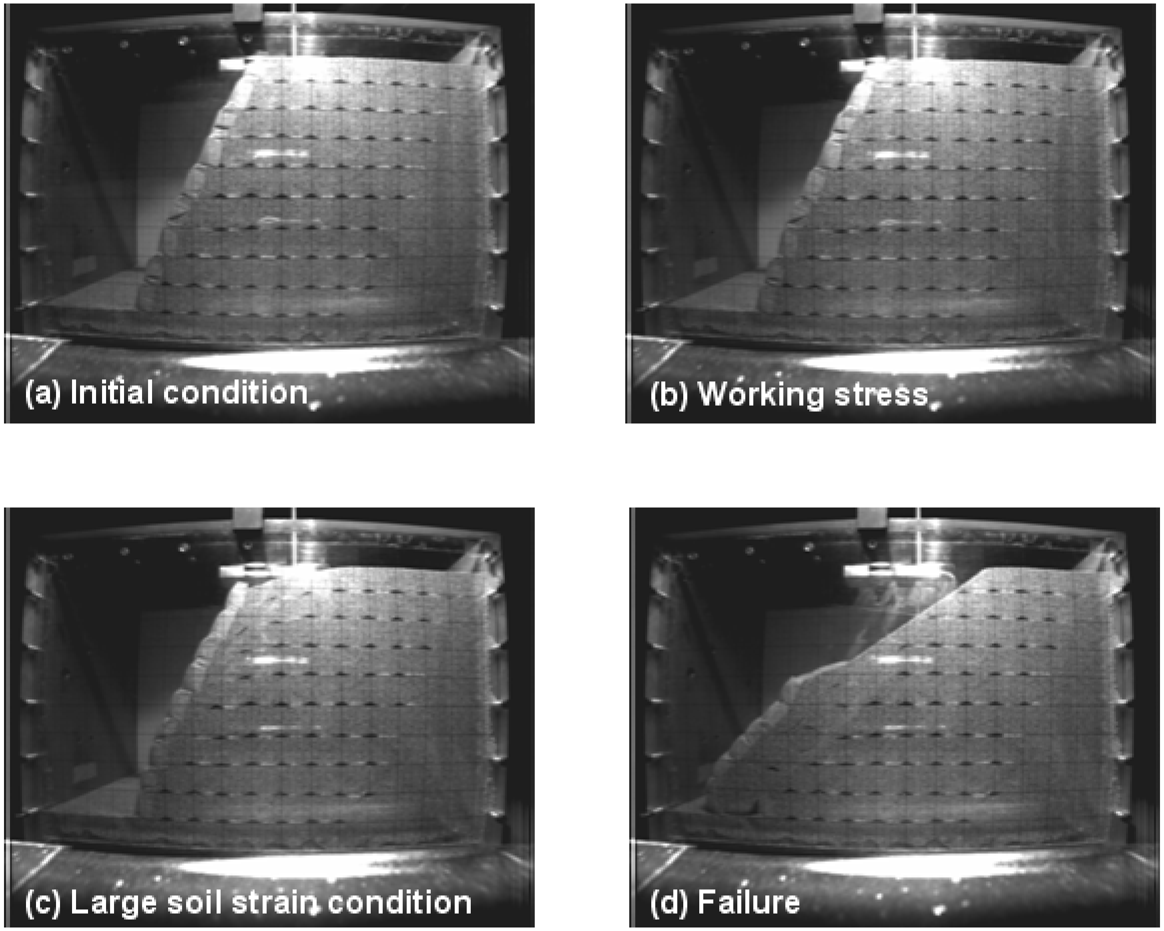

Figure 6.8: Photos from centrifuge slope model M1: (a) initial (1g); (b) working stress (10g, *FS*=2.0); (c) large soil strain conditions (40g, *FS*=1.1); (d) failure (50g, *FS*=1.0)

Table 6.2: Data from centrifuge tests for finite element comparison

Data	**Obtained from**
Failure g-level	LVDT
Deformation pattern	High-speed digital camera
Location of failure surface	1. Observed tears in each layer of reinforcements 2. Determined by limit equilibrium analysis
Settlement vs. g-level	LVDT
Displacements along reinforcements	High-speed digital camera and image processing technique

6.1.5 Factor of Safety vs. G-Level

A series of limit equilibrium analyses were conducted by Arriaga (2003) to examine the failure mechanism observed from the centrifuge tests (i.e., determine the location of failure surface and the ultimate confined tensile strength of reinforcements). Most importantly, the factor of safety *FS* calculated from limit equilibrium analysis was evaluated for increasing centrifugal g-levels.

Limit equilibrium calculations were performed using Spencer's method (Spencer 1967) as coded in the computer program UTEXAS3 (Wright, 1990). This method satisfies all conditions of equilibrium (i.e., horizontal, vertical forces and moment) and assumes that the interslice forces are all parallel. Circular critical surfaces were used during limit equilibrium calculations. The plane strain friction angle of backfill was used to characterize the shear strength of Monterey No. 30 sand. Experimental results showed that the overlap reinforcement layers increased the stability of the centrifuge models. Consequently, the contribution of the geotextile overlap layers to the stability of the models was incorporated in the limit equilibrium analyses. The reinforcement forces were assumed to act in directions horizontal to the potential failure surface. The values used to characterize the tensile strength of the geotextiles used as reinforcements were backcalculated for each mode at failure, as discussed in Section 6.1.3.2. A uniform distribution of reinforcement forces with depth was assumed in the limit equilibrium analysis. The effect of side friction along the model boundary Plexiglas (walls) was not taken into account in the limit equilibrium analyses due to experimental evidences that indicated these effects are negligible. Specifically, the breakage pattern of the geotextile reinforcements was perpendicular to the direction of loading and showed no curvature towards the sides of the sample box. The centrifugal force was simulated by increasing the unit weight of backfill by *N* times corresponding to the target g-level; for example, the unit weight for the modeling of centrifugal force at 45g was computed as 723.6 kN/m^3 (=16.08x45).

It should be noted that the calculated *FS* does not account for reduction factors on the ultimate tensile strength of the reinforcements. An allowable unconfined tensile strength of reinforcements by considering several reduction factors due to installation damage, creep and degradation is recommend in conventional design. However, an ultimate confined tensile strength of reinforcements without the consideration of all reduction factors was used to estimate the *FS* of centrifuge model under increasing g-level. As discussed previously, this is because the construction of centrifuge model was carefully handled with a sure warrant of no installation damage and the test duration was relatively short without any long-term behavior like creep and degradation observed.

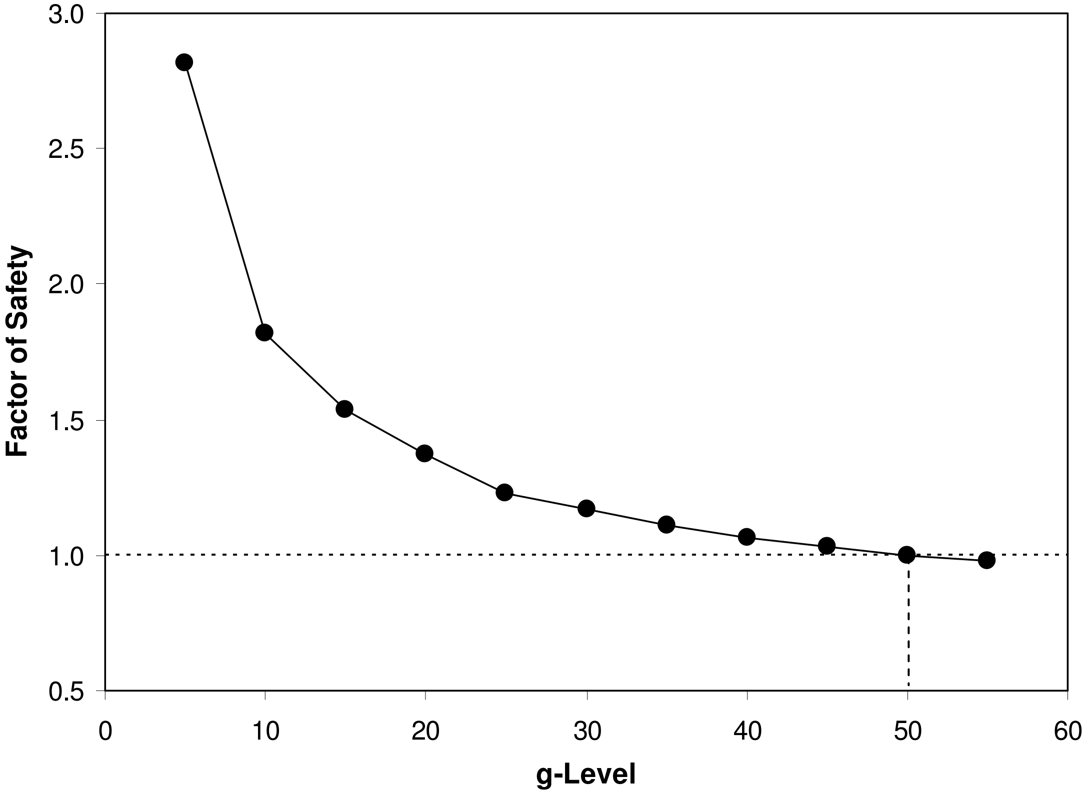

Figure 6.9: Calculated factor of safety vs. g-level for model M1 (Arriaga 2003)

Figure 6.9 shows a typical example of calculated *FS* for model M1 subject to the increase of g-level (Arriaga 2003). Figure 6.9 shows the decrease of *FS* with the increase of g-level which indicates the stability of slope model decreases with the increase of g-level. The failure of slope model M1 at g-level of 50g is indicated as *FS*=1 in the limit equilibrium analysis.

6.2 FINITE ELEMENT MODEL

A finite element model was established to simulate centrifuge slope model M1. The simulation was conducted on the finite element program ANLOG, as discussed previously in Chapter 3. The initial layout and settings of finite element model are shown in Fig. 6.10 and explicated as follows.

6.2.1 Initial Settings

6.2.1.1 Mesh Configurations

The finite element simulation was constructed using the geometry and layout of centrifuge slope model M1. An 8-node quadratic quadrilateral solid element (Q8) under plane strain conditions was designated for backfill and foundation. A total four Gauss points were assigned for each solid element. A 3-node quadratic truss element (B3) was selected for reinforcement. A total two Gauss point were assigned for each truss element.

The solid elements were arranged in such a way that more elements were concentrated in the front position of slope. This side of slope contains the failure surface along which the development of stresses and strains in the soils and reinforcements is of the most interest in this study. The height of solid elements was carefully selected so the truss elements can be properly placed into the location according to the reinforcement layouts of slope model M1. Because the geotextile was folded backward to form wrap-around facing and a secondary layer (overlap) of 50 mm long in centrifuge model. The secondary reinforcements were also included in the numerical model as indicated in Fig.6.10. The finite element model consists of 623 nodal points, 188 solid elements and 114 reinforcement elements (302 elements in total).

A sensitivity study of various mesh sizes was performed as shown in Fig. 6.11. The model with large mesh size totally has 176 elements (Fig. 6.11a) and the model with fine mesh size has 772 elements (Fig. 6.11b)

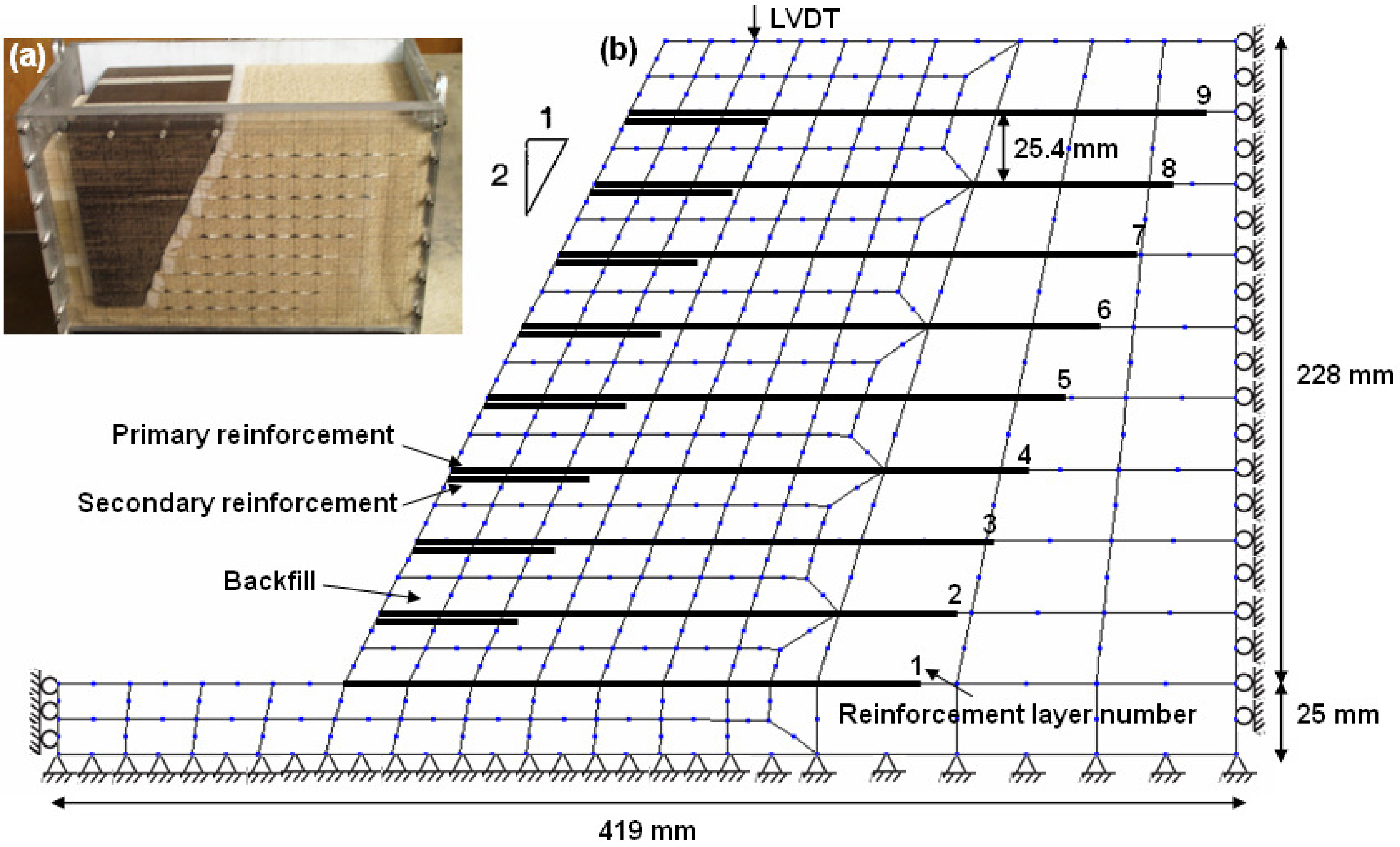

Figure 6.10: Initial Setting: (a) centrifuge model; (b) finite element model

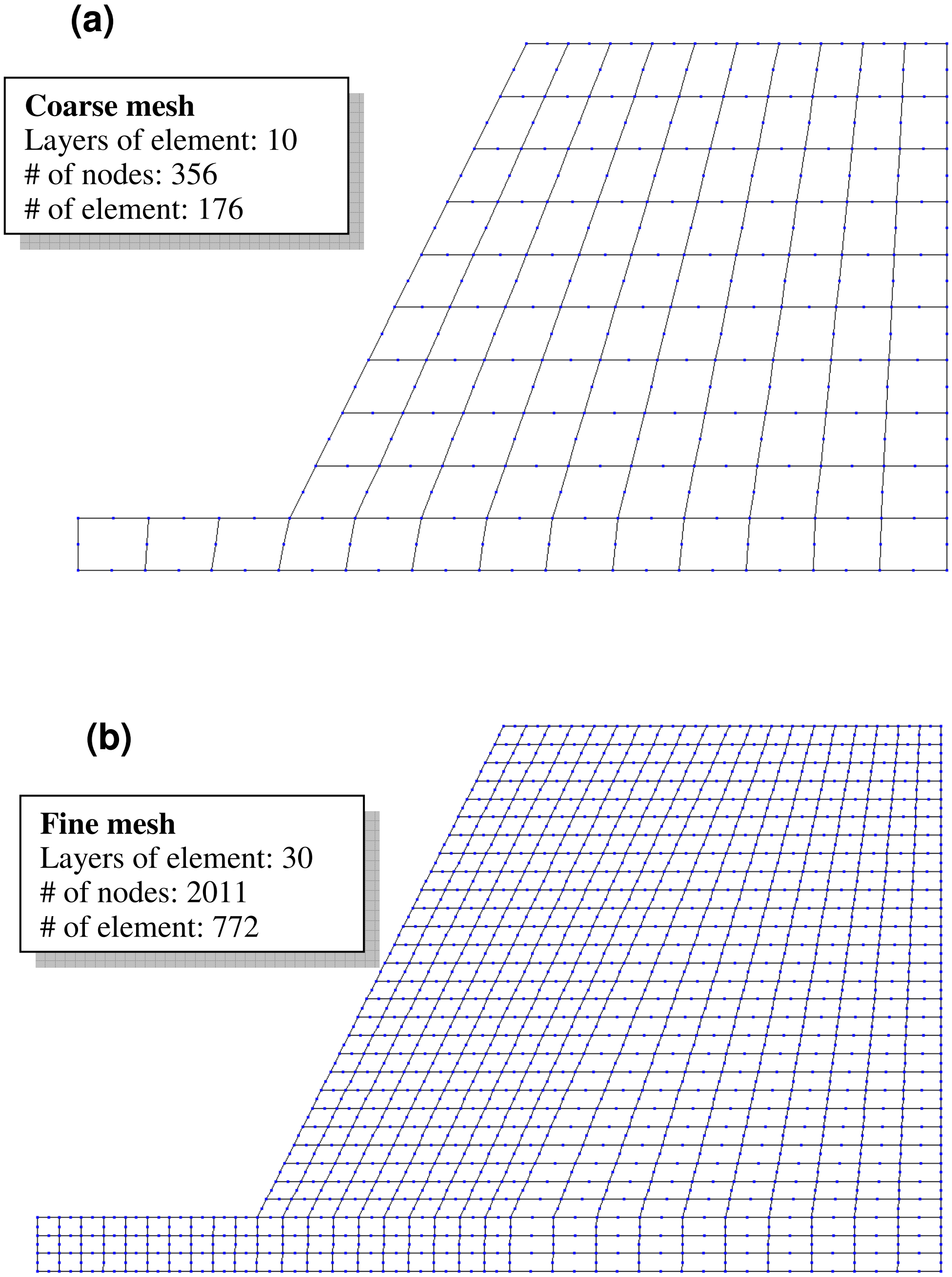

Coarse mesh
Layers of element: 10
# of nodes: 356
# of element: 176

Fine mesh
Layers of element: 30
# of nodes: 2011
# of element: 772

Figure 6.11: Sensitivity study of mesh size: (a) coarse mesh; (b) fine mesh

The preliminary results indicated that the predicted maximum total displacement was increased only 5% by using fine mesh size. The increase of displacement can be probably explained by the increase of degree of freedom in the system, which would decrease the system stiffness. However, the pre-processing effort (manually create reinforcement elements) and computation cost (time and size of output files) were significantly increased approximately in proportion to the ratio of number of nodes between different mesh configurations. As a result, the model configuration shown in Fig. 6.10 was selected to concurrently optimize accuracy, preprocessing effort and computation speed.

6.2.1.2 Boundary Conditions

In the centrifuge test, the slope model was contained within an aluminum centrifuge box. The remaining walls of the box were aluminum plates lined with Teflon to minimize side friction. To simulate the boundary conditions of the physical model, standard boundary conditions were imposed to simulate the effect of confinement from aluminum boxes.

A horizontal fixity was added to the numerical nodal points of the solid elements along both lateral ends of the slope model. Vertical movement was allowed for those nodal points. Because of the side friction in centrifuge slope model was minimized by applying layers of Teflon along the side walls, the effect of interface friction between soil and wall was not considered in the simulation.

A total fixity (fixed boundary conditions in the both vertical and horizontal directions) was added to the nodal points of elements at the base of foundation. The sensitivity analysis indicated that the horizontal fixity on solid elements at the base of foundation had negligible effect on the predicted slope response. This is probably due to the constraint of horizontal movement at two lateral ends of the slope model. However, computation time was slightly shorter when horizontal degrees of freedom on the backfill bottom boundary were fixed, and hence this boundary condition (i.e., total fixity) was applied for the base of foundation in the simulation.

6.2.2 Material Constitutive Model

6.2.2.1 Backfill and Foundation Soils

The Lade-Kim soil constitutive model and the new softening model proposed in Section 4 were implemented into ANLOG and used to represent the behavior of soil particularly under large soil strain conditions in this simulation. The model parameters for the Monterey No. 30 sand, calibrated using triaxial tests were summarized in Table 4.3.

In order to take into account the plane strain conditions in the centrifuge tests, as discussed previously in Section 6.1.2.3, the friction angle under triaxial compression conditions ϕ_{tc} is multiplied by a strength increase ratio of 1.15. Instead of using friction angle as a shear strength property, the Lade-Kim model defines material shear strength by the failure criterion parameter η_1. The strength increase ratio for η_1 at relative density of 70% can be calculated as:

$$\frac{\eta_{1,ps}}{\eta_{1,tc}} = \frac{\tan(\phi_{ps})}{\tan(\phi_{tc})} = \frac{\tan(42^{o})}{\tan(36.4^{o})} \approx 1.22 \qquad (6.1)$$

where subscripts ps and tc indicate the plane strain and triaxial compression conditions, respectively. This strength increase ratio was applied for both backfill and foundation. As a result, the failure criterion parameter η_1 under plane strain conditions was modified as 29.3 (=24x1.22).

Marachi et al. (1981) reported that for the same minor principal stress value, the initial plane-strain response was stiffer than the response for the same material under triaxial test conditions. The stiffer behavior under plane-strain conditions is due to the intermediate principal stress being larger than the minor principal stress ($\sigma_2 > \sigma_3$). In addition, by inspection of the data from triaxial compression and plane strain tests, Hatami and Bathurst (2005) reported the ratio of initial elastic modulus of Royal Military College (RMC) sand from plane strain test results to triaxial compression test results is about 2.25. However, this ratio is only valid for $\sigma_3 \leq 30\ \text{kPa}$. For $\sigma_3 \geq 30\ \text{kPa}$, the difference of initial elastic modulus between two conditions is small. The ratio of initial elastic modulus from plane strain test results to triaxial compression test results was close to 1.0. Due to the previous reason and because of lack of actual data of testing Monterey No. 30 sand under plane strain conditions, the effect of stiffer initial elastic modulus due to plane strain conditions was not considered in the simulation.

In addition, a small cohesion of 1 kPa was used in the backfill elements along slope face not only to simulate the confinement of soil from wrap-around facing but also to improve the numerical stability (e.g., prevent premature soil yielding locally in the area of low confinement). A cohesion of 10 kPa was used in the foundation elements to simulate the firm foundation as described by Arriaga (2003). In Lade-Kim model, the tensile strength $a' p_a$ can be approximately used to represent the cohesion, where a' is one of the failure criterion parameters and p_a is the atmosphere pressure. As a result, a' was adopted as 0.01 for the backfill along the slope face and 0.1 for the foundation.

The values of softening model parameters correlated with confining pressure were obtained by linear regression as shown in Fig. 6.12. Table 6.3 compares the soil model parameters obtained form triaxial compression conditions and plane strain conditions used in this simulation.

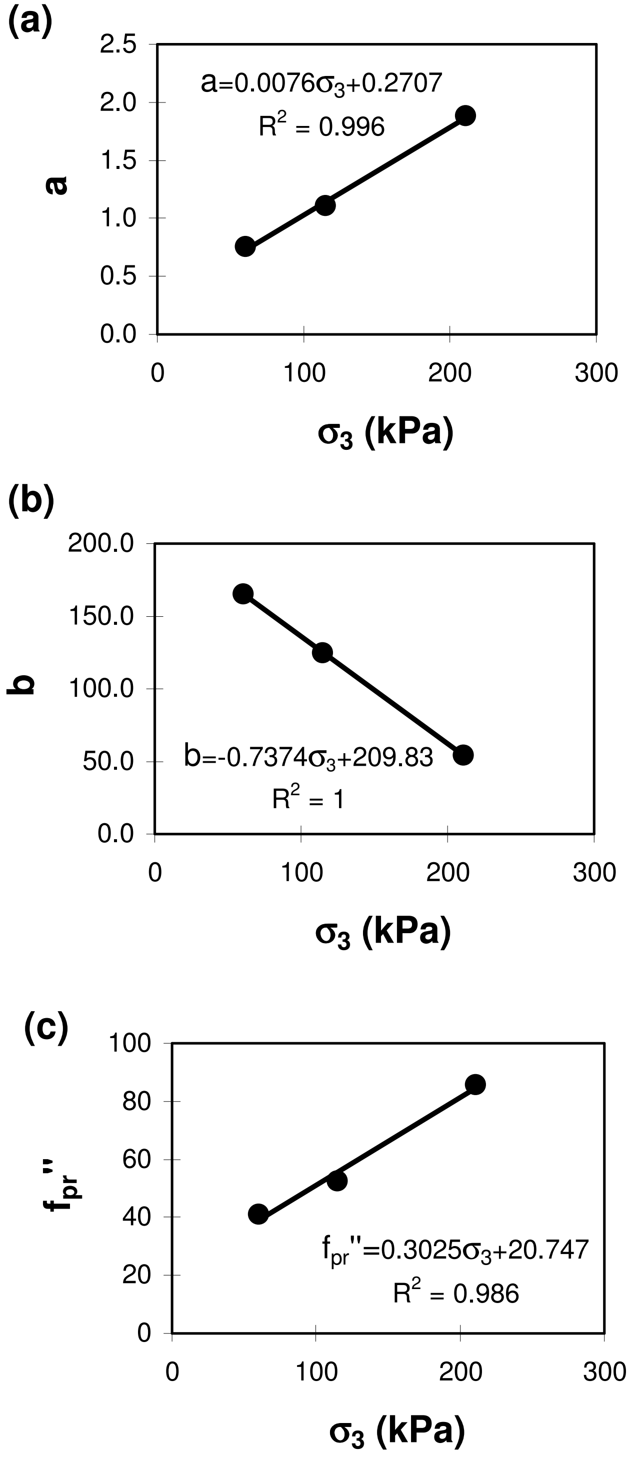

Figure 6.12: Linear regression of softening model parameters with confining pressures: softening parameter (a) a; (b) b; (c) f_{pr}''

Table 6.3: Summary of material properties for backfill and foundation soils

		Boundary Condition	
Model component	**Parameter**	**Triaxial compression**	**Plane strain in this simulation**
Unit weight	γ	16.08 kN/m^3	16.08 kN/m^3
Elastic model	M, λ, ν	705, 0.257, 0.35	705, 0.257, 0.35
Failure criterion	m, η_1, a'	0.0214, 24, 0	Backfill: 0.0214, 29.3*, 0 Slope face: 0.0214, 29.3*, 0.01* Foundation: 0.0214, 29.3*, 0.1*
Plastic potential	ψ_2, μ	-8.51, 2.2	-8.51, 2.2
Yield criterion	h, α	0.67, 0.2	0.67, 0.2
Hardening law	C, p	5.07E-05, 1.9	5.07E-05, 1.9
Softening law		Linear regression (slope and interception)	
	a	0.0076, 0.2707	0.0076, 0.2707
	b	-0.737, 209.8	-0.737, 209.8
	f''_{pr}	0.302, 20.74	0.302, 20.74

* Parameter value is adjusted according to the condition of centrifuge model

6.2.2.2 Reinforcement

Reinforcements were simulated using truss elements with only one degree of freedom per node in the longitudinal direction. A nonlinearly elastic model proposed by Karpurapu and Bathurst (1995) was implemented and applied to represent the nonlinear behavior of reinforcements under large deformations. The reinforcement model is a second order polynomial function. The governing equation and incremental form are:

$$T(\varepsilon) = C_1\varepsilon + C_2\varepsilon^2 \tag{6.2}$$

and

$$\frac{dT(\varepsilon)}{d\varepsilon} = C_1 + 2C_2\varepsilon \tag{6.3}$$

where T is the reinforcement tension and ε is the corresponded tensile strain. Parameters C_1 and C_2 are the initial stiffness and stiffness reduction coefficient, respectively. Equation (6.3) is the incremental form for implementation which also indicates the reinforcement tangential stiffness. Because the geosynthetic reinforcements can not resist compressions, this can be simulated by assigning a negligible value of stiffness in the direction of compression. Therefore, when compressive strains are developed in the reinforcements, the reinforcement compressive forces will be very small.

It is well known that the load-extension behavior of geotextile is affected by the strain rate. The strain rate of wide-width tensile test discussed in Section 6.1.3.1 is of 10% per minute. For the centrifuge test, the final failure of centrifuge model is due to breakage of geotextile at approximate 40% of strain (Fig. 6.5). The test duration of the slope mode M1 is of approximately 2700 sec. The strain rate is of approximate 1% (=40%/2700secondsx60minute/second) during the centrifuge test. The tensile strength of reinforcements is expected to be varied due to different strain rates. Although this difference can not be directly included by using the data with the strain rate corresponding to that in the centrifuge test, the impact of different strain rates on tensile strength difference could still be included in a procedure of backcalculating the confined tensile strength discussed in the following paragraph. In addition, the current analysis also does not include time-dependent behavior of geotextile because of the short test duration (5 minutes).

As discussed in Section 6.1.3.2, the confined tensile strength of nonwoven geotextiles differs from the unconfined tensile strength. Arriaga (2003) reported that the ultimate confined tensile strength of Pellon Sew-In geotextile is approximately 4 times higher than unconfined tensile strength. Besides the increase in tensile strength, the effect of soil confinement on the load-extension response of nonwoven geotextile also has been reported to lead to an increase in stiffness. However, the strain levels are not significant affected by the soil confinement (e.g., Leschinsky and Field 1987, Wu 1991, Ling et al. 1992, Ballegeer and Wu 1993). Specifically, approximately the same value of strain at failure is reached regardless of the level of confinement. In addition, the experimental results presented by Leshchinsky and Field (1987), Wu (1991), Ling et al. (1992), and Ballegeer and Wu (1993) indicate that it is adequate to assume the load-extension response of a nonwoven geotextile under soil confinement to follow a similar trend as that for the unconfined conditions.

Summarizing the discussion above, the load-extension response of nonwoven geotextile under confinement is obtained using following equation and shown in Fig. 6.13

$$T_{confined} = T_{unconfined} \times \frac{T_{ult\_confined}}{T_{ult\_unconfined}} \tag{6.4}$$

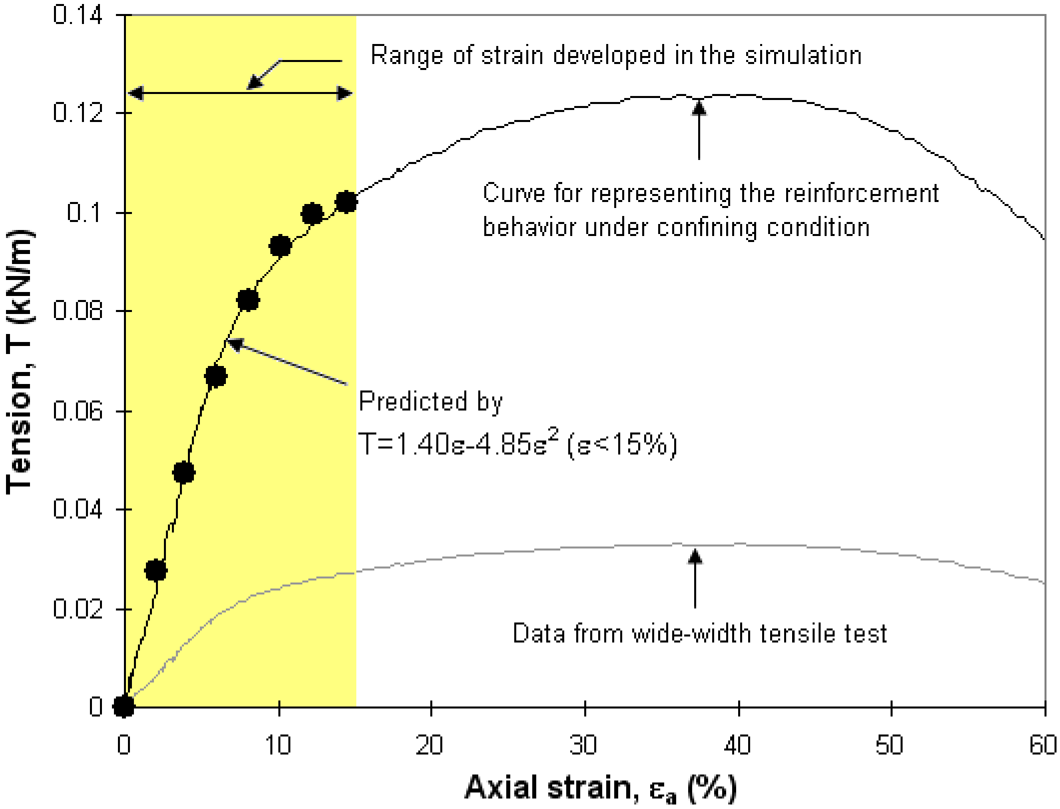

Figure 6.13: Unconfined and confined reinforcement tensile strengths and prediction results

where $T_{confined}$ is the confined tensile stress at any reinforcement strain; $T_{unconfined}$ is the unconfined tensile stress which can be obtained from conventional wide-width tensile test; $T_{ult\_confined}$ is the ultimate confined tensile strength of geotextile backcalculated from limit equilibrium analysis. $T_{ult\_confined}$ is 0.124 kN/m for Pellon Sew-In; $T_{ult\_unconfined}$ is the ultimate unconfined tensile strength of geotextile. $T_{ult\_unconfined}$ is 0.03 kN/m for Pellon Sew-In. Figure 6.13 also shows the calibration of reinforcement model parameters. Reinforcement parameters C_1=1.4 and C_2= -4.85 were obtained and used in further finite element analyses.

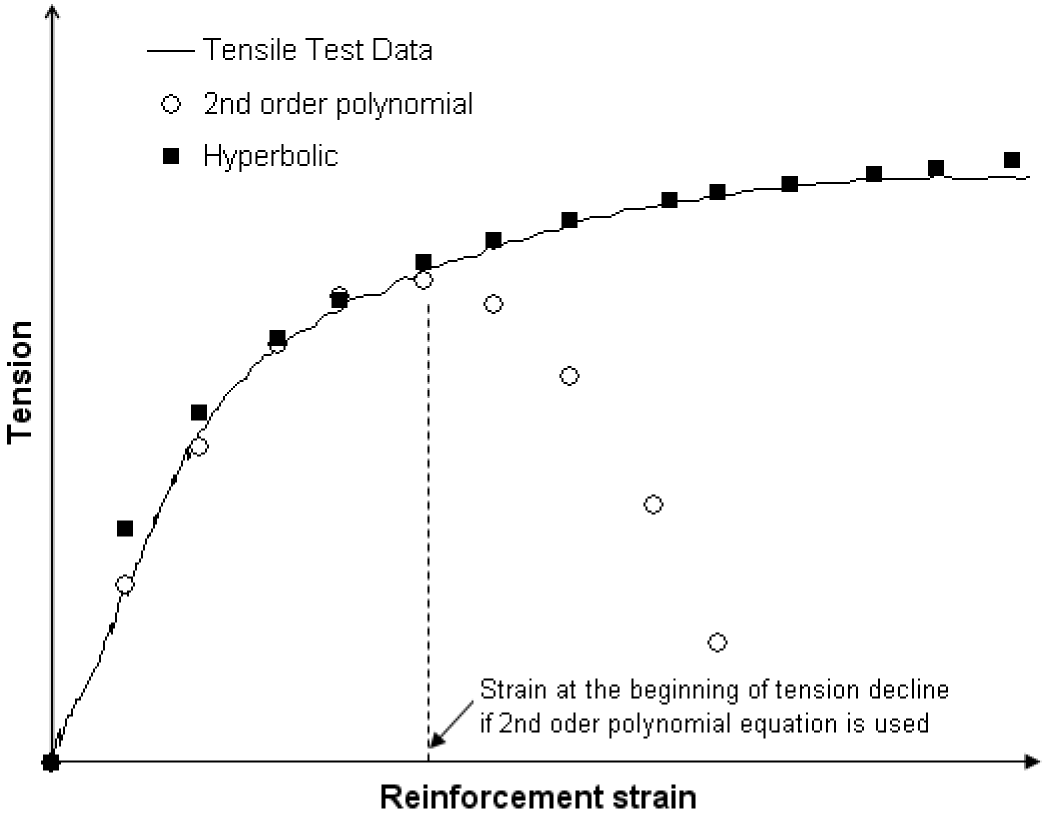

Figure 6.14: Illustration of the effect of 2^{nd} order polynomial function and hyperbolic function on predicting reinforcement load-extension response

Last but not least, although 2^{nd} order polynomial equation can predict the nonlinear behavior of reinforcements successfully, due to the parabolic nature of Eq (6.2), the predicted tension tends to decline when the predicted strain crosses the apex of parabola, as shown in Fig. 6.14. If the developed strain along reinforcements in the simulation is less than the strain according to the apex of parabola, Eq (6.2) is satisfactory; otherwise, a higher order equation should be considered. A hyperbolic function proposed by Ling et al. (2001) is recommended to better describe the reinforcement behavior at large strain conditions.

The governing equation and incremental form of hyperbolic model are:

$$T(\varepsilon) = \frac{\varepsilon}{\dfrac{1}{E_i} + \dfrac{R_f.\varepsilon}{T_{ult}}} \tag{6.5}$$

and

$$\frac{dT(\varepsilon)}{d\varepsilon} = E_i(1 - \frac{R_f T}{T_{ult}})^2 \tag{6.6}$$

where parameter E_i is the initial stiffness; T_{ult} is the ultimate tensile strength of reinforcements; R_f is the failure ratio, the ratio of the ultimate tensile strength of reinforcements to the predicted tensile strength of reinforcements at asymptote of hyperbolic curve. Parameters E_i and T_{ult} can be calibrated to the load-extension curve of reinforcements. Parameter R_f needs to be determined by best fitting the prediction curve to the measured load-extension curve.

6.2.2.3 Soil and Reinforcement Interaction

In ANLOG, the interaction and relative movement between the reinforcement layer and the backfill can be modeled using the 6-noded joint element of zero thickness. Figure 6.15 shows the arrangement of solid, truss and interface elements.

A sensitivity study was conducted to investigate the effect of using interface elements on the predicted slope response. The shear strength and stiffness behavior of interfaces can be modeled using elasoplastic constitutive model, linearly elastic in the direction normal to the interface and non associative, without hardening and elastic perfectly plastic in the direction tangential to the interface.

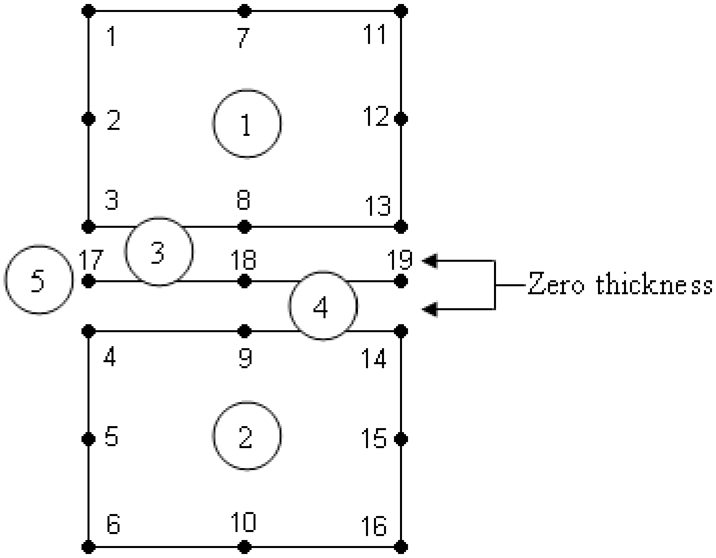

Element	Type	Material	Nodes
1	Quadrilateral Q8	Backfill/Foundation	1-2-3-8-13-12-11-7
2	Quadrilateral Q8	Backfill/Foundation	4-5-6-10-16-15-14-9
3	Joint J6	Interface	13-3-17-19-8-18
4	Joint J6	Interface	19-17-4-14-18-9
5	Truss B3	Reinforcement	17-18-19

Figure 6.15: Detail of finite element arrangement

The interface slip strength is defined by the Mohr-Coulomb criterion. The stiffness parameters include shear stiffness K_s in the direction tangential to the interface and the normal stiffness K_n in the direction normal to the interface The shear strength parameters include friction angle ϕ, cohesion c and dilatancy angle ψ.

The parameters of interface model were determined from the direct shear tests by Zornberg (1994). Zornberg (1994) performed a series of direct shear tests to evaluate the interface friction between Monterey No.30 sand and two nonwoven geotextiles (Pellon Sew-In and Pellon Tru-Grid). The direct shear test results are shown in Fig 6.16.

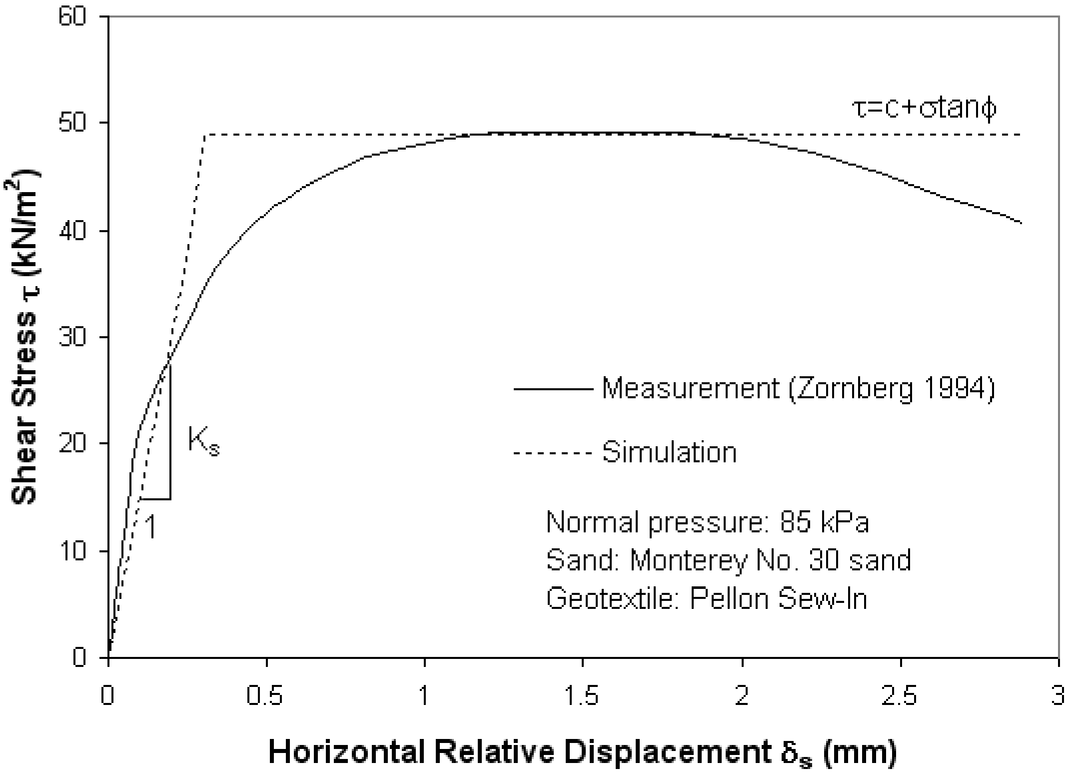

Figure 6.16: Comparison of direct shear test and calibration result

Table 6.4: Summary of properties for interface elements

Properties	**Parameters**	**Sand/Geotextile Interface**
Stiffness		
Secant normal stiffness	K_n	10^{10} (kN/m^3)
Secant shear stiffness	K_s	1.5×10^5 (kN/m^3)
Strength		
Friction angle	ϕ	31°
Cohesion	c	0
Dilatancy Angle	ψ	0

Also, Zornberg (1994) reported that no significant post-peak softening behavior was observed in the tests. This indicates that even though the selected interface model is incapable of simulating the softening behavior in the interface, it can still represent well the overall interaction behavior between sand and geotextile. The calibration result is plotted in Fig 6.16. The value of shear stiffness K_s is determined as the slope of a secant line at approximate 50% of interface shear strength.

The value of normal stiffness K_n have to be calibrated to the relationships between normal stress and vertical relative displacement. However, these relationships are often not available through the direct shear test and also not reported by Zornberg (1994). Therefore, the normal stiffness K_n was assumed a large value. The large value of K_n prevents the relative movement between backfill and reinforcement in the vertical direction and avoids the intrusion of the adjacent elements (a numerical effect, also recognized as the problem of interlocking).

The interface shear strength properties were calibrated to the peak strength obtained from the direct shear tests. Although the dilatancy angle can be evaluated approximately proportional to the difference between peak and residual friction angle, the effect of dilatancy was not considered in this sensitivity study because the post-peak softening behavior was not significant in the interface between backfill and Pellon Sew-In geotextile. A summary of interface properties used in the sensitivity study is listed in Table 6.4.

Sensitivity study indicated that the finite element model with interface element only increase the displacement of slope slightly. This is likely because the use of interface elements incorporates additional degrees of freedom in the finite element analysis. By inspecting the calculated shear forces on interface elements, it was found the developed shear forces were small compared to the normal stresses. The range of developed shear forces was below 10kPa. With this value of shear forces, the corresponded relative shear displacements approximately did not exceed 0.1 mm (see Fig. 6.16). This fact may be explained by the orientation of principle planes. The main source of loading in this simulation comes from the downward centrifugal force. With this loading condition, the major and minor principle planes, the plane without shear stresses, are close to horizontal and vertical planes and will not change the orientation of planes too much during loading. Therefore, the shear stresses on horizontal plane (also the direction of interface) are expected to be less.

In addition, for the final adopted mesh, 522 additional nodes would have been required if interface elements were used, representing an 85% increase on the number of degrees of freedom. Accordingly, the pre-processing effort (manually create interface elements) and computation cost (time and size of output files) would have been significantly increased. Also, by author's own experience, careless mistakes have been frequently committed during manual pre-process and they were difficult to detect from the input text file.

The simulation without interface elements can be justified by the physical mechanics of pullout. Without the interface elements, the nodes of the truss elements are rigidly attached to the nodal points of the backfill mesh. This approach means that no relative displacement is allowed in the numerical model. Consequently, this prevents the pullout of the reinforcement from the backfill in the simulation. The approach used in the numerical modeling was supported by visual reconnaissance after slope collapse. The failure of reinforcement specimens was due to breakage rather than pullout.

Based on discussion above, and since the sensitivity study showed that the use of interface elements had only a minor influence on the results, final analysis was performed without interface elements.

6.2.3 Issues Related to Model Construction

6.2.3.1 Incremental Sequence of Construction

Stage construction was included into the modeling procedure to simulate the sequential bottom-up placement of the backfill and reinforcement layers during slope model construction. First, solid and reinforcement elements were activated as the height of each reinforcement elevation was reached. A small isotropic initial stress (0.01 atm) was applied to initialize the plastic variables in the selected soil constitutive model. Then, the numerical models were solved to equilibrium, with a prescribed tolerance of convergence, before the activation of next cycle of solid and reinforcement elements. The analysis was conducted in a total of 10 steps to simulate slope construction.

However, the preliminary study showed the stage construction could be ignored because the development of soil stresses during construction phase was negligible compared to those during loading phase. Further, all the data from centrifuge tests were monitored when centrifuge started to spin rather than the beginning of model construction. Accordingly, any deformation developed during model construction was not recorded.

6.2.3.2 Backfill Compaction

The effect of soil compaction from the field or large-scaled retaining structure tests is commonly simulated by applying a uniform vertical stress to the entire surface of each new soil layer before solving the model to equilibrium (Gotteland et al. 1997, Hatami and Bathurst 2005). Hatami and Bathurst (2005) recommended applying an 8kPa surcharge pressure during the numerical placement of the lift and then removed prior to the simulation of the next lift. The 8kPa vertical stress increment resulted in satisfactory agreement between predicted and measured wall responses for all of the test walls investigated.

However, during the construction of slope model, the density of backfill was controlled by pluviation rather than compaction. In addition, the effect of backfill density due to pluviation was already included in the selected soil constitutive model as presented earlier. Therefore, the effect of compaction was not included in this simulation.

6.2.4 Issues Related to Computation

6.2.4.1 Centrifugal Force

The centrifugal force within slope models was simulated by the increase of body force. The equation of body force has been derived in Chapter 3 and shown in Eq. (3.26). Similar to Eq. (3.26), the equation of centrifugal force is:

$$F_b^e = N_g \times \int_{Ve} N^T b^e dV_e \tag{6.7}$$

where $F_b{}^e$ is the centrifugal force at each solid element; N_g is the corresponded g-level in the centrifuge test; N is the shape function matrix , V is the volume of each solid element; b is the body force vector

$$b = \begin{Bmatrix} b_x \\ b_y \end{Bmatrix} = \begin{Bmatrix} \gamma \sin\theta \\ -\gamma \cos\theta \end{Bmatrix} \tag{6.8}$$

where γ is the unit weight of backfill; θ is the angle between the direction of -y and the direction of centrifugal force. Since the direction of centrifuge force corresponds to the direction of negative y axis in this simulation, $\theta=0$, $b_x=0$ and $b_y=-\gamma$.

Each loading stage included 5g increment and then, the numerical models were solved to reach equilibrium within a prescribed tolerance of convergence. A total of 10 loading stages was applied. The target g-level of this simulation was to reach 50g, corresponding to the failure g-level of slope model M1.

6.2.4.2 Updated Mesh

Large deformation effects are accounted for in numerical simulations by updating the FE mesh. The mesh can be updated by adding the corresponding displacement increments of nodes at every load step to the coordinates of nodes at previous load step.

$$X_{i+1} = X_i + \Delta\hat{u} \tag{6.9}$$

where X_{i+1} is the updated coordinate vector of nodes; X_i is the current coordinate vector; $\Delta\hat{u}$ is the nodal displacement increment vector due to current load increment; i is the number of load increments.

6.2.4.3 Tolerance in Stress Integration Scheme

The modified forward Euler scheme with error control was implemented and adopted to integrate stresses at each strain subincrement. Different from forward Euler scheme commonly used in the finite element analysis, the size of each strain subincrement in the modified forward Euler scheme is determined so that the new stress state fulfils the specified tolerance and only the absolutely necessary number of strain subdivision are applied, as discussed previously in Chapter 5.

When the tolerance of modified forward Euler scheme was set as 10^{-3} in the example demonstrated in Section 5.4, the maximum error E_{max} of calculated stresses is 10^{-3} and the average error E_{avg} is approximately $5x10^{-4}$. In centrifuge test, a maximum stress of 200 kPa is expected to occur as the vertical stress at base of foundation when g-level reaches 50g. Therefore, for the range of stresses in the simulation, the maximum error of calculated stresses is only approximately $0.2(=200kPax10^{-3})$ kPa when the tolerance of 10^{-3} was prescribed. The value of maximum error is considered acceptable in the simulation.

Also demonstrated in Section 5.4, in order to obtain same order of accuracy, the conventional forward Euler scheme in finite element analysis requires the number of subincrements larger than 1000 (m>1000). However, the computation time of forward Euler scheme is approximate 30 times longer than that when the modified forward Euler scheme with tolerance of 10^{-3} is selected. If the time spent in the iteration scheme to find the correct displacements using the Newton Raphson iteration scheme is also included, the required time will be even longer. Based on the previous discussion, it clearly shows that the modified forward Euler scheme can increase both computation accuracy and speed. As a result, the modified forward Euler scheme with tolerance of 10^{-3} was selected for the stress integration in this analysis.

6.2.4.4 Global Convergence Criterion

Because the nonlinear equation system in finite element analysis can not be solved directly, an iteration scheme like the Newton-Raphson method should be applied to satisfy the convergence in each external load increment. The detail process of the Newton-Raphson iteration scheme and the definition of convergence criterion (i.e., unbalanced force divided by current external force) were addressed in Section 3.2.6.

A sensitivity study was performed to investigate the effect of convergence criterion on predicted results (i.e., maximum total displacement and computation time) in this simulation. In the sensitivity study, three convergence criteria of 10^{-1},10^{-2} and 10^{-3} were used. All three simulations have same tolerance of 10^{-3} in the stress integration algorithm. Figure 6.17 shows the results of sensitivity study. The predicted results are presented in term of percentage of increase compared to the results obtained using convergence criterion of 10^{-2}. It can be observed the convergence criterion has little influence on the maximum total displacement. This is likely because the tolerance in the stress integration scheme ($tol=10^{-3}$) influences the global convergence. It confirms that stress integration scheme has a direct impact on both accuracy and efficiency of finite element computation (Jakobsen and Lade 2002). It is also expected when convergence criterion is less than 10^{-3} which corresponds to the value of tolerance in the stress integration algorithm, the predicted results will start to be noticeable.

However, as also shown in Fig. 6.17, the required computation time for convergence criterion of 10^{-3} is approximately 80% increased compared to that for convergence criterion of 10^{-2}. Therefore, the global convergence criterion of 10^{-2} was selected in the simulation. A total of 20 steps of solution increments (10 steps for stage construction and 10 steps for centrifugal loading) were considered in the analysis.

The components in the finite element model are summarized in the Table 6.5.

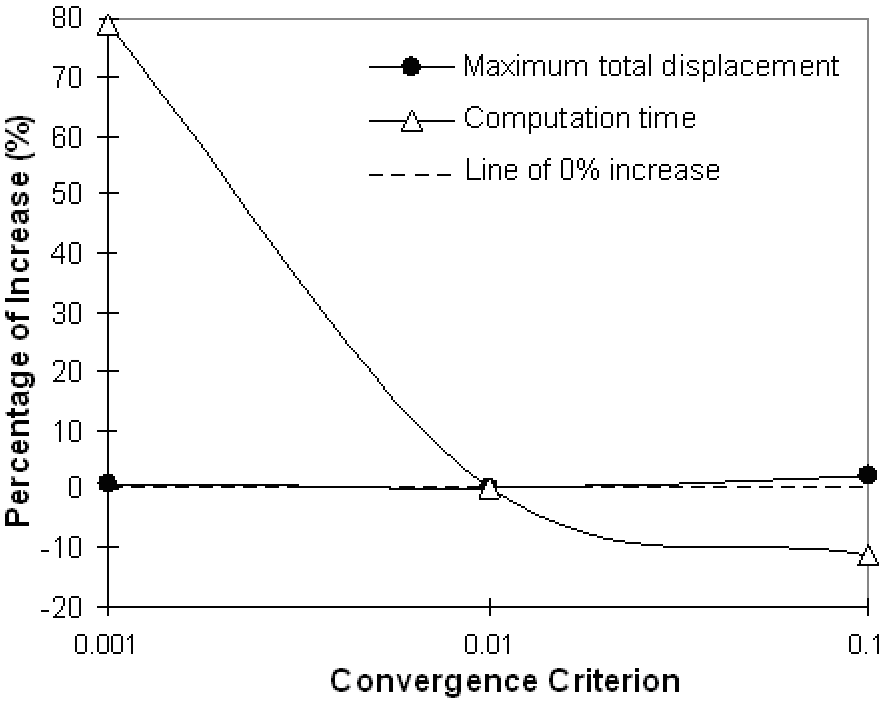

Figure 6.17: Sensitivity study of convergence criteria

Table 6.5: Summary of components in finite element model

FE model	Selection	Remark
Mesh configuration		
Mesh	Medium mesh size; 623 nodes; 302 elements	
Boundary condition	Standard fixities	
Material model		
Backfill and foundation	Lade-Kim soil model + proposed soil-softening model	Model parameters were calibrated to plane strain conditions
Reinforcement	Nonlinear reinforcement model	Model parameters were calibrated to confined conditions
Soil/geotextile interaction	Not included	
Model construction		
Stage construction	The analysis was conducted in 10 steps to simulate slope construction.	Study showed the stress developed during construction phase is insignificant compared to load phase
Compaction	Not included	Density of backfill was controlled by pluviation rather than compaction
Computation		
Centrifugal force	Simulated by the increase of body force	
Large deformation effects	Updated mesh	
Tolerance in SIA	Tolerance=10^{-3}	
Global convergence criterion	Convergence =10^{-2}	

6.2.5 Potential Sources of Error

All the previously discussed components in the finite element model are attempted to replicate the realistic behavior of centrifuge slope model as similarly as possible. However, due to the complex interaction between soil and reinforcement in the centrifuge model, the potential sources of error in the simulation could be:

First, the values of soil model parameters were calibrated to the measured data under triaxial compression conditions. Then, the value of failure criterion parameter η_1 was multiplied a strength increase ratio to account for the plane strain conditions. However, the realistic soil behavior under plane strain conditions likely differs from that predicted by numerical extrapolation. Further, the actual stress states of soil, specifically for soil close to the slope crest and face, are intricate and not necessary under plane strain conditions.

Second, although the effect of soil confinement on reinforcement was included in the calibration of reinforcement model parameters. The load-extension curve of reinforcements under soil confinement was extrapolated using the data from wide-width tensile test and multiplying the ratio of ultimate confined tensile strength (backcalculated from limit equilibrium analysis) to ultimate unconfined tensile strength (measured from wide-width test). However, the realistic load-extension response of reinforcements under soil confinement may differ from the extrapolation. Besides, the normal pressure acting on reinforcements varies with the location of reinforcements and g-levels, the currently used reinforcement model is not able to reflect the influence of different confinement magnitudes on reinforcement behavior.

Third, although the effect of large deformation was accounted by the updated meshes, Bathe et al. (1975) suggested that, in addition to the linear strain-displacement relationships (first order), the nonlinear strain-displacement relationships (second order) should be included into large deformation effects in the simulation. However, this option is not available in the current version of ANLOG.

Last, at the first g-level increment (5g) in the centrifuge test, the slope model is originally in the vertical position and then span into the horizontal position. This change of position may introduce some extra deformation. This slope deformation is not considered in the simulation. However, this slope deformation can be eliminated by comparing the data at certain g-level relative to that at 5g instead of at 1g (the beginning of the test).

Chapter 7: Validation of the Finite Element Simulations

After the finite element model was established in previous chapter, the proposed finite element model is validated using the data from the centrifuge test in this chapter. The data from centrifuge test involves significant volume of displacement and strain information. The numerical results from finite element analysis are used to compare with those measured from centrifuge test.

7.1 FAILURE G-LEVEL

Figure 7.1 shows the relationships among settlement, time and g-level measured from the centrifuge test. The failure indicated in Fig. 7.1 was determined by an increase of the settlement measured by LVDT. In each g-level increment, acceleration was increased during a loading duration of approximate 100 seconds and held constant for another 200 seconds to allow equalization of the load. The total loading duration was of approximate 5 minutes for each g-level increment.

The failure g-level of slope model M1 was of 50g reported by Arriaga (2003) in Table 6.1. However, as shown in Fig. 7.1, the slope failure can be assessed by the increases in settlement during the last g-level increment (from 45g to 50g). Because a total of 5g was increased for each g-level increment, it is not possible to determine the exact g-level that triggered the failure of the slope. By author's own interpretation, the failure was caused by only few increase of g-level (i.e., 1 or 2 g) after 45g.

Consistent with the g-level increment in the centrifuge test, each loading stage in the FE simulation included 5g increments. The computation successfully completed the 45g and "failed" at next load increment at loading ratio of approximate 20%. Therefore, the slope "failure" in the FE simulation was approximately at 46g (=45g+5gx0.2).

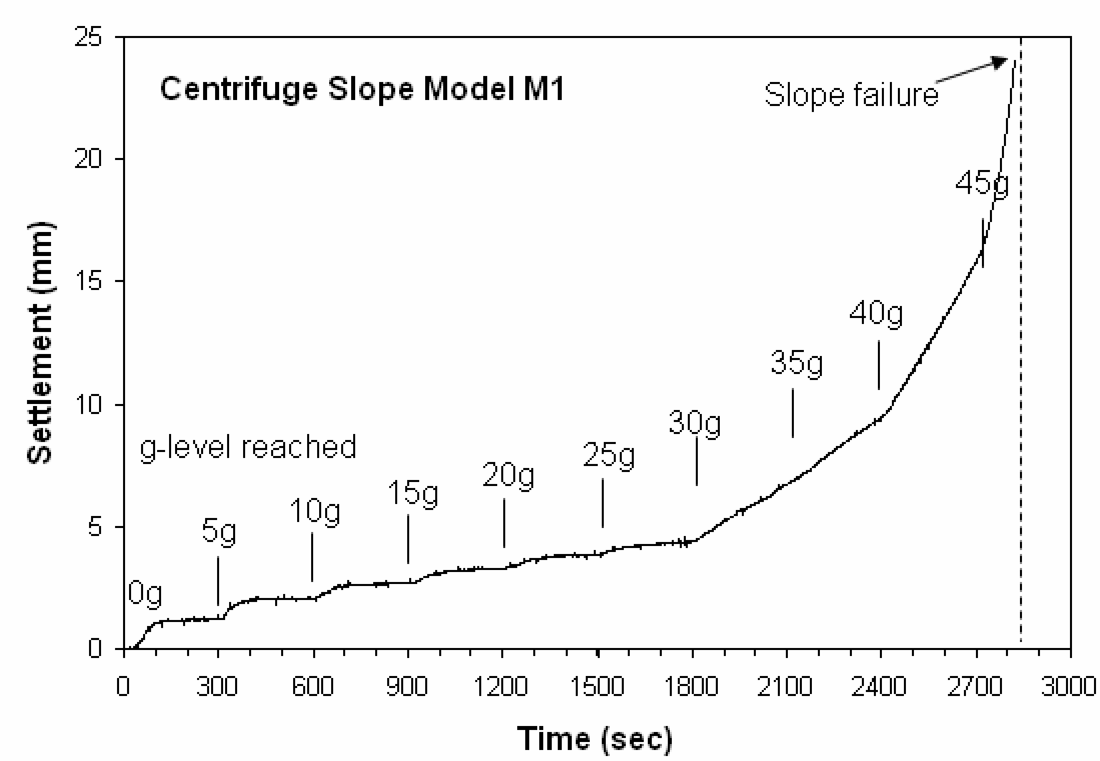

Figure 7.1: Predicted results as a function of settlement, time and g-level

In the FE simulation, the slope failure was not caused by the problem global convergence which can not reach the specified criterion. The problem of global convergence would indicate the remaining of unsolved out-of-balance force between external and internal force. In the physical point of view, the unsolved out-of-balance force represents the current load increment exceeds the system capacity, which corresponds to the definition of failure in the physical model. The slope failure was determined by the termination of simulation due to numerical illness occurred in the system. In Lade-Kim soil model, most of the equations (i.e., Eqs (4.4), (4.7), (4.11), (4.12) and (4.17)) contain the power functions like $(I_1/p_a)^x$ where I_1 is the first invariant of stress tensor, p_a is the atmosphere pressure and x is the soil model parameters according to the different model components. The numerical illness occurs and the simulation is terminated when the value of I_1 turns into negative and the value of exponent x of power functions less than 1.0.

As shown in Eq. (4.2), since I_1 is the combination of normal stresses in three perpendicular directions, the negative value of I_1 means the combination of three normal stresses is under tension. The tensions occur likely due to the simulation of soil dilatancy in the soil model. Under plane strain conditions ($\varepsilon_z=0$), the volumetric dilatancy of soil will cause the tensile strains developed in horizontal direction ($\varepsilon_x<0$). The strains in vertical direction may still remain in compression ($\varepsilon_y>0$) due to the centrifugal force acting in vertical direction. However, the compressive strains in vertical direction are less than the tensile strains in horizontal direction ($|\varepsilon_x|>|\varepsilon_y|$). With this combination of strains, the normal stresses in horizontal direction are decreased and then become tensions as the increase of the soil tensile strains in horizontal direction. Eventually, the combination of three normal stresses will be under tension, leading to the negative value of I_1.

In the simulation, it was observed that high soil tensile strains ε_x in the horizontal direction were developed along the potential failure surface (shown in Chapter 8). These high soil tensile strains increased with increasing of g-level. The observation in the numerical simulation can be justified by the physical model. The dilatancy of frictional soils occurs under shearing, specifically for those soils along the failure surface. This leads to the development of the soil tensile strains in the horizontal direction and the sliding of the soil failing wedge from the remaining soil mass. The soil tensile strains in the horizontal direction increased with increasing of loading, which eventually causes the soil failure mass to slide and the failure of soil slope to occur.

In conclusion, the failure g-level (46g) predicted by the simulation is within the range of failure g-level (45g~50g) observed from the centrifuge test. Due to the soil dilatancy, the soil tensile strains are developed in horizontal direction along the failure surface. The soil tensile strains in horizontal direction increase with the increase of loading and eventually lead to the failure of soil slope in the simulation.

7.2 OVERBURDEN PRESSURE VS. G-LEVEL

Vertical stresses obtained in the simulation are compared to the overburden pressure calculated by the simple method. The simple method is defined as:

$$\sigma_v = N_g \gamma z \tag{7.1}$$

where σ_v is the overburden pressure; N_g is the g-level; γ is the unit weight of backfill; and z is the depth from top of the slope.

The location of overburden pressure for comparison is at the base of foundation and the corner of two boundaries, which has less influence from slope face. The vertical stress in the simulation was obtained from Gauss point in close proximity to the location where the overburden pressure is calculated. It should be noted that the calculation of vertical stresses in finite element analysis is not as straightforward as using Eq.(7.1). As indicated in Fig. 3.6, the overall procedure of finite element computation involves six steps. 1) Calculating external forces from given boundary conditions, 2) calculating displacements from just-calculated external forces, 3) converting displacements to strains based on compatibility, 4) integrating stresses based on material constitutive relationships, 5) calculating internal forces from the known stresses in the problem domain of interest, and 6) checking the convergence of out-of-balance force between external and internal forces.

Additionally, errors in each step should be reduced by carefully selecting the tolerance criterion in computation algorithms like stress integration algorithms and iteration schemes. In the author's opinion, the overburden pressure should be the first place to be checked when the verification of finite element model is conducted.

The comparison of two approaches in Fig. 7.2 shows a good agreement in general. A slight discrepancy between two approaches occurs at 45g. A likely reason is the height *H* in Eq. (7.7) is not adjusted for the settlement at high g-level. Therefore, the simple method slightly overestimates the overburden pressure at 45g.

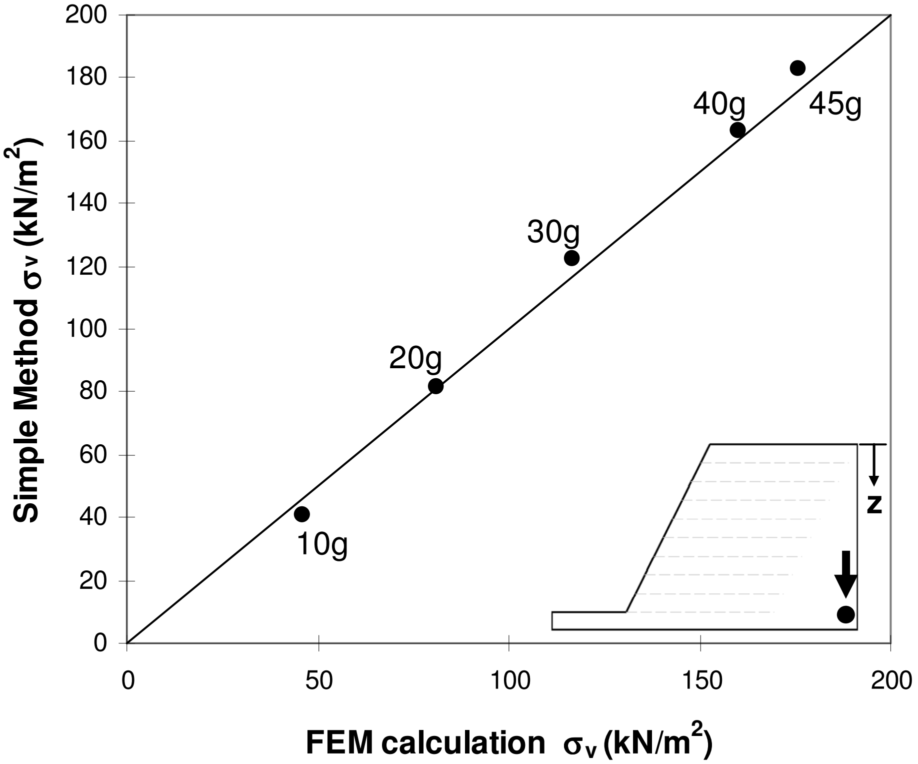

Figure 7.2: Comparison of overburden pressure vs. g-level

7.3 DEFORMATION PATTERN

The qualitative comparison of slope deformation pattern at the moment of failure is shown in Fig. 7.3. In Fig. 7.3b, the deformed meshes and displacement vectors are enlarged 20 times for the purpose of better visualization. The total displacement contour D_T is included in the Fig. 7.3b and calculated as,

$$D_T = \sqrt{D_x^2 + D_y^2} \tag{7.2}$$

where D_x and D_y is the deformation in the horizontal and vertical direction.

Overall, the finite element model can capture well the deformation pattern of the centrifuge model. For a more detailed comparison, additional focus is placed on the deformations at the following three locations at: 1. slope failure mass, 2. rear of slope top and 3. slope toe.

At the slope failure mass, both centrifuge and numerical models show a similar sliding trend. At the rear of slope top, the settlement can be recognized by the difference between original soil surface at the top of the slope (corresponding to the horizontal grid line) and the line of slope top at failure in the slope model M1 (see Fig 7.3a). In the numerical simulation, this settlement also can be observed by the difference between the horizontal soil surface of original mesh and the surface of deformed mesh towards the rear of the slope (see Fig 7.3b). At the slope toe, the failure surface for the slope on the firm foundation is expected to pass through the toe in the limit equilibrium analysis. However, as shown in Fig. 7.3a, the failure surface of slope model M1 passed through the slope face at the second layer of reinforcement. This behavior is also captured in the simulation as shown in Fig. 7.3b.

In fact, this is not only a special case for slope model M1. Figure 7.4 shows the locations of failure surface (determined by the locations of reinforcement tears) for all the slope models with slope angle 1H:2V. It is shown Fig. 7.4 that the failure surfaces for all models do not pass through the slope toe. The reason of failure surfaces not passing through the slope toe may be explained by the influence of boundary constraint at base of foundation. This can be observed from the vertical displacement contour D_y in Fig. 7.5. The vertical displacement less than 0.5 mm (D_y<0.5mm) is at the area approximately below the second layer of reinforcement. This indicates the influence of boundary conditions at the base of foundation is transferred through the firm shallow foundation to the area approximately below the second layer of reinforcement. As a result, the developed strains in first layer of reinforcement are too small to reach the strain at failure.

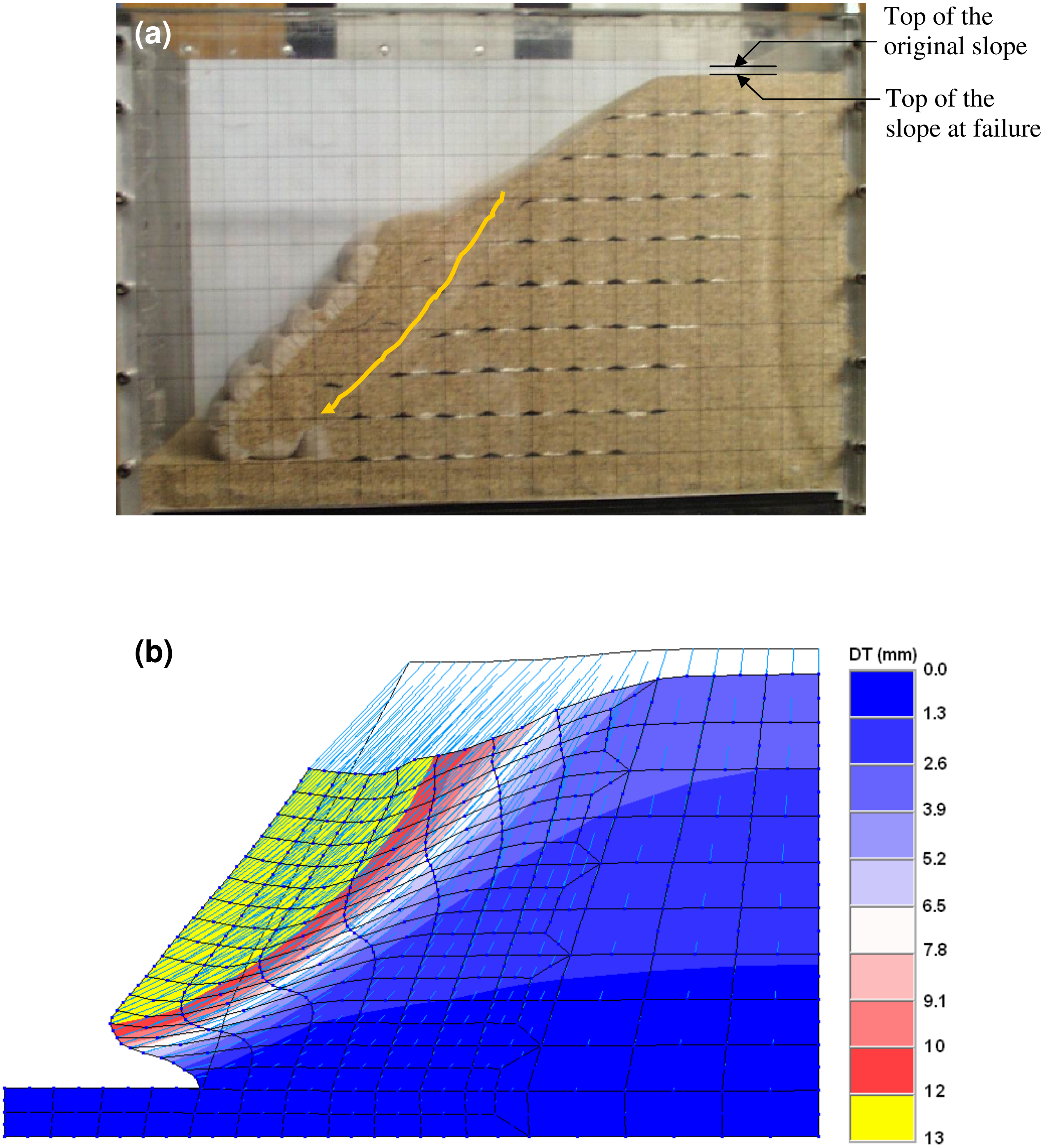

Figure 7.3: Comparison of deformation patterns: (a) centrifuge model; (b) finite element model (deformed mesh (x20), total displacement contour and vector)

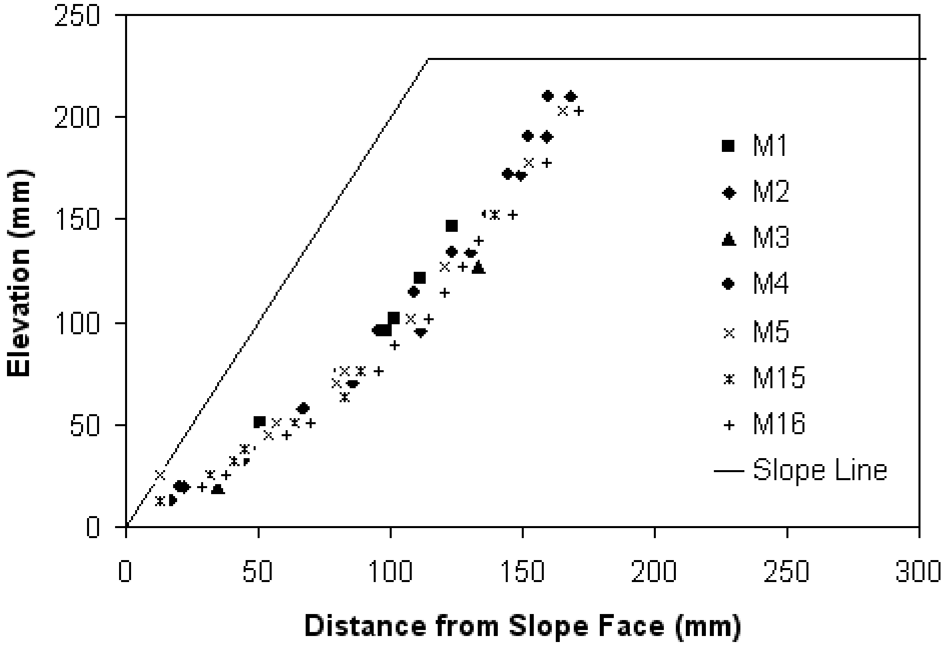

Figure 7.4: Location of failure surface for models with 1H:2V slope angle (Arriaga 2003)

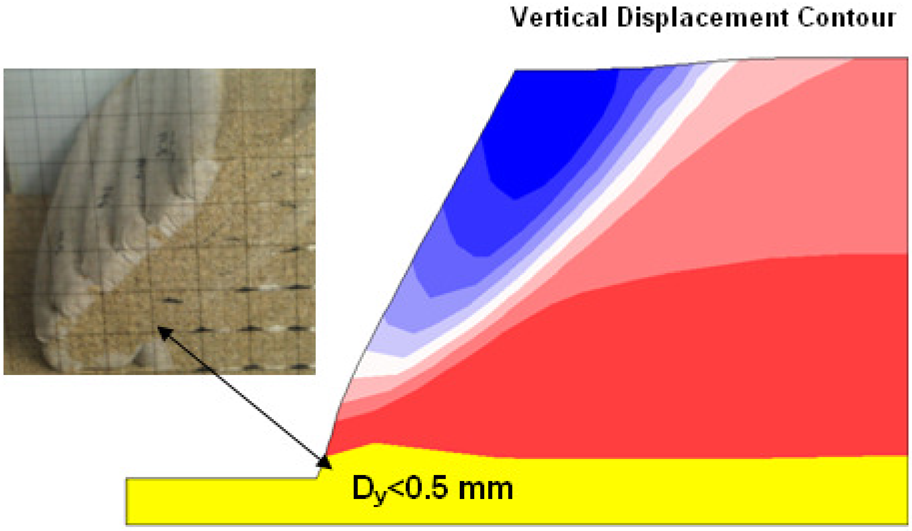

Figure 7.5: Vertical displacement contour to indicate by the influence of boundary constraint at base of foundation

7.4 LOCATION OF FAILURE SURFACE

The locations of failure surfaces determined from various methods are compared in this section. As indicated in Fig. 7.6, the blue triangle represents the location of failure surface from observed tears (ruptures) in each layer of reinforcement in the centrifuge model. The dashed circular line represents the failure surface identified by limit equilibrium analysis.

The failure surface from the finite element simulation is identified as the zone where soil-softening is obtained. The soil-softening can be evaluated using stress level *S* defined in Eqs. (4.12) and (4.46). *S* is less than 1.0 during hardening, equals to 1 when reaches soil peak strength and ranges from 1.0 (excluding 1.0) to 2.0 during softening. Further, by the data from a field reinforced slope, Zornberg (1994) reported the location of maximum strain in each reinforcement layer corresponds to the location of potential failure surface within the slope. Therefore, in the simulation, the developed reinforcement tensions with the increase of g-level are also included for comparison.

Because the failure surface was forced to pass through the slope toe in the limit equilibrium analysis, the location of predicted failure surface shows a slightly shift from those identified by the other measures. Overall, the locations of failure surfaces obtained from different approaches are in a good agreement. Fig. 7.6 also confirms the observation by Zornberg (1994) that the location of maximum strain in each reinforcement layer corresponding to the location of failure surface.

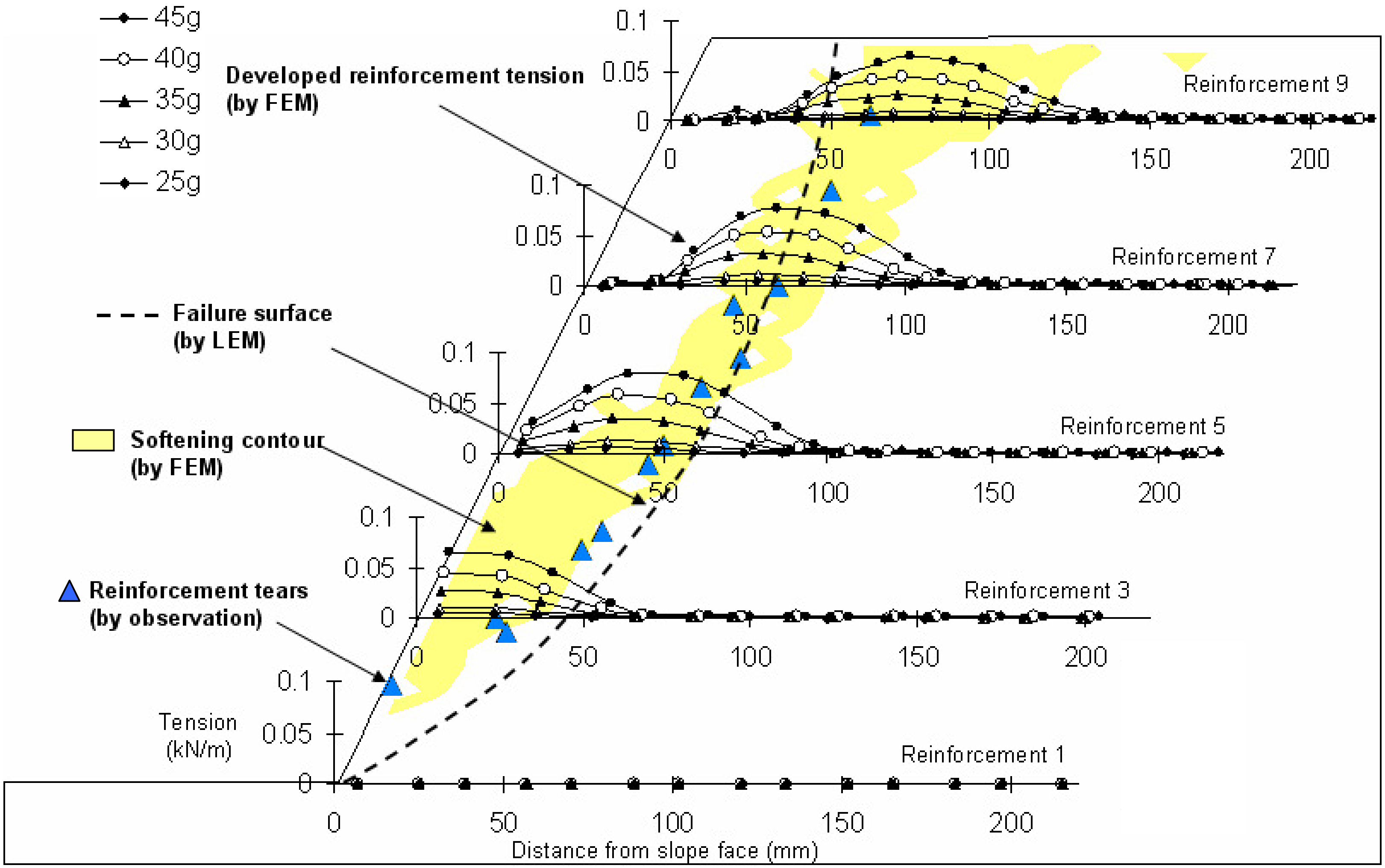

Figure 7.6: Comparison of location of failure surface

7.5 SETTLEMENT VS. G-LEVEL

Figure 7.7 shows the comparison of measured (monitored by LVDT) and predicted settlement with various g-level. As discussed in Section 6.2.5, the slope model is originally in the vertical position and then span into horizontal position at the first g-level increment (5g) in the centrifuge test. This change of position may introduce extra deformation which probably contributes the nonlinear increase of settlement observed at first loading increment indicated in Fig. 6.1. Therefore, the data obtained from the first g-level increment is usually not reliable and not included in the analysis. Accordingly, both measured and predicated settlement is relative to the condition at 5g. A good agreement can be observed from the comparison in Fig. 7.7.

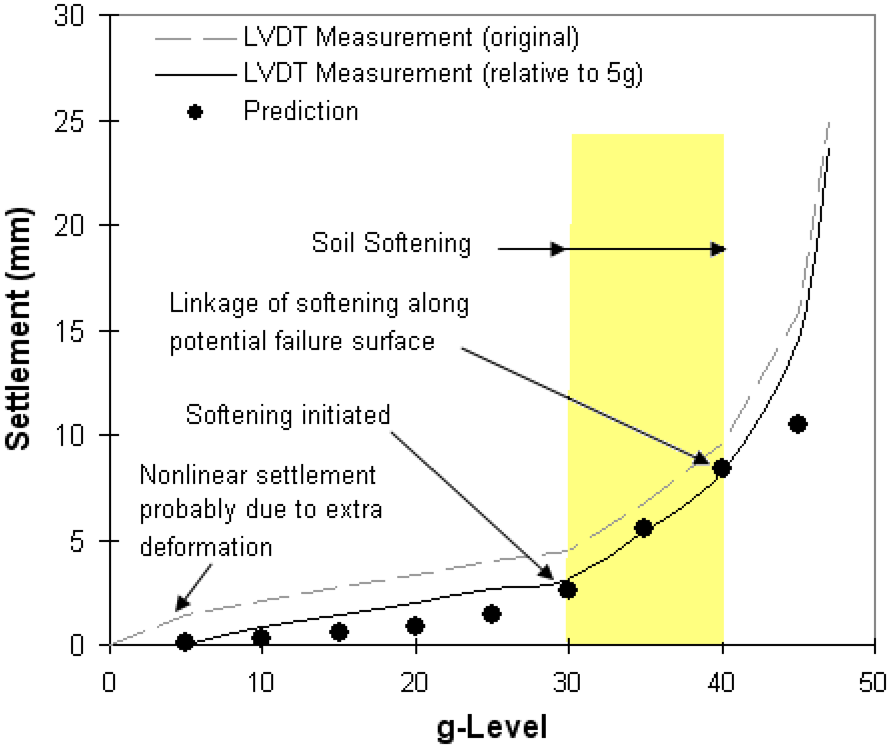

Figure 7.7: Comparison of settlement with g-level

Another important observation from the numerical simulation is that the soil-softening is initiated in some elements around 30g and the linkage of softening zone along failure surface is completed around 40g as indicated in Fig 7.7. The point of inflection in settlement (increase of settlement rate) corresponds to the status of soil-softening developed along the failure surface. After the initiation of soil strength softening around 30g, the increased reinforcement strains indicating load transfer from soils to reinforcements (see Fig. 7.6). The stability of the system is sustained mainly by the mobilization of reinforcement tensile forces. After few additional load increments, the slope fails when the reinforcement reaches its ultimate tensile strength.

The increase of settlement rate can be explained by the decrease of system stiffness. From the numerical point of view, the system stiffness is expressed as global stiffness matrix K in the finite element analysis. In constitutive model, the hardening and softening modulus H in Eq.(4.45) changes from positive to negative when soil state shifts from hardening to softening (H=0 at soil peak strength). The negative H would decrease the elasto-plastic stiffness matrix D_{ep} in Eq. (4.24) and subsequently decrease the element stiffness matrix K^e in Eq. (3.17). Further, because the global stiffness K is assembled from the element stiffness matrix K^e, the global stiffness K also decrease specifically for the those elements whose stress states are under softening region. Last, as shown in Eqs. (3.32) and (3.31), at a given external force increment, the displacement would increase when the value of global stiffness K is decreasing or the value of inverse global stiffness K^{-1} is increasing.

Similar observations were reported by Bathurst (1993) and Karpurapu and Bathurst (1995). Two instrumented large-scaled GRS retaining walls in 3m height were tested in the Royal Military College (RMC) retaining wall test facility. The GRS walls contained a dense sand fill and layers of extensible geogrid reinforcements attached to two different facing treatments: incremental panel and full-height panel. Both walls were taken to collapse under uniform surcharge pressure applied to the top of walls.

Figure 7.8a show the reinforcement displacements measured by extensometers at reinforcement layer 3 within the fill of the incremental panel wall test. The displacements increase approximately linearly with the increase of surcharge for low surcharges. The rate of displacement increases significantly at surcharge of 70kPa. The soil failure was observed corresponding to this surcharge level. Thereafter, it was reported that load was shed to the extensible geosynthetic reinforcing layers. The creep of these polymeric materials led to ultimate collapse of the wall several hours after soil failure. Similar results were reported for outward facing movements of the full height panel wall as shown in Fig. 7.8b. The facing deformation increases approximately with increasing surcharge for low surcharges. The rate of displacement elevates greatly at a surcharge of 80kPa. This surcharge magnitude also results in soil failure followed thereafter by reinforcement failure.

Last, the development of soil failure indicated in Figs. 7.8 is delayed several hours after the beginning of the last surcharge increment. This is because the soil failure in large-scaled GRS wall tests can not be identified until a well-developed shear plane was observed. Therefore, the soil failure indicated in Figs. 7.8 would be associated to the completed linkage of soil-softening indicated in Fig. 7.7. The actual initiation of soil-softening likely occurred earlier, which is suspected to have occurred right at the beginning of the last surcharge increment.

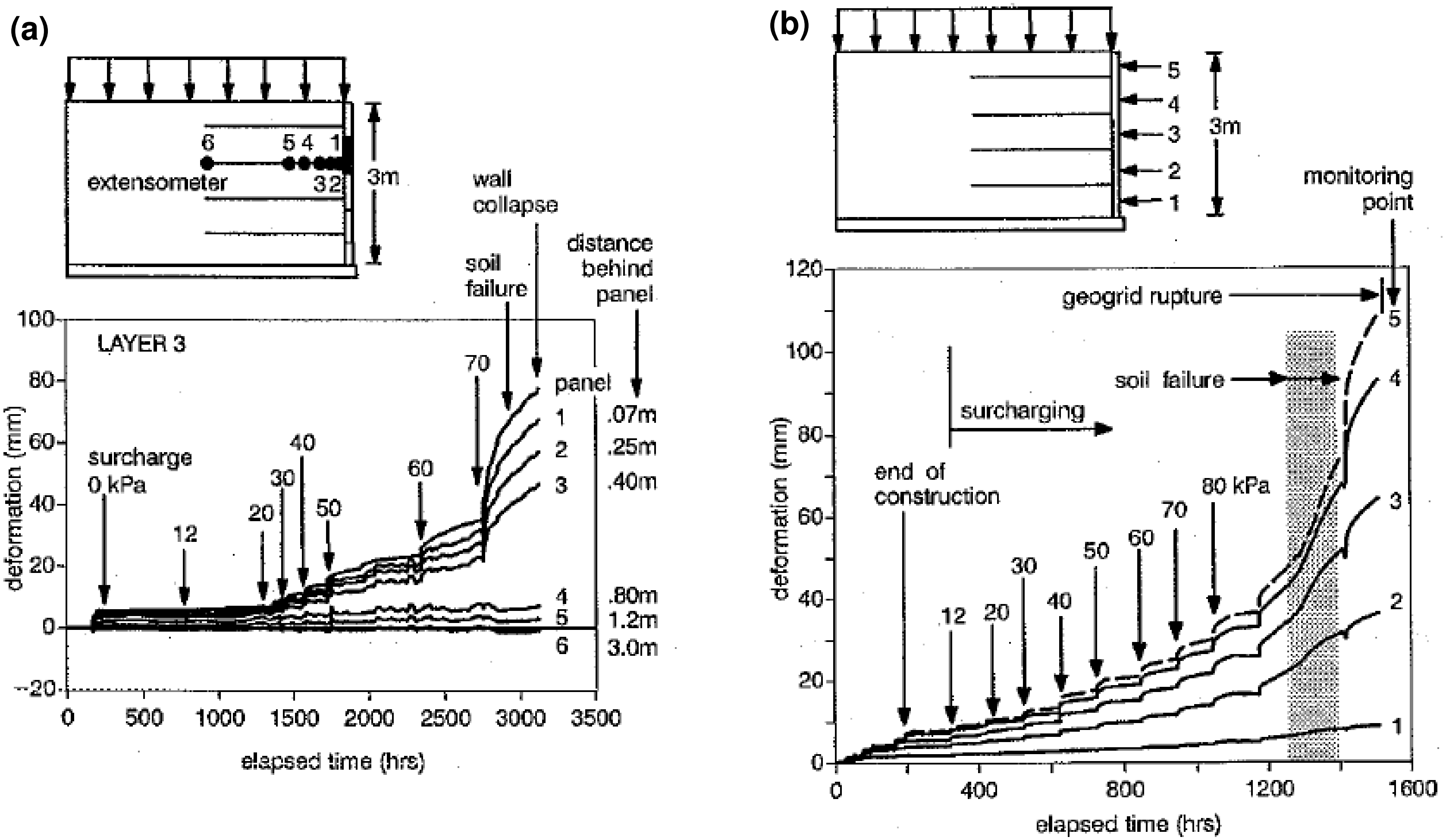

Figure 7.8: Displacements vs. increasing surcharge: (a) incremental panel wall and (b) full-height panel wall (Bathurst 1993)

7.6 DISPLACEMENTS ALONG REINFORCEMENTS

Measured and predicted displacements along reinforcements at different g-levels are compared in Fig 7.9. As discussed previously, because of the centrifuge data not reliable at the first g-level increment, the displacements along reinforcements was calculated relative to 5g. The measured displacements along the reinforcement layers were obtained by processing the images recorded from high-speed digital cameras. The coordinates of center of colored sand markers (see Fig. 6.1b) at the locations of interest were tracked. Then, the displacement relative to 5g can be calculated using the equation of distance as:

$$d = \sqrt{(X_{Ng} - X_{5g})^2 + (Y_{Ng} - Y_{5g})^2} \tag{7.3}$$

where:

d is the relative displacement between 5g and Ng; N is any interested g-level;

X_{5g} and Y_{5g} are the coordinates of center of colored sand markers at 5g;

X_{Ng} and Y_{Ng} are the coordinates of center of colored sand markers at 5g;

In Fig. 7.9, the error bar with a length of 0.35mm long in each side represents the image resolution of 1 pixel. The displacements along reinforcements at g-level below 30g (the beginning of soil-softening) are not included. This is because the displacements at low g-levels are too small, only few times large than the image resolution. As a result, the obtained displacements are not accurate enough for comparison.

The predicted displacements in the simulation were obtained directly from the nodal total displacements at the locations of interest excluding the total displacements at 5g. Overall, the displacements along reinforcements obtained from centrifuge test and finite element analyses are in a good agreement.

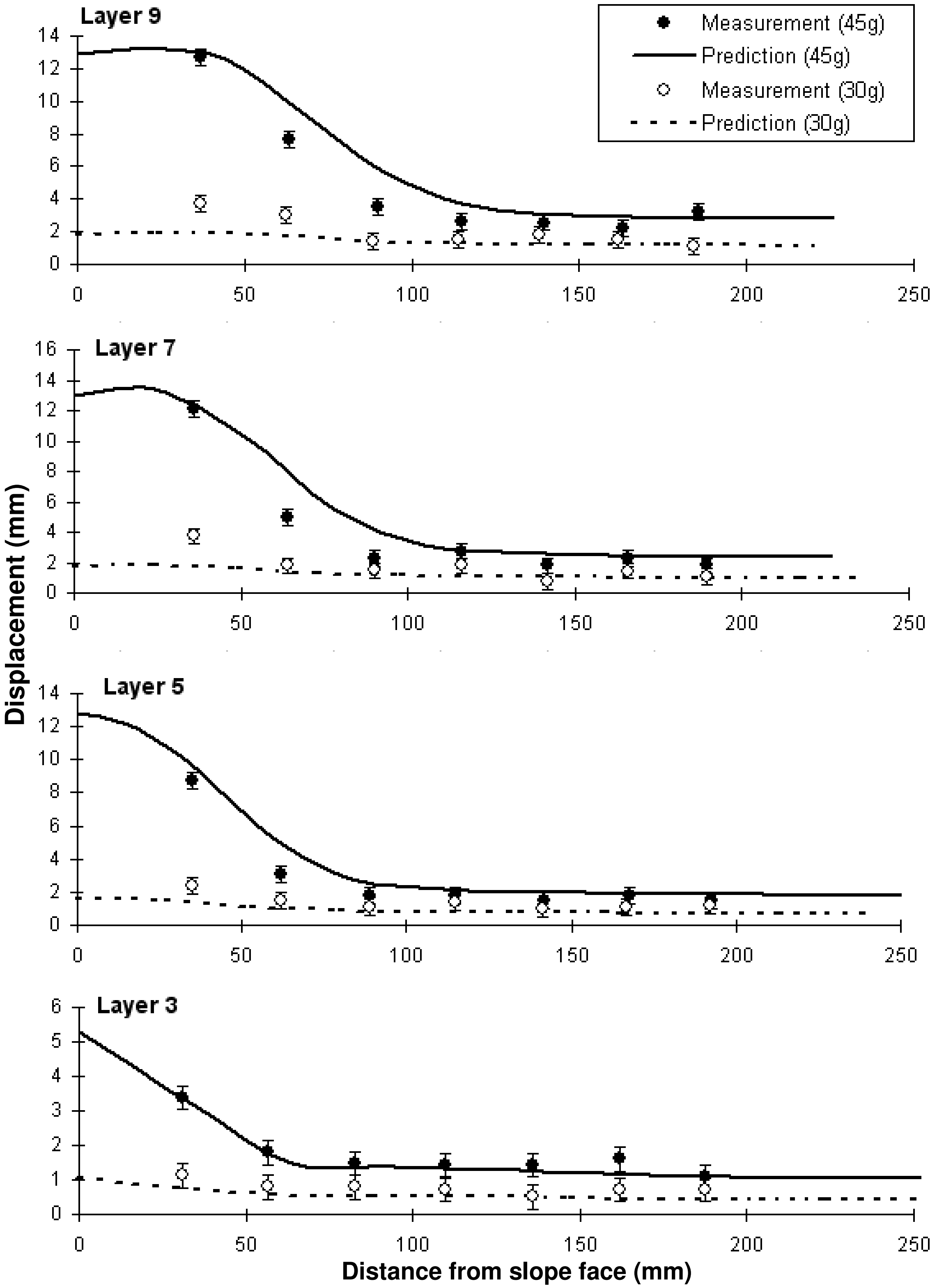

Figure 7.9: Comparison of displacements at different reinforcement layers and g-levels

7.6 EVALUATE THE EFFECT OF SOIL-SOFTENING

7.6.1 Simulation of GRS Slopes using the Original Softening Model

In this section, the effect of soil-softening is evaluated by two simulations. The first simulation is conducted to model the GRS slopes M1 using the original softening model in the Lade-Kim soil model. The results predicted by the proposed soil-softening model and the original soil-softening are compared. A constant value of softening parameter $b' = 0.7$ was selected for simulation. According to Fig. 4.8, this value of b' was determined to represent the average value of b' covering the range of confining pressure in the centrifuge slope model.

The result of simulation shows the simulation terminated at g-level of 34g. The maximum soil stress level S reached approximate 1.9 in the element located at top of slope. The high value of S (2.0 is the maximum value based on the definition in the dissertation) means the size of yield surface shrinks closely to zero. It is because there is no limitation for the decreasing yield surface size in the original softening model.

This simulation emphasizes the important features introduced in the proposed softening model such as: 1) limit the decrease of yield surface until a residual yield surface; and 2) model parameters are function of confining pressure.

7.6.2 Simulation of GRS Slopes without Soil-Softening

The second simulation is conducted to model the GRS slopes using the soil constitutive model without considering soil-softening. In this case, a perfectly plastic constitutive model is employed to describe the soil post-peak behavior. The results predicted by with and without soil-softening are compared. Figure 7.10 shows the comparison of the settlement vs. g-level between measurement and prediction by using the soil constitutive model with and without soil-softening. The settlement is underestimated by the soil constitutive model without soil-softening, as shown in Fig. 7.10. In numerical aspect, it is likely due to the elastoplastic constitutive matrix D_{ep} is stiffer when the simulation is conducted without considering soil-softening in the soil constitutive model. Consequently, the deformation would be less compared to that predicted by considering the soil-softening in the soil constitutive model. In physical explanation, the soil shear strength in the soil post-peak region would decease with the increasing loading. Under this circumstance, the additional loading due to loss of soil shear strength would be shed to neighbor soils. As a result, the deformation would increase rapidly under soil strain conditions. However, this mechanism of load transfer can not be captured if the simulation is conducted without considering soil-softening in the soil constitutive model. What is worse, the consequence of under-predicted displacement will cause the underestimate of stresses and strains in soils and reinforcements.

Moreover, another advantage of considering soil-softening in the soil constitutive model allows us to track and distinguish the soil stress status in the post-peak region. Figure 7.11 shows the soil stress level S contour predicted by with and without the soil-softening model in the soil constitutive model. The simulation conducted by considering the soil-softening is able to identify the soil post-peak stress status and is better representative of the actual mobilization of soil strength.

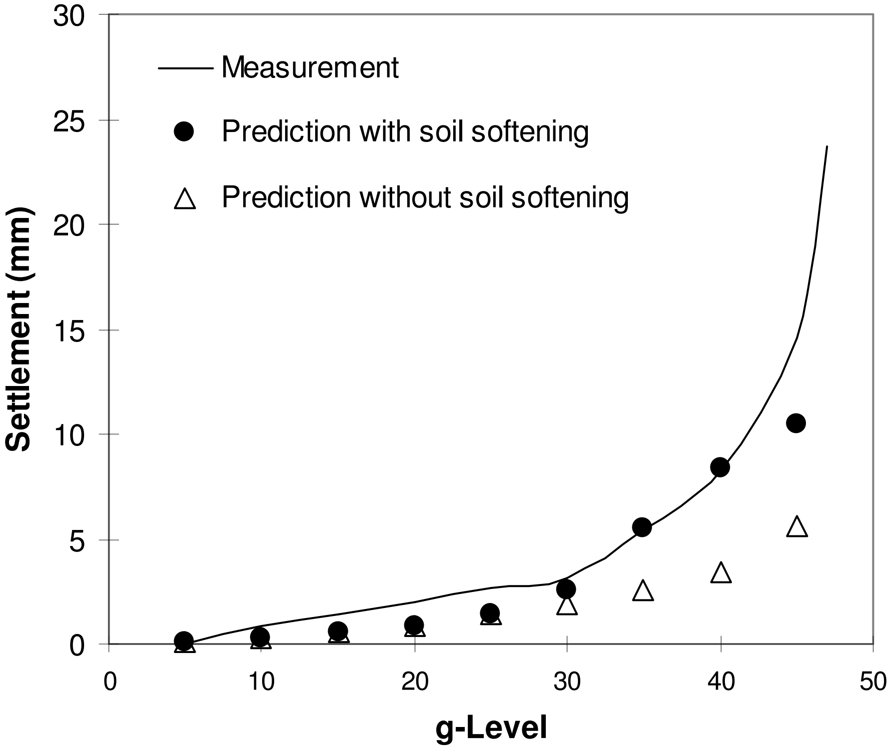

Figure 7.10: Comparison of settlement vs. g-level between measurement and prediction by with and without soil-softening

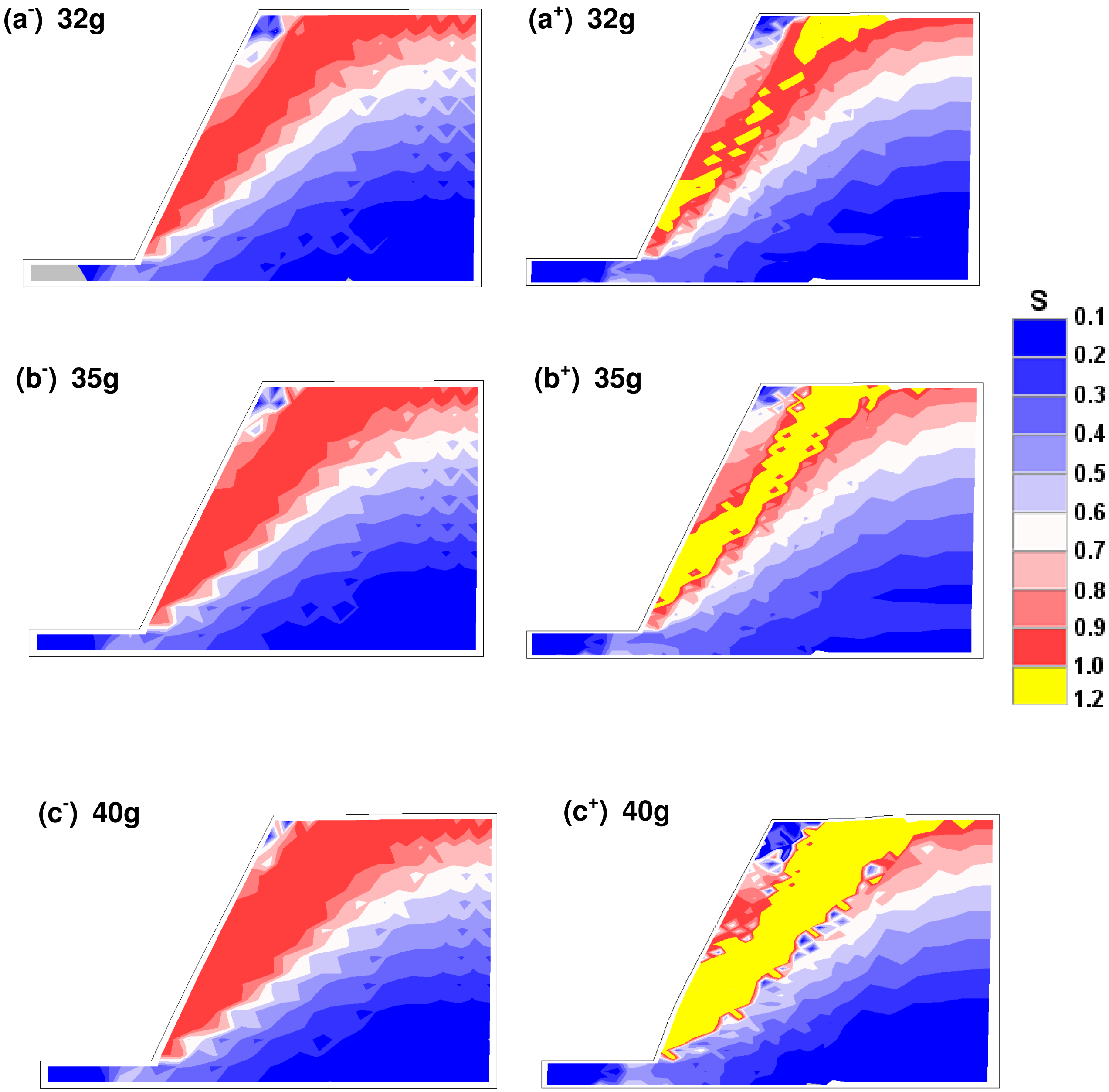

Figure 7.11: Comparison of soil stress level predicted by with and without soil-softening in the soil constitutive model: (a$^-$) 32g without soil-softening; (a$^-$) 32g with soil-softening; (b$^-$) 35g without soil-softening; (b$^-$) 35g with soil-softening; (c$^-$) 40g without soil-softening; (c$^-$) 40g with soil-softening;

Chapter 8: Stress Distribution within GRS Structures

This chapter examines the soil and reinforcement stress information obtained from the finite element simulation. The stress development and distribution within the GRS retaining structures is the basis of much of current design. The issues in Section 1.3.1 regarding the basis of design and the arguments of current design will be discussed. The design of GRS structures in current design guidelines will be examined. Also, the revealed stress information from finite element simulation can help to provide the design consideration and implication for the design of GRS structures.

8.1 THE EVOLUTION OF STRESSES AND STRAINS ALONG THE FAILURE SURFACE

8.1.1 Background

The failure surface within retaining soil structures is an important factor for design, specifically for internal stability. Along the failure surface, the development of soil and reinforcement stresses reflects and governs the failure mechanism of internal stability. However, until now, the knowledge of failure surface is only limited on the prediction of the location. The information in regard to the development of soil stresses (or strains) along failure surface has not been fully understood yet. The main reason is because the stress information is often not directly accessible through most of current physical or numerical methods. The problems of accessing stress information by current research and design methods have been discussed previously in Section 1.4. As a result, after the finite element model was verified, the stress information obtained from the simulation will be applied to study the development of failure surface.

8.1.2 Soil Stresses along Failure Surface

In the FE simulation, the evolution of failure surface can be described by the development of soil stress level *S*. Figs.8.1 illustrates typical soil stress level contours within the slope and the corresponding stress states. As discussed in Sections 4.2.4 and 4.3.3, stress level *S* is defined as the ratio of current mobilized soil shear strength to peak soil shear strength, which can also be viewed as an index of soil strength mobilization. The value of *S* is less than 1.0 when the soil current stress state is below soil peak strength (Fig. 8.1a). *S* equals 1.0 when the current stress state reaches peak strength (Fig. 8.1b). *S* is larger than 1.0 when soil stress state crosses peak strength and reaches the strength softening region (Fig. 8.1c). Readers should be reminded that the illustration of the concept of stress level is plotted in 1-D in Fig. 8.1. However, the actual computation of stress level in the selected soil model involves a 3-D evaluation.

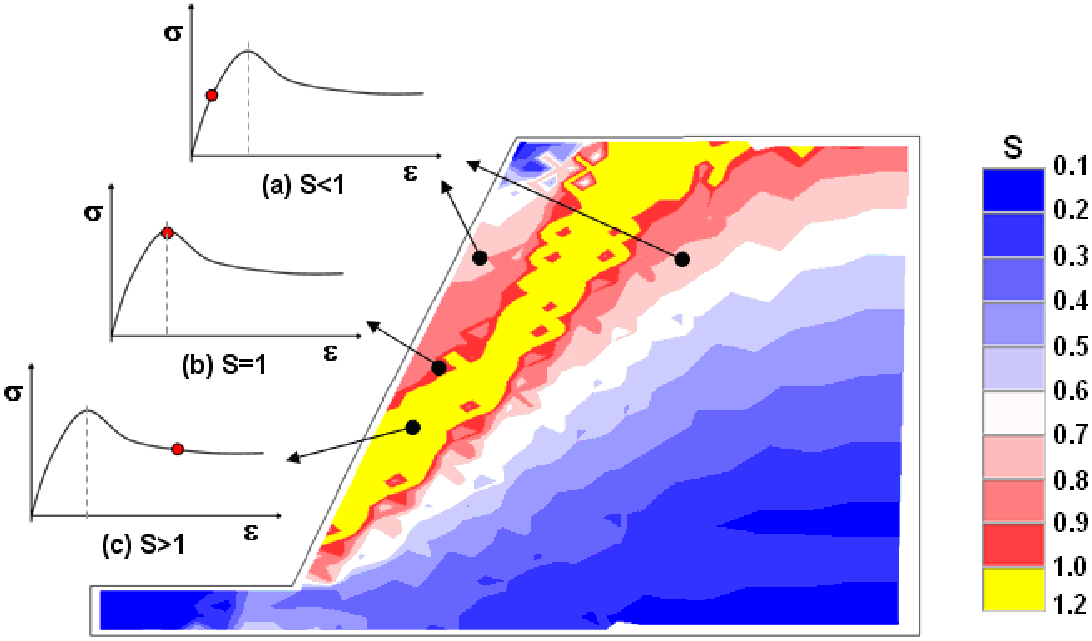

Figure 8.1: Soil stress level contour and the illustration of corresponded stress states

The evolution of soil stresses along failure surface under different g-levels is shown in Figs. 8.2. Fig. 8.2a shows the mobilization of soil shear strength is nonuniform. The areas of high stress level are developed when the loading increases. Two high stress level spots reach *S*=0.9 and propagated along the potential failure surface at 20g. In Fig. 8.2b a clear high stress level band formed. The stress level reaches unity (*S*=1) and strength softening is initiated immediately at top and toe of slope at 30g corresponding to *FS*=1.2 from the limit equilibrium analysis discussed in Section 6.1.5. Then, the softening occurs randomly along the failure surface and a clear softening band forms (Fig. 8.2c and 8.2d). The linkage of soil-softening band through entire potential failure surface occurs at 40g where *FS*=1.1 (Fig. 8.2e).

Several studies on the shear behavior of sand in the context of the development of shear band, support the formation of failure surface observed in this study. Taking into account the work of Desrues et al. (1996), Suzuki and Yamada (2006) described the typical progressive failure of sands in the drained triaxial test as follows:

1. In Fig. 8.3a, the initial condition of stresses and strains is assumed homogenous throughout the specimen under isotropic confining pressure.
2. In Fig. 8.3b, as the deviatoric stress increased, tiny compressive and dilative volumetric strain areas occur randomly at various locations, but the uniformity and homogeneity of stresses and strains are macro-mechanically maintained.
3. In Fig. 8.3c, when the loading approached the soil peak strength, the dilative strain areas begin to link continuously to form a shear band. The start of this process coincides with the peak strength. As shear band progresses from being weakly developed to fully developed, the deformation is mostly absorbed by sliding at the shear band, so that the dilative strain increment areas of the specimen gradually decrease.

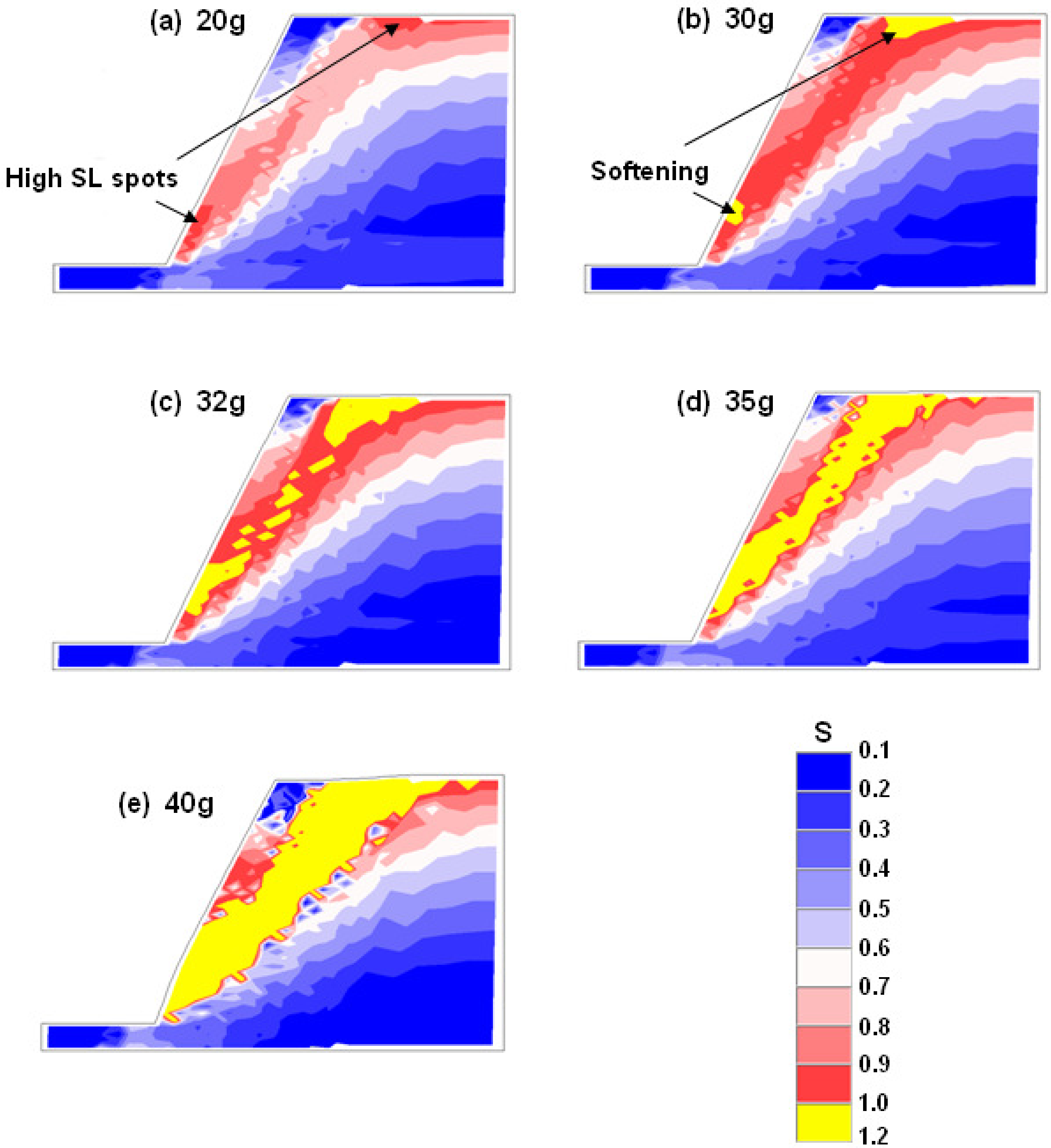

Figure 8.2: Stress evolution along failure surface: (a) 20g (*FS* ≈1.35); (b) 30g (*FS* ≈1.2); (c) 32g; (d) 35g; (e) 40g (*FS* ≈1.1)

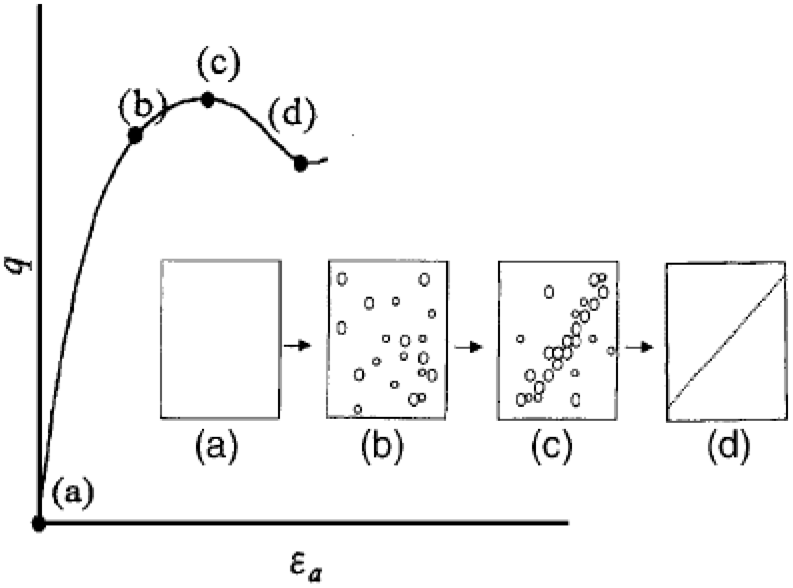

Figure 8.3: Illustration of progressive failure of sands in drained triaxial tests: (a) initial condition; (b) occurrence of dilative strain areas; (c) continuous linking of dilative strain areas; (d) fully developed shear band (Suzuki and Yamada, 2001)

4. In Fig. 8.3d, when the shear band is fully developed, the change of volumetric strain becomes zero and the volumetric strain remains constant even within shear bands. A new equilibrium is reached.

Also, some experimental studies are related to this mechanism. Desrues (1991) found from plane strain experiments that several incipient shear bands appear simultaneously near the peak load, of which only one develops fully. Yoshida et al. (1993) observed in the plane strain compression test that strain localization begins immediately before peak strength is reached.

8.1.3 Soil Strains along the Failure Surface

It is also observed from the FE results that the failure surface corresponds to the locus of intense soil strains in the horizontal and vertical directions shown in Figs. 8.4 and Fig 8.5, respectively and intense soil shear strains in the octahedral plane in Fig. 8.6. Due to the dilatancy of frictional materials, the soil horizontal strains along failure surface appear in expansion. It seems that the final collapse of slope due to the breakage of reinforcements is driven by the intense soil strains developed along the failure surface.

This observation supports the statement made by Zornberg (1998) to explain the mechanism governing the failure of slope observed from the centrifuge tests. He plausibly proposed that although the soil may have failed (reached active state) due to large horizontal strains because of the extensible nature of the reinforcements, the final failure of slope (sliding of the active reinforced wedge) could occur only when large shear displacements take place along the failure surface.

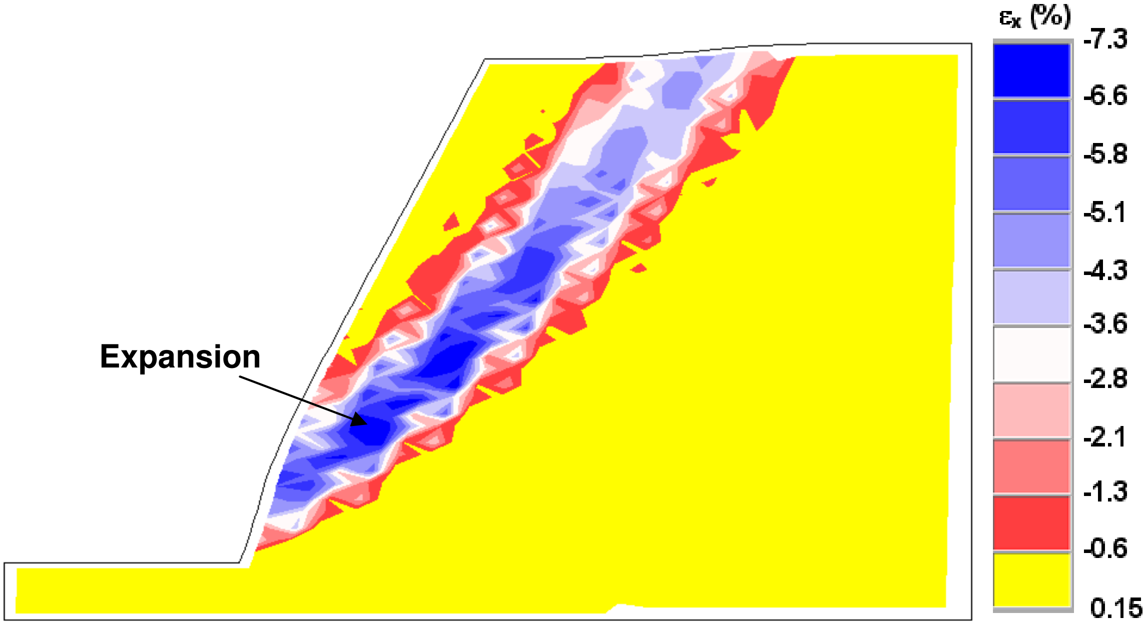

Figure 8.4: Developed soil horizontal strains at 45g. High tension strains along failure surface are due to the dilatancy of frictional material

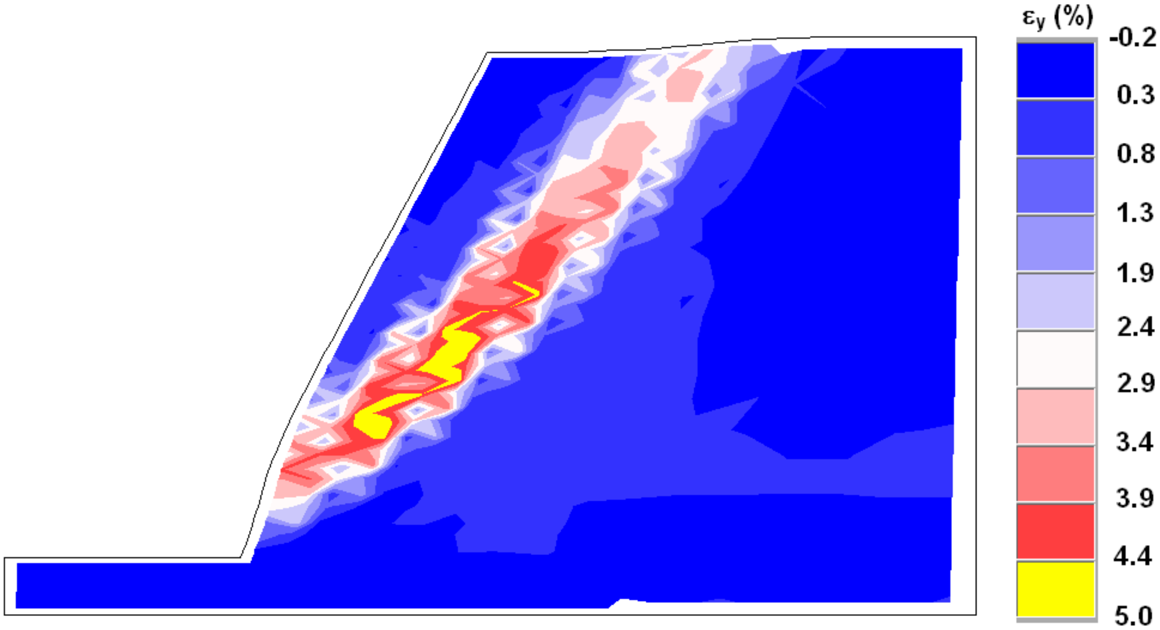

Figure 8.5: Developed soil vertical strains at 45g

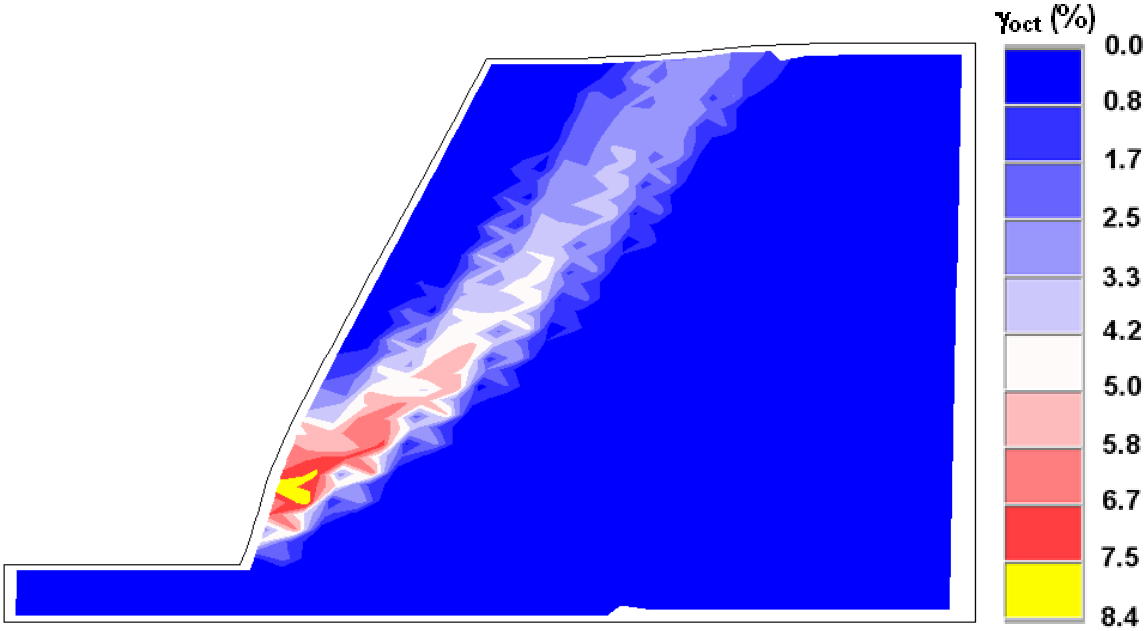

Figure 8.6: Developed soil shear strains in the octahedral plane at 45g

8.1.4 Reinforcement Tensions along the Failure Surface

It is also observed from numerical analysis that the failure surface corresponds to the locus of the peak reinforcement tension at each layer, as shown in Fig. 7.6. This numerical observation also confirms the field observation by Zornberg (1994). By the data from a full-scale, instrumented reinforced soil slope, Zornberg (1994) reported the location of maximum strain in each instrumented reinforcement layer corresponds to the location of potential failure surface within the slope.

It is also observed in the FE simulation and the centrifuge tests that the system stability is mainly sustained by reinforcement strength after the completed linkage of soil-softening band. At this stage, the high reinforcement tensions indicate load transfer from soils to reinforcements. The developed reinforcement tensions balance the increasing centrifuge loading and, meanwhile, the loss of soil strength during softening (dropping from peak to residual strength). When intense soil strains along the failure surface reach certain level, the mobilized reinforcement strengths will reach ultimate value and finally reinforcement breakage occurs. The system will reach failure (*FS*=1.0) soon by few loading increments depended on the tensile strength of reinforcements.

8.2 SOIL STRENGTH PROPERTIES GOVERNING THE STABILITY OF GRS STRUCTURES

8.2.1 Background

There has been a series of debates regarding the appropriate selection of shear strength properties (peak or residual strength) for GRS retaining structure design (Leshchinsky 2001, Zornberg 2003, 2002, 2002a, 2002b and 2002c, Zornberg and Leshchinsky 2001). As summarized in Table 8.1, Zornberg and Leshchinsky (2001) presented a review of current design criteria used by different agencies for geosynthetic-reinforced walls, geosynthetic-reinforced slopes, and embankments.

The extensible nature of geosynthetic reinforcements has led to the recommendation by several agencies and reinforced soil designers toward the use of the residual shear strength for design. This is because geosynthetics are classified as extensible reinforcements; consequently, the soil strength may be expected to mobilize rapidly, reaching and crossing its peak strength before the reinforcements achieve their ultimate strength.

However, common practice in the US recommends the use of the peak shear strength. The use of peak shear strength parameters in the design of GRS structures is justified by the results from experimental tests (Zornberg 2002, Zornberg et al. 1998). In their tests, the failure g-levels of two series of centrifuge slope models in the B- and D-series were compared. Slope models of two series were reinforced using the same geotextile reinforcement but using sand backfill placed at two different relative densities (55% for B series and 75% for D series). The Monterey sand at these two relative densities has the same soil residual friction angle (32.5°) but different peak friction angles (35° and 37.5°). The results of comparison indicate the models in the D-series failed at higher g-levels than models in the B-series built with the same reinforcement spacing and reinforcement type. Since the backfill soils in models from the B- and D-series have the same residual soil shear strength, the higher g-level at failure in the D-series models is due to the higher peak soil shear strength in this test series. The use of a single residual shear strength value, common to the two backfill materials used in the test series, cannot explain the experimental results. Further, the perceived conservatism by using residual strength in design is also not supported by the generally observed good performance of monitored reinforced soil structures designed by using peak strength.

A hybrid approach was proposed by Leshchinsky (2001). He proposed a design procedure in which peak soil shear strength properties would be used to locate the critical slip surface, while the residual shear strength properties would subsequently be used along the located slip surface to compute the reinforcement requirements.

Table 8.1: Summary of guidelines on selection of soil shear strength parameters for geosynthetic -reinforced soil design (Zornberg and Leshchinsky 2001)

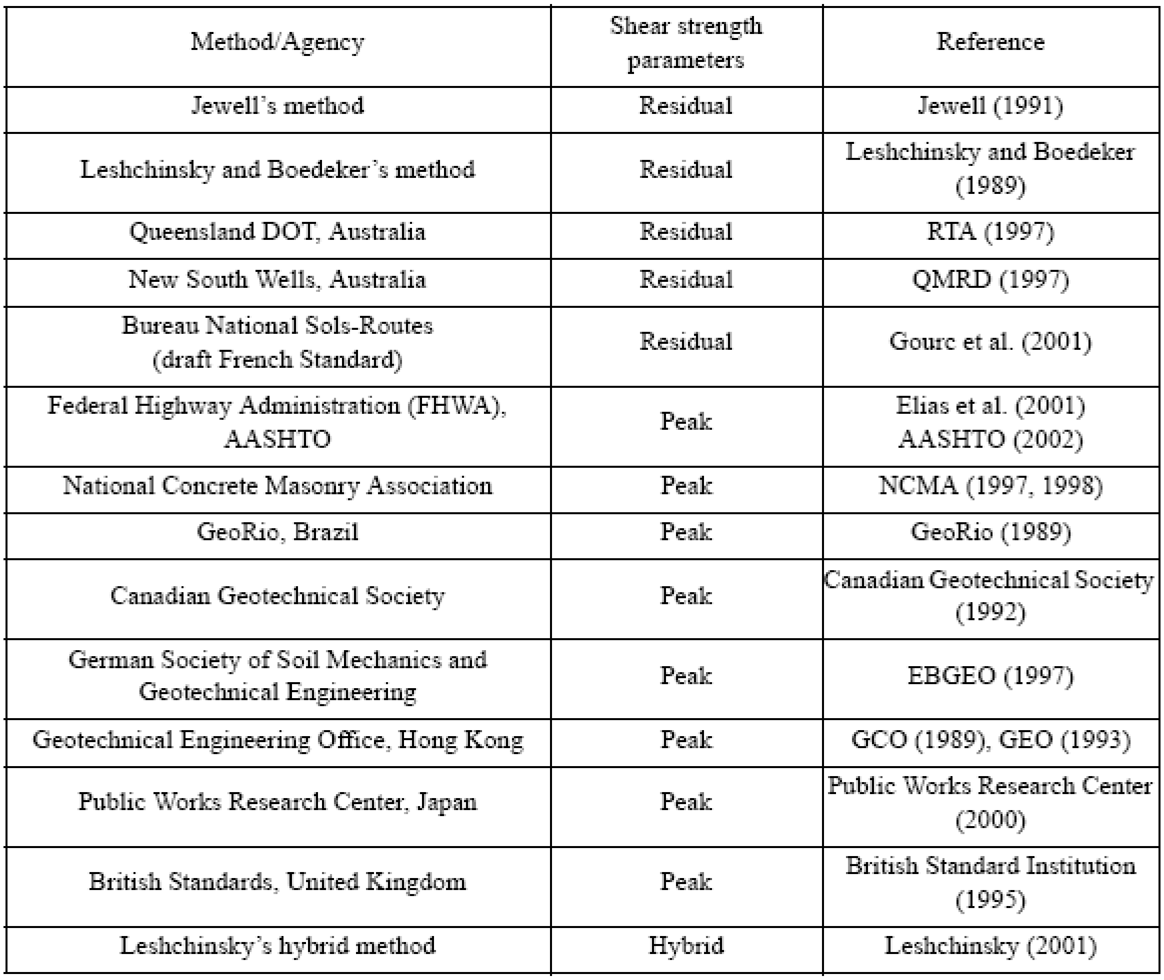

Method/Agency	Shear strength parameters	Reference
Jewell's method	Residual	Jewell (1991)
Leshchinsky and Boedeker's method	Residual	Leshchinsky and Boedeker (1989)
Queensland DOT, Australia	Residual	RTA (1997)
New South Wells, Australia	Residual	QMRD (1997)
Bureau National Sols-Routes (draft French Standard)	Residual	Gourc et al. (2001)
Federal Highway Administration (FHWA), AASHTO	Peak	Elias et al. (2001) AASHTO (2002)
National Concrete Masonry Association	Peak	NCMA (1997, 1998)
GeoRio, Brazil	Peak	GeoRio (1989)
Canadian Geotechnical Society	Peak	Canadian Geotechnical Society (1992)
German Society of Soil Mechanics and Geotechnical Engineering	Peak	EBGEO (1997)
Geotechnical Engineering Office, Hong Kong	Peak	GCO (1989), GEO (1993)
Public Works Research Center, Japan	Peak	Public Works Research Center (2000)
British Standards, United Kingdom	Peak	British Standard Institution (1995)
Leshchinsky's hybrid method	Hybrid	Leshchinsky (2001)

The consequence of selecting soil peak strength would lead to design GRS structures using the reinforcements with lower ultimate tensile strength. However, the design is likely unconservative side if the most of soil stress states within structures are actually close to residual strength. In the authors' opinion, the key of answering the argument above is to identify the soil stress state within GRS retaining structures specifically along the failure surface. For this purpose, the following parametric study was conducted to provide the numerical perspectives of view into this issue.

8.2.2 Parametric Study of Slope Model M3

In the parametric study, the simulation of centrifuge slope model M3 was conducted. The idea of the parametric study is similar to the previously discussed experimental studies by Zornberg (2002) and Zornberg et al. (1998). As shown in Table 6.1, the slope model M1 and M3 were reinforced using the same geotextile reinforcement, the same number of layers but using sand backfill placed at two different relative densities (70% and 50%). The test results showed the two slope modes failed at different failure g-level (50g and 36g).

It should be noted that the emphasis of this parametric study is not to verify again the proposed finite element model by comparing the predicted and measured results of slope model M3. The sole purpose of parametric study herein is to study soil strength properties governing structure stabilities by comparing the stress information available from two finite element models. The result of parametric study is expected to explain the observed difference of failure g-level due to different soil densities.

The arrangement of finite element model to simulate the centrifuge slope model M3 has no difference to that of slope model M1 discussed in Chapter 6 except for the parameter values applied for the selected soil model. First, the input soil density in this simulation is 15.7 kN/m^3 as the reported value for soil relative density of 50%. Further, as shown in Figs. 6.3, because of different soil densities, the soil behaves differently in peak strength and dilatancy magnitude. Table 8.2 compares the values of soil model parameters calibrated to the data of triaxial testing on Monterey No. 30 sand with relative density of 65% and 48% (close to the targeted densities 70% and 50% in centrifuge tests). The difference of soil behavior due to different soil densities has influence on the value of parameters η_1 and μ, which are the two main parameters to control the soil peak strength and the dilatancy magnitude, respectively.

Although the soil density will not influence soil residual strength, the values of soil-softening parameters in Table 8.2 change with different soil densities. This is because the values of soil-softening parameters are calibrated by referring to the yield surface at soil peak strength (S=1) which would change according to soil density. As a result, the values of soil-softening parameters changes with different soil densities, too. However, this does not indicate the residual strength of soil varies with different soil densities in the simulation. The values of other soil parameters are remained unchanged in the simulation. Figure 8.7 shows the predicted results of triaxial compression testing on Monterey No.30 sand with the relative density of 48%.

Last, as discussed previously in Section 6.1.2.3 and 6.2.2.1, the failure criterion parameter η_1 at relative density of 50% was multiplied by the strength increase ratio of 1.17(=tan(ϕ_{ps}=39.1^o)/tan(ϕ_{tc}=34.7^o)) to take account of plane strain conditions in the centrifuge tests. As a result, the failure criterion parameter η_1 under plain strain conditions was modified as 20.47(=17.5x1.17) in the simulation of slope model M3.

Table 8.2: Material parameters for Monterey No. 30 sand under different density conditions

		Monterey No. 30 sand	
Model component	**Parameter**	**D_r=65%**	**Dr=48%**
Elastic model	M, λ, ν	705, 0.257, 0.35	705, 0.257, 0.35
Failure criterion	m, η_1, a'	0.0214, 24 (29.3**), 0	0.0214, 17.5* (20.47**), 0
Plastic potential	ψ_2, μ	-8.51, 2.2	-8.51, 2.4*
Yield criterion	h, α	0.67, 0.2	0.67, 0.2
Hardening law	C, p	5.07E-05, 1.9	5.07E-05, 1.9
Softening law	Confining Pressures (kPa)	60.5, 115, 211	60.5, 115, 211
	a	0.75, 1.10, 1.88	2.41*, 1.93*, 1.78*
	b	165.4, 124.7, 54.3	89.9*, 54.67*, 39.29*
	f''_{pr}	41.19, 52.48, 85.68	44.83*, 88.96*, 106.03*

* Parameter value is adjusted according to different density conditions

** Parameter η_1 is adjusted according to the condition of centrifuge model

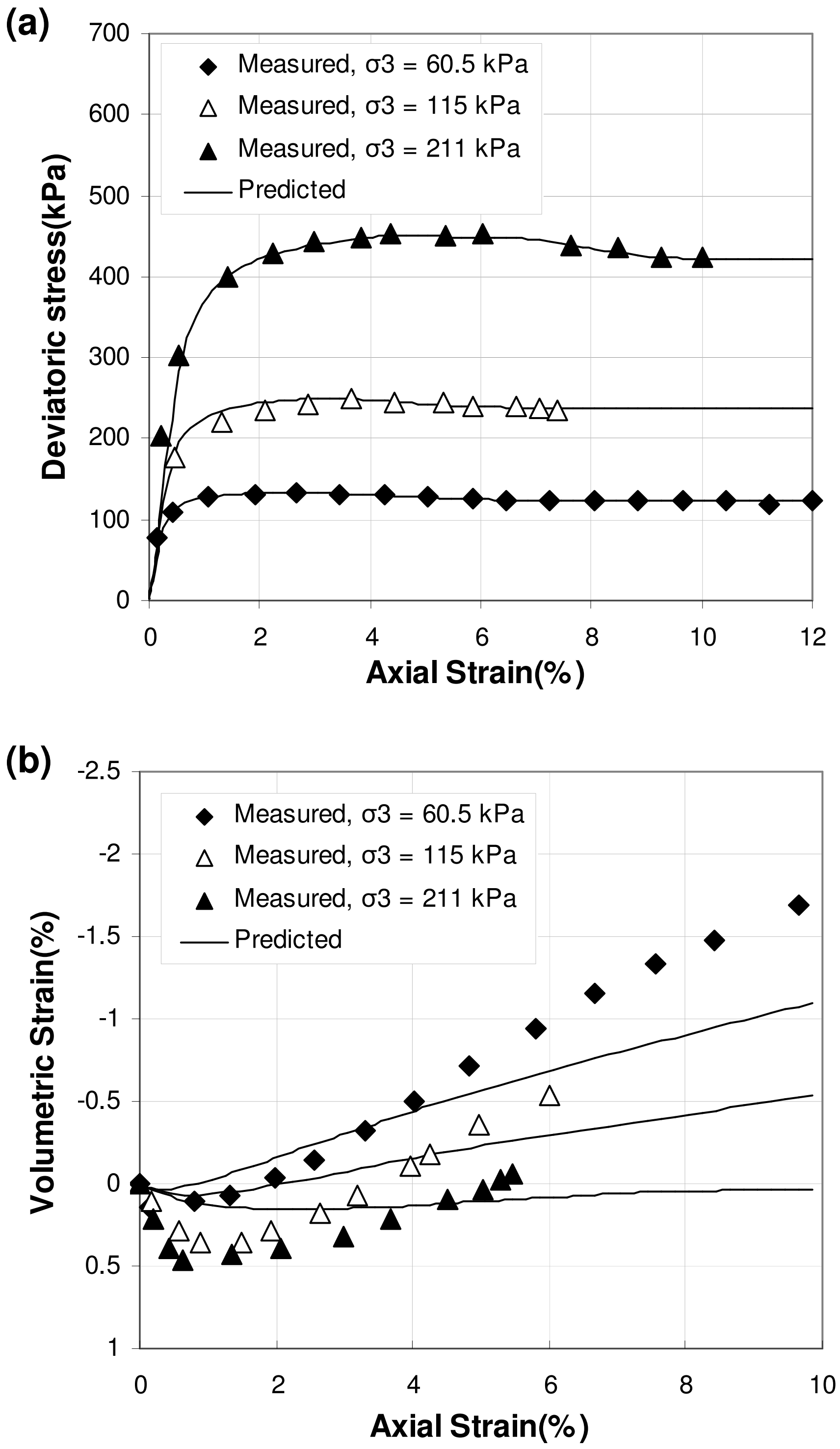

Figure 8.7: Predicted and measured results of Monterey No. 30 sand with D_r=48%: (a) deviatoric stress and axial strain; (b) volumetric and axial strain

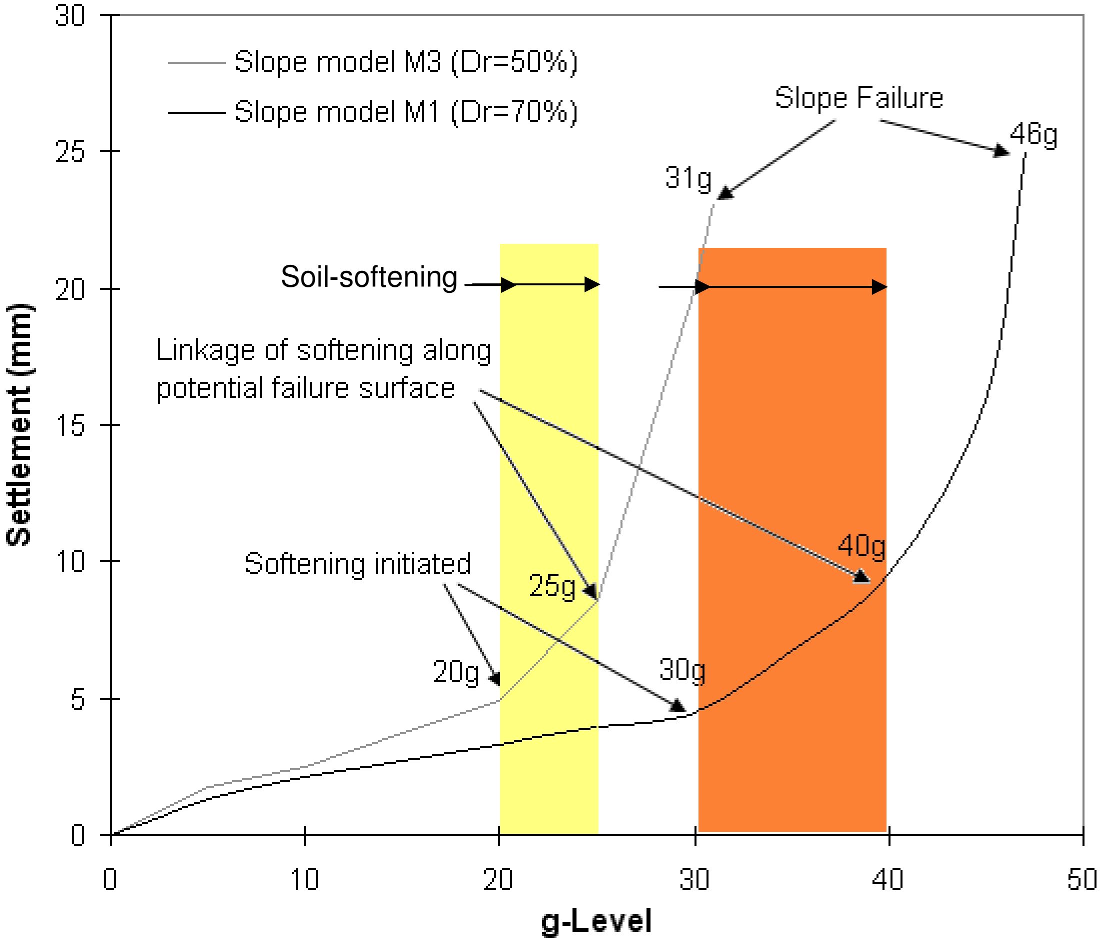

Figure 8.8: Status of soil-softening indicated in the settlement vs. g-level curve

8.2.3 Effect of Soil Strength on Slope Stability

The stress information obtained from the simulation is used to explain the observed difference of failure g-level due to different soil densities and to understand the soil strength properties governing structure stabilities. Figure 8.8 shows the measured settlement vs. g-level for slope model M1 and M3. The developed soil stress states observed from two simulations are also indicated in Fig. 8.8. The FE results of simulating centrifuge slope model M3 show the initiation of soil-softening occurs approximately at

20g, the linkage of soil-softening along failure surface is completed approximately at 25g and the slope model M3 fails approximately at 31g. Several observations from Fig. 8.8 are discussed as follows:

First, the FE results indicate the point of inflection in settlement (increase of settlement rate) corresponds to the status of soil-softening developed along the failure surface for both slope model M1 and M3. The first point of inflection indicates the initiation of soil-softening and the second one indicates the completed linkage of softening along failure surface. Separated by these two points of inflection, the slopes of settlement curve can be divided into three approximately linear sections corresponding to before, during and after soil-softening is developed along the failure surface.

Second, by comparing two slope models in Fig 8.8, it is observed the initiation of soil-softening and the failure of slope occur earlier for the slope model M3. In addition, the duration of soil-softening (from the initiation of soil-softening to the completed linkage of soil-softening) for the slope model M3 is also shorter. This numerical observation agrees with the experimental observation by Zornberg et al. (1998). The physical explanation for the observation above is because of different soil peak strengths due to different soil densities for slope model M1 and M3.

The physical effect of different soil peak strengths is modeled by using different input values of failure criteria parameter η_1 in the simulation. The failure criteria parameter η_1 represents the size of peak failure envelope of soil illustrated in Fig. 8.9a from the view of octahedral plane and in Fig. 8.9b from the view of triaxial plane. Because of lower soil density, the η_1 in the simulation of slope model M3 is lower than that of slope model M1. Accordingly, the size of peak failure envelope is smaller than that of slope model M1. Before applying centrifugal force, the developed soil stresses are negligible and stress state of soil is probably close to the origin of octahedral plane.

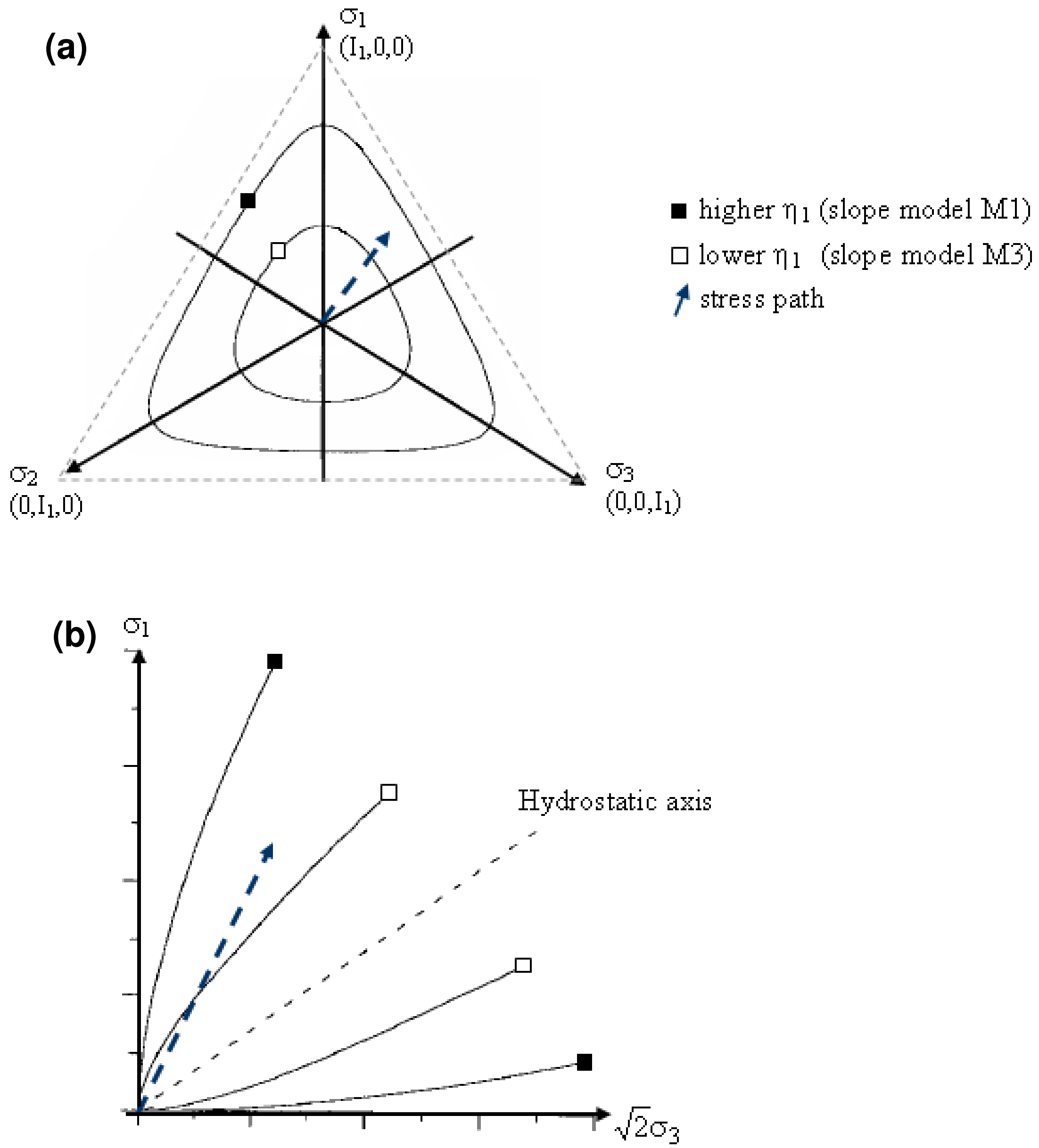

Figure 8.9: Illustration of failure envelope and stress path in the: (a) octahedral plane; (b) triaxial plane

Subsequently, with the same increment of g-level, the development of soil stresses follow the similar loading path for two slope models. As shown in Fig. 8.9, the loading path will reach the peak failure envelope of slope model M3 (the smaller failure envelope) first before reaches that of slope model M1 (the larger one). When the soil stresses reaches the peak failure envelope, the soil-softening initiated immediately. Therefore, the initiation of soil-softening for the slope model M3 is earlier. Because two slope models have same soil residual strength and reinforcement tensile strength, the failure of slope model M3 also occurs earlier.

Third, one can view the failure envelope of soil as the resistance and the g-level as the driving force in the slope system. It can be found that the ratio of resistance in two slope models approximately equals to the ratio of driving force, demonstrated as follows:

$$\frac{\eta_{1(M1)}}{\eta_{1(M3)}} = \frac{29.3}{20.47} = 1.43 \tag{8.1}$$

and

$$\frac{N_{g(M1)}}{N_{g(M3)}} = \frac{46g}{31g} = 1.48 \tag{8.2}$$

The comparison above indicates in the numerical simulation the failure of slope is governed by the peak failure criteria of soil. In other words, the failure of slope is governed by the soil peak strength by the physical meaning. This observation supports the experimental conclusion by Zornberg et al. (1998). From the experimental studies, they concluded the soil peak strength governs the stability of GRS structures. As a result, they recommended the use of the peak shear strength parameters in the design of GRS structures as the common practice in the US.

It should be cautious to adopt the conclusion of selecting soil peak strength in the design of GRS structures. The conclusion above is based on results of numerical analysis of centrifuge tests. In centrifuge test, the initial soil stresses developed within slope model are almost negligible at beginning of centrifuge loading, as illustrated in Fig 8.10. Therefore, the soil stress state first has to cross the *threshold* of soil peak shear strength before reaches its residual shear strength. Therefore, the peak strength would govern the system stability in this case. However, providing a GRS retaining structure is design under soil active conditions and all the reduction factors and factor of safety are not considered (design without conservatism), one may expect the standing point of current soil stress state after construction is already under its peak shear strength. Any further deformation due to traffic loading would cause the soil stress state to cross its peak shear strength and advance to large soil strain conditions. Under this circumstance, the soil shear strength in post-peak region and the tensile strength of reinforcement would maintain the stability of system.

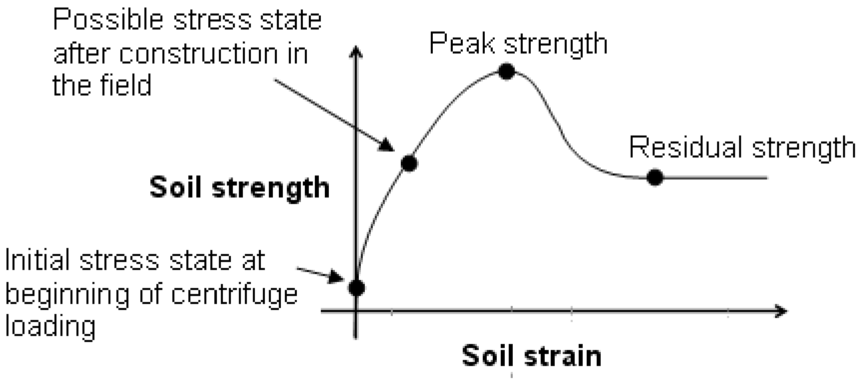

Figure 8.10: Schematic illustration of soil stress states in the centrifuge test and in the field

This can be demonstrated by comparing the increase of g-level of two slope models from all soils along failure surface reaching peak strength to the failure of slope. The increase of g-level from all soils along failure surface reaching peak strength to the failure of slope for both slope models is 6g (46g-40g for slope model M1 and 31g-25g for slope model M3). The same value of the increase of g-level for two slope models is because two slope models have the same soil residual strength and ultimate tensile strength of reinforcements.

8.2.4 Suggestion for Current Practice

As the discussion above, the key for the selection of soil strength properties for the design of GRS structures is to know the soil stress states developed along the failure surface after construction. If the developed soil stress state along failure surface is below soil peak shear strength, soil peak shear strength will control system stability. If the developed soil stress state reaches or crosses the soil peak shear strength, the soil shear strength in the post-peak region and the reinforcement tensile strength maintain system stability.

Unfortunately, the information of soil stress state is not easy to be obtained unless the analysis using the finite element method equipped with the soil-softening model and advanced stress integration algorithm is conducted. Even though the determination of actual stress states within GRS structures is a problem, for the general practice the GRS structures are designed for its serviceability under working stress conditions by the consideration of a high factor of safety. In addition, the stability contributed by the facing elements is often ignored in the design. Also, past performance of GRS structures has provided strong evidence that methodologies in current design are overly conservative.

By all reasons above, the actual soil stress states within GRS structures are presumed not to reach its peak strength, as indicated in Fig. 8.10. Under this circumstance, the stability of structures is controlled by soil peak strength and, accordingly, the use of the peak shear strength parameters in the design of GRS structures as the common practice in the US should be recommended.

8.3 MOBILIZATION OF REINFORCEMENT TENSIONS

8.3.1 Background

As discussed previously in Section 1.3.1.3, there are two concepts of considering the mobilization of reinforcement tensions in the limit equilibrium analyses of reinforced structures. In Method A, the reinforcement forces used in the analysis are allowable forces and are not divided by the factor of safety calculated during the slope stability analysis. The factor of safety in the slope stability analysis is defined as the ratio of the mobilized soil stress to the peak soil shear strength, as shown in Eq. (1.1). Therefore, the mobilized reinforcement strength is constant as the input value through entire analysis. In Method B, the reinforcement forces used in the analysis are ultimate forces and are divided by the factor of safety calculated in the slope stability analysis. The factor of safety in the slope stability analysis is defined as the ratio of the peak soil shear strength to the mobilized soil stress as well as the ratio of the reinforcement ultimate tensile strength to the mobilized reinforcement tensions, as shown in Eq. (1.2). Therefore, the mobilized reinforcement strength corresponding to the mobilized soil strength follows a 1:1 relationship, which is also called a balanced factor of safety.

The mobilization of reinforcement strength corresponding to the mobilization of soil strength in Method A and B is illustrated in Fig. 1.4. It has been discussed that the constant reinforcement strength designated in Method A fails to reflect the real case that reinforcement strength is mobilized with the mobilization of soil strength. In addition, the 1:1 relationship between the mobilized reinforcement strength and the mobilized soil strength implied in Method B is also questionable. Should the same factor of safety for soil be used for reinforcements? If different factors of safety are used for soil and reinforcements, is there any relationship and correlation between these two factors of safety or just two independent values?

These questions could be potentially answered by examining the mobilization of reinforcement tensions corresponding to the mobilization of soil strength using the stress information obtained in the simulation. This information can also potentially help to explain the conservatism of design methods in current design guidelines.

8.3.2 Development of Reinforcement Tensions with G-Level

Figure 8.11 shows the mobilization of reinforcement tensions with g-level for the simulation of slope model M1. The reason of almost no reinforcement tension developed in the first reinforcement layer has already been discussed in Section 7.5. This is because the influence of boundary conditions at the base of foundation is transferred through the firm shallow foundation to the area approximately below the second layer of reinforcement. As a result, the developed strain and tension in the first layer of reinforcement are negligible. Allen et al. (2003) addressed the similar effect of stiff competent foundations on the attenuation of reinforcement loads at the base of the wall.

The reinforcement tensions at 30g are highlighted using red bold line in Fig.8.11. The g-level of 30g corresponds to the g-level when soil along the failure surface first reaches its peak strength and soil-softening is initiated. It is clear that the tension at each reinforcement layer is barely mobilized before soil-softening occurs. Afterward, the reinforcement tensions start to be mobilized evenly with each increment of 5g.

Figure 8.12 shows the development of peak reinforcement tension at each reinforcement layer subjected to the increasing g-level. In order to quantify the mobilization of reinforcement tensions, the reinforcement stress level S_R is defined as:

$$S_R = \frac{T_m}{T_{ult}} \tag{8.3}$$

where T_m is the mobilized reinforcement tension; T_{ult} is the ultimate tensile strength of reinforcement which is 0.124 kN/m used in the simulation. Figure 8.12 shows only less than 10% of reinforcement strength is mobilized before soil-softening occurs. Afterward, reinforcement strength is evenly mobilized approximate 16% with each increment of 5g.

Similar observations were reported by Bathurst (1993) and Karpurapu Bathurst (1995) as discussed in Section 7.5.Two instrumented large-scaled GRS retaining walls in 3m height were tested in the RMC retaining wall test facility. Both walls were taken to collapse under stage uniform surcharge pressure applied to the top of walls. They observed the load began to be shed from backfill to the extensible geosynthetic reinforcing layers after the soil failed which was identified by the observation of a well-developed shear plane within GRS walls.

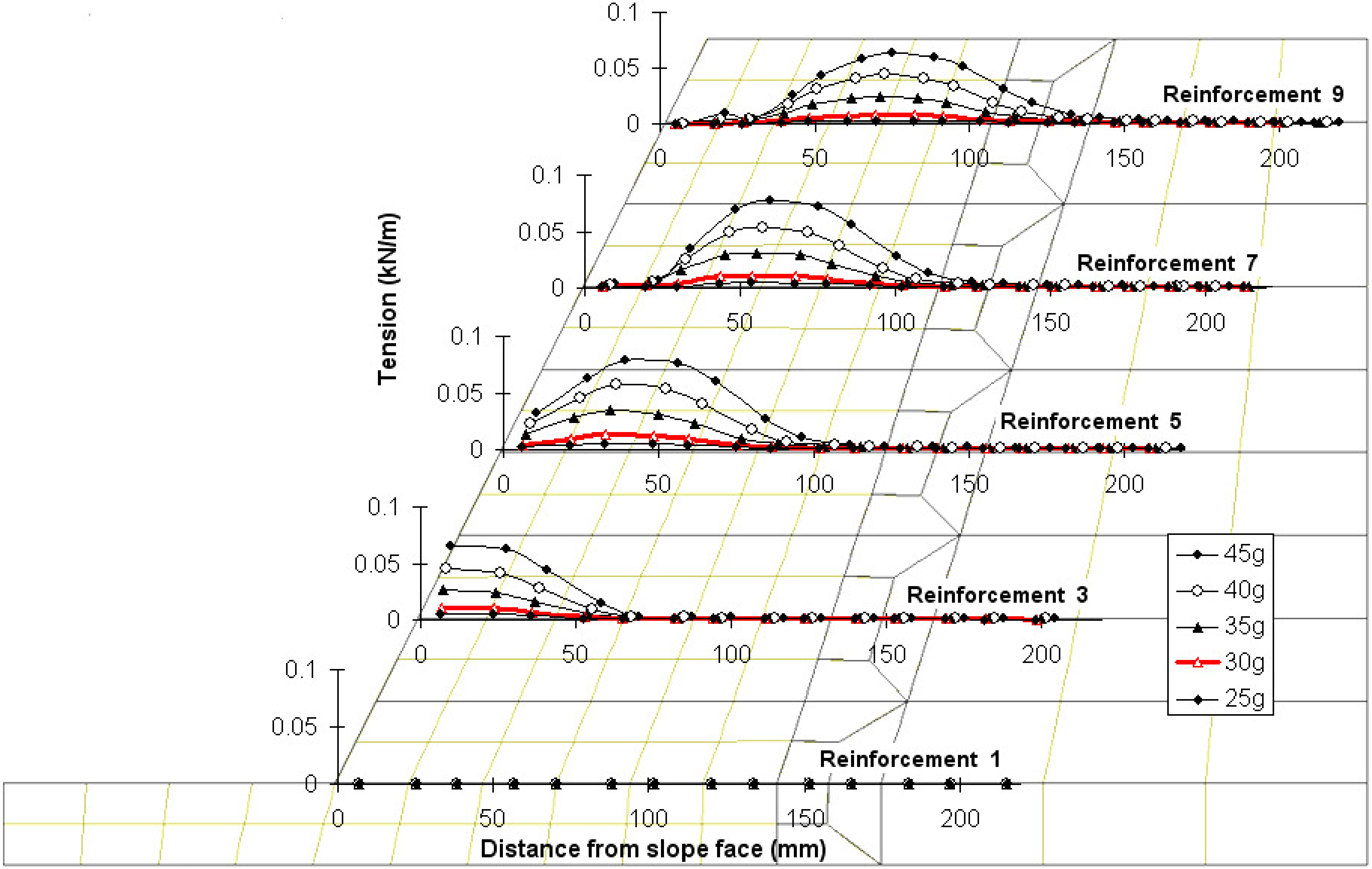

Figure 8.11: Mobilization of reinforcement tensions

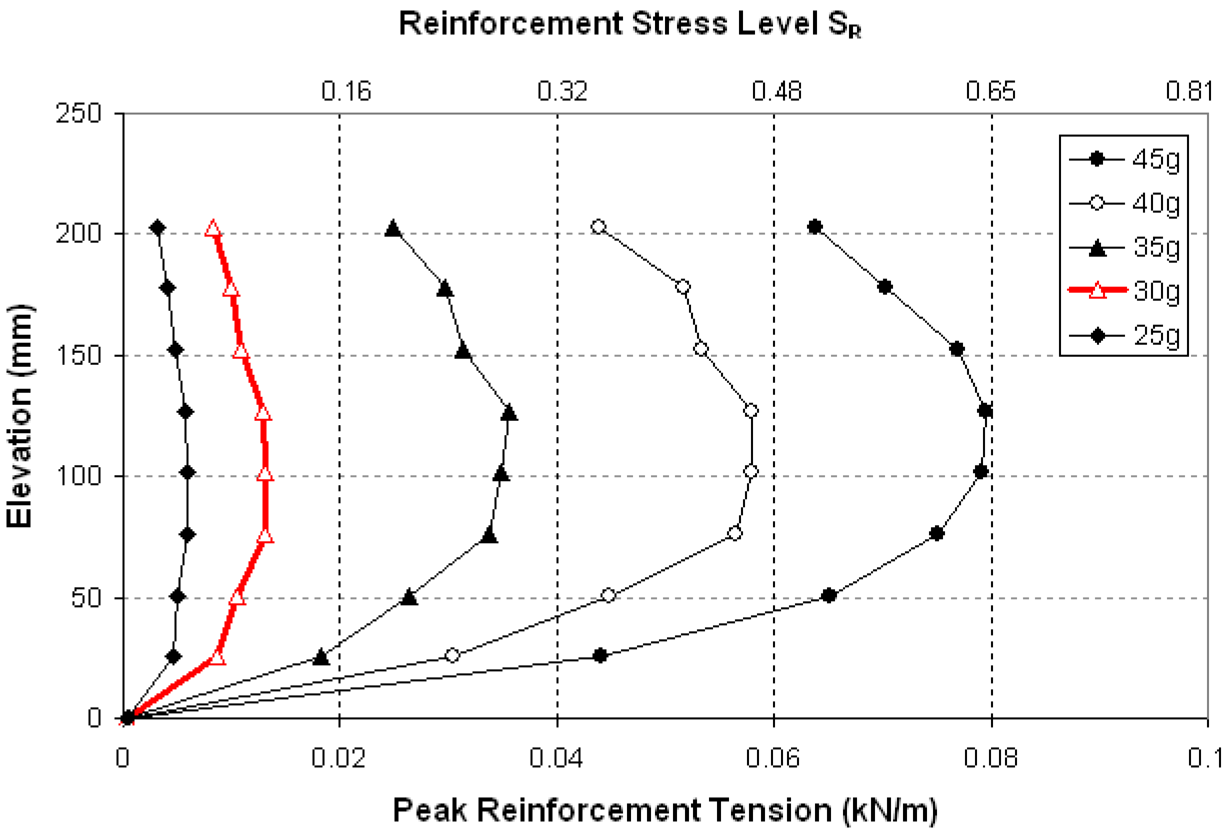

Figure 8.12: Mobilization of peak reinforcement tensions with depth

8.3.3 Distribution of Peak Reinforcement Tensions

Because solving the general problem of GRS structures in limit equilibrium analysis is statically indeterminate, the determination of the peak tension developed at each layer of reinforcement requires assumptions. The distribution of peak reinforcement tensions with depth has been known mainly function of structure face inclination (slope or wall), reinforcement type (extensible or inextensible) and the stability status of structures (working stress or large soil strain conditions).

As discussed previously in Section 2.3.2, current design methodologies assume a triangular distribution (proportional to the overburden pressure) with depth for geosynthetic walls and slopes (see Fig. 2.4a). However, the measured field data shows nearly uniform mobilization of reinforcement strength with depth for GRS walls under working stress conditions (Allen et al. 2003, Bathurst et al. 2008) (see Fig. 2.4b). For GRS slopes, a series of centrifuge testing on reinforced soil slopes under working stress conditions (Zornberg and Arriaga 2003) and failure conditions (Zornberg et al. 1998) was conducted. In their analysis, digital image analysis techniques are used to determine the displacement distribution along reinforcement layers in reduced-scale models subjected to increasing *g* levels. Then, a sigmoid function was introduced to fit raw displacement data and estimate the strain distribution along reinforcement layers.

They found the pattern of reinforcement peak strains with height obtained for pre-failure conditions is similar to that obtained for failure conditions. The results of analyzed reinforcement strains shows the distribution of peak reinforcement forces with depth does not follow a triangular distribution conventionally assumed in current design methods. The location of the reinforcement maximum peak strain does not occur near the toe of the structure, but was located approximately at midheight of the reinforced slopes (for 2V:1H slopes), at the point along the critical failure surface directly below the crest of the slope (see Fig. 2.4c).

By the observation from the results of the numerical simulation shown in Fig. 8.12, the distributions of peak reinforcement tensions for GRS slopes under working stress (below 30g) and large soil strain conditions (over 30g) are proposed in Figs. 8.13.

For GRS slopes under working stress conditions, the distribution of peak reinforcement tensions with depth is nearly uniformly with the depth at low g-level before the soil-softening is initiated (see Fig. 8.13a). This distribution agrees with the field observation from the instrumented GRS walls under working stress conditions (Allen et al. 2003, Bathurst et al. 2008).

For GRS slopes under large soil strain conditions, the distribution of peak reinforcement tensions at high g-level is more like a trapezoidal shape with the location of the reinforcement maximum peak strain located approximately at midheight of the reinforced slopes (see Fig. 8.13b). This observation in generally agrees with the experimental observation from centrifuge testing on GRS slopes at failure conditions (Zornberg et al. 1998). Analysis of reinforcement strain results shows a clear maximum peak strain developed at one reinforcement layer located approximately at midheight of the reinforced slopes for slopes near failure conditions. However, in the simulation in this dissertation, the peak reinforcement tensions developed at the reinforcement layers 4, 5 (middle layer) and 6 are approximately equally mobilized. The locations of maximum peak reinforcement strains observed in the centrifuge model and finite element model are compared in Fig. 8.14.

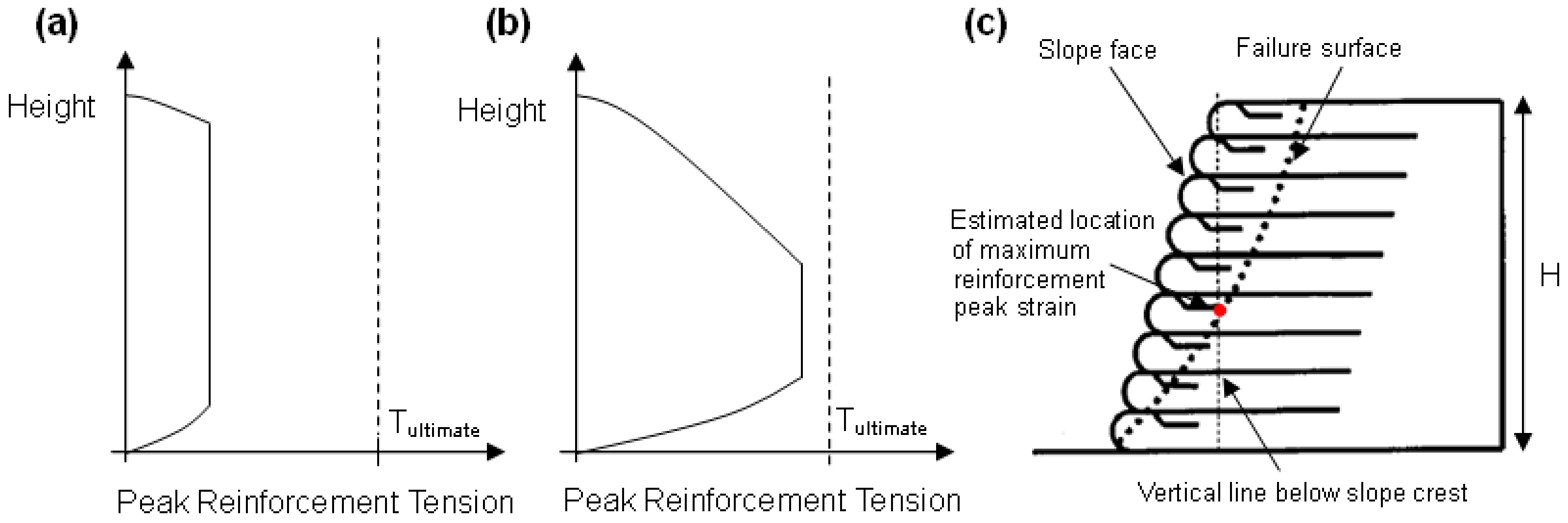

Figure 8.13: Proposed distribution of peak reinforcement tensions with height: (a) uniform shape for working stress conditions; (b) trapezoidal shape for large soil strain conditions; (c) schematic cross section of a GRS slope

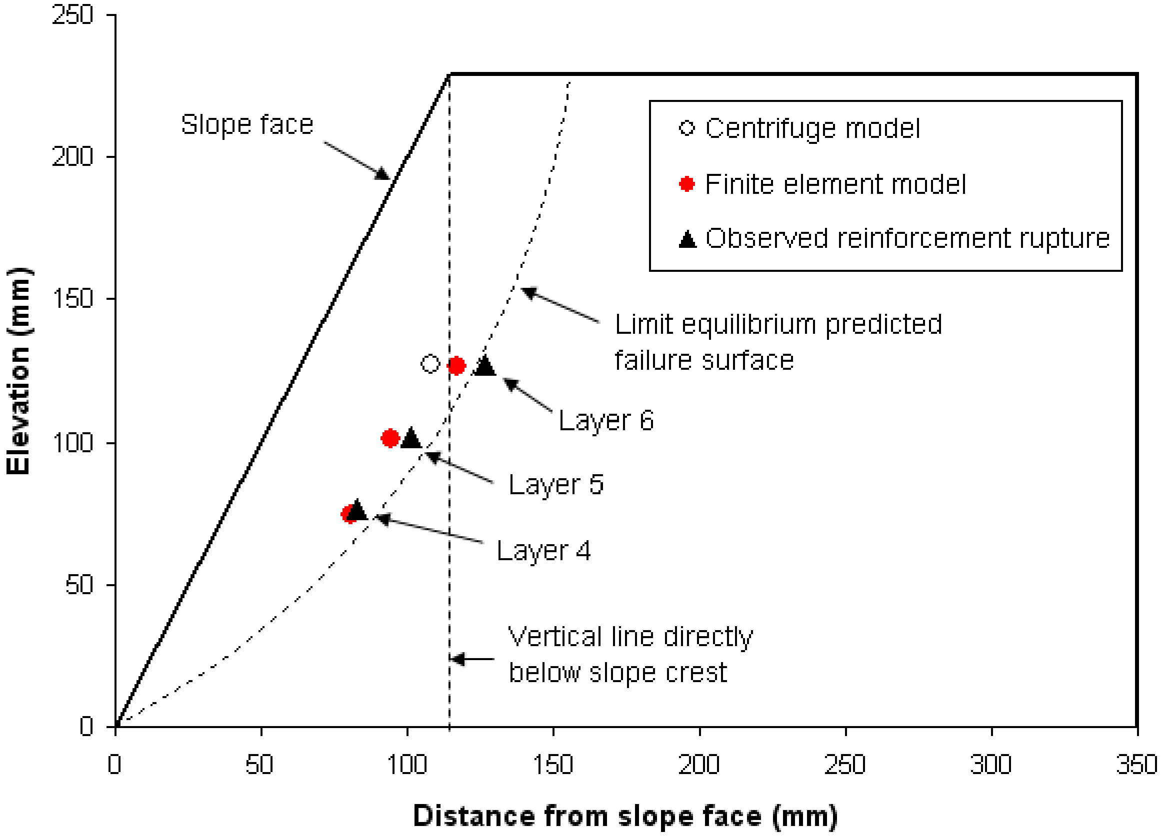

Figure 8.14: Comparison of the observed locations of maximum peak reinforcement strains

8.3.4 Mobilization of Reinforcement Tension and of Soil Shear Strength

In this section, the mobilization of reinforcement tensions corresponding to the mobilization of soil strength is investigated. Because the stresses of soils and reinforcements developed along the failure surface are critical factors for the system stability, focus of this evaluation will specifically be placed along the failure surface. The mobilization of reinforcement tensions is quantified by the reinforcement stress level S_R defined in Eq. (8.3). Table.8.3 summaries the peak reinforcement stress level S_R at each reinforcement layer subjected to the increasing g-level. The mobilization of soil strength is obtained from soil stress level S at the Gaussian point in close proximity to the location of peak reinforcement stress level at each reinforcement layer. The corresponding soil stress level S is summarized in Table 8.4.

The generic definition of factor of safety is the available soil shear strength divided by the mobilized soil stress needed for equilibrium. The soil stress level is defined as the mobilized soil strength divided by the soil peak strength. Two definitions have an inverse relationship. Therefore, the soil stress level can also be obtained by the inverse of factor of safety from the limit equilibrium analysis in Section 6.1.5. The soil stress level obtained from the limit equilibrium analysis is an average value through entire failure surface. Therefore, the soil stress levels along the failure surface obtained from finite element analysis are averaged for the purpose of comparison. The results are compared to those obtained from limit equilibrium analyses shown in Figure 8.15.

Fig. 8.15 shows that the limit equilibrium analyses underestimate the developed stress level at each increment of g-level. The limit equilibrium analysis of GRS slopes conducted in Arriaga's study (2003) is categorized as Method A.

Table 8.3: Reinforcement stress level with different g-levels

Reinforcement Stress Level, S_R					
Layer	25g	30g	35g	40g	45g
9 (Top)	0.025	0.067	0.201	0.355	0.515
8	0.033	0.08	0.24	0.417	0.567
7	0.039	0.088	0.253	0.429	0.621
6	0.046	0.104	0.287	0.467	0.641
5	0.048	0.105	0.282	0.467	0.638
4	0.048	0.106	0.273	0.455	0.605
3	0.04	0.084	0.212	0.361	0.525
2	0.037	0.07	0.147	0.246	0.356
1 (Bottom)	0.003	0.003	0.003	0.004	0.004
Average	0.039	0.088	0.237	0.400	0.558

* S_R in the first layer of reinforcement is not included in the average

Table 8.4: Soil stress level with different g-levels

Soil Stress Level, S					
Layer	25g	30g	35g	40g	45g
9 (Top)	0.9	1.02	1.03	1.06	1.08
8	0.81	0.925	1.02	1.03	1.07
7	0.82	0.92	1	1.02	1.07
6	0.82	0.92	1.03	1.04	1.08
5	0.86	0.945	1.04	1.04	1.06
4	0.89	0.96	1.02	1.03	1.05
3	0.92	1.01	1.03	1.04	1.06
2	1	0.94	1	1.03	1.06
1 (Bottom)	0.75	0.8	0.86	0.9	0.93
Average	0.863	0.938	1.003	1.021	1.034

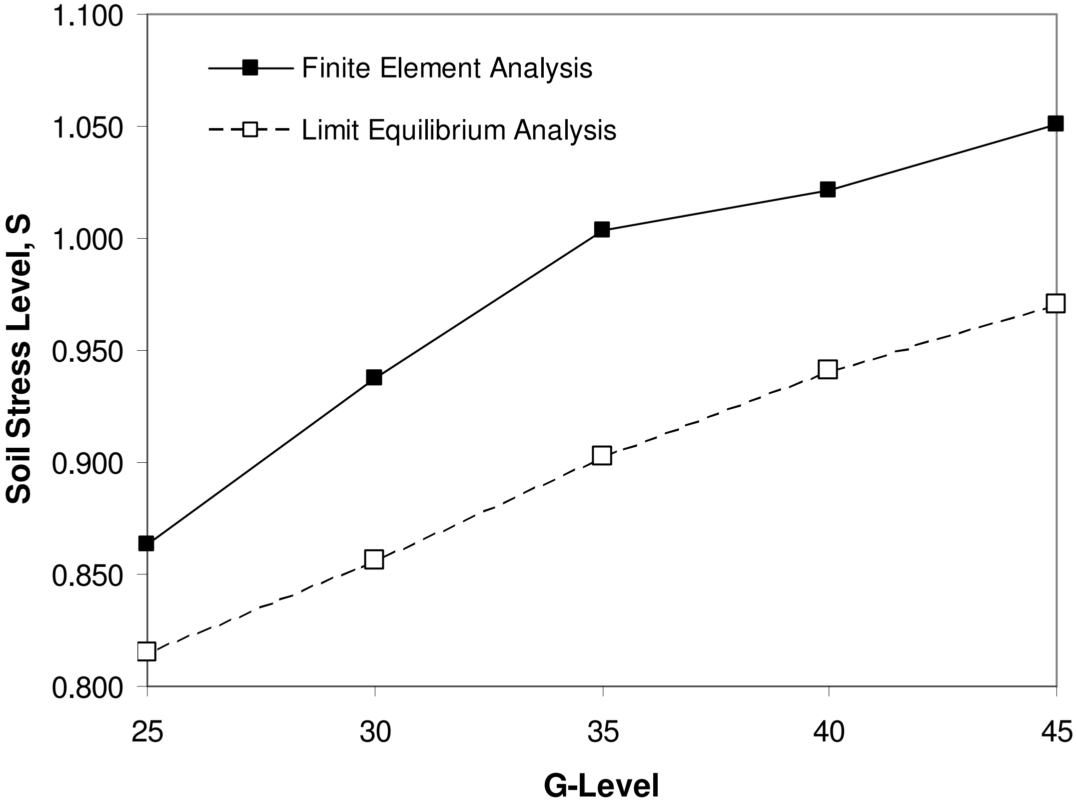

Figure 8.15: Comparison of soil stress level obtained from finite element and limit equilibrium analyses

In Method A, the reinforcement strength used in the analysis is a constant value and not divided by the factor of safety calculated during the slope stability analysis. This indicates that the reinforcement tensile strength has been already fully mobilized at beginning of the analysis, which would depress the requirement of mobilization of soil strength for equilibrium during the slope analysis. It may be argued that the finite element analysis used the actual mobilized reinforcement forces would lead to the calculation of the mobilized soil strength more accurately. As a result, only the soil stress level from the finite element analysis is used in the following discussion.

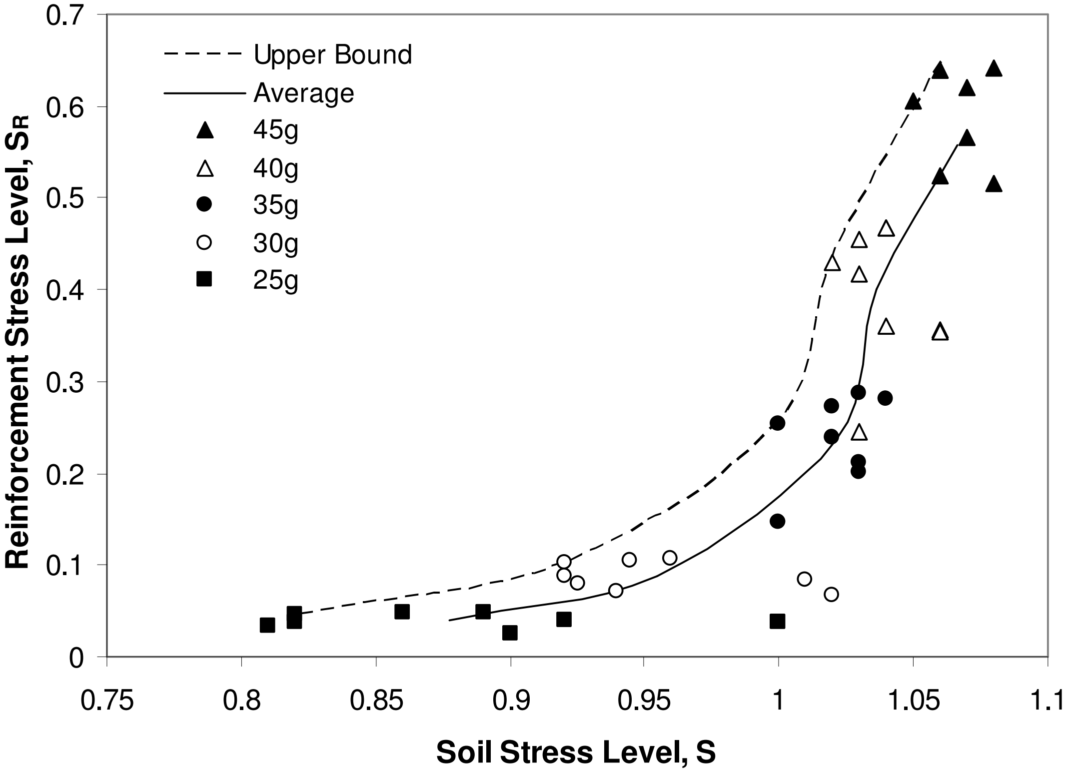

Figure 8.16: Comparison of the mobilization of reinforcement tensions and of soil strength

The mobilization of reinforcement tensions and soil strength subjected to the increasing of g-level are compared in Figure 8.16. As indicated in Figure 8.16, the variations of *S* are observed at low g-level and the scatter of S_R is observed at high g-level. It implies the mobilization of soil strength is not homogenous along the failure surface at low g-level and becomes more homogenous at high g-level. Oppositely, the mobilization of reinforcement tensions at each layer is uniform at low g-level and becomes non uniform at high g-level as discussed in Section 8.3.3. Because of the scatter, it would be more meaningful to focus on the average and upper bound value of reinforcement stress level. The average value of reinforcement stress level is obtained by the average of reinforcement stress level at each layer except for that at reinforcement layer 1. Because the developed tensions in the first layer of reinforcement are negligible, the S_R in the first layer of reinforcement is not included in the average. The upper bound value represents the mobilization of maximum peak reinforcement tension at each g-level.

The most important observation in Fig. 8.16 is the mobilization of reinforcement tensions is disproportional to the mobilization of soil strength. The mobilization trend can be grouped into two stages. In the first stage, the mobilization of reinforcement tensions is increased slightly up to approximate 10% of its ultimate tensile strength when the average of mobilized soil strength along the failure surface reaches 95% of its peak strength. During the second stage, when the average of mobilization of soil strength exceeds 95%, the reinforcement tensions start to be mobilized rapidly. Even so, still over 30% of average reinforcement strength has not been mobilized yet when the average of mobilized soil strength reaches its peak strength (S=1).

Field data from closely monitored prototype scale walls to support the numerical observation above is very little (if any). This is because the field test is mainly emphasized on working stress conditions. Two instrumented large-scaled GRS walls, as discussed in Section 7.5, were found to be tested to the failure in the RMC facility (Bathurst 1993, Bathurst and Benjamin 1990, Bathurst et al. 1989, Karpurapu and Bathurst 1995). The walls were taken to collapse under stage uniform surcharge pressure applied to the top of walls. The loading stages for two walls are indicated in Fig. 7.8. The earliest geogrid reinforced soil wall models constructed in the RMC facility were built using a high strength uniaxial polyethylene geogrid (Tensar SR2). However, the structures could not be failed with the surcharge capacity at hand when this product was employed (Bathurst et al. 1987). For this reason, other tests were carried out using a weaker and more extensible biaxial polypropylene geogrid (Tensar SS1) oriented with its weakest direction in the plane strain direction of the wall. Although this material has not been used for retaining wall construction but its use in their study ensured that collapse of structures could be anticipated.

The reinforcement strains of two instrumented large-scaled GRS retaining walls were intensively monitored with the increase of surcharge. The strains developed at each reinforcement layer corresponding to the various surcharges increment are provided in Figure 8.17 and 8.18. The data of reinforcement strains can be used to examine the mobilization of reinforcement tensions in the field and compare with the numerical results. By using the reinforcement load-extension response reported by Bathurst (1993), the reinforcement strains can be converted into the mobilized tensions and, further, to the mobilization of peak tension S_R at each reinforcement layer by dividing the mobilized tensions by the ultimate tensile strength of reinforcements as reported of 12 kN/m. Similar to the discussion in Section 8.3.2, due to the influence of stiff concrete foundation used on the attenuation of reinforcement loads at the base of the wall, the developed reinforcement strains in the first reinforcement layer are very little in both walls. As a result, the calculated S_R in first layer of reinforcement is negligible and not included in the further analysis.

The soil failure in large-scaled GRS wall tests was identified by the observation of a well-developed shear plane. Therefore, the average soil stress level S corresponding to this stage is most likely equal to 1.0 or slightly larger than 1.0 as discussed in Section 7.5. Because the soil stress levels along the failure surface before or after the soil failure can not be directly quantified by the reported information, the development of soil stress levels are assumed uniform along the failure surface and proportional to the stage of applied surcharge. The S is given as zero at end of construction before the application of surcharge.

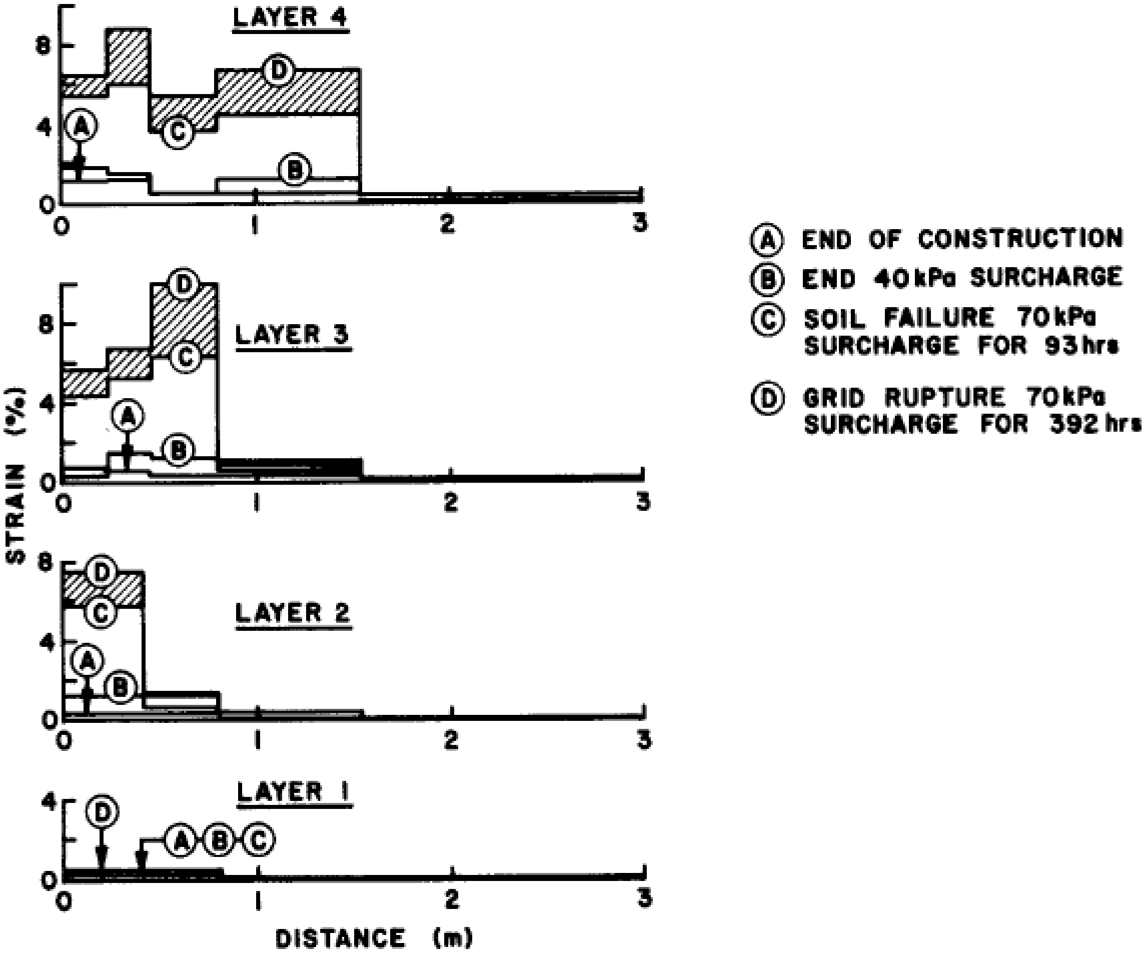

Figure 8.17: Mobilized reinforcement strains within incremental panel GRS wall (Bathurst et al. 1989)

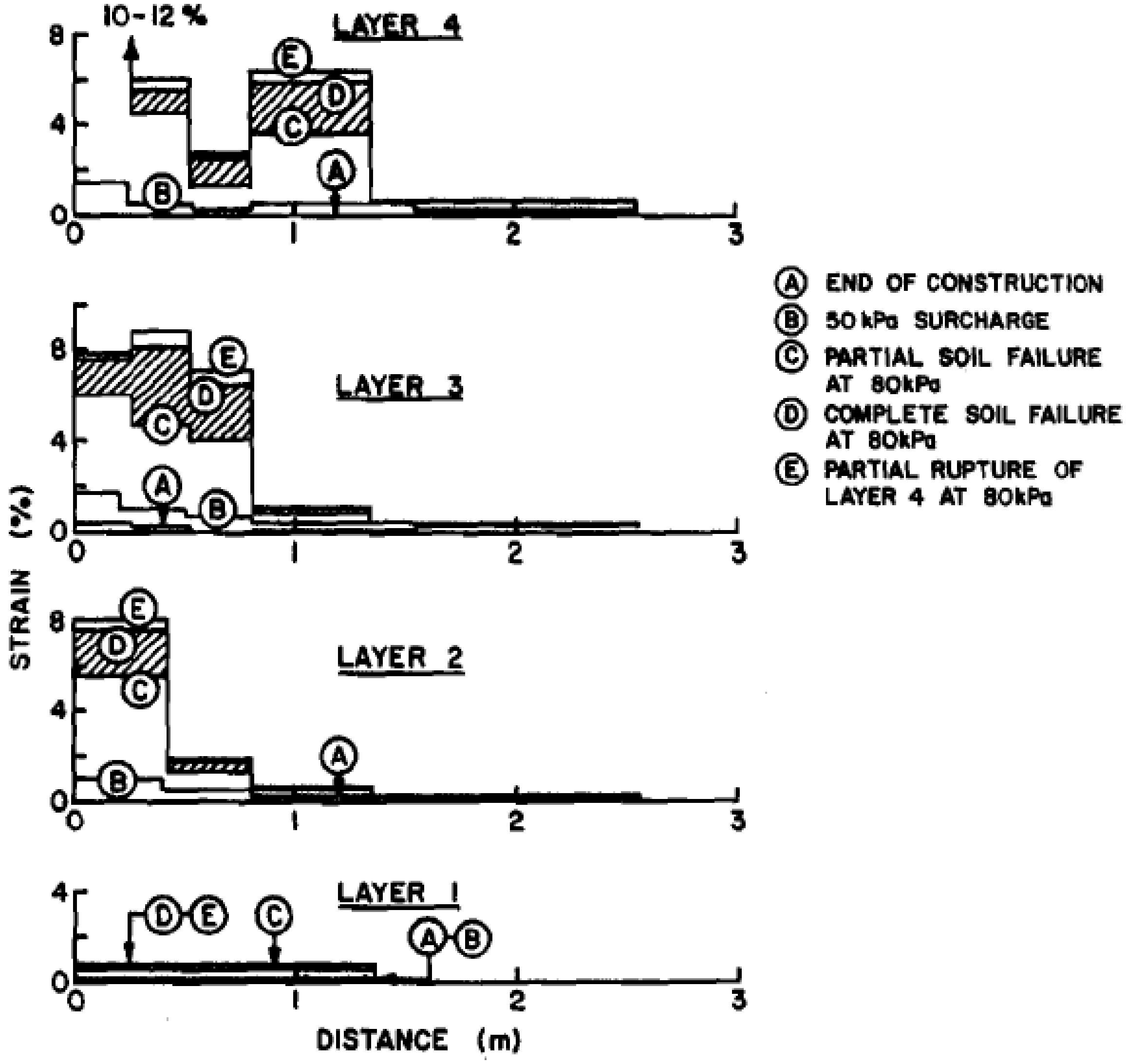

Figure 8.18: Mobilized reinforcement strains within full-height panel GRS wall (Bathurst and Benjamin 1990)

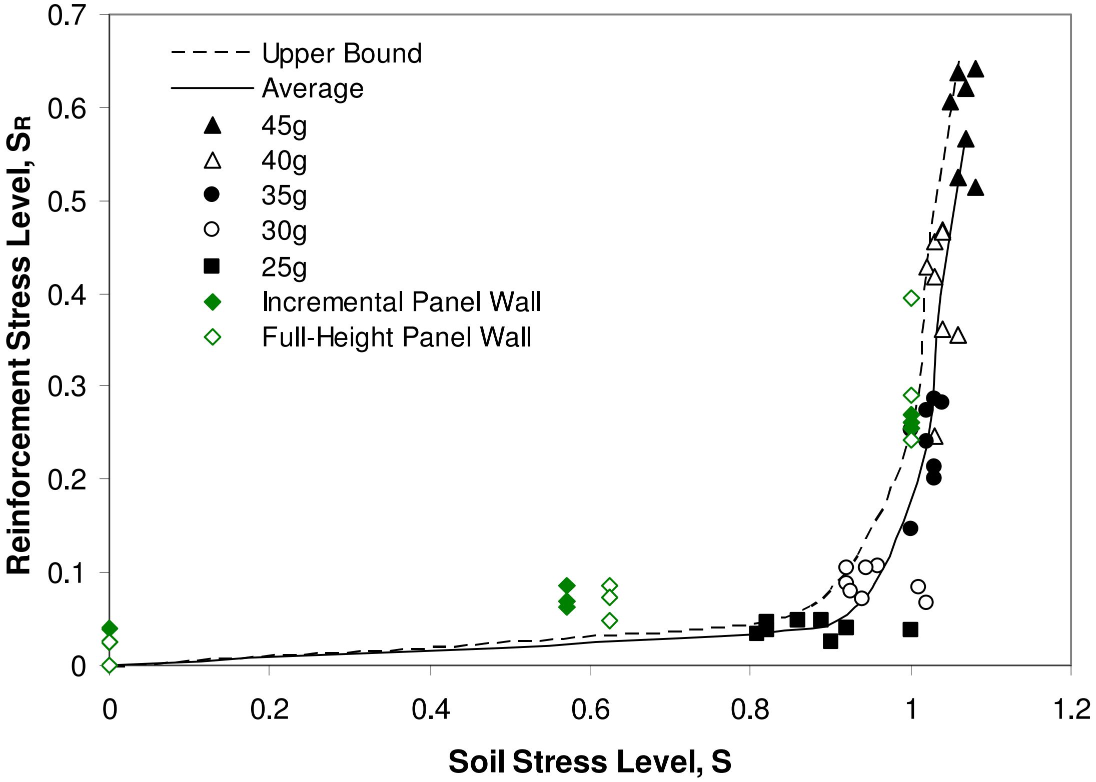

Figure 8.19: Comparison of the mobilization of reinforcement tensions and of soil strength (incorporate the data from two instruments walls)

Figure 8.19 indicates the result obtained from two instrumented walls. The results also show a rapid increase of the mobilization of reinforcement tensions. The reinforcement stress level S_R is generally higher than those obtained from numerical analysis of centrifuge tests when $S<1$. The difference of reinforcement stress level may be contributed from compaction which is not included in the centrifuge tests. Although the observed trend in Fig. 8.19 may be anticipated to vary with the stiffness of system (i.e., the stiffness of soil and reinforcement), in general, the results obtained from two instrumented walls follow the similar trend of those obtained from numerical analysis of centrifuge tests.

8.3.5 Explanation of the Strength Mobilization Using Soil Mechanics

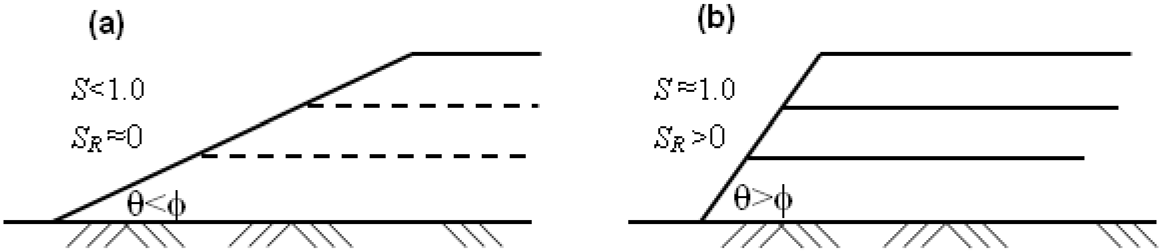

Figure 8.20: Schematic illustration of the effect of reinforcement in two slopes with different slope angles

Both numerical results and data from instrumented walls show that reinforcement tensions are only mobilized after soil strength reaches its peak strength. This observation can be justified by a simple example illustrated in Figure 8.20. The focus of the example in Fig. 8.20 is to compare the mobilization of reinforcement tensions in two slopes with different slope angles. In Slope A (Fig. 8.20a), the slope angle is less than the friction angle of the backfill. Stability of the slope can be maintained by the soil itself from the mobilized soil strength. Because the slope angle is less than the friction angle of backfill, the soil strength will not be fully mobilized (S<1.0). The slope can stand stably even without the help of from reinforcements. The presence of reinforcements will barely contribute to the slope stability; therefore, the mobilization of reinforcement strength is expected to be negligible ($S_R \approx 0$).

At Slope B (Fig. 8.20b), the slope angle is greater than the friction angle of backfill. Even the full mobilization of soil peak strength (S≈1.0) is not sufficient to sustain the slope stability. The slope needs the help from reinforcements. The presence of reinforcements will improve the slope stability by the mobilization of reinforcement strength (S_R>0).

To conclude from the discussion above, the effect of reinforcement only takes place when soil needs help, the soil strength is fully mobilized. This statement supports that the increase of the mobilized reinforcement strength is observed after soil reaches it peak strength in the numerical simulation.

The knowledge of the behavior of frictional materials under shearing can be applied to explain the mobilization of reinforcement tensions after soil strength is fully mobilized. The experimental results of conventional triaxial compression test on Toyoura sand conducted by Suzuki and Yamada (2006) is shown in Figs. 8.21. They described when soil is in pre-peak region, the soil adjusts it volumetric strain by dilatancy to accommodate the increase of loading and sustain system equilibrium. When soil reaches it peak strength, the ratio of volumetric strain increment $d\varepsilon_v$ to the axial strain increment $d\varepsilon_a$ also reach its maximum values, as shown in Fig 8.21c. After soil crosses peak strength and in post-peak region, the volumetric dilatancy attenuates and even decreases to zero at soil residual strength.

The similar behavior is observed from the experimental results of triaxial compression test on Monterey No. 30 sand shown in Figs. 8.22. It is found when soil reaches it peak strength at ε_a=3%, the ratio of volumetric strain increment $d\varepsilon_v$ to the axial strain increment $d\varepsilon_a$ also reach its maximum values at ε_a=3%. Accordingly, by author's own interpretation, after soil crosses peak strength along the failure surface in the centrifuge test, the ability of adjusting the volumetric strain by dilatancy to accommodate the increase of loading is attenuated. The reinforcement tensions then start to be mobilized to accommodate the increasing loading and to maintain system equilibrium.

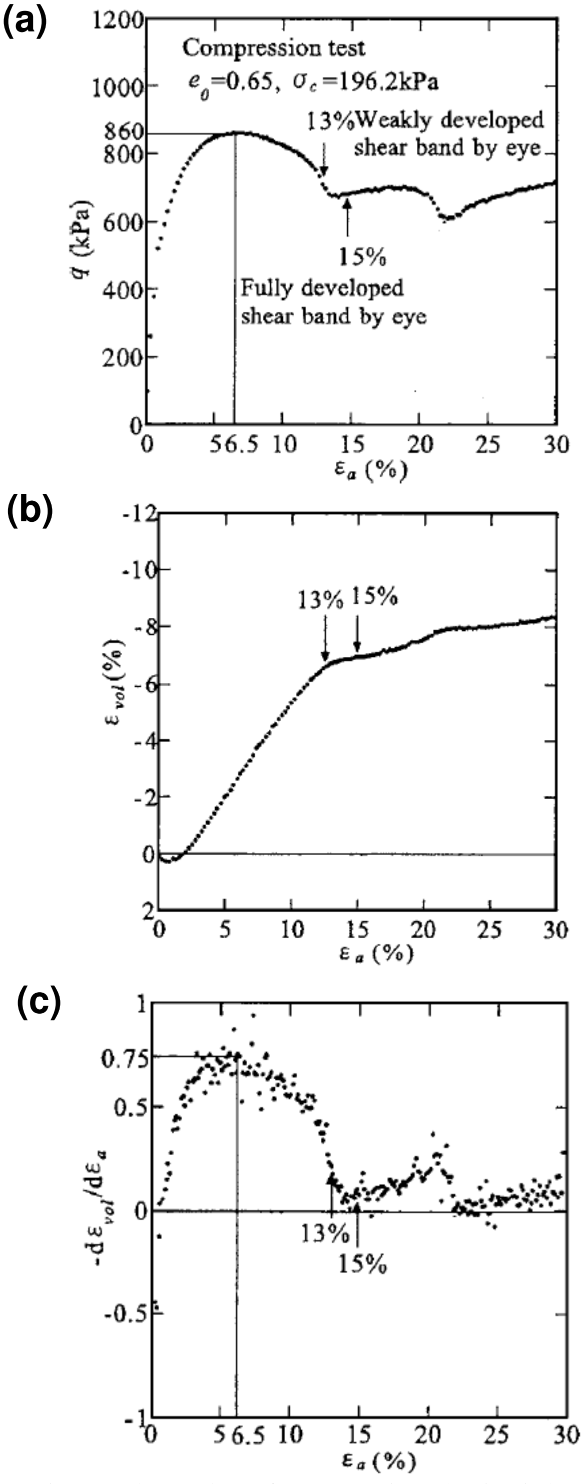

Figure 8.21: Experimental results of conventional triaxial compression test on Toyoura: (a) deviatoric stress vs. axial strain; (b) volumetric strain vs. axial strain; (c) volumetric strain change rate vs. axial strain (Suzuki and Yamada 2006)

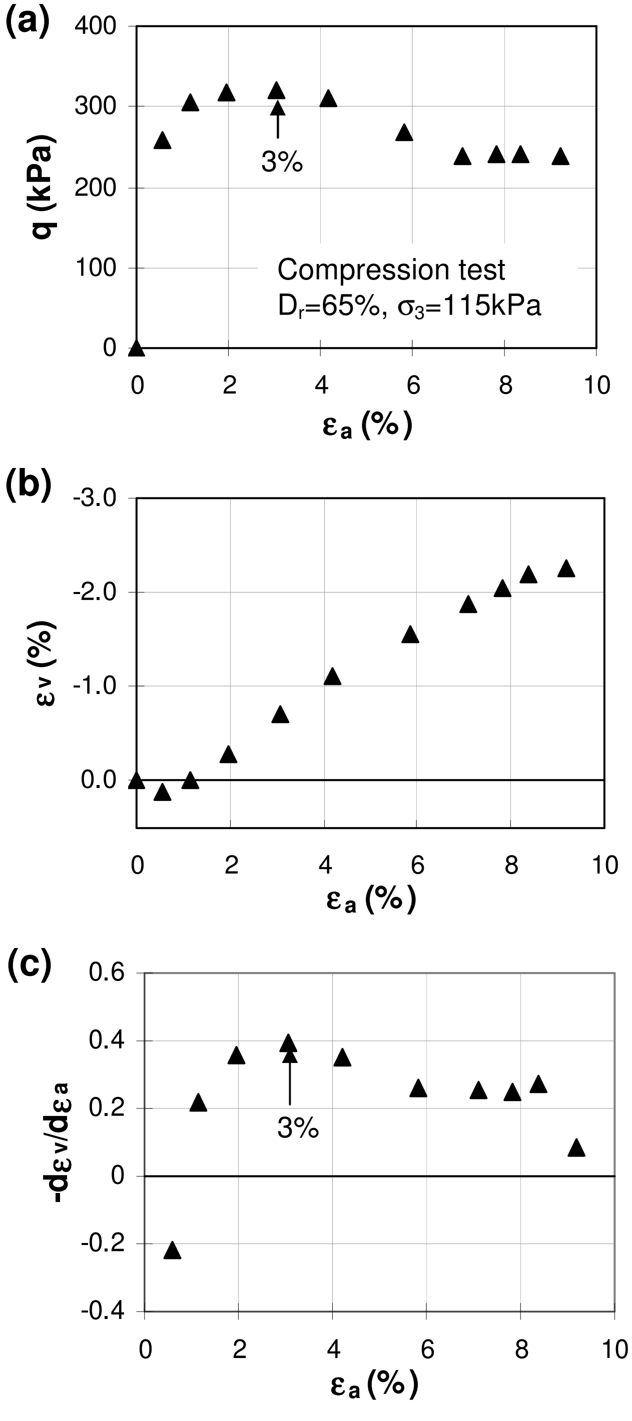

Figure 8.22: Experimental results of conventional triaxial compression test on Monterey No. 30 sand: (a) deviatoric stress vs. axial strain; (b) volumetric strain vs. axial strain; (c) volumetric strain change rate vs. axial strain

8.3.6 Discussion of Conservatism in Current Design Methods

The numerical result can be used to explain the over conservative design of GRS structures reported in recent years. Christopher et al. (2005) reported the maximum reinforcement forces estimated by using the lateral earth pressure approach could be over-predicted by as much as a factor of over two. In addition, based on a database of 11 well-monitored full-scale field walls, Bathurst et al. (2005) also reported that predicted loads for GRS walls are approximately five to eight times greater than observed values for full-scaled instrumented walls.

The explanation is because the soil strength within the GRS structures designed by earth pressure theory is expected to be fully mobilized (S=1) under active conditions. Based on the results shown in Fig. 8.16, only less than half of reinforcement strength is mobilized corresponding to S=1. Therefore, the over-prediction of maximum reinforcement forces by as much as a factor of over two is expected. If the GRS structure is designed by using a high FS, e.g., FS=1.3 against global stability required in current design guidelines, the soil would not reach its peak strength and the average soil stress level along the failure surface can be estimated as 0.76(=1/1.3). According to Fig. 8.16, the reinforcement tensions would be mobilized even less than 10%.

It also has been shown in Fig. 8.16 that the mobilized reinforcement tensions are disproportional to the mobilized soil strength. Because soils and reinforcements were not equally mobilized, neither the concept of Method A nor Method B in the limit equilibrium analysis was valid to represent the interaction of strength mobilization between soil and reinforcement observed in the simulation. A Method C, based on the numerical results presented in Fig. 8.16, may be proposed to obtain the actual FS in the limit equilibrium analysis of GRS slopes.

Moreover, because the soil and reinforcement strains, in fact, are all driven together by the displacements within slope, the mobilized reinforcement tensions within GRS structures should be a function of the elongation of the geosynthetic as it interacts with the confining soil. As are results, instead of using the design methodologies based on force equilibrium (i.e., earth pressure theory and limit equilibrium analysis), the displacement-based design (i.e., finite element analysis) is recommended for the determination of the reinforcement strength for the internal stability of GRS structures. However, because the displacement-based design is complicated and often impractical, typically it requires a computational effort by a trained analyst and also requires a comprehensive characterization of strength and compressibility for all materials (soils, reinforcements and facings) to produce relevant results. For above reasons, the simplified design method based on the displacement-based design is recommended to be development for practice. For example, this may involve the development of a series of design charts for various conditions of interest (e.g., various soil and reinforcement properties and different geometries of GRS structures).

Chapter 9: Summary, Conclusions and Recommendations

9.1 SUMMARY OF RESEARCH COMPONENTS

The primary goals of this study were to evaluate the behavior of Geosynthetic-Reinforced Soil (GRS) retaining structures under various soil stress states. The specific interest was in the development and distribution of soil and reinforcement stresses within GRS structures. The stress distribution within the GRS structures provides the basis for many current designs. There are limitations to obtaining stress information using most current physical testing and numerical methods. Hence part of this dissertation was concerned with developing and implementing numerical procedures. The study is expected to improve the prediction of performance of GRS structures specifically under large soil strain conditions. The specific objectives of this study were reached by conducting the following research components:

- Introduce a non-commercial finite element program ANLOG for the implementation of advanced constitutive models and computational techniques (Chapter 3).
- Develop a soil-softening model to better predict the post-peak behavior of frictional geomaterials (Chapter 4).
- Evaluate the effect of the integration algorithms in regard to computational accuracy, error tolerances and efficiency specifically for the proposed soil-softening model (Chapter 5).
- Establish a finite element model to simulate the GRS structures under various soil stress states (Chapter 6).
- Validate the proposed finite element model using the data from centrifuge GRS slope model (Chapter 7).

- Examine the soil and reinforcement stress information obtained from the finite element simulation (Chapter 8).

A better understanding of the actual developed soil and reinforcement stresses offers important insights into the basis of design and clarifies some current design arguments. Based on the results of this study, the following issues were discussed: 1) the evolution of stresses and strains along the failure surface; 2) soil strength properties (peak or residual strength) that govern the stability of GRS structures; 3) the mobilization of reinforcement tensions.

9.2 SUMMARY AND CONCLUSIONS OF EACH RESEARCH COMPONENT

A finite element program, ANLOG, and the basic computational algorithm in the finite element method was introduced. The advantage of using ANLOG is to fully access an open source code. This allows users on a specific project to modify existing routines and implement new features into the original source code. For the purpose of this dissertation, advanced soil and reinforcement models as well as new computational algorithms were implemented into ANLOG.

The overall procedure of finite element computation involves six steps. 1) Calculating external forces from given boundary conditions, 2) calculating displacements from just-calculated external forces, 3) converting displacements to strains based on compatibility, 4) integrating stresses based on material constitutive relationships, 5) calculating internal forces from the known stresses in the problem domain of interest, and 6) checking the convergence of out-of-balance force between external and internal forces. Additionally, errors in each step should be reduced by carefully selecting the tolerance criterion in computation algorithms like stress integration algorithms and iteration schemes.

An isotropic work-softening model was developed for better predicting the post-peak behavior of frictional geomaterials. There are two benefits from using plastic work characterizing yield behavior—it includes all possible stress-strain combinations and it avoids tests with complicated stress-paths. The development of the softening model was based on the Lade-Kim soil constitutive model. It improved on previous work, however, by characterizing the size of decaying yield surface by using an inverse sigmoid function. Compared to the original softening model using the exponential decay function, the inverse sigmoid function more realistically captured the softening behavior in two ways: 1) at the peak strength point, it provided a smooth transition from hardening to softening and 2) it limited the decrease of yield surface until a residual yield surface. The proposed softening model requires three parameters, a, b, and f''_{pr} . a controls the size of the yield surface at initiation of softening and the curvature of upper part of softening curve; b controls the curvature of the lower part of the softening curve; and f''_{pr} controls the size of the yield surface at residual strength. Three softening model parameters a, b, and f''_{pr} could be easily calibrated to a set of triaxial tests.

Data from triaxial compression testing on two frictional geomaterials (Monterey No. 30 sand and Sacramento River sand) was applied to demonstrate the calibration procedure and examine the variation of model parameters with different loading conditions. Calibration results showed three parameters were highly correlated to confining pressures. This study concludes that the proposed softening model can obtain better calibration results and, as a result, produce more accurate prediction results of stress-strain relationships during softening. After being implemented into the finite element program, the proposed softening model will be able to provide a useful tool for evaluating those structures on which the post-peak behavior of frictional materials should be emphasized, e.g., earth structures under large loading or deformation conditions or the structures having an intensive soil-structures interaction.

The effect of the integration algorithms in regard to computational accuracy, error tolerances and efficiency was evaluated specifically for the proposed soil-softening model. Two integration algorithms, the forward Euler scheme with subincrements and the modified forward Euler scheme with error control, were discussed. The forward Euler integration scheme is commonly used in the finite element analysis. This scheme requires subdividing the strain increment into a fixed number of subincrements with equal size. However, this approach may be computationally intensive and inefficient. In the modified forward Euler scheme with error control, the size of the subincrements can be adjusted flexibly through the integration process. The size of each subincrement varies depending on the required tolerance and only the absolutely necessary number of subdivisions is applied.

The results of the evaluation of two integration algorithms indicated that the forward Euler scheme with fewer subincrements tended to over-predict the stresses in the soil pre-peak region and under-predict the stresses in the soil post-peak region. As the number of subincrements in the forward Euler scheme increased, so did the accuracy. Results were closer to those obtained by using the modified forward Euler scheme. The computational efficiency, however, was sacrificed to the increased number of subincrements. In addition, the forward Euler scheme showed a largely proportional growth in the number of subincrements and computational time. However, the modified Euler scheme showed a slight increase in computational time the error tolerance was reduced. For the soil-softening model, it was concluded that in terms of accuracy and computational costs, the modified forward Euler integration scheme was superior to the forward Euler schemes.

A finite element model was established to simulate the GRS structures under various loading conditions. The soil behavior under large soil strain conditions (i.e., soil dilatancy and strength softening) were simulated using the Lade-Lim soil model and the proposed soil-softening model. The parameter value of the soil model was calibrated to account for soil plane strain conditions in the centrifuge test. The nonlinear reinforcement model was applied to model the nonlinear behavior of reinforcements. The back-calculated reinforcement load-extension response under soil confinement was used to calibrate the reinforcement parameters.

A sensitivity study found only a slight influence of the interface element on the predicated slope response. However, the pre-processing effort (manually creating interface elements) and computation cost (time and size of output files) increased significantly. The final analysis was performed without interface elements. This can also be justified by the lack of visible evidence of pullout failure in the centrifuge test. The failure of reinforcement specimens was due not to pullout but to breakage. Stage construction was included in the simulation. The preliminary study showed, however, the stage construction could be ignored because soil stresses developed during it were negligible compared to those during the loading phase. The effect of soil compaction was not included in the simulation because the density of backfill was controlled by pluviation rather than compaction during the construction of slope model. Large deformation effects were accounted for in numerical simulations by updating the meshes. Based on sensitivity studies, the value of tolerance in the stress integration algorithm and the value of the convergence criterion were selected to concurrently optimize accuracy and computation speed.

The proposed finite element model was validated using data from the centrifuge GRS slope model. The numerical results from the finite element analysis were used to compare with those measured from centrifuge test of slope model M1. The comparison of failure g-level showed the failure g-level (46g) predicted in the simulation was within the range of failure g-level (45g~50g) observed from the centrifuge test. Due to the soil dilatancy, the soil tensile strains were developed in a horizontal direction along the potential failure surface. The horizontal soil tensile strains increased as the loading increased and eventually lead to the failure of soil slope in the simulation.

At the moment of failure, the finite element model captured well the deformation pattern of the slope, specifically for three locations: at the slope sliding mass, the slope top and the slope toe. The numerical simulation can explain why, in the physical testing, the failure surface didn't pass through the slope toe. A likely reason is that the influence of the boundary constraint at the base of foundation was transferred through the firm shallow foundation to the area approximately below the second layer of reinforcement. As a result, the strains developed in the first layer of reinforcement were too small to reach the failure strain.

The locations of failure surfaces obtained from the centrifuge model, limit equilibrium, and finite element analyses were all in good agreement. Furthermore, it was demonstrated in the simulation that in each reinforcement layer the location of the failure surface corresponded to the location of maximum strain. Measured and predicted settlements (relative to 5g) were in good agreement. It was also observed in the simulation that the increase of settlement rate reflected the status of soil-softening developed along the failure surface. A similar phenomenon was observed by Bathurst (1993) and Karpurapu and Bathurst (1995) from two instrumented large-scaled GRS retaining wall tests.

The soil and reinforcement stress information obtained from the finite element simulation was examined. Three issues in regard to the basis of design and the arguments of current design were discussed.

For the issue of evolution of stresses and strains along the failure surface

The evolution of a failure surface can be described as the development of soil stress level *S*, defined as the mobilized soil strength divided by soil peak strength. As loading increased, the areas of high stress level were developed and propagated along the potential failure surface. Immediately after the stress level reached unity (*S*=1.0), soil strength softening was initiated at the top and toe of the slope at 30g. This corresponds to *FS*=1.2 in the limit equilibrium analysis discussed in Section 6.15. Occurring subsequently was the linkage of the soil-softening band through the entire potential failure surface. The formation of the soil-softening band along the failure surface completed at 40g corresponded to *FS*=1.1. Afterward, the system soon reached failure by a few loading increments depending on the tensile strength of reinforcements. The numerical results also indicated that the failure surface corresponded to the locus of intense soil strains and the peak reinforcement strain at each reinforcement layer.

For the issue of soil strength properties governing the stability of GRS structures

Slope models M1 and M3 were reinforced with the same geotextiles, the same number of layers but their sand backfill was placed at two different relative densities

(70% and 50%). When their numerical results were compared, it was found the initiation of soil-softening and failure of slope occurred earlier for slope model M3. Also found with slope model M3 was a shorter duration of soil-softening developed along the failure surface.

The physical effect of different soil densities was modeled by using different input values for failure criteria parameter η_1 which represented the size of peak failure envelope of soil in the simulation. As loading increased, the loading path reached the peak failure envelope of slope model M3 (the smaller failure envelope) before reaching that of slope model M1. Therefore, the initiation of soil-softening for slope model M3 was earlier. Likewise, because the two slope models had the same soil residual strength and reinforcement tensile strength, the failure of slope model M3 also occurred earlier.

The numerical results showed if most of the soil stress states along the failure surface were below its peak shear strength, the soil first had to cross the *threshold* of peak shear strength before reaching residual shear strength. Therefore, the peak shear strength would dominate the system's stability. After most of the soil along the failure surface reaches peak shear strength, the stability of GRS structures is sustained mainly by soil shear strength in the post-peak region and the tensile strength of reinforcements.

For the issue of mobilization of reinforcement tensions

For GRS slopes under working stress conditions, numerical results showed the distribution of peak reinforcement tensions with depth to be nearly uniform. For GRS slopes under large soil strain conditions, the distribution of peak reinforcement tensions was shaped more like a trapezoid, with the location of the reinforcement maximum peak strain located approximately at midheight of the reinforced slopes

The numerical results also found the mobilization of reinforcement tensions is inconsistent with the mobilization of soil strength and can be separated into two stages. In the first stage, the mobilization of reinforcement tensions is increased slightly, up to approximate 10% of its ultimate tensile strength, when the average of mobilized soil strength along the failure surface reaches 95% of its peak strength. During the second stage, when the average of mobilization of soil strength exceeds 95%, the reinforcement tensions start to be mobilized rapidly. Even so, still over 30% of average reinforcement strength has not been mobilized yet when the average of mobilized soil strength reaches 1.0. A similar trend was also observed in two instrumented, large-scaled, GRS retaining wall tests discussed in the dissertation.

The numerical observation of the increase of mobilized reinforcement tensions after soil strength reaches its peak strength was justified by a simple example discussing the mobilization of reinforcement tensions within two slopes with different slope angles. An understanding of soil mechanics was applied to explain the mobilization of reinforcement tensions after the soil strength was fully mobilized.

The numerical observations were used to explain the over-conservative designs of GRS structures reported in recent years. Last, because soils and reinforcements were not equally mobilized, neither Method A nor Method B in the limit equilibrium analysis was valid to represent the interaction of strength mobilization between soil and reinforcement. A Method C, based on the numerical results presented in Fig. 8.16, may be proposed to obtain the actual *FS* in the limit equilibrium analysis of GRS slopes.

9.3 RECOMMENDATIONS FOR FUTURE RESEARCH

9.3.1 Test of Material Properties corresponding to Field Conditions

Recommendations for future research include the need for the correct evaluation of the mechanical properties of soil and geotextiles corresponding to field conditions. In the simulation, the values of soil model parameters were calibrated to the measured data under triaxial compression conditions. Then the value of failure criterion parameter η_1 was multiplied by a strength increase ratio to account for the plane strain conditions. Realistic soil behavior under plane strain conditions, however, is likely to differ from that predicted by numerical extrapolation. To provide actual soil strength properties, rather than mere quality control values, additional tests of soil strength properties under plane strain conditions should be carried out to obtain properties that duplicate field conditions. Similar to soil strength properties, the load-extension curve of reinforcements under soil confinement was extrapolated using the data from wide-width tensile test and multiplying the ratio of ultimate confined tensile strength to ultimate unconfined tensile strength. Rather than numerical extrapolation, additional reinforcement tests under soil confinement should be conducted to obtain the actual load-extension response of reinforcements corresponding to or approximating field conditions.

9.3.2 Evaluation of Stress Developed in the Field

The results and observations presented in this dissertation are based on the numerical modeling of the centrifuge testing on GRS slopes. What this study does not consider are the stresses developed within GRS structures in the field. These include such factors as construction, soil compaction, and long-term effects (e.g., creep). As a result, these factors' impact requires further investigation. One possible research direction is gathering data at different stages during and after construction of GRS structures in the field. Next, conduct a numerical model for the analysis of GRS structures and verify the proposed numerical model using the measured data from the different stages of construction. Then researchers could develop and implement new features into a finite element program for modeling the behavior of GRS structures, specifically in the field if necessary. Afterwards, the verified numerical model could be applied to investigate the stresses developed due to the factors of construction, soil compaction, and long-term effect.

9.3.3 Parametric Study of Various Soil and Reinforcement Properties

The results and observations presented in this dissertation are only based on one specified type of soils and reinforcements (i.e., Monterey No. 30 sand and Pellon Sew-In Geotextile). The influence of soil and reinforcement strengths has been included in the study by normalizing the mobilized soil stresses and reinforcement tensions to their peak strengths. Nevertheless, the effect of soil and reinforcement stiffnesses on the mobilization of soil strength and reinforcement tensions is not covered. The results and observations presented in this dissertation may be applied to examine the design methodologies only based on soil and reinforcement strength properties (i.e., earth pressure theory and limit equilibrium analysis). However, it may be insufficient for the evaluation of design methodology based on both strength and stiffness properties like the K-stiffness method. As a result, the effect of soil and reinforcement stiffness is recommended for further investigation.

9.3.4 Examination of Current Design Methods

By using the finite element model established in this dissertation, a numerical simulation ought to be conducted to determine the development of reinforcement tensions within GRS structures. The results can be used to compare the reinforcement strength determined by various design methods as discussed in Section 2.3. The accuracy of various design methods to determine the reinforcement tensions can be examined under a range of material properties, structures' geometries, and loading conditions.

9.3.5 Development of Displacement-Based Design Charts

Finally, based on the stress information discussed in this dissertation, the mobilization of reinforcement tensions was inconsistent with the mobilization of soil strength. The design methodologies based on force equilibrium (i.e., earth pressure theory and limit equilibrium analysis) may not be able to represent the actual interaction of strength mobilization between soil and reinforcement. Consequently, the overestimation of reinforcement tensions by using design methods based on force equilibrium has been reported in several relevant documents. Therefore, the displacement-based design (i.e., finite element analysis) should be recommended to determine the reinforcement strength for the internal stability of GRS structures. However, because the displacement-based design is often complicated and impractical, it typically requires a computational effort by a trained analyst. Furthermore, it requires a comprehensive characterization of strength and compressibility for all materials (soils, reinforcements and facings) to produce relevant results. For these reasons, it is recommended that the simplified design method based on the displacement-based design be developed for practice. For example, this may involve the development of a series of design charts for various conditions of interest (e.g., various soil and reinforcement properties and different geometries of GRS structures).

Appendix A: Lade-Kim Soil Model and Soil Softening Model

A.1 ELASTIC MATRIX OF LADE-KIM SOIL MODEL

```
SUBROUTINE DE_LADE (DE,PROPS,TENSAO,SUP)

USE Global_variables
USE Local_variables
USE Properties_declare

IMPLICIT NONE

INTEGER :: I

REAL(8) :: TENSAO(NCOMPM), PSTR(3), DE(NCOMP,NCOMP),
PROPS(NPROPM), G, SUP(5), I1, I2, I3, I1D, I2D, I3D, LAME,R
REAL (8), DIMENSION (:), ALLOCATABLE :: TENSAOG

! Import Elastic Paramters of Lade-Kim Model

CALL PROPERTIES (PROPS)

ALLOCATE(TENSAOG(NCOMP))
TENSAOG=0.0D0

DO I=1,NCOMP
    TENSAOG(I)=TENSAO(I)
END DO

TENSAOG(1)=TENSAOG(1)+AMP*PA
TENSAOG(2)=TENSAOG(2)+AMP*PA
TENSAOG(3)=TENSAOG(3)+AMP*PA

IF(SUP(5)==5.0D0)THEN
        NI=0.495D0
        E=0.0001D0*PA
ELSE

    IF(LCODE==7.OR.LCODE==8.OR.LCODE==11.OR.LCODE==10)THEN
          IF(NCOMP==4)CALL PRSTR (TENSAOG,PSTR)
          IF(NCOMP==6)CALL PRSTR3D (TENSAOG,PSTR)
          IF(PSTR(3)<=0.001D0*PA)PSTR(3)=0.001D0*PA
```

```
        E = KUR*PA*(PSTR(3)/PA)**N

        ELSE IF(LCODE==14.OR.LCODE==141)THEN
                CALL DCAL_INVI (TENSAOG,NCOMP,I1,I2,I3)
                CALL DCAL_INVID (TENSAOG,NCOMP,I1D,I2D,I3D)
                R= 6.0D0*(1.0D0+NI)/(1.0D0-2.0D0*NI)
                E = M*PA*( (I1/PA)*(I1/PA) + R*I2D/(PA*PA) )**LL
        END IF
END IF

LAME = E*NI/((1.0D0+NI)*(1.0D0-2.0D0*NI))
G = E/(2.0D0*(1.0D0+NI))

IF(NCOMP==4)CALL MATD(DE,LAME,G)
IF(NCOMP==6)CALL MATD_3D(DE,LAME,G)

DEALLOCATE(TENSAOG)

RETURN
END
```

A.2 Elastic-Plastic Constitutive Matrix of Lade-Kim Soil Model

```
SUBROUTINE DLKIM (ET,DE,DT,PROPS,TENSAO,SUP,ENDUC,SLMAX,WPS1)

USE Local_variables
USE Global_variables
USE Properties_declare

IMPLICIT NONE

INTEGER I,J

REAL(8) :: DE(NCOMP,NCOMP), DP(NCOMP,NCOMP), DT(NCOMP,NCOMP),
TENSAO(NCOMPM), SUP(5),ENDUC(2), ET(NCOMP), DEN, MP, H, FP, WP,
PROPS(NPROPM), SLMAX, WPS1
REAL(8),    DIMENSION (:), ALLOCATABLE :: TENSAOG,GA,GB
REAL(8), DIMENSION (:,:), ALLOCATABLE :: CP

DT=0.0D0
DP=0.0D0
```

```
ET=0.0D0

! Check Elastic Deformation

IF (SUP(5)==2.0D0)THEN
          DT=DE
RETURN
END IF

ALLOCATE(GA(NCOMP))
ALLOCATE(GB(NCOMP))
ALLOCATE(TENSAOG(NCOMP))
ALLOCATE(CP(NCOMP,NCOMP))

TENSAOG=0.0D0
GA=0.0D0
GB=0.0D0
CP=0.0D0

DO I=1,NCOMP
     TENSAOG(I)=TENSAO(I)
END DO

TENSAOG(1)=TENSAOG(1)+AMP*PA
TENSAOG(2)=TENSAOG(2)+AMP*PA
TENSAOG(3)=TENSAOG(3)+AMP*PA

FP=SUP(1)
WP=ENDUC(1)

! Import Lade-Kim Soil Model Parameters

CALL PROPERTIES(PROPS)

! Calculate Stress
! Calculate Vector of A and B

CALL DLKIM_AB (NCOMP,TENSAOG,GA,GB,FP)

! Calculate den=H+a*de*a

CALL DLKIM_H (GA,GB,TENSAOG,H,MP,DE,DEN,WP,SUP,SLMAX,WPS1)

! Calculate CP=(AT*B)/den
```

```
DO I=1,NCOMP
            DO J=1,NCOMP
                   CP(I,J) = (1.0D0/DEN)*GB(I)*GA(J)
            END DO
END DO

! Calculate [DP]= [D EL] * [CP] [D EL]

DP=MATMUL(MATMUL(TRANSPOSE(DE),CP),DE)

! Calculate [DT]= [D EL] - [DP]

DT=DE-DP

! Calculate ET=A*DE*(MP/DEN)

ET = MATMUL(GA,DE)*(MP/DEN)

DEALLOCATE(GA,GB,CP,TENSAOG)

RETURN
END
```

A.3 DERIVATIVES OF YIELD AND PLASTIC POTENTIAL FUNCTIONS

```
SUBROUTINE DLKIM_AB (NCOMP,TENSAO,AG,BG,FP)

USE Properties_declare

IMPLICIT NONE

INTEGER:: NCOMP

REAL(8) :: TENSAO(NCOMP), AG(NCOMP), I1, I2, I3, C1, C2, QQ, GA, WK1, S,
DFDQ, DQDS, DS1, DS3, DF1, DF2, DF3, G, C3, BG(NCOMP), FP
REAL(8), DIMENSION (:), ALLOCATABLE ::    A1, A2, A3, A4, DI1, DI2, DI3

ALLOCATE (A1(NCOMP))
ALLOCATE (A2(NCOMP))
ALLOCATE (A3(NCOMP))
ALLOCATE (A4(NCOMP))
ALLOCATE (DI1(NCOMP))
```

```
ALLOCATE (DI2(NCOMP))
ALLOCATE (DI3(NCOMP))

A1=0.0D0
A2=0.0D0
A3=0.0D0
A4=0.0D0
DI1=0.0D0
DI2=0.0D0
DI3=0.0D0

! Calculate Invariants of Stress Tensor I1, I2 and    I3

CALL DCAL_INVI (TENSAO,NCOMP,I1,I2,I3)

DI1(1:3)=1.0D0

IF(NCOMP==4)THEN
        DI2(1) = (-TENSAO(2)-TENSAO(3))
        DI2(2) = (-TENSAO(3)-TENSAO(1))
        DI2(3) = (-TENSAO(1)-TENSAO(2))
        DI2(4) = (2.0D0*TENSAO(4))

        DI3(1) = TENSAO(2)*TENSAO(3)
        DI3(2) = TENSAO(3)*TENSAO(1)
        DI3(3) = TENSAO(1)*TENSAO(2)-TENSAO(4)**2.0D0
        DI3(4) = - 2.0D0*TENSAO(3)*TENSAO(4)

ELSE IF(NCOMP==6)THEN
        WRITE(2,*)'Under Implementation”
STOP
END IF

!   Calculate A1=dfdq*dqds

WK1 = 0.00155D0*MM**(-1.27D0)
S = (I1*I1*I1/I3 - 27.0D0)*(I1/PA)**MM

IF (S<0.0D0) S=0.00001D0
S = S/ETA1
IF(S>1.0D0) S=1.0D0
QQ = ALFA1*S/(1.0D0-(1.0D0-ALFA1)*S)
DFDQ = FP
DQDS = ALFA1/((1.0D0-(1.0D0-ALFA1)*S)**2.0D0)
C1 = (3.0D0+MM)*(I1*I1/I3)
```

```
C2 = - 27.0D0*MM/I1
DS1 = (1.0D0/ETA1)*((I1/PA)**MM)*(C1+C2)
DS3 = (-1.0D0/ETA1)*((I1/PA)**MM)*I1*I1*I1/(I3*I3)
A1 = DFDQ*DQDS*(DS1*DI1+DS3*DI3)

! Calculate A2=df1*di1

C1 = DEXP(QQ)*(I1/PA)**HH
GA = WK1*(HH + 3.0D0)*I1*I1/I3
GA = GA - (HH + 2.0D0)*I1/I2
DF1 = GA*C1
A2 = DF1*DI1

! Calculate A3=df2*di2

DF2 = C1*(I1/I2)**2.0D0
A3 = DF2*DI2

! Calculate A4=df3*di3

DF3 = - WK1*C1*((I1**3.0D0)/(I3**2.0D0))
A4 = DF3*DI3

! Summate A1, A2, A3 and A4

AG=A1+A2+A3+A4

!    Calculate B

G    =    WK1*(MI+3.0D0)*((I1**2.0D0)/I3)
G    =    G - (MI+2.0D0)*(I1/I2)
G    =    G +    MI*PSI2/I1
C1 = G*(I1/PA)**MI
C2 = ((I1/I2)**2.0D0)*((I1/PA)**MI)
C3 = WK1*((I1**3.0D0)/(I3**2.0D0))*((I1/PA)**MI)
BG = C1*DI1 + C2*DI2 - C3*DI3

DEALLOCATE (A1,A2,A3,A4,DI1,DI2,DI3)

RETURN
END
```

A.4 HARDENING AND SOFTENING MODULUS

```
SUBROUTINE DLKIM_H
(AG,BG,TENSAO,H,MP,DE,DEN,WP,SUP,SLMAX,WPS1)

USE Properties_declare
USE Global_variables
USE Local_variables

IMPLICIT NONE

REAL(8) :: TENSAO(NCOMP), BG(NCOMP), AG(NCOMP), H,MP,
DE(NCOMP,NCOMP), DEN, WP, D, RO,WK1, SUP(5), DFDW, BB, AA, FPR,
SLMAX, R, PSTR(3),WPS1

! Calculate Mp

MP=DOT_PRODUCT(TENSAO,BG)

IF(MP<0.0D0)MP=0.0D0

! Calculate    H=(dFWP/dWP)*MP
!              DfWP/dWP=(1/(RO*PA*D))*(WP/(PA*D))**(1/RO-1)
!              DEN = A*DE*B + H

IF(LCODE==14) THEN
        IF (SLMAX<1.0D0) THEN
                 RO=P/HH
                    WK1 = 0.00155D0*MM**(-1.27D0)
                    D = C/(27.0D0*WK1+3.0D0)**RO
                    DFDW=(1/(PA*D*RO))*SUP(1)**(1.0D0-RO)
        ELSE
                ! Original Softening Model
                DFDW=(1/(PA*D*RO))*SUP(2)**(1.0D0-RO)
                SB=1.0 ! Input Softening Parameter b'
                BB=SB*PA*DFDW/((1-R)*SUP(2))
                AA=SUP(2)*DEXP(BB*(PA*D*SUP(2)**RO)/PA)
                DFDW=-AA*BB/PA*DEXP(-BB*WP/PA)
        END IF

IF(LCODE==141) THEN
        IF (SLMAX<1.0D0) THEN
              RO=P/HH
              WK1 = 0.00155D0*MM**(-1.27D0)
              D = C/(27.0D0*WK1+3.0D0)**RO
```

```
            DFDW=(1/(PA*D*RO))*SUP(1)**(1.0D0-RO)
      ELSE
      !Proposed Softening Model
       CALL PRSTR (TENSAO,PSTR)
      ! Input Softening Parameter a,b and fpr''
                   AA=0.0076*PSTR(3)+0.2707
                   BB=-0.7374*PSTR(3)+209.83
                   FPR=0.3025*PSTR(3)+20.747
                   IF(R<0.0)R=0.0
                   CC=1/(SUP(2)-FPR)
                   DFDW=-AA*BB/PA*DEXP(-BB*(WP/PA-WPS1/PA))
                   DFDW=DFDW/(CC+AA*DEXP(-BB*(WP/PA-WPS1/PA)))**2
       END IF
END IF

H=MP*DFDW
DEN=DOT_PRODUCT(AG,MATMUL(DE,BG)) + H

RETURN
END
```

Appendix B: Modified Forward Euler Scheme with Error Control

```fortran
SUBROUTINE TCALC_MFE (TENSAO, DEF, DDEF, PROPS, SUP, ENDUC,
ENDUCD, SLMAX, IELEM, WPS1)

USE Global_variables
USE Local_variables
USE Solve_variables
USE Properties_declare

IMPLICIT NONE

INTEGER:: I,NIS,ISUB,ENDUCD,IELEM

REAL (8):: PROPS(NPROPM), TENSAO(NCOMPM), DEF(NCOMPM),
DDEF(NCOMP), SUP(5), ENDUC(2), DENDUC, DEFMOD, I1, I3, I2, S, QQ, FP, RO,
D, WP, AAA, BBB, SLMAX, DFDW, q, xi, tol, DENDUC1, DENDUC2,WPS1
REAL (8), DIMENSION (:), ALLOCATABLE :: ET, DTENSAO, DTENSAO1,
TENSAO2, Difference, Average, DDEF2, DDEFT
REAL (8), DIMENSION (:,:), ALLOCATABLE :: DE, DT

ALLOCATE (DTENSAO(NCOMP))
DTENSAO=0.0D0
ALLOCATE (DTENSAO1(NCOMP))
DTENSAO1=0.0D0
ALLOCATE (DTENSAO2(NCOMP))
DTENSAO2=0.0D0
ALLOCATE (Difference(NCOMP))
Difference=0.0D0
ALLOCATE (Average(NCOMP))
Average=0.0D0
ALLOCATE (DDEF2(NCOMP))
DDEF2=0.0D0
ALLOCATE (DDEFT(NCOMP))
DDEFT=0.0D0
ALLOCATE (ET(NCOMP))
ET=0.0D0
ALLOCATE(DE(NCOMP,NCOMP))
DE=0.0D0
ALLOCATE(DT(NCOMP,NCOMP))
DT=0.0D0

! Import Lade-Kim Soil Model Parameters
```

```
CALL PROPERTIES(PROPS)

! Initial Trial of Subincrement

   q=1.0D0/(NSUB*100)
   DDEF2=DDEF
   DO ISUB=1,NSUB*100 ! Maximum Subincrement Number

67 CONTINUE

DDEF2=q*DDEF2

IF(ABS(DDEF2(1))>= ABS (DDEF(1)-DDEFT(1)))THEN ! Last Subincrement Step
DDEF2=DDEF-DDEFT
END IF

DO NIS=1,2 !Two Iterations

     ! Calculate Elastic Matrix

     CALL DE_LADE(DE,PROPS,TENSAO,SUP)

     ! Calculate Elastoplastic Matrix

     CALL DLKIM(ET,DE,DT,PROPS,TENSAO,SUP,ENDUC,SLMAX,WPS1)

     ! Update Stress

     DTENSAO=MATMUL(DT,DDEF2)
     IF(NIS==1) DTENSAO1=DTENSAO
     IF(NIS==2) DTENSAO2=DTENSAO
     TENSAO=TENSAO+DTENSAO

     ! Update Plastic Work

     DENDUC = DOT_PRODUCT(ET,DDEF2)
     IF(NIS==1) DENDUC1=DENDUC
     IF(NIS==2) DENDUC2=DENDUC
     ENDUC(1) = ENDUC(1) + DENDUC

END DO ! Complete the Loop of Two Iterations

Difference=0.5*(DTENSAO2-DTENSAO1)  ! Calculate Difference b/w Iteration 1 and 2
TENSAO=TENSAO-DTENSAO1-DTENSAO2 !Reset Stress
ENDUC(1)=ENDUC(1)-DENDUC1-DENDUC2 !Reset Plastic Work
```

```
Average=TENSAO+0.5*(DTENSAO1+DTENSAO2) !Calculate Average Stress

! Calculate Error

xi=DSQRT(DOT_PRODUCT(Difference,Difference))/DSQRT(DOT_PRODUCT(Average,Average))

tol=0.001    !Set Tolerance

!!Note: Parametric study show the tolerance should be less than 10E-3

IF(xi>tol)THEN
q=Max(0.9*DSQRT(tol/xi),0.01)
GOTO 67

ELSE
        IF(xi==0.0)THEN
            q=2.0
        ELSE
            q=Min(0.9*DSQRT(tol/xi),2.0)
END IF

TENSAO=Average    !Update Stress
ENDUC(1)=ENDUC(1)+0.5*(DENDUC1+DENDUC2)    !Update Plastic Work
DDEFT=DDEFT+DDEF2 !Update Strain
DEF=DEF+DDEF2

! Update Model Components

DTENSAO=TENSAO
W1 = 0.00155D0*MM**(-1.27D0)
DTENSAO(1)=DTENSAO(1)+AMP*PA
DTENSAO(2)=DTENSAO(2)+AMP*PA
DTENSAO(3)=DTENSAO(3)+AMP*PA
CALL DCAL_INVI(DTENSAO,NCOMP,I1,I2,I3)
IF(I3.EQ.0.0D0) I3=0.000001D0
SUP(3) = (I1*I1*I1/I3 - 27.0D0)*(I1/PA)**MM
IF (SUP(3)<0.0D0) SUP(3)=0.00001D0
S = SUP(3)/ETA1
IF(S>1.0D0) S=1.0D0
QQ = ALFA1*S/(1.0D0-(1.0D0-ALFA1)*S)
SUP(1) = DEXP(QQ)*(I1/PA)**HH
SUP(1) = SUP(1)*( W1*(I1**3.0D0)/I3 - (I1**2.0D0)/I2 )
IF (SUP(1)<0.0D0)SUP(1)=0.00001D0
SUP (4) = ETA1
```

```
SUP (3) = SUP(3)/SUP(4)
IF (SUP(3)>1.0D0) SUP(3)=1.0D0

! Update Stress Status SUP(5)

IF (SLMAX<1.0D0)THEN
                    IF (SUP(1)>SUP(2))SUP(5) = 1.0D0 !Loading
                    IF (SUP(1)<=SUP(2)) SUP(5) = 2.0D0 !Unloading during Hardening
                    IF (SUP(3)==1.0D0) SUP(5) =5.0D0 ! Reach Soil Peak Shear Strength

ELSE IF (SLMAX==1.0D0)THEN
                  IF (ENDUCD==1) THEN
                       SUP(5) = 4.0D0    !Softening
                  ELSE
                       SUP(5)=2.0D0 !Unloading during Softening
                  END IF
END IF

! Stop Subincrement Loop after Reach Last Subincrement

IF(ABS(DDEFT(1))>=ABS(DDEF(1)))THEN

DEALLOCATE(DTENSAO, DE, DT, ET, DTENSAO1, DTENSAO2, Difference,
Average, DDEF2, DDEFT)

RETURN
END IF

Write(*,*) 'Required Strain Is Not Reached'
PAUSE

END DO ! END of Subincrement Loop

RETURN
END
```

Appendix C: Constitutive Matrix for Element B3

```
SUBROUTINE MATDT_B (PROPS,DEF,DT)

USE Global_variables
USE Local_variables
USE Properties_declare

IMPLICIT NONE

REAL (8) :: JT, DT(1,1), PROPS(NPROPM), DEF(NCOMPM), ET, DEFMAX,
SIGMAX, BFACT

BFACT=0.00001D0

CALL PROPERTIES(PROPS)

!Linear-Elastic

IF (LCODE==21)THEN
    DT=E

!Bilinear Elastic (Compression)

ELSE IF (LCODE==22)THEN
       IF(DEF(1)>=0.0D0)DT=E                ! Positive Is Compression
       IF(DEF(1)<0.0D0) DT=BFACT*E         ! Negative Is Tension

!Bilinear Elastic (Tension)

ELSE IF (LCODE==23)THEN
       IF(DEF(1)<=0.0D0)DT=E
       IF(DEF(1)>0.0D0)DT=BFACT*E

!Parabolic

ELSE IF (LCODE==24)THEN
       JT=A+2.0D0*B*DABS(DEF(1))
       IF(JT<=0.0D0)JT=0.00001D0
       ET=JT/THICK
       IF(DEF(1)<=0.0D0)DT=ET
       IF(DEF(1)>0.0D0)DT=BFACT*ET

!Bilinear Elastic-Perfect
```

```
ELSE IF (LCODE==25)THEN
        SIGMAX=TMAX/THICK
        DEFMAX=SIGMAX/E
        IF(DABS(DEF(1))<=DEFMAX)DT=E
        IF(DABS(DEF(1))>DEFMAX)DT=BFACT*E

END IF

RETURN
END
```

Glossary

Centrifuge Modeling	A device used to generate different levels of gravity to small-scaled model to mimic the stress field in the prototype.
Constitutive Model	A numerical model used to describe the stress-strain relationships of materials.
Finite Element Analysis	A numerical technique used to simulate and predict the behavior of structures of interest.
Geosynthetics	A range of generally polymeric products used to solve civil engineering problems.
GRS Structures	Geosynthetics-reinforced soil structures. Walls or slopes reinforced by geosynthetics used to hold back soil or rock from a building, structure or area.
Soil Softening Model	A soil constitutive model used to model soil post-peak behavior including strength softening and volumetric dilatancy.
Stress Integration Algorithm	A numerical algorithm used to obtain stresses by summating many finite stress increments.

References

AASHTO, (2002), “Standard Specifications for Highway Bridges”, *American Association of State Highway and Transportation Officials*, Seventeenth Edition, Washington, DC, USA, 689 p

ABAQUS. (1995), “*ABAQUS Manuals Version 5.5”*, Hibbit, Karlson and Sorensen Inc.

Allen, T.M.; Bathurst, Richard J.; Holtz, Robert D.; Walters, D.; Lee, Wei F., Walters D (2004) “A New Method for Prediction of Loads in Steel Reinforced Soil Walls”, *Journal of Geotechnical and Geoenvironmental Engineering*, v 130, n 11, p 1109-1120

Allen, T.M.; Bathurst, Richard J.; Holtz, Robert D.; Walters, D.; Lee, Wei F. (2003) “A New Working Stress Method for Prediction of Reinforcement Loads in Geosynthetic Walls”, *Canadian Geotechnical Journal*, v 40, n 5, p 976-994

Allen, T.M., and Bathurst, R.J. (2002a), “Soil Reinforcement Loads in Geosynthetic Walls at Working Stress Conditions”. *Geosynthetics International*, 9(5–6): 525–566.

Allen, T.M., and Bathurst, R.J. (2002b), “Observed Long-Term Performance of Geosynthetic Walls, and Implications for Design”. *Geosynthetics International*, 9(5–6): 567–606.

Arriaga, F. (2003), “Response of Geosynthetic-Reinforced Structures under Working Stress and Failure Conditions” PhD Dissertation, Department of Civil Engineering, the University of Colorado, Boulder.

ASTM (1995), “ASTM standards on Geosynthetics”. Sponsored by ASTM Committee D-35 on Geosynthetics, Fourth Edition, 178p

ASTM D4253. “Standard Test Methods for Maximum Index Density and Unit Weight of Soils Using a Vibratory Table”. *The American Society for Testing and Materials*. West Conshohoken, PA.

ASTM D4254. “Standard Test Methods for Minimum Index Density and Unit Weight of Soils and Calculation of Relative Density”. *The American Society for Testing and Materials*. West Conshohoken, PA.

ASTM D4595. “Standard Test Method for Tensile Properties of Geotextiles by the Wide-Width Strip Method”. *The American Society for Testing and Materials*. West Conshohoken, PA.

Atkinson, J. H. (1981). "Foundations and Slopes: An Introduction to Applications of Critical State Soil Mechanics". *Halsted Press*, New York, N.Y.

Ballegeer, J. P., and Wu, J. T. H. (1993). "Intrinsic Confined and Unconfined Load-Deformation Properties of Geotextiles". *Geosynthetic Soil Reinforcement Testing Procedures, ASTM STP* 1190, S. C. J. Cheng, Ed, American Society for Testing and Materials, Philadelphia, p. 16-31.

Bathe, K.J., Ramm, E., and Wilson, E.L., (1975), "Finite Element Formulation for Large Deformation Dynamic Analysis", *Jnt. .I. Num. Meth. in Erg.,* 9, 353-386.

Bathurst, R.J. (2007) "Geosynthetics Classification". IGS Leaflets on Geosynthetics Applications, IGS Education Committee, at www.geosyntheticssociety.org

Bathurst, R.J. (1993). "Investigation of Footing Restraint on Stability of Large-Scale Reinforced Soil Wall Tests". *46th Canadian Geotechnical Conference*, 389–398.

Bathurst, R.J., Miyata, Y., Nernheim, A. and Allen, T.M. (2008), "Refinement of K-Stiffness Method for Geosynthetic Reinforced Soil Walls", *Geosynthetics International*, Vol. 15, No. 4, pp. 269–295.

Bathurst, R. J., Allen, T. M. & Walters, D. L. (2005). "Reinforcement Loads in Geosynthetic Walls and the Case for a New Working Stress Design Method. *Geotextiles and Geomembranes*, 23, No. 4, 287–322.

Bathurst, R.J., and Benjamin, D.J., (1990), "Failure of a Geogrid Reinforced Soil Wall", transportation Research Record 1288, Washington, D.C., 109-116.

Bathurst, R.J., Benjamin, D.J. and Jarrett, P.M. (1989). "An Instrumented Geogrid Reinforced Soil Wall", *Proceedings of the twelfth International Conference on Soil Mechanics and Foundation Engineering*, Rio de Janeiro, 13-18 August 1989

Bathurst, R.J., Wawrychuk, W. and Jarrett, P.M. (1987). "Laboratory Investigation of Two Large-Scale Geogrid Reinforced Soil Walls", *The Application of Polymeric Reinforcement in Soil Retaining Structures,* NATO Advanced Study Institute Series, Kluwer Academic Publisher, pp. 71-125.

Baxevanis, T. Papamichos, E. Flornes, O. Larsen, I. (2006), "Compaction Bands and Induced Permeability Reduction in Tuffeau of Maastricht Calcarenite". *Acta Geotechnica-Springer Verlag.* vol. 1, n. 2, pp.123-135.

Bishop, A. W. (1955), "The Use of the Slice Circle in the Stability of Slopes", *Geotechnique*, London, U.K., 5, 7-17.

Bolton, M., (1986), "The Strength and Dilatancy of Sands", *Géotechnique*, Vol. 36, No.1, pp. 65-78.

Bolton, J. M., Durnford, D. S., and Charlie, W. A. (1994). “One-Dimensional Shock and Quasi-Static Liquefaction of Silt and Sand”. J. of Geotech. Engr., 120(10), p. 1874-1889.

Bonaparte, R., and Schmertmann, G. R. (1987) “Reinforcement Extensibility in Reinforced Soil Wall Design”, *The Application of Polymeric Reinforcement in Soil Retaining Structures*, P.M. Jarrett and A. McGown, eds., Nato Advanced Research Workshop, Royal Military College of Canada, Ont., Canada, 409-457pp.

Borja, R.I. (2004). “Computational Modeling of Deformation Bands in Granular Media, II: Numerical Simulations”. *Computer Methods in Applied Mechanics and Engineering*. vol. 193, pp. 2699-2718.

Chen WF, Mizuno E (1990), “Nonlinear Analysis in Soil Mechanics”, *Elsevier:* New York

Christopher B. R., Leshchinsky D. and Stulgis R. (2005). “Geosynthetic-Reinforced Soil Walls and Slopes: US Perspective”, *International Perspectives on Soil Reinforcement Applications. ASCE Geotechnical Special Publication No. 141,* ASCE Press, Reston, Virginia, January 2005, ISBN 0-7844-0769-X, 166 p.

Crisfield, M. (1991), “Nonlinear Finite Element Analysis of Solids and Structures”, *John Wiley and Sons*, England.

Chu, J., Lo, S. and Lee, I.K. (1996), “Strain Softening and Shear Band Formation of Sand in Multi-axial Testing” *Geotechnique*, vol. 46, n. 1, pp. 63-82.

Desrues, J. (1991) “An Introduction to Strain Localization in Granular Media.”*Physics of Granular Media—Proc., Winter School Les Houches*, 127–142.

Duncan, M and Wright S. G., (2005), “Soil Strength and Slope Stability”, John Wiley & Sons, Inc. 297p

Duncan, J. M., and Chang, C. Y. (1970), “Nonlinear Analysis of Stress and Strain in Soils”. *Journal of the Soil Mechanics and Foundations Division*, ASCE, vol. 96, n. SM5, pp. 1629-1653.

Elias, V., Christopher, B.R., and Berg, R.R., (2001), “Mechanically Stabilized Earth Walls and Reinforced Soil Slopes Design and Construction Guidelines” Report No. FHWA-NHI-00-043, *National Highway Institute, Federal Highway Administration*, Washington, D.C. March

Gotteland, Ph., Gourc, J.P., and Villard, P. (1997). “Geosynthetics Reinforced Structures as Bridge Abutments: Full Scale Experimentation and Comparison with

Modelisations”. *In International Symposium on Mechanically Stabilized Backfill*, Denver, Colo., 6–8 February 1997. The Netherlands. pp. 25–34

Hammouri, N. A; Husein M., A. I.; Yamin, M. M.A. (2008), “Stability Analysis of Slopes using the Finite Element Method and Limiting Equilibrium Approach” *Bulletin of Engineering Geology and the Environment*, v 67, n 4, p 471-478

Hatami, K and Bathurst R. J.(2005), “Development and Verification of a Numerical Model for the Analysis of Geosynthetic-Reinforced Soil Segmental Walls under Working Stress Conditions” *Canadian Geotech Journal*, v 67, n 4, p 1066-1085

Huang, C., Tatsuoka, F., and Sato, Y. (1994) “Failure Mechanisms of Reinforced Sand Slopes Loaded with A Footing”. *Soils and Foundations*. vol. 34 n.2, pp. 27-40.

Jakobsen KP and Lade PV. (2002), “Implementation Algorithm for a Single Hardening Constitutive Model for Frictional Materials”. *International Journal for Numerical and Analytical Methods in Geomechanics*. 26: pp. 661-681.

Janbu, N. (1954), “Stability Analysis of Slopes with Dimensionless Parameters”, *Harvard Soil Mechanics Series*, No. 46.

Jewell, R. A., (1991) “Application of Revised Design Charts for Steep Reinforced Slopes”, *Geotextiles and Geomembranes*, Vol. 10, No. 3, pp. 203-233.

Jewell, R.A., (1990), “Strength and Deformation in Reinforced Soil Design”, *Proceedings of Fourth International Conference on Geotextiles, Geomembranes and Related Products,* Balkema, The Hague, Netherlands, May 1990, pp. 913-946.

Johnston, R. S. and Romstad, K.S., (1989) “Dilation and Boundary Effects in Large Scale Pullout Tests”, *Proc. XIII Int. Conf. Soil Mech. and Found. Engrg*, Rio de Janeiro, 1263-1266

Karpurapu, R.G., and Bathurst, R.J. (1995). “Behaviour of Geosynthetic Reinforced Soil Retaining Walls Using the Finite Element Method”. *Computers and Geotechnics*, 17(3): 279–299.

Kim, M.K. and Lade, P.V. (1988), “Single Hardening Constitutive Model for Frictional Materials - I. Plastic Potential Function”. *Computers and Geomechanics*, 5, pp. 307-324.

Kulhawy, F.H., and Mayne, P.W., (1990), “Manual on Estimating Soil Properties for Foundation Engineering”, *Report EL 6800, Electric Power Research Institute*, Palo Alto, California, USA, 306 p.

Lade, P.V. and Prabucki, M.J. (1995), “Softening and Preshearing Effects in Sand”. *Soils and Foundations* 1995; vol. 35 n. 4, pp. 93–104.

Lade, P.V. and Kim, M.K. (1995) “Single Hardening Constitutive Model for Soil, Rock and Concrete”, *International Journal Solids and Structures*, vol. 32, n.14, pp. 1963-1978.

Lade, P.V. and Kim, M.K. (1988a) “Single Hardening Constitutive Model for Frictional Materials – II. Yield Criterion and Plastic Work Contours”. *Computers and Geomechanics*, 6, pp. 13-29.

Lade, P.V. and Kim, M.K. (1988b). “Single Hardening Constitutive Model for Frictional Materials – III. Comparisons with Experimental Data”. *Computers and Geomechanics*. 6, pp. 31-47.

Lade, P.V. and Duncan J.M. (1977) “Elastoplastic Stress-Strain Theory for Cohesionless Soil with Curved Yield Surface”, *International Journal Solids and Structures*, vol. 13, pp. 1019-1035.

Lade, P.V. and Duncan J.M. (1975), “Elastoplastic Stress-Strain Theory for Cohesionless Soil”, *J. Soil Mechanics and Foundation Division.*, ASCE, vol. 101, n. GT10, pp. 1037-1053.

Lade, P. and Duncan, J.M., (1973), “Cubical Triaxial Tests on Cohesionless Soil”, *Journal of the Soil Mechanics Division*, ASCE, Vol. 99, No. SM10, pp. 793-812.

Lee, D.H., Juang, C.H., Lin, H.M., and Yeh, S.H. (2002). “Mechanical Behavior of Tien-Liao Mudstone in Hollow Cylinder Tests”. *Canadian Geotechnical Journal*, vol. 39, n. 3, pp. 744-756.

Lee, K.L. and Seed, H.B. (1967), “Drained Strength Characteristics of Sands”. *J. Soil Mechanics and Foundation Division.*, ASCE, vol. 93, n. SM6, pp. 117-141.

Leshchinsky, D., (2001) “Design Dilemma: Use Peak or Residual Strength of Soil”, *Geotextiles and Geomembranes*, Vol. 19, No. 2, pp. 111-125.

Leshchinsky, D. and Boedeker, R.H., (1989) “Geosynthetic Reinforced Soil Structures”, *Journal of Geotechnical Engineering*, ASCE, Vol. 115, No. 10, pp.1459-1478.

Leshchinsky, D., and Field, D. A. (1987). “In-Soil Load Elongation, Tensile Strength and Interface Friction Angle of Nonwoven Geotextiles”. *Geosynthetics ’87*, New Orleans, p. 238-249.

Li, C., (2005), “*Mechanical Response of Fiber-Reinforced Soil”*, Ph.D. Dissertation, the University of Texas at Austin.

Ling, H.I., Cardany, C.P., Sun, L.-X., and Hashimoto, H. (2000). “Finite Element Study of a Geosynthetic-Reinforced Soil Retaining Wall with Concrete-Block Facing”. *Geosynthetics International*, ***7***(3): 163–188.

Ling, H. I., Wu, J. T. H., and Tatsuoka, F. (1992). “Short-Term Strength and Deformation Characteristics of Geotextiles under Typical Operational Conditions”. *Geotextiles and Geomembranes*, (11), p. 185-219.

Liu, J., Xiao, H.B., Tang, J., and Li, Q.S. (2004). “Analysis of Load-Transfer of Single Pile in Layered Soil”. *Computers and Geotechnics*, vol. 31, n. 2, pp. 127-135.

Lopes, M.L., Cardoso, A.S., and Yeo, K.C. (1994). “Modelling Performance of a Sloped Reinforced Soil Wall Using Creep Function”.*Geotextiles and Geomembranes*, 13:181–197.

Marachi, N., Duncan, J.M., Chan, C., and Seed, H.B., (1981), “Plane-Strain Testing of Sand”, *Laboratory Shear Strength of Soil*, Yong, R.N. and Townsend, F.C., Editors, ASTM Special Technical Publication 740, proceedings of a symposium held in Chicago, Illinois, USA, June 1980, pp. 294-302.

Montalvo, J. R., and Sickler, W. (1993), “Comparison of Geotextiles – The Correlation between Test Methods and Practical Performance”, *Proceedings of the Geosynthetics 93 Conference*, Vancouver, Canada, p. 547-559.

Morgenstern, N. R. and Price, V. E. (1965), “The Analysis of the Stability of Generalized Slip Surfaces”, *Geotechnique*, London, U.K., 15, 79-93.

Murff, J.D. (1980). “Pile Capacity in A Softening Soil”. *International Journal for Numerical and Analytical Methods in Geomechanics*, vol. 4, n. 2, pp. 185-189.

National Concrete Masonry Association, (1998), “Segmental Retaining Walls – Seismic Design Manual”, Bathurst, R.J., Editor, First Edition, Herndon, Virginia, USA, 187p

National Concrete Masonry Association, (1997), “Design Manual for Segmental Retaining Walls”, Collin, J., Editor, Second Edition, Herndon, Virginia, USA, 289 p

Nogueira, C. L. (1998) “Análise não linear de escavações e aterros.” DSc thesis, Pontifícia Universidade Católica do Rio de Janeiro, Rio de Janeiro, Brazil (in Portuguese).

Nogueira, Christianne L.; Machado Jr., José. C. (1999) “A Computational Model Based on FEM for Analysis of Seepage Problem in Unsaturated Porous Media” *Revista da Pesquisa e Pós Graduação*, v.1, p.37 - 42. (in Portuguese)

Pinto, M.I., Pereira, R.V.C., Lopes, M.L., and Mendonca, A. (1998). "Brick-Faced Retaining Walls Reinforced with Geosynthetics: A Numerical Analysis. *In Proceedings of the 6th International Conference on Geosynthetics*, Atlanta, Ga. *Edited by* R.K. Rowe. Industrial Fabrics Association International, Roseville, Minn. Vol. 2, pp. 593–596.

PLAXIS. 2005. "*Plaxis Finite Element Code for Soil and Rock Analyses*", Version 8.2, P.O. Box 572, 2600 AN Delft, The Netherlands (Distributed in the United States by GeoComp Corporation, Boxborough, MA).

Riemer, M.F., (1992), "*The Effects of Testing Conditions on the Constitutive Behavior of Loose, Saturated Sand under Monotonic Loading*", Ph.D. Dissertation, Dept. of Civil Engineering, University of California, Berkeley, California, USA.

Schanz, T., Vermeer, P.A., Bonnier, P.G., (1999), "Formulation and Verification of the Hardening-Soil Model". *Beyond 2000 in Computational Geotechnics*. Balkema, Rotterdam. pp. 281-290.

Schmertmann, G. R., Chouery-Curtis, V.E. Johnson, R.D., and Bonapart R. (1987), "Design Charts for Geogrid-Reinforced Soil Slopes", *Proc., Geosynthetics' 87 Conf.*, New Orleans, La., 108-120.

Simonini, P., Schiavo, M., Gottardi, G., and Tonni, L. (2000). "Numerical Analysis of a Model Wall Reinforced with Polypropylene Geogrids". In Proceedings of EuroGeo 2, the 2nd European Geosynthetic Conference, Bologna, Italy, 15–18 October 2000. *Edited by* A. Cancelli, D. Cazzuffi, and C. Soccodato. Patron Editore, Bologna, Italy. Vol. 1, pp. 231–236.

Sloan SW, Booker JR (1992), "Integration of Tresca and Mohr-Coulomb Constitutive Relations in Plane Strain Elastoplasticity", *International Journal for Numerical Methods in Engineering*, vol 33:pp 163-169

Sloan SW, (1987), "Substepping Schemes for the Numerical Integration of Elasto-Plastic Stress-Strain Relations", *International Journal for Numerical Methods in Engineering*, vol 24:pp 893-911

Smith IM, Griffiths DV, (1988), "Programming the Finite Element Method", *Wiley*: New York. 2nd Edition Spencer. E. (1967), "A Method of Analysis of the Stability of Embankment Assuming Parallel Inter-Slice Forces", *Geotechnique*, London, U.K., 17, 11-26.

Spencer, E (1967). "A Method of Analysis of the Stability of Embankments Assuming Parallel Inter-Slice Forces". *Geotechnique*, 24(4), p. 661-665.

Suzuki, K and Yamada, T. (2006). "Double Strain Softening and Diagonally Crossing Shear Bands of Sand in Drained Triaxial Tests". *International Journal of Geomechanics*, vol. 6, n. 6, pp. 440-446.

Tan, D., Sarma, S.K. (2008) "Finite Element Verification of An Enhanced Limit Equilibrium Method for Slope Analysis", *Geotechnique*, v 58, n 6, p 481-487

Troncone, A. (2005). "Numerical Analysis of A Landslide in Soils with Strain-Softening Behavior" *Geotechnique*, vol. 55, n. 8, pp. 585-596.

Veyera, G. E., and Charlie, W. A. (1990), "Laboratory Study of Compressional Liquefaction", *Journal of Geotechnical Engineering*, 116(5), p. 790-803

Wood, D.M (1974) "Some Aspects of The Mechanical Behavior of Kaolin under Trurly Triaxial Conditions of Stress and Strain", Ph.D. Thesis, Cambridge University.

Woodruff, R. (2003) "*Centrifuge Modeling of MSE-Shoring Composite Walls*," Master Thesis, Department of Civil Engineering, the University of Colorado, Boulder.

Worth, C.P. (1958). "Soil Behavior During Shear –Existence of Critical Voids Ratios" *Engineering* 186, 409-413.

Wright, S. G. (1990). "*UTEXAS3 A Computer Program for Slope Stability Calculations*", Austin Texas.

Wu, J. T. H. (1991). "Measuring Inherent Load-Extension Properties of Geotextiles for Design of Reinforced Structures". *Geotech. Testing J.*, 14(2), p. 157-165.

Yang K-H, Gupta R. and Zornberg J.G. (2009),"Location of Failure Plane within Narrow GRS Wall Systems", *Proceedings of the Geosynthetics 2009 Conference*, Salt Lake, Utah, February, 2009.

Yogarajah, I., and Andrawes, K.Z. (1994). "Modelling Construction Effects in Polymeric Grid Reinforced Soil Walls". In Proceedings, 5th International Conference on Geotextiles, Geomembranes and Related Products, Singapore, 5–9 September 1994. *Edited by* G.P. Karunaratne, S.H. Chew, K.S. Wong, and S.A. Tan. Vol. 1, pp. 177–182.

Yoshida, T., and Tatsuoka, F. (1997). "Deformation Property of Shear Band in Sand Subjected to Plane Strain Compression and Its Relation to Particle Characteristics". *Proceedings of the 14th International Conference on Soil Mechanics and Foundation Engineering*. Hamburg, September. Balkema, Rotterdam, pp. 237-240.

Yoshida, T., Tatsuoka, F., Siddiquee, M. S. A., and Kamegai, Y. (1993) "Shear Banding in Sands in Plane Strain Compression." *Proc., 3rd Int. Workshop Localisation and Bifurcation Theory for Soils and Rocks*, Grenoble, France, 165–179.

Zienkiewicz, O. C. (1989), "The Finite Element Method", *London; New York: McGraw-Hill,* 4th edition.

Zornberg, J.G., (2003) "Peak versus Residual Shear Strength in Geosynthetic-Reinforced Soil Design," Discussion and Response 4. *Geosynthetics International*, December, Vol. 10, No. 6, pp. 234-237

Zornberg, J.G. (2002) "Peak versus Residual Shear Strength in Geosynthetic-Reinforced Soil Design." *Geosynthetics International*, Vol. 9, No. 4, pp. 301-318.

Zornberg, J.G. (2002a) "Peak versus Residual Shear Strength in Geosynthetic-Reinforced Soil Design," Discussion and Response 1. *Geosynthetics International*, Vol. 9, No. 4, pp. 381-386.

Zornberg, J.G.,(2002b) "Peak versus Residual Shear Strength in Geosynthetic-Reinforced Soil Design," Discussion and Response 2. *Geosynthetics International*, Vol. 9, No. 4, pp. 387-390.

Zornberg, J.G.,(2002c) "Peak versus Residual Shear Strength in Geosynthetic-Reinforced Soil Design," Discussion and Response 3. *Geosynthetics International*, Vol. 9, No. 4, pp. 391-393.

Zornberg, J.G. and Arriaga, F., (2003) "Strain Distribution within Geosynthetic-Reinforced Slopes", *Journal of Geotechnical and Geoenvironmental Engineering*, ASCE, Vol. 131, No. 2, Feb., pp. 141-150.

Zornberg, J.G., (1994), "*Performance of Geotextile Reinforced Soil Structures*", Ph.D. Dissertation, Dept. of Civil Engineering, University of California, Berkeley, California, USA.

Zornberg, J. G. (1989), "Análise por Elemntos Finitos do Comportamento de Escavações Utilizando um Mofrl Elasto-Plástico", Master Thesis, Department of Civil Engineering, Pontificia Universidade Catolica do Rio de Janeiro, Brazil. (in Portuguese)

Zornberg, J.G. and Leshchinsky, D., (2001) "Comparison of International Design Criteria for Geosynthetic-Reinforced Soil Structures", *Geosynthetics and Earth Reinforcement*, H. Ochiai, J. Otani, and Y. Miyata, Editors, ISSMGE-TC9, pp. 106-117.

Zornberg, J.G., Sitar, N., and Mitchell, J.K. (1998) "Limit Equilibrium as Basis for Design of Geosynthetic Reinforced Slopes." *Journal of Geotechnical and Geoenvironmental Engineering, ASCE,* Vol. 124, No. 8, pp. 684-698.

Zornberg, J.G., and Azevedo, R.F. (1989), "Finite Element Analysis of Potential Failure Surfaces in Open-Cut Excavations using a Non-Associated Elasto-Plastic Model." *Computational Mechanics*, Argentinean Society of Computational Mechanics, AMCA, June, Vol. 7, pp. 361-374.

Vita

Kuo-Hsin Yang is the second son of Yi-Long Yang and Li-Chi Dai Yang. Kuo-Hsin was born in Tainan, Taiwan on November 05, 1978. Kuo-Hsin attended the Tainan First High School, and graduated in 1996. Kuo-Hsin entered the National Taiwan University from 1996 to 2000. After he fulfilled the obligatory military service for two years, Kuo-Hsin worked as a research assistant at the National Taiwan University with Dr. Fu-Chun Wu. During this time, Kuo-Hsin discovered his research passion on finding engineering solutions to improve living and natural environment. One year later, Kuo-Hsin started graduate studies at the University of Michigan at Ann Arbor and obtained his Master degree in 2004. Afterward, Kuo-Hsin entered the University of Texas at Austin for his doctoral degree under the supervision of Dr. Jorge Zornberg.

Kuo-Hsin received the Outstanding Undergraduate Thesis Award at National Taiwan University in 2000. Kuo-Hsin participated in the graduate engineering student paper competition at UT in 2006. His paper was ranked the top 10 papers and selected for the oral presentation. Kuo-Hsin was awarded the North America Taiwanese Engineers Association Scholarship in 2007. In 2007, Kuo-Hsin also represented UT team for the Student Paper Retaining Wall Competition at Geo-Denver conference. Their design paper was awarded the top ranked team and the travel grant. Kuo-Hsin received the Graduate Student Professional Development Award at UT in 2009. Kuo-Hsin received financial support for his doctoral study from TXDOT, Cockrell School of Engineering scholarship and graduate fellowship in Civil Engineering. Kuo-Hsin taught the undergraduate-level Geotechnical Engineering laboratory for three classes as a TA and two graduate-level courses for two semesters as a grader. To date, Kuo-Hsin has published 4 technical articles in journals, 6 papers in conferences and 3 reports (including this dissertation).

Permanent address: No. 66, Ho-Ping St.
Tainan City, 703
Taiwan, R.O.C.

This dissertation was typed by Kuo-Hsin Yang